

Fluidics of Thin Polymer Films
-
**Boundary Conditions and Interfacial
Phenomena**

Dissertation
zur Erlangung des Grades
des Doktors der Naturwissenschaften
der Naturwissenschaftlich-Technischen Fakultät II
- Physik und Mechatronik -
der Universität des Saarlandes

von

Oliver Bäumchen

Saarbrücken

2010

Tag des Kolloquiums: 30.07.2010

Dekan: Univ.-Prof. Dr. rer. nat. Ch. Becher

Mitglieder des Prüfungsausschusses:

Vorsitzender: Univ.-Prof. Dr. rer. nat. L. Santen

Gutachter: Univ.-Prof. Dr. rer. nat. K. Jacobs

Univ.-Prof. Dr. rer. nat. Ch. Wagner

Univ.-Prof. Dr. rer. nat. A. Magerl, Universität Erlangen-Nürnberg

Akademischer Mitarbeiter: Dr. rer. nat. Ch. Hoffmann

Kurzzusammenfassung

Fließprozesse auf der Mikro- und Nanometerskala sind von enormem grundlagenwissenschaftlichem Interesse und bergen, z.B. in Lab-on-a-Chip-Anwendungen, zudem großes technologisches Potential. Das Verständnis der Stabilität und Dynamik dünner Flüssigkeitsfilme erlaubt Rückschlüsse auf Wechselwirkungen an Grenzflächen und auf das Verhalten von Flüssigkeiten auf molekularer Ebene.

Dünne Polymerfilme auf hydrophoben Substraten unterliegen unterschiedlichen Entnetzungsmechanismen wie z.B. der Nukleation von Löchern. Der Fokus dieser Arbeit lag dabei im Speziellen auf der Quantifizierung der hydrodynamischen Randbedingung an der fest/flüssig Grenzfläche, der sog. Sliplänge.

Im ersten Teil wurde die Dynamik des Lochwachstums studiert. Hierbei konnte der Einfluss des Substrats auf die Entnetzungsdynamik quantifiziert werden. Zudem hat die Länge der Polymerketten einen enormen Einfluss auf die Sliplänge und somit auf das Fließverhalten. Im zweiten Teil dieser Arbeit wurde die Morphologie des Randwulstes untersucht, der das Loch umgibt. Basierend auf theoretischen Modellen konnte die Sliplänge zur Charakterisierung der Randbedingung bestimmt werden. Es zeigte sich, dass diese mit der dritten Potenz der Kettenlänge des Polymers skaliert, sobald Verhakungen auftreten. An der Grenzfläche selbst ist die Dichte dieser Verhakungen um den Faktor drei bis vier reduziert. Diese Erkenntnisse unterstreichen die Bedeutung von Polymer-Konformationen an der fest/flüssig Grenzfläche für das Fließverhalten.

Abstract

Flow processes on the micro- and nanometer scale are of enormous scientific interest and additionally hold, e.g. in lab-on-a-chip applications, large technological potential. The understanding of the stability and the dynamics of thin liquid films allows for drawing conclusions about the interactions at interfaces and on the behavior of liquids on the molecular level.

Thin polymer films on hydrophobic substrates are subject to different dewetting mechanisms such as e.g. the nucleation of holes. The focus of this study lies in particular on the quantification of the hydrodynamic boundary condition at the solid/liquid interface, the slip length.

In the first part, the dynamics of hole growth was studied. Thereby, the impact of the substrate on the dewetting dynamics is quantified. Moreover, it is found that the length of the polymer chains exerts a dominating influence on the slip length and, thus, on the flow properties. In the second part of this thesis, the morphology of the rim surrounding the hole is studied. Based on theoretical models, the slip length characterizing the boundary condition is determined. It is shown that the slip length scales with the third power of the chain length of the polymer as soon as chain entanglements occur. At the interface itself, the density of entanglements is reduced by a factor of 3 to 4. These findings emphasize the relevance of polymer conformations at the solid/liquid interface for the flow properties.

Contents

1	Introduction	9
2	Basic Principles, Theoretical Concepts and State of the Art	13
2.1	Stability of Thin Liquid Films	13
2.2	Basic Principles of Hydrodynamics, Boundary Conditions and Thin Film Models	13
2.3	Flow Dynamics of Dewetting Thin Polymer Films	14
	Addendum I - Can Liquids Slide? Stability and Dynamics of Liquids on Sur-	
	faces	17
	Addendum II - Slip Effects in Polymer Thin Films	33
3	Preparative and Experimental Techniques	55
3.1	Substrate Preparation	55
3.1.1	Materials and Preparation	56
3.1.2	Characterization by AFM and Ellipsometry	56
3.1.3	Wetting Properties	59
3.2	Preparation of Thin Polymer Films	61
4	Hole Growth Dynamics in Metastable Thin Polymer Films	63
4.1	Estimation of Relaxation Times, Shear Rates and Weissenberg Numbers	63
4.2	Evaluation of the Dewetting Exponent	65
4.3	Evaluation of the Viscous Velocity Contribution	69
4.4	Evaluation of the Slip Length	71
4.5	Summary	73
	Addendum III - Probing Slippage and Flow Dynamics of Thin Dewetting Poly-	
	mer Films	75
5	Morphological Characterization and Analysis of Liquid Rim Profiles	85
5.1	<i>In situ</i> Measurement of the Evolution of the Rim Shape	85
5.2	<i>Ex situ</i> Measurement and Analysis of the Rim Shape at fixed Hole Radii	87
5.2.1	<i>Ex situ</i> AFM Measurements of Rim Profiles	87
5.2.2	Evaluation of the Slip Length	91
5.2.3	Evaluation of the Capillary Number vs. the Ratio of Slip Length to Film Thickness	94
5.2.4	Evaluation of the Viscosity from the Rim Profile Analysis	95
5.2.5	Correlation of Slip Length, Viscosity and Friction Coefficient	98
5.3	Results and Discussion	100

5.3.1	Reduced Interfacial Entanglement Density and its Implications	100
5.3.2	Quantitative Comparison of Slip Lengths: Rim Profile Analysis vs. Hole Growth Dynamics	102
5.3.3	Viscosity of Thin Polymer Films at the Solid/Liquid Interface	105
5.3.4	Comparison with Previous Results on OTS and DTS Substrates	106
5.3.5	Viscoelastic Effects	110
5.4	Summary	111
Addendum IV - Comprehensive Analysis of Dewetting Profiles to Quantify Hydrodynamic Slip		113
Addendum V - Reduced Interfacial Entanglement Density Affects the Bound- ary Conditions of Polymer Flow		129
6	Continuative Experimental Studies	135
6.1	Impact of Polydispersity - Chain Length Specific Polymer Mixtures	135
6.2	Dewetting Experiments of PMMA Melts	137
7	Summary and Outlook	139
7.1	Summary	139
7.2	Outlook	143
Bibliography		147
Publications and Conference Contributions		153

1 Introduction

Flow processes play a huge role in many fields of science and facets of everyday life. In particular, its manifestations on very differing length scales have drawn the attention of scientists on the understanding of the flow dynamics and on the way flows of different liquids can be manipulated [1]. On macroscopic scales, flows of e.g. magma or sea currents are of extraordinary importance in earth sciences. Even granular media can show flow properties, as can be seen in the case of land slides after heavy rains. On smaller scales, everybody can observe manifold representations of flows: Water droplets roll off plant leaves such as lady's mantle or the lotus plant even at tiny inclinations, known as the *lotus effect* [2, 3]. Nowadays, many industrial processes rely on the flow of liquids confined in specially designed geometries: Oil pipelines and water tubes represent examples of such flows.

In recent years, it was shown that the condition of geometrical confinement exerts a very unique influence on the flow dynamics on microscopic scales: The no-slip boundary condition, usually assumed in the case of macroscopic flows to calculate the flow profile, fails on the micro- and nanoscale. Liquids can slip over solid surfaces and the phenomenon called *slippage* has attracted the attention of researchers. Besides the fundamental physical interest to understand this process, especially on the level of molecular liquid flow and solid-liquid interactions, many applications in the field of micro- and nanofluidics benefit from this research [4]. *Lab-on-a-chip* devices, for example, are developed to perform a large-scale integration of chemical reactions or analysis of biological fluids, on the lines of electronic integrated circuits performing calculations as fabricated by the semiconductor industry [5, 6]. In such microfluidic devices, the throughput of liquid volume is dominated by the hydrodynamic boundary condition and can be significantly enhanced if slippage is present.

The aim of this study is the understanding of flow processes of thin polymer films on the nanometer scale. In particular, the quantification of *slippage* concerning two different aspects is the main goal: First, the impact of the solid substrate on the dewetting dynamics and the morphology of liquid rims is studied. The second aspect applies to the polymer itself and the correlation between the boundary condition and interfacial phenomena on the molecular level: What is the influence of the chain length of the polymer? What happens if inter-chain entanglements become relevant for longer polymer chains? Finally, the question arises as to whether the flow of polymer chains at the solid-liquid interface deviates on the molecular scale from the behavior in the bulk.

Thin liquid films are of extraordinary importance in many fields: Lubricants minimize the friction between different parts or components of engines; coatings and paints protect surfaces from environmental influences such as corrosion. Polymeric photo-resists are utilized for the realization of nanometric structures that are extensively fabricated in the case of computer chips. The conditions of thin film stability and their dewetting dynamics in cases of unstable situations are therefore of enormous fundamental and practical interest.

Polymers are chosen as model liquids due to the refined chemical fabrication and purification possibilities. They can be obtained as nearly monodisperse liquids with different chemical properties. Their physical properties, such as viscosity, can be easily controlled. Temperatures close to the glass transition temperature of the polymer melt allow for tuning the flow dynamics over several orders of magnitude due to the unique dependence of the viscosity on temperature. Fundamental research and industrial processes concerning semiconductor fabrication and miniaturization, as mentioned above, have moreover supported the development of diverse techniques realizing thin uniform polymeric films on the nanometer scale.

Chapter 2 of this thesis covers the fundamental concepts of the stability of thin liquid films and the basic ideas of dewetting situations under non-stable conditions. In ADDENDUM I, the stability conditions of thin liquid films are discussed in particular in view of interfacial forces. Different dewetting scenarios and their characteristics are introduced. Moreover, ADDENDUM II illuminates diverse further aspects such as polymer properties and basic concepts of hydrodynamics: the Navier-Stokes equations, the *slip/no-slip* boundary condition and thin film models. This part, furthermore, includes an overview of state-of-the-art techniques to quantify slippage and a discussion of the results obtained for various configurations of liquids and surfaces with regard to diverse properties. Dewetting studies are used to obtain information about the hydrodynamic boundary condition at the solid/liquid interface. Consequently, driving forces for dewetting and the dissipation mechanisms including sliding friction are considered and discussed in detail. Moreover, recently proposed concepts concerning molecular mechanisms of slippage are also included. The analysis of experimental results presented in this study is based on the assumption of Newtonian flow. Deviations from non-Newtonian behavior caused by the relaxation of stresses was the subject of numerous studies which are also summarized. The presentation of rather new concepts such as non-linear friction and time-dependent slippage completes this chapter.

The preparation of smooth hydrophobic surfaces is the subject of the first part of **Chapter 3**. Silicon wafers are covered by a self-assembled monolayer of silanes (dodecyl-trichlorosilane (DTS) and octadecyl-trichlorosilane (OTS)) or an amorphous Teflon[®] layer, named AF 1600, to render these smooth surfaces hydrophobic. Polymer film preparation is the subject of the second part of this chapter. Based on the spin-coating technique, thin polystyrene (PS) films can be prepared on a hydrophilic surface and then transferred to the hydrophobic substrate. Finally, the substrate with the polymer film is heated above the glass transition temperature to capture the growth of holes within the polymer film and the morphology of liquid rims.

Chapter 4 contains the analysis of the growth dynamics of holes nucleated in thin polymer films. Based on the assumption of the superposition of two dissipation mechanisms, i.e. viscous friction within the liquid and sliding friction at the solid/liquid interface, first conclusions concerning the slip length can be drawn using a rather simple energy balance (as described in ADDENDUM III). Along the perimeter of the hole, polymer material is accumulated in a rim according to the conservation of mass. The *mature stage* of hole growth is characterized by a fully developed rim that is rounded by the surface tension and that grows in a self-similar manner. Besides the strong impact of the substrate on the slippage properties, the results of the analysis suggest a correlation between the slip length and polymer chain entanglements as soon as the formation of such entanglements becomes relevant. To exclude the presence of

viscoelastic effects causing non-Newtonian behavior, the chapter is introduced by a calculation and a detailed discussion of Weissenberg numbers for the present system.

As soon as the holes have reached a certain radius, the experiment is stopped by quenching the sample to room temperature. As described in **Chapter 5**, the rim is then imaged by atomic force microscopy (AFM). Morphological differences concerning the cross-sectional shape of the rim are explained and analyzed by the application of thin film models (as described in ADDENDUM IV). Variation of the polymer chain length reveals a morphological transition of the rim profile that is correlated to the interplay of chain entanglements and slippage (see ADDENDUM V). This phenomenon and its implications are in detail discussed in this chapter.

Continuative studies are subject of **Chapter 6**. The impact of the polydispersity of the polymer melt is studied by dewetting experiments using polymer mixtures that consist of two distinct chain lengths. Finally, first results of dewetting studies of a different polymer, poly(methyl methacrylate) (PMMA), are discussed.

The main results of this thesis are discussed and summarized in **Chapter 7**. Subsequently, new pathways for forthcoming studies are illuminated in an outlook section.

2 Basic Principles, Theoretical Concepts and State of the Art

2.1 Stability of Thin Liquid Films

The fundamental concept to understand the stability of thin liquid films on top of solid substrates is the *effective interface potential* [7]. This potential summarizes the relevant interactions resulting from short-range (repulsive) and long-range (attractive) van-der-Waals interactions [8]. The combination of the liquid and the surface characteristics, in particular concerning their polarizability in the case of van-der-Waals interactions, determines whether a thin liquid film is stable or whether it starts to dewet [7]. Distinct rupture mechanisms occur depending on the effective interface potential of the solid/liquid system and the thickness of the liquid film [9, 10, 11, 12]: *spinodal dewetting* and *homogeneous/heterogeneous nucleation of holes*. In the present study, thin film flow is induced by dewetting according to heterogeneous nucleation of holes. Under good preparation conditions, the density of nucleated holes is low. These holes grow and start to coalesce in a later stage. Moreover, straight liquid fronts¹ retract from the solid substrate. Subsequently, coalescence of holes and fronts leads to the formation of liquid ridges that become unstable according to the *Rayleigh-Plateau instability* (see [13, 14]) and start to decay into liquid droplets [15, 16, 17, 18, 19, 20, 21, 22]. At the end of the dewetting process, a set of droplets typically remains on the substrate. A final equilibrium configuration can be reached by further transport of liquid, which can solely occur via an equilibrium liquid film between the droplets or via the gas phase. In case of polymer melts, however, this process takes too long to be experimentally observed.

A detailed description of the stability of thin liquid films, the effective interface potential and the rupture mechanisms, in particular of spinodal dewetting, is given in ADDENDUM I.

2.2 Basic Principles of Hydrodynamics, Boundary Conditions and Thin Film Models

The theoretical models applied in this study are based on the Navier-Stokes equations and the assumption of Newtonian flow [23]. The latter implies a linear relationship between shear stress and strain. Deviations from this behavior are usually summarized as viscoelastic effects. The basic concepts of polymers, i.e. the correlation between viscosity, temperature and molecular weight, their viscoelastic properties and their properties in confined geometries are described

¹Straight fronts are caused by "floating gaps" during the transfer of the thin film from the hydrophilic to the hydrophobic substrate (see section 3.2).

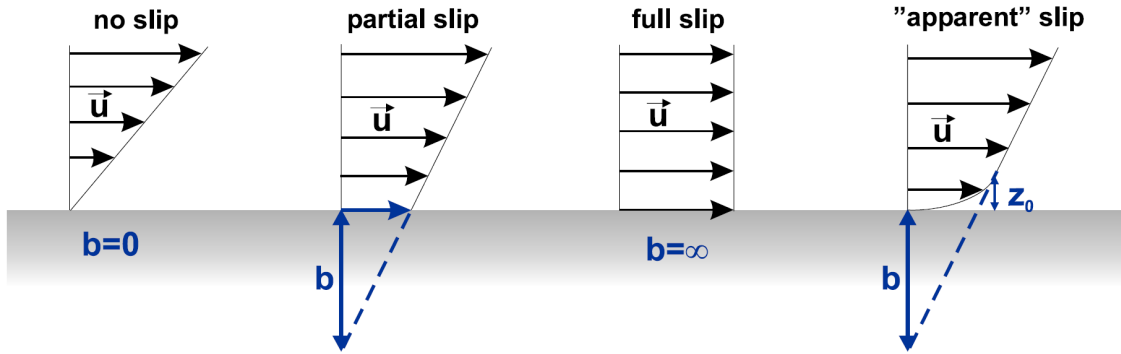


Figure 2.1: Flow velocity profiles in the vicinity of the solid/liquid interface and illustration of the slip (extrapolation) length b . "Apparent" slip is illustrated on the right: According to a thin liquid layer of thickness z_0 exhibiting a significantly reduced viscosity, the slip velocity $u_x|_{z=0}$ is zero, but a substantial slip length is measured.

in detail in ADDENDUM II. Besides the boundary condition at the free interface, i.e. the liquid/air interface, the hydrodynamic boundary condition at the solid/liquid interface has to be considered (see Fig. 2.1). This *slip/no-slip* boundary condition is of special interest for this study. As a measure for slippage, Navier introduced the slip length as the linear extrapolation length of the velocity profile in the vicinity of the solid/liquid interface [24]. Consequently, for a simple shear flow in a certain direction the slip length represents the constant of proportionality of the velocity and the velocity gradient perpendicular to the surface plane at the interface. A detailed description of the boundary conditions, an overview of established techniques (including a discussion of drawbacks) to determine the slip length and a discussion of the parameters which influence slippage are given in ADDENDUM II.

The analysis of liquid rim profiles (see Chapter 5, ADDENDUM IV and V) is based on mathematical thin film models for Newtonian liquids [25, 26, 27, 28, 29, 30]. The derivation of these models according to the *lubrication approximation* and an overview concerning their validity and applicability in view of certain slip regimes is likewise given in ADDENDUM II.

2.3 Flow Dynamics of Dewetting Thin Polymer Films

The theoretical description of the growth of heterogeneously nucleated holes in thin polymer films is based on an energy balance of the driving force for dewetting and friction mechanisms, namely viscous friction within the liquid and sliding friction at the solid liquid interface. The *spreading parameter* S describes the difference of the energy of a dry surface and of a surface covered with a liquid layer. Consequently, dewetting occurs for systems exhibiting $S < 0$. Basically, S can be written in terms of the surface tension of the liquid and the Young's contact angle of the liquid on top of the surface [31]. Assuming a no-slip boundary condition, the exclusive dissipative force is given by viscous friction of liquid molecules within the liquid itself. In this case, a linear growth of the hole radius R with time t , i.e. $R \propto t$, is expected

from a power balance [19, 32]. Assuming dominating sliding friction, on the contrary, leads to $R \propto t^{2/3}$ [22, 32]. Based on the superposition of both mechanisms [33], it was shown that a first estimation of the slip length can be obtained from hole growth measurements (as described in ADDENDUM III) [34].

A detailed survey of driving forces, energy dissipation mechanisms and further models is given in ADDENDUM II. Moreover, this article reviews and comments experimental results obtained by different groups for diverse liquid/substrate configurations. In particular, the role of viscoelastic relaxation of stresses and recently proposed models considering non-linear friction and a potential temporal evolution of the slip length are currently under debate.

Addendum I - Can Liquids Slide? Stability and Dynamics of Liquids on Surfaces

submitted to Soft Matter (invited "Highlight" article), 2010.

Authors: O. BÄUMCHEN and K. JACOBS

Department of Experimental Physics, Saarland University, D-66123 Saarbrücken, Germany.

Author contributions: The article was written by O. Bäumchen. Writing was supervised by K. Jacobs.

Abstract - Whether a lubricant or a coating wets a surface or not is of great technical importance. Theoretically, it is possible to predict the stability of a thin liquid film on a surface, since it is governed by the effective interface potential. In practice, however, a prediction can be quite cumbersome, since liquids as well as surfaces often consist of numerous components which all influence the effective interface potential. A molecular layer on a substrate's surface like a self-assembled monolayer mainly changes the short-range potential whereas the composition of the substrate below the surface determines the long-ranged interactions such as the van der Waals potential. The interplay of short- and long-range interactions determines the stability of a liquid film. If the film is not stable, distinct rupture mechanisms can be observed causing characteristic film morphologies: spinodal dewetting and dewetting by nucleation of holes, which both entail liquid flow and reveal new routes to study the hydrodynamic boundary condition at the solid/liquid interface. A rather old question turns out to become very important again: Can liquids slide? The article aims at giving a short overview of the stability and dynamics of liquids at the nanoscale.

Can liquids slide? Stability and dynamics of liquids on surfaces

Oliver Bäumchen and Karin Jacobs

Department of Experimental Physics, Saarland University, D-66123 Saarbrücken, Germany. o.baeumchen@physik.uni-saarland.de

Summary. Whether a lubricant or a coating wets a surface or not is of great technical importance. Theoretically, it is possible to predict the stability of a thin liquid film on a surface, since it is governed by the effective interface potential. In practice, however, a prediction can be quite cumbersome, since liquids as well as surfaces often consist of numerous components which all influence the effective interface potential. A molecular layer on a substrate's surface like a self-assembled monolayer mainly changes the short-range potential whereas the composition of the substrate below the surface determines the long-ranged interactions such as the van der Waals potential. The interplay of short- and long-range interactions determines the stability of a liquid film. If the film is not stable, distinct rupture mechanisms can be observed causing characteristic film morphologies: spinodal dewetting and dewetting by nucleation of holes, which both entail liquid flow and reveal new routes to study the hydrodynamic boundary condition at the solid/liquid interface. A rather old question turns out to become very important again: Can liquids slide? The article aims at giving a short overview of the stability and dynamics of liquids at the nanoscale.

1 Introduction

Thin liquid films play an important role in everyday life: Paints, coatings, lubricants and glues are demanded to form stable films on various surfaces. In the semiconductor industry, for example, stable polymeric photo-resists on Silicon wafers are utilized for chip manufacturing. Gaining control over the stability of liquid coatings is therefore also of enormous technological interest. Though the basic theoretical treatment of wetting was performed in the 1960s and 1970s [1, 2, 3] and the inspiring work of de Gennes and others in the 1980s [4, 5, 6], it was not until the 1990s that quantitative studies of the theoretical predictions were possible, either with cryogenic systems [7, 8] or with macromolecular liquids [9, 10, 11, 12, 13].

Thin film stability is governed by the effective interface potential $\phi(h)$ given as the free energy per unit area which is necessary to bring two interfaces

from infinity to a certain distance h [2, 3, 14]. In case of a thin liquid film confined between the air/liquid and the liquid/solid interface, h corresponds to the film thickness. A direct link between $\phi(h)$ and the experimental wetting properties (contact angle, pattern formation etc.) was successfully established after 2000 [15, 16, 17, 18]. Nowadays, theoretical and experimental interest concentrates on dynamical aspects of wetting, seeking again a correspondence of theory and experiments. Here, the boundary condition of the liquid in the vicinity of the substrate plays an enormous role [19, 20].

In macroscopic fluid dynamics usually a no-slip boundary condition at a wall is assumed to describe the velocity profile e.g. in a water tube or an oil pipeline. However, the no-slip boundary condition turns out to fail in case of confined geometries [21] such as micron-sized channels or gaps and also for thin liquid films (confined between the air/liquid and the liquid/solid interface). Slippage of liquid molecules strongly affects the throughput of liquid and the time scale of fluidic processes. As already introduced by Navier [22] in 1823, the hydrodynamic boundary condition is characterized by the slip length b given as the extrapolation length of the liquids' velocity profile at the solid/liquid interface (cf. Fig. 1).

For both, theorists and experimentalists, the description and the measurement of properties at the interface is a challenge. During the last years, experimental evidence for slip has been found for different solid/liquid configurations using a variety of experimental techniques [23, 24, 25]. The results promise, on the one hand, insights into fundamental aspects of non-bulk properties of liquids at interfaces and may provide, on the other hand, technical improvements for e.g. polymer extruders, injection molding machines, mixers and similar machines in the macro world. Indeed, a boundary condition that allows for a non-zero velocity component at the interface (enabling a "sliding" of the fluid) could help to significantly reduce the hydraulic resistance. Therefore, also lab-on-chip devices with channels in the micrometer range will profit from a sliding fluid, since longer or thinner channels can be filled with

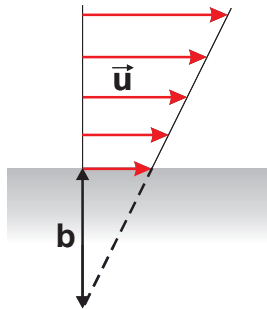


Fig. 1. Schematic representation of the definition of the slip length b as the extrapolation length of the velocity profile \mathbf{u} at a solid/liquid interface.

the same pumping power [26, 27, 28]. Promising results have been achieved for aqueous systems, where hydrophobic walls can generate a liquid/gas-type of boundary condition [29, 30].

In this article we aim to link state-of-the-art knowledge concerning thin film stability conditions and rupture mechanisms with recently obtained achievements regarding the impact of the slip boundary condition on dewetting processes. Moreover, we present two methods for determining the slip length from thin film dewetting dynamics.

2 Stability of a Liquid Film

Understanding the interplay of short- and long-range interactions is essential to judge whether or not a thin liquid film forms a stable layer on a solid substrate. The system is able to reduce its energy by minimizing its contact area with the substrate resulting in the formation of temporally growing dry patches. This process is called dewetting.

For non-ionic systems (i.e. without the incorporation of charges and electrostatic interactions), $\phi(h)$ consists of two major contributions, one of short and one of long range: Steric repulsive and chemical interactions contribute to short-range forces dominating within the first few Å. Van der Waals forces between molecules acting through a certain medium - or in this case through two interfaces separated by a liquid film - add a characteristic attractive part to the effective interface potential $\phi(h)$. In summary, we write $\phi(h)$ as a superposition of a repulsive $\phi_{rep}(h)$ and a non-retarded van der Waals potential $\phi_{vdW}(h)$:

$$\phi(h) = \phi_{rep}(h) + \phi_{vdW}(h) = \frac{C}{h^8} - \frac{A}{12\pi h^2} , \quad (1)$$

where C denotes a characteristic repulsion constant, A the Hamaker constant and h the film thickness (or in general the distance between the two interfaces). For a more detailed description of intermolecular interactions, their theoretical derivation and the determination of the Hamaker constant we refer to the book by J. Israelachvili [31].

In principle, three different morphologies of the shape of the effective interface potential can be obtained. A monotonic decrease of the effective interface potential for increasing film thickness corresponds to a *stable* liquid film covering the substrate. The liquid film is not stable, if $\phi(h)$ obtains a global minimum at a specific film thickness (cf. Fig. 2). In the *metastable* situation, the effective interface potential is additionally characterized by a potential barrier that the system has to overcome to minimize its energy (cf. Fig. 2). If the second derivative of the effective interface potential is negative, i.e. $\phi''(h) < 0$, film rupture via *spinodal dewetting* sets in (cf. section 5). The term has been coined in analogy to spinodal decomposition in a demixing

process. An detailed description of the rupture mechanisms, associated with specific shapes of the effective interface potential, is given in section 4.

The position of the minimum defines the equilibrium film thickness h_{eq} due to the fact that a stable residual film of this thickness remains after dewetting, also called the wetting layer. This has been experimentally verified by X-ray diffraction measurements for short-chained polystyrene films ($h_{eq} = 1.3 \text{ nm}$ for a molecular weight of 2 kg/mol , termed 'PS(2k)') on a Si wafer with a 191 nm SiO_2 layer [16]. For larger molecular weights, typical dimensions of polymer coils can easily exceed a theoretically predicted h_{eq} . The continuum approach of the theory then fails for the experimental system. In the experiments, dewetting films then leave dry surfaces behind. Aside from the position of the global minimum of $\phi(h)$, also its depth $\phi(h_{eq})$ is important, as it is linked to the Young's contact angle θ_Y and the surface tension of the liquid γ_{lv} [32]:

$$\frac{\phi(h_{eq})}{\gamma_{lv}} = \cos \theta_Y - 1 . \quad (2)$$

While the shape of the effective interface potential determines thin film stability or rupture, the quantitative examination of the depth of the minimum leads to the capillary driving force and, therefore, impacts the dynamics of dewetting.

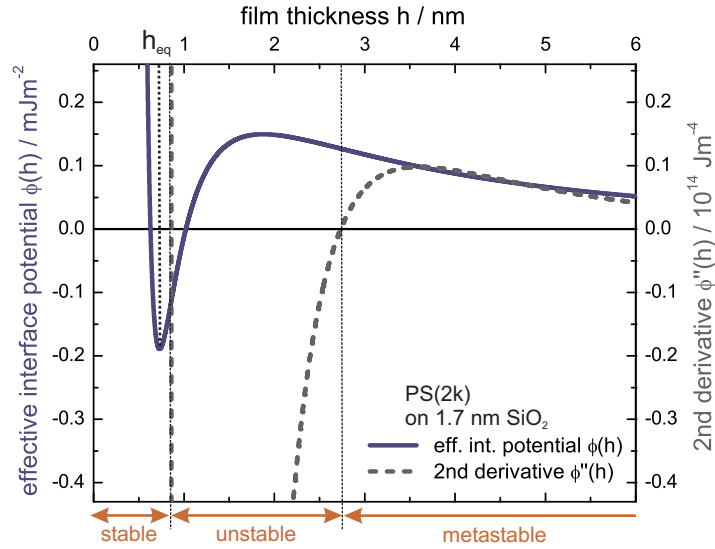


Fig. 2. Effective interface potential $\phi(h)$ (solid line) and its second derivative $\phi''(h)$ (dashed line) for a liquid polystyrene PS(2k) film prepared on a Si wafer with a 1.7 nm SiO_2 layer (taking Hamaker constants and the repulsion constant C from ref. [16]). The sign reversal of $\phi''(h)$ characterizes the stability of the film.

3 Tuning the Effective Interface Potential

A variety of possibilities exist to tune the shape of the effective interface potential $\phi(h)$ via the choice of substrate. Si wafers are usually covered with a thin native oxide layer (amorphous SiO_2), typically in the range of 1-2 nm. The shape of the effective interface potential for a liquid PS film on such a Si wafer corresponds to a metastable situation (cf. Fig. 2). Here, the PS film interacts by van der Waals forces with the SiO_2 layer as well as with the underlying Si. Considerably larger oxide thicknesses (obtained e.g. by thermal growth processing) reduce the influence of the interactions between PS and Si. A variation of the oxide layer thickness therefore substantially changes the long-range force contributions and consequently impacts the shape of the effective interface potential [16]. For sufficiently small PS film thicknesses, even an unstable situation can be obtained.

The short-range part of $\phi(h)$ can also be influenced by a judicious preparation of the substrate as it is determined by the chemical composition of the uppermost layer of atoms, which, according to Eq. (2), also influences the wettability. Self-assembled monolayers (SAMs) [33, 34] are a very versatile method to change the wetting properties and to change essentially the short range forces. By grafting a SAM of e.g. hydrocarbon chains with a hy-

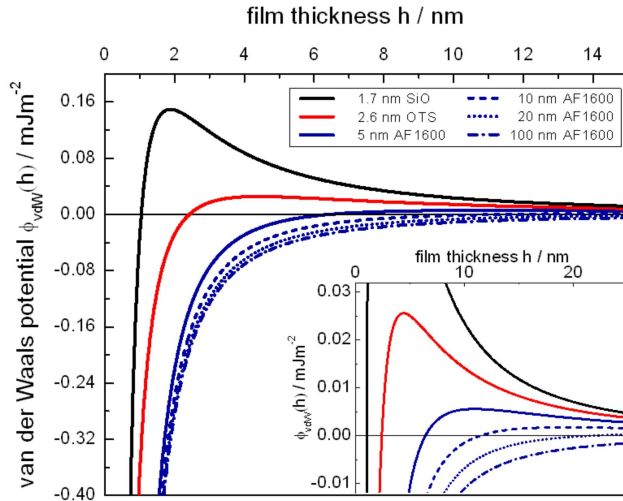


Fig. 3. Impact of an additional layer (on top of a Si wafer with a 1.7 nm oxide layer) on the long-range van der Waals potential $\phi_{vdW}(h)$: a hydrophobic self-assembled octadecyl-trichlorosilane (OTS) monolayer with $A_{OTS} = 1.9(3) \cdot 10^{-20} J$ (Hamaker constants were taken from ref. [15]) or an amorphous AF 1600 coating of thicknesses between 5 nm and 100 nm. The Hamaker constant $A_{AF1600} = 4.3(2) \cdot 10^{-20} J$ was calculated (see ref. [31]) from the dielectric properties of the material.

drophobic $-CH_3$ -terminated tail pointing towards the liquid, an intrinsically hydrophilic Si wafer can be rendered hydrophobic. Two types of SAM are widely used, *silanes*, which form covalent bonds with a SiO network, and *thiols*, which form SAMs on metal surfaces such as gold (Au) layers. The quality of a SAM, however, is inevitably correlated to careful preparation according to sophisticated procedures and recipes [35, 36, 37].

Instead of SAMs, also very thin layers (in the nm range) of macromolecules with homogeneous and controllable thickness can be utilized to influence preferentially the short-range interactions. Spin- or dip-coating techniques are used for the preparation. Examples are Teflon AF 1600 films which can be spin-coated out of solution onto a Si wafer, rendering the surface strongly hydrophobic.

As indicated, it is not possible to change the short-range interactions without also slightly influencing the long-range contributions to $\phi(h)$: Since the SAM or surface layer has a non-zero thickness, is polarizable and has a specific index of refraction, it is also affected by the long-ranged electromagnetic forces which are responsible for e.g. van der Waals interactions [31]. Consequently, the SAM or the thin layer has to be considered when calculating Hamaker constants A_{layer} for the system to determine the long-range van der Waals potential [15]:

$$\phi(h)_{vdW} = -\frac{A_{layer}}{12\pi h^2} + \frac{A_{layer} - A_{SiO_2}}{12\pi(d + d_{layer})^2} + \frac{A_{SiO_2} - A_{Si}}{12\pi(d + d_{SiO_2} + d_{layer})^2}, \quad (3)$$

where d_{layer} is the SAM or layer thickness and A_i are the Hamaker constants for the PS film interacting with the i -th component of the substrate. Fig. 3 illustrates the impact of the layer thickness d_{layer} and the Hamaker constant A_{layer} of a hydrophobic coating on the shape of the van der Waals contribution to $\phi(h)$ for a PS film.

Up to now, we exclusively considered uniform surfaces. Chemically structured substrates, however, offer the possibility to design a laterally alternating wettability and are therefore of special experimental interest. Thereby, experiments probing the impact of short- and long-range interactions can be performed simultaneously for different system configurations. Seemann *et al.* thermally evaporated thin Au (higher index of refraction n compared to amorphous SiO₂) and MgF₂ (lower n compared to amorphous SiO₂) layers through a micron-sized mask on Si wafers to locally tune the effective interface potential [15]. By preparing a thin PS(2k) film on top, distinct differences in the stability of the polymer film were enforced (cf. Fig. 4b).

Soft lithography methods [38] such as micro-contact printing (μ CP) offer further possibilities for surface structuring and allow the preparation of controlled patterns down to the nanometer range. Fig. 4a shows an example of a Au surface structured by μ CP using thiol molecules (11-mercaptoundecanoic acid).

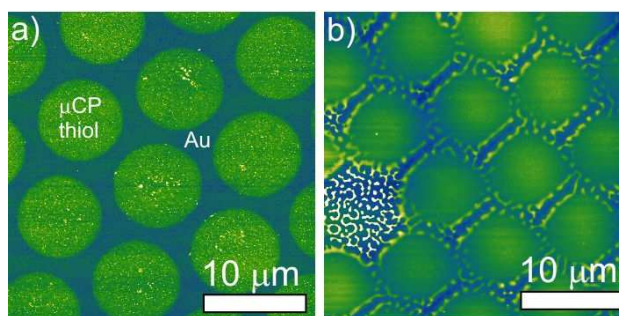


Fig. 4. Atomic force microscopy (AFM) images: a) Gold (Au) surface as a substrate for micro-contact printing (μ CP) using thiol molecules (11-mercaptoundecanoic acid). The measured step height to the Au substrate was 1.1 nm. b) 4.2(3) nm PS(2k) film on a structured surface. A 1.5(2) nm thick Au layer has been evaporated through a mask on top of a Si wafer with a 191(1) nm SiO₂ layer, resulting in circular Au patches. The sample was kept for 1.5 h at 60 °C. The Au layer stabilizes the PS film (courtesy of R. Seemann).

4 Rupture Mechanisms and Dewetting Morphologies

Polymer melts, such as atactic polystyrene (PS), that are prepared as thin films on solid, smooth substrates are ideal model systems to study the conjunction of the effective interface potential with the stability conditions and the wetting properties. 'Thin' means that gravitational forces are negligible over intermolecular (dispersion) forces, which is the case for films below the capillary length, i.e. below some hundreds of μ m thickness. Above the glass transition temperature¹, a film may become unstable, rupture and dewetting - a dynamic flow process - begins [9, 10, 13, 15, 17, 18].

In general, three major rupture mechanisms of thin liquid films can be distinguished: *Spinodal dewetting* and *nucleation of holes*, whereas the latter can be subdivided into *heterogeneous* and *homogeneous* (also called *thermal nucleation*). Fig. 5 shows typical atomic force microscopy (AFM) snapshots of experimentally observed patterns that allow a classification of the corresponding mechanisms [15]:

Fig. 5a shows the corrugated surface of a 3.9(2) nm PS(2k) film on a thick 191(1) nm SiO₂ layer, where crests and valleys become clearly observable and it can be shown that spinodal dewetting is responsible for this pattern [15]. A Fourier transform of the image (see inset) clearly reveals a preferred distance of the valleys in the pattern. Figs. 5b-c illustrate the impact of the film thickness on the dewetting pattern on wafers with a thin 2.4(2) nm SiO₂ layer. For the smaller PS film thickness of 4.1(1) nm, as shown in Fig. 5b, a set of holes within

¹ Note that the glass transition temperature of a very thin polymer film (below 100 nm) may be below the bulk glass transition temperature, see e.g. refs. [39, 40].

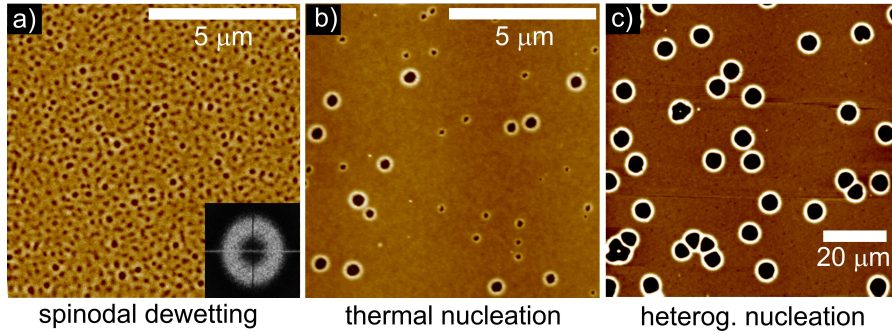


Fig. 5. Dewetting of thin PS(2k) films from Si substrates with variable oxide layer thickness (captured by AFM). The z -scale ranges from 0 (black) to 20 nm (white). a) 3.9(2) nm PS film on a Si wafer with 191(1) nm oxide layer. The inset displays a Fourier transform of the AFM image. b)-c) 2.4(2) nm thick oxide layer for variable PS film thicknesses: b) 4.1(1) nm, c) 6.6(4) nm. Adopted from ref. [15].

a uniform film surface is clearly observable. These holes exhibit randomly distributed positions and different sizes. Fig. 5c corresponds to a PS film thickness of 6.6(4) nm that also shows randomly distributed holes, but of the same size (within the experimental error bar). For a detailed description of characterizing the different dewetting patterns, the reader is referred to refs. [15, 18].

After having identified the description of the rupture mechanisms of thin liquid films, we will focus in the following on dewetting dynamics. This leads to the question whether liquids can slide or not: Section 5 describes the dynamics of spinodally dewetting liquid films, whereas section 6 focuses on growth dynamics in case of heterogeneously nucleated holes.

5 Spinodal Dewetting

Spinodal dewetting of a thin liquid film can be monitored *in situ* e.g. by AFM. A range of modes q (from 0 up to a critical wavenumber q_c) of the capillary wave spectrum gets amplified and produces detectable film thickness undulations [2]. Their amplitudes increase exponentially with time t and, as soon as they exceed the initially prepared thickness of the un-corrugated liquid film, dry spots appear and subsequently grow. Before these dry spots coalesce, the amplitude of the corrugations evolves proportional to $\exp(t/\tau)$, where τ is a time constant (see Fig. 6). According to Ruckenstein and Jain [3], τ is governed by a strong dependence on the film thickness h (i.e. $\tau \propto h^5$) and further parameters (viscosity η , surface tension of the liquid γ_{lv} and the Hamaker constant A of the solid layer in contact with the liquid):

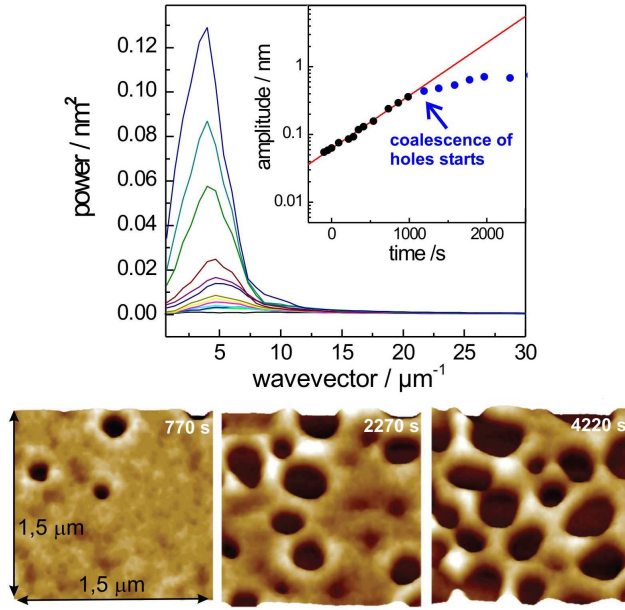


Fig. 6. Power spectral density analysis of the Fourier transforms of a temporal series of *in situ* AFM images (see below). A 3.9 nm PS(2k) film dewets spinodally from a Si wafer with a 190 nm thick oxide layer at elevated temperature of $T = 53^\circ\text{C}$. A preferred wavelength becomes clearly observable. The inset illustrates the temporal evolution of the undulation amplitude in semi-logarithmic representation. The solid line depicts a fit of an exponential growth to the experimental data. The data starts to deviate from this fit as soon as holes in the PS film coalesce. Adopted from [15].

$$\tau = 48\pi\eta\gamma_{lv}h^5/A^2. \quad (4)$$

The fastest growing mode q_0 of the capillary wave spectrum can be determined by e.g. a Fourier transform of the height data from AFM measurements (cf. inset of Fig. 5a). It is correlated to a preferred wavelength called spinodal wavelength λ_s . Already in the 1960s, Vrij [2] found that λ_s depends on the film thickness h and is given by

$$\lambda_s = \sqrt{-\frac{8\pi^2\gamma_{lv}}{\phi''(h)}}, \quad (5)$$

where $\phi''(h)$ again denotes the second derivative of $\phi(h)$ with regard to the film thickness h . For systems that can be described by $\phi(h) = -A/(12\pi h^2)$ due to long-range van der Waals forces that dominate for sufficiently large film thicknesses, $\lambda_s \propto h^2$ follows. Bischof *et al.* were able to detect thickness undulations of thin gold films on quartz substrates and experimentally confirmed the aforementioned scaling law [41]. Herminghaus *et al.* utilized

Minkowski functionals as measures for the geometry of the film surface to quantitatively analyze spinodal dewetting and nucleation in case of thin gold and liquid-crystalline films [13].

For a thin PS film on top of a Si wafer with different oxide layer thicknesses, Seemann *et al.* [16] performed measurements of the spinodal wavelength λ_s as a function of PS film thickness h and determined $\phi''(h)$ via Eq. (5). In conjunction with AFM measurements of the Young's contact angle of PS on top of the surface and the equilibrium layer thickness h_{eq} , cf. Eq. (2), a quantitative reconstruction of the effective interface potential $\phi(h)$ could be accomplished [16]. Becker *et al.* compared different experimental dewetting scenarios (nucleation and spinodal dewetting) to advanced numerical simulations under consideration of the effective interface potential for the aforementioned system [42]. The evolution of complex dewetting patterns could be well reproduced by the simulations, however, a discrepancy in dewetting dynamics as compared to the (faster) experiment has been observed. This mismatch could be recently resolved by Fetzer *et al.* demonstrating the impact of thermal fluctuations (by expanding the Navier-Stokes equations with a stochastic noise term) on thin film dynamics that cause an acceleration of film rupture in line with experimental studies [43].

A recent theoretical study by Rauscher and co-workers [44] brings a further parameter into play: slippage. The increased mobility at the solid/liquid interface for large slip lengths b is predicted to shift the preferred wavenumber q_0 to smaller values. Consequently, the spinodal wavelength λ_s is expected to be larger as compared to a no-slip substrate. The reconstruction of $\phi(h)$ in case of systems with substantial amount of slip therefore requires at least a reliable measurement of the slip length b . How to access the slip length by examination of the nucleation mechanism featuring characteristic dewetting dynamics will be described in the following two sections.

6 Nucleation and Growth of Holes

Heterogeneous nucleation of holes can be initiated by singular impurities at the solid/liquid interface, e.g. dust particles or imperfections of the surface, or even by the liquid itself according to localized stress in case of a polymer film. The impurities locally change $\phi(h)$ such that the second derivative is negative and dewetting is possible. During hole growth, the three-phase contact line radially retracts from the nucleation spot. A rim is formed along the perimeter of the hole due to conservation of liquid volume. *In situ* AFM imaging of the rim during dewetting reveals that the rim continuously enlarges with time and, as soon as it has fully developed, grows in a self-similar manner [45]. This 'mature stage' of hole growth is accompanied with a rim profile that can be described by a circular arch and is caused by the Laplace pressure in conjunction with the liquid's surface tension. Recently, Fetzer *et al.* have shown that this stage offers two distinct pathways to gain access to slippage

properties [45, 46, 47, 48, 49]. While the focus in the following section is on more simple qualitative arguments, we also provide references for quantitative analysis techniques based on theoretical hydrodynamic models.

7 How to detect Slippage?

Since the theoretical derivation by Brochard-Wyart [50, 51], measurements (mostly by optical microscopy) of the temporal evolution of the radius R of a nucleated hole has been widely used to gain information about energy dissipation mechanisms prevailing in dewetting situations. According to the power balance of the capillary driving forces [4] (given by the depth of the global minimum of $\phi(h)$) and dissipation (friction) forces, $R \propto t$ is expected for a no-slip situation [9], whereas $R \propto t^{2/3}$ is obtained if sliding friction dominates viscous dissipation within the liquid [52]. As an illustrative example, the $R(t)$ behavior for the dewetting of a Newtonian liquid, i.e. in this case an unentangled PS melt, is compared for two different substrates (cf. Fig. 7a). The occurrence of a temporally decreasing dewetting velocity is consequently, as a simple approach, a clear indication of slip at the solid/liquid interface. More elaborate models assume the additive superposition of the aforementioned dissipation mechanisms [53] at which a special data evaluation even allows to obtain an estimation for the slip length b [45].

Besides the analysis of hole growth dynamics by means of e.g. bright-field optical microscopy, AFM techniques offer a further way to access information about slippage. The shape of the rim profile in the mature stage of hole

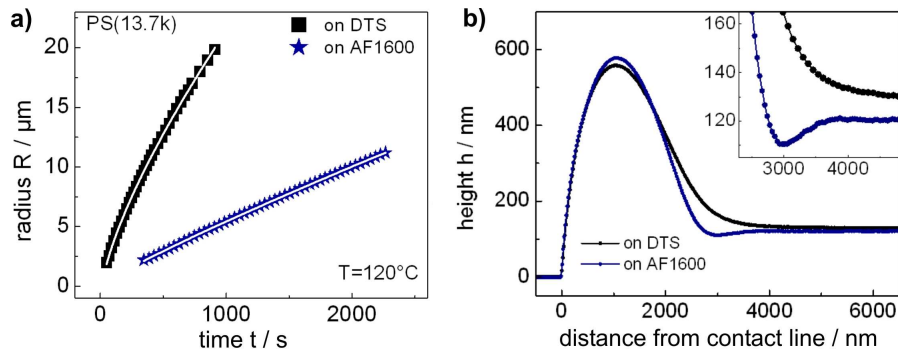


Fig. 7. a) Hole growth dynamics for PS(13.7k) at $T = 120^\circ\text{C}$ on two different substrates (a SAM made from dodecyl-trichlorosilane, termed DTS, and a 21 nm AF 1600 layer on a Si wafer) that show substantial differences in slip properties. b) Comparison of characteristic rim profiles on DTS and AF 1600. The inset illustrates morphological differences: A monotonic decay is observed on DTS (strong-slip), whereas on AF 1600 (weak-slip) a 'trough' is found. DTS data by R. Fetzer.

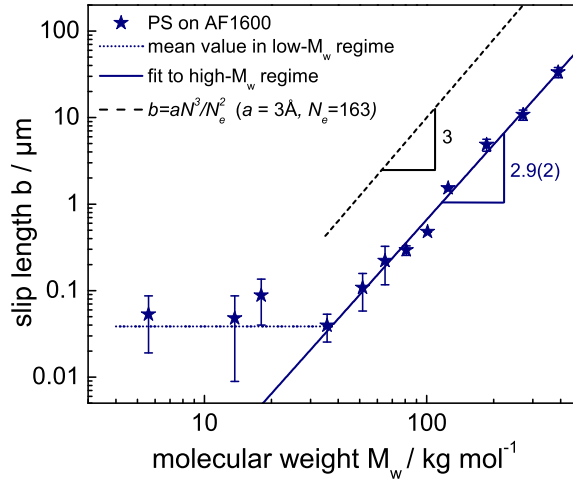


Fig. 8. PS films on AF 1600: Slip length b , obtained from the rim profile analysis, versus the molecular weight M_w [58]. Data points represent mean values of different measurements. The dotted blue line corresponds to the average of slip lengths from PS(5.61k) to PS(18k). The solid blue line is a fit to the data from PS(35.6k) to PS(390k). The dashed black line represents Eq. (6) using literature values for a and N_e . Adopted from [58].

growth, obtained by a cross-section of an AFM height image, is significantly influenced by the hydrodynamic boundary condition at the solid/liquid interface [46, 47, 48, 49]. Depending on the capillary number $Ca = \eta\dot{R}/\gamma_{lv}$, where \dot{R} denotes the current dewetting velocity, and the slip length to film thickness ratio b/h , different rim morphologies are observed (cf. Fig. 7b): The profile can be described by a monotonic exponential decay (in case of fast dewetting and large b/h) of the rim into the unperturbed film or a damped oscillation with a substantial 'trough' (for slow dewetting and small b/h). Consequently, a monotonically decaying rim compared to a profile exhibiting a trough for the same liquid properties (viscosity, surface tension) and film thickness h is a clear evidence for the presence of significantly larger slip length. A quantitative route to determine values for b requires theoretical thin film models [54, 55, 56] based on the Navier-Stokes equations applied to the aforementioned characteristic rim morphologies and is described in detail in previous publications [47, 48, 49].

Aside from the impact of the substrate on the slippage properties of a polymer melt for a fixed chain length N and viscosity (cf. Fig. 7), the liquid itself can also influence the slip length b : de Gennes predicted a scaling of $b \propto N^3$ (or alternatively $b \propto M_w^3$) for long entangled polymer chains on a passive non-adsorbing surface [57]:

$$b = a \frac{N^3}{N_e^2}, \quad (6)$$

where a denotes a polymer specific molecular size and N_e stands for the entanglement length of the polymer, i.e. the number of monomers in an entanglement strand. Recently, we were able to quantify the slip length with regard to the polymer chain length by means of the aforementioned analysis of liquid rim profiles [58]: For PS melts on AF 1600 substrates (cf. Fig. 8), de Gennes' scaling prediction can be experimentally reproduced, however, slip lengths are roughly one order of magnitude smaller than calculated from Eq. (6) by using literature values for a ($= 3\text{\AA}$) and bulk N_e ($= 163$ for PS). Keeping $a = 3\text{\AA}$, the experiments indicate a significantly (3 to 4 times) larger entanglement length or, alternatively, a lowered *effective* entanglement density in the vicinity of the substrate. This result is in line with a study of Brown and Russell [59], who expect N_e of a polymer melt near an interface to be about 4 times that in the bulk according to geometric restrictions.

8 Summary and Conclusions

To conclude, stability conditions and rupture mechanisms of thin liquid films offer various pathways to gain access to interfacial forces. Thin film rupture results in diverse dewetting scenarios and morphologies that have shown to be influenced by processes at the solid/liquid interface on the molecular level: Liquids can slide over solid surfaces. The molecular picture, however, is still unclear and is subject of ongoing studies. Interfacial interactions and the interplay of driving forces and dissipation mechanisms are of extraordinary importance in view of a variety of systems that are not restricted to thin polymer films. Even beyond these aspects, tailoring the effective interface potential opens up manifold perspectives for further chemical or biological systems [60, 61, 62, 63]. Thereby, spatially structured substrates enable a direct and simultaneous experimental comparison of the impact of different surface properties and layer compositions.

Acknowledgements

The authors acknowledge financial support from the German Science Foundation (DFG) under grants JA905/3 within the priority program 1164 '*Micro- and Nanofluidics*' and GRK 1276.

References

1. J. W. Cahn, *J. Chem. Phys.*, 1965, **42**, 93.

2. A. Vrij, *Discuss. Faraday Soc.*, 1966, **42** 23.
3. E. Ruckenstein and R. K. Jain, *J. Chem. Soc. Faraday Trans. II*, 1974, **70**, 132.
4. P.-G. De Gennes, *Rev. Mod. Phys.*, 1985, **57**, 827.
5. S. Dietrich, in *Phase Transition and Critical Phenomena*, ed. C. Domb and J. L. Lebowitz, Vol. 12, Academic Press, London, 1988.
6. M. Schick, in *Liquids at Interfaces*, eds. J. Charvolin *et al.*, Elsevier Science, Amsterdam, 1989.
7. J. E. Rutledge and P. Taborek, *Phys. Rev. Lett.*, 1992, **69**, 937.
8. S. Herminghaus, J. Vorberg, H. Gau, R. Conradt, D. Reinelt, H. Ulmer, P. Leiderer, and M. Przyrembel, *Ann. Physik*, 1997, **6**, 425.
9. C. Redon, F. Brochard-Wyart and F. Rondelez, *Phys. Rev. Lett.*, 1991, **66**, 715.
10. G. Reiter, *Phys. Rev. Lett.*, 1992, **68**, 75.
11. R. Yerushalmi-Rozen, J. Klein and L. J. Fetters, *Science*, 1994, **263**, 793.
12. R. Xie, A. Karim, J. F. Douglas, C. C. Han, and R. A. Weiss, *Phys. Rev. Lett.*, 1998, **81**, 1251.
13. S. Herminghaus, K. Jacobs, K. Mecke, J. Bischof, A. Fery, M. Ibn-Elhaj, and S. Schlagowski, *Science*, 1998, **282**, 916.
14. M. B. Williams and S. H. Davis, *J. Colloid Interface Sci.*, 1982, **90**, 220.
15. R. Seemann, S. Herminghaus and K. Jacobs, *J. Phys.: Condens. Matter*, 2001, **13**, 4925.
16. R. Seemann, S. Herminghaus and K. Jacobs, *Phys. Rev. Lett.*, 2001, **86**, 5534.
17. R. Seemann, S. Herminghaus, C. Neto, S. Schlagowski, D. Podzimek, R. Konrad, H. Mantz, and K. Jacobs, *J. Phys.: Condens. Matter*, 2005, **17**, 267.
18. K. Jacobs, R. Seemann and S. Herminghaus, in *Polymer Thin Films*, ed. O. K. C. Tsui and T. P. Russell, World Scientific, Singapore, 2008.
19. M. Rauscher and S. Dietrich, *Annu. Rev. Mater. Res.*, 2008, **38**, 143.
20. L. Bocquet and E. Charlaix, *Chem. Soc. Rev.*, 2010, **39**, 1073.
21. L. Bocquet and J.-L. Barrat, *Soft Matter*, 2007, **3**, 685.
22. C. L. M. H. Navier, *Mem. Acad. Sci. Inst. Fr.*, 1823, **6**, 389 and 432.
23. C. Neto, D. R. Evans, E. Bonaccorso, H.-J. Butt, and V. S. J. Craig, *Rep. Prog. Phys.*, 2005, **68**, 2859.
24. E. Lauga, M. P. Brenner and H. A. Stone, in *Springer Handbook of Experimental Fluid Mechanics*, ed. C. Tropea, A.L. Yarin, and J. F. Foss, Springer, Berlin Heidelberg New York, 2007.
25. O. Bäumchen and K. Jacobs, *J. Phys.: Condens. Matter*, 2010, **22**, 033102.
26. T. Thorsen, S. J. Maerkl and S. R. Quake, *Science*, 2002, **298**, 580.
27. T. M. Squires and S. R. Quake, *Rev. Mod. Phys.*, 2005, **77**, 977.
28. D. C. Leslie, C. J. Easley, E. Seker, J. M. Karlinsey, M. Utz, M. R. Begley, and J. P. Landers, *Nature Physics*, 2009, **5**, 231.
29. D. C. Trethewey and C. D. Meinhart, *Phys. Fluids*, 2002, **14**, L9.
30. D. C. Trethewey and C. D. Meinhart, *Phys. Fluids*, 2002, **16**, 1509.
31. J. Israelachvili, *Intermolecular and Surface Forces*, Academic Press, New York, 2nd edition, 1992.
32. A. N. Frumkin, *J. Phys. Chem. USSR*, 1938, **12**, 337.
33. F. Schreiber, *Prog. Surf. Sci.*, 2000, **65**, 151.
34. F. Schreiber, *J. Phys.: Condens. Matter*, 2004, **16**, R881.
35. S. R. Wasserman, Y.-T. Tao and G. M. Whitesides, *Langmuir*, 1989, **5**, 1074.
36. S. R. Wasserman, G. M. Whitesides, I. M. Tidswell, B. M. Ocko, P. S. Pershan, and J. D. Axe, *J. Am. Chem. Soc.*, 1989, 111, 5852.

37. J. B. Brzoska, I Ben Azouz and F. Rondelez, *Langmuir*, 1994, **10**, 4367.
38. Y. Xia and G. M. Whitesides, *Angew. Chem. Int. Ed.*, 1998, **37**, 550.
39. J. L. Keddie, R. A. L. Jones and R. A. Cory, *Europhys. Lett.*, 1994, **27**, 59.
40. S. Herminghaus, K. Jacobs and R. Seemann, *Eur. Phys. J. E*, 2001, **5**, 531.
41. J. Bischof, D. Scherer, S. Herminghaus, and P. Leiderer, *Phys. Rev. Lett.*, 1996, **77**, 1536.
42. J. Becker, G. Grün, R. Seemann, H. Mantz, K. Jacobs, K. R. Mecke, and R. Blossey, *Nature Materials*, 2003, **2**, 59.
43. R. Fetzer, M. Rauscher, R. Seemann, K. Jacobs, and K. Mecke, *Phys. Rev. Lett.*, 2007, **99**, 114503.
44. M. Rauscher, R. Blossey, A. Münch, and B. Wagner, *Langmuir*, 2008, **24**, 12290.
45. R. Fetzer and K. Jacobs, *Langmuir*, 2007, **23**, 11617.
46. R. Fetzer, K. Jacobs, A. Münch, B. Wagner, and T. P. Witelski, *Phys. Rev. Lett.*, 2005, **95**, 127801.
47. R. Fetzer, M. Rauscher, A. Münch, B. A. Wagner, and K. Jacobs, *Europhys. Lett.*, 2006, **75**, 638.
48. R. Fetzer, A. Münch, B. Wagner, M. Rauscher, and K. Jacobs, *Langmuir*, 2007, **23**, 10559.
49. O. Bäümchen, R. Fetzer, A. Münch, B. Wagner, and K. Jacobs, in *IUTAM Symposium on Advances in Micro- and Nanofluidics*, ed M. Ellero, X. Hu, J. Fröhlich and N. Adams, Springer, 2009.
50. F. Brochard-Wyart, P.-G. De Gennes, H. Hervet, and C. Redon, *Langmuir*, 1994, **10**, 1566.
51. F. Brochard-Wyart, G. Debregeas, R. Fondecave, and P. Martin, *Macromolecules*, 1997, **30**, 1211.
52. C. Redon, J. B. Brzoska and F. Brochard-Wyart, *Macromolecules*, 1994, **27**, 468.
53. K. Jacobs, R. Seemann, G. Schatz, and S. Herminghaus, *Langmuir*, 1998, **14**, 4961.
54. A. Oron, S. H. Davis and S.G. Bankoff, *Rev. Mod. Phys.*, 1997, **69**, 931.
55. K. Kargupta, A. Sharma and R. Khanna, *Langmuir*, 2004, **20**, 244.
56. A. Münch, B. A. Wagner and T. P. Witelski, *J. Eng. Math.*, 2005, **53**, 359.
57. P. G. de Gennes, *C.R. Seances Acad. Sci. Ser. B*, 1979, **288**, 219.
58. O. Bäümchen, R. Fetzer and K. Jacobs, *Phys. Rev. Lett.*, 2009, **103**, 247801.
59. H. R. Brown and T. P. Russell, *Macromolecules*, 1996, **29**, 798.
60. M. Bellion, L. Santen, H. Mantz, H. Hähl, A. Quinn, A. Nagel, C. Gilow, C. Weitenberg, Y. Schmitt, and K. Jacobs, *J.Phys.: Condens. Matter*, 2008, **20**, 404226.
61. A. Quinn, H. Mantz, K. Jacobs, M. Bellion, and L. Santen, *Europhys. Lett.*, 2008, **81**, 56003.
62. K. Autumn, M. Sitti, Y. C. A. Liang, A. M. Peattie, W. R. Hansen, S. Sponberg, T. W. Kenny, R. Fearing, J. N. Israelachvili, and R. J. Full, *Proc. Natl. Acad. Sci. USA*, 2002, **99**, 12252.
63. G. Huber, H. Mantz, R. Spolenak, K. Mecke, K. Jacobs, S. N. Gorb, and E. Arzt, *Proc. Natl. Acad. Sci. USA*, 2005, **102**, 16293.

Addendum II - Slip Effects in Polymer Thin Films

Journal of Physics: Condensed Matter **22**, 033102 (2010).

Authors: O. BÄUMCHEN and K. JACOBS

Department of Experimental Physics, Saarland University, D-66041 Saarbrücken, Germany.

Author contributions: The article was written by O. Bäumchen. Writing was supervised by K. Jacobs.

Abstract - Probing the fluid dynamics of thin films is an excellent tool for studying the solid/liquid boundary condition. There is no need for external stimulation or pumping of the liquid, due to the fact that the dewetting process, an internal mechanism, acts as a driving force for liquid flow. Viscous dissipation, within the liquid, and slippage balance interfacial forces. Thus, friction at the solid/liquid interface plays a key role towards the flow dynamics of the liquid. Probing the temporal and spatial evolution of growing holes or retracting straight fronts gives, in combination with theoretical models, information on the liquid flow field and, especially, the boundary condition at the interface. We review the basic models and experimental results obtained during the last several years with exclusive regard to polymers as ideal model liquids for fluid flow. Moreover, concepts that aim to explain slippage on the molecular scale are summarized and discussed.

TOPICAL REVIEW

Slip effects in polymer thin films

O Bäumchen and K Jacobs

Department of Experimental Physics, Saarland University, D-66041 Saarbrücken, Germany

E-mail: k.jacobs@physik.uni-saarland.de

Received 10 September 2009, in final form 11 November 2009

Published 16 December 2009

Online at stacks.iop.org/JPhysCM/22/033102**Abstract**

Probing the fluid dynamics of thin films is an excellent tool for studying the solid/liquid boundary condition. There is no need for external stimulation or pumping of the liquid, due to the fact that the dewetting process, an internal mechanism, acts as a driving force for liquid flow. Viscous dissipation, within the liquid, and slippage balance interfacial forces. Thus, friction at the solid/liquid interface plays a key role towards the flow dynamics of the liquid. Probing the temporal and spatial evolution of growing holes or retracting straight fronts gives, in combination with theoretical models, information on the liquid flow field and, especially, the boundary condition at the interface. We review the basic models and experimental results obtained during the last several years with exclusive regard to polymers as ideal model liquids for fluid flow. Moreover, concepts that aim to explain slippage on the molecular scale are summarized and discussed.

(Some figures in this article are in colour only in the electronic version)

Contents

1. Introduction	
2. Basic theoretical concepts	
2.1. Polymer properties	
2.2. Navier–Stokes equations	
2.3. Free interface boundary condition	
2.4. Slip/no-slip boundary condition	
2.5. Thin film equation for Newtonian liquids	
3. Flow dynamics of thin polymer films—experimental studies and theoretical models	
3.1. Dewetting dynamics—driving forces	
3.2. Dewetting dynamics—dissipation mechanisms	
3.3. Dynamics of growing holes	
3.4. Molecular mechanisms of slippage	
3.5. Impact of viscoelasticity and stress relaxation	
3.6. Non-linear friction	
3.7. Temporal evolution of the slip length	
4. Conclusions and outlook	
Acknowledgments	
References	

1. Introduction

1	Understanding liquid flow in confined geometries plays a huge role in the field of micro- and nanofluidics [1]. Nowadays, microfluidic or ‘lab-on-chip’ devices are utilized in a wide range of applications. Pure chemical reactions, as well as biological analysis performed on such a microfluidic chip, allow high performance with only small amounts of chemicals being needed. Thus, analogies to electronic large-scale integrated circuits are evident. Thorsen <i>et al</i> fabricated a microfluidic chip with a high density of micromechanical valves and hundreds of individually addressable chambers [2]. Recent developments tend to avoid huge external features such as pumps to control the flow by designing analogs to capacitors, resistors or diodes that are capable of controlling currents in electronic circuits [3].
3	
3	
5	
6	
6	
7	
10	
10	
11	
14	
14	
15	
16	
17	
17	
18	

polydisperse liquids or mixtures, a low dispersity according to lower velocity gradients perpendicular to the flow direction is generated. Confined geometries are realized in various types of experiments: the physics and chemistry of the imbibition of liquids by porous media is of fundamental interest and enormous technological relevance [4]. Channel-like three-dimensional structures can be used to artificially model the situation of fluids in confinement. Moreover, the small gap between a colloidal probe and a surface filled with a liquid (e.g. realized in surface force apparatus or colloidal probe atomic force microscopy experiments) is a common tool to study liquid flow properties. Besides the aforementioned experimental systems, knowledge in preparation of thin polymer films has been extensively gained due to its enormous relevance in coating and semiconductor processing technology. Such a homogeneous nanometric polymer film supported by a very smooth substrate, as for example a piece of a silicon (Si) wafer, exhibits two relevant interfaces, the liquid/air and the substrate/liquid interface. Si wafers are often used due to their very low roughness and controllable oxide layer thickness. Yet, also highly viscous and elastically deformable supports, such as e.g. polydimethylsiloxane (PDMS) layers, are versatile substrates.

The stability of a thin film is governed by the effective interface potential ϕ as a function of film thickness h . In the case of dielectric systems, $\phi(h)$ is composed of an attractive van der Waals part and a repulsive part [5–8]. For the description of the van der Waals forces of a composite substrate, the layer thicknesses and their respective polarization properties have to be taken into account [9]. Therefore, three major situations of a thin liquid film have to be distinguished: *stable*, *unstable* and *metastable* films. As illustrated in figure 1 by the typical curves of $\phi(h)$, a *stable* liquid film is obtained if the effective interface potential is positive and monotonically decaying (cf curve (1) in figure 1). The equilibrium film thickness h_{eq} is infinite and the liquid perfectly wets the substrate. In the case of a global minimum of $\phi(h)$, curves (2) and (3) in figure 1, the system can minimize its energy and a finite value for h_{eq} results. The *metastable* situation is further characterized by a potential barrier that the system has to overcome to reduce its potential energy (cf curve (2) in figure 1). Curves (3) and (4) characterize *unstable* conditions, since every slight fluctuation in film height will drive the system towards the global minimum. The wettability of the substrate by the liquid is correlated to the depth of the minimum at $\phi(h_{eq})$. The deeper the global minimum of ϕ , the larger the equilibrium contact angle of the liquid on the surface is. A nearly 180° situation is depicted by curve (4) in figure 1.

For a 100 nm polystyrene (PS) film on a hydrophobized Si wafer with a native oxide layer, dewetting starts after heating the sample above the glass transition temperature of the polymer. Holes nucleate according to thermal activation or nucleation spots (dust particles, inhomogeneities of the substrate or of the polymer film) and grow with time, cf figure 2. The subsequent stages of dewetting are characterized by the formation of liquid ridges through the coalescence of growing holes and traveling fronts. Very thin films in the range of several nanometers may become unstable and can

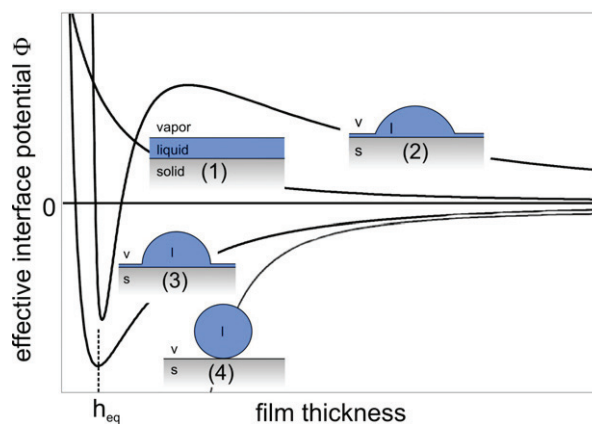


Figure 1. Different shapes of the effective interface potential $\phi(h)$ associated with different wetting conditions. Curve (1) characterizes a *stable* liquid film. Curve (2) represents a *metastable*, curve (3) and (4) an *unstable* situation.

dewet according to thermally induced capillary modes, which are amplified by forces contributing to the effective interface potential. This phenomenon is characterized by the occurrence of a preferred wavelength and is called *spinodal dewetting*. To study thin film flow with regard to the influence of slippage, specially nucleated holes enable an easy experimental access for temporal and spatial observation.

While fronts retract from the substrate and holes grow, a liquid rim is formed at the three-phase contact line due to conservation of liquid volume. A common phenomenon is the formation of liquid bulges and ‘fingers’ due to the fact that the liquid rim becomes unstable, similar to the instability of a cylindrical liquid jet that beads up into droplets (e.g. in case of a water tap). This so-called *Rayleigh–Plateau instability* is based on the fact that certain modes of fluctuation become amplified and surface corrugations of a characteristic wavelength become visible. If two holes coalesce, a common ridge builds up, that in the end decays into single droplets due to the same mechanism. The final stage is given by an equilibrium configuration of liquid droplets arranged on the substrate exhibiting a static contact angle. Actually, the final state would be one single droplet, since the Laplace pressure in droplets of different size varies. Yet, a substantial material transport must take place, either through the gas phase or via an equilibrium film between the droplets. This phenomenon is also called *Ostwald ripening*. In polymeric liquids, these transport pathways are usually extremely slow so that a network-like pattern of liquid droplets is already termed ‘final stage’. Besides the dynamics and stability of thin liquid films driven by inter-molecular forces, a recent article by Craster and Matar reviews further aspects, such as e.g. thermally or surfactant driven flows [11].

In the first part of this topical review, basic concepts from hydrodynamic theories in the bulk situation to corresponding models with regard to confinement are introduced. Polymers are regarded as ideal model liquids due to their low vapor pressure, the available chemical purity and, furthermore, the fact that their viscosity can be controlled in a very reliable manner. By setting the viscosity via temperature,

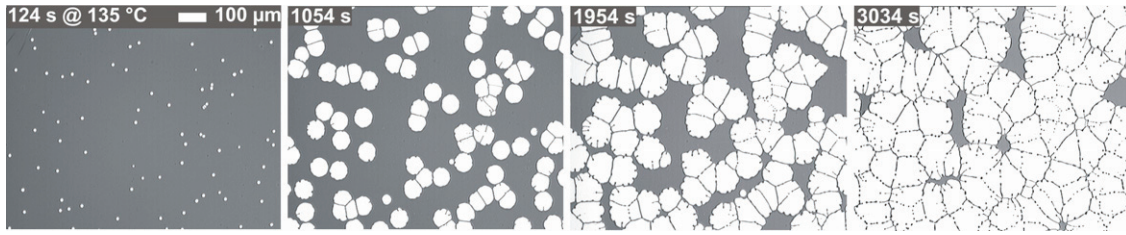


Figure 2. Dewetting of a 80 nm PS(65 kg mol^{-1}) film at $T = 135 \text{ °C}$ from a hydrophobized Si substrate captured by optical microscopy (adapted with permission from [10]. Copyright 2000 by Springer Science + Business Media).

the experimental conditions can be tuned so that dewetting dynamics can be easily captured. Mass conservation can safely be assumed, which consequently simplifies the theoretical description. The dewetting dynamics governed by the driving forces and the mechanisms of energy dissipation will also be discussed with regard to the shape of liquid ridges. The second part summarizes experimental studies concerning the dynamics of two different dewetting geometries: straight front geometry and the growth of holes. The influence of parameters such as dewetting temperature, viscosity and molecular weight of the polymer will be discussed in detail. Moreover, we focus on various scenarios at the solid/liquid interface on the molecular level. Simulations such as, for example, molecular-dynamic (MD) studies help to obtain more information and are supportive to gaining insight into the molecular mechanism of slippage.

2. Basic theoretical concepts

In this section, we aim to describe the main concepts of fluid dynamics, especially in a confined geometry. Depending on the type of liquid, viscous or even viscoelastic effects have to be considered, and deviations from Newtonian behavior might become non-negligible. Since we concentrate in this article on polymer melts, viscosity and viscoelasticity can be varied by chain length and branching of the polymer. An important aspect of a moving liquid is the velocity profile.

2.1. Polymer properties

For a comprehensive understanding of slippage, some important polymer properties such as glass transition temperature, viscosity and viscoelasticity have to be taken into account. Especially in geometries like those in a liquid film, confinement effects are a concern. A detailed description can be found in textbooks [12, 13].

2.1.1. Polymer physics. Polymers are synthesized by polymerization of monomers of molar mass M_{mono} . To characterize the polydispersity of polymer chains in a solution or in a melt, the polydispersity index M_w/M_n is calculated as the ratio of mean values given by the weight M_w and number averaged molecular weight M_n . Polymers are able to change their conformations. The radius of gyration characterizes the spatial dimension of the polymer and is given as the mean square displacement between monomers and the polymer's

center of mass. In an isotropic configuration, the shape of the polymer chain can be approximated as a spherical entity. Polystyrene, abbreviated PS, which is commonly used as a melt in dewetting experiments, is a linear homopolymer with $M_{\text{mono}} = 104 \text{ g mol}^{-1}$. In addition to other properties concerning the micro-structure of polymer chains such as the tacticity and the architecture (linear, branched, ring-shaped), physical properties are of special interest. If a melt is heated above its glass transition temperature T_g , a phase transition from the glassy phase to the liquid phase occurs and the polymer becomes liquid. Randomly structured macromolecules such as atactic polymers avoid the formation of semi-crystalline domains below T_g and exhibit a purely amorphous phase. The glass transition of a bulk polymer or of a polymeric thin film can be observed, e.g. via probing its linear expansion coefficient. Although the glass transition is based on a kinematic effect and does not occur due to a rearrangement process of polymer chains. Therefore, the glass transition usually takes place at a specific temperature range and not at an exactly allocable temperature. According to the increased mobility of shorter chains, their glass transition temperature is decreased significantly. For PS with a sufficiently large chain length, $T_g = 100 \text{ °C}$.

The viscosity η of a polymer melt measures the inner friction of polymer chains and governs the timescale of flow processes. Due to the fact that the mobility of chains increases while the temperature increases, the viscosity decreases. Internal stresses relax and dynamical processes proceed faster. The most common description of the functional dependency of the viscosity η of a polymer on temperature T was developed by Williams, Landel and Ferry:

$$\eta = \eta_g \exp \frac{B(T_g - T)}{f_g(T - T_\infty)}. \quad (2.1)$$

In this so-called WLF-equation, η_g denotes the viscosity at T_g , B an empirically obtained constant, T_∞ the so-called Vogel temperature and f_g the free liquid volume fraction.

Besides the above discussed impact of temperature on the viscosity of a polymer melt, the molecular weight M_w also strongly influences η . While M_w increases, the chain mobility decreases and, therefore, the relaxation times and, thus, η increase. For sufficiently small M_w , the Rouse model predicts a linear increase of η for increasing M_w . At this point, another characteristic number of polymer physics has to be introduced: the critical chain length for entanglements M_c . Above M_c , the polymer chains form chain entanglements exhibiting a specific

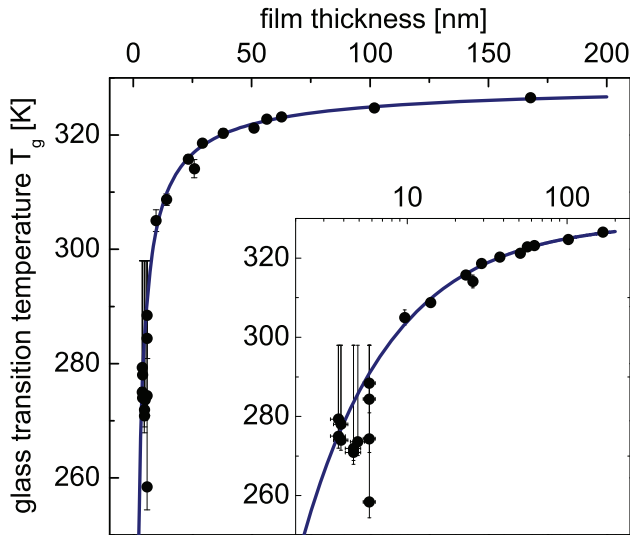


Figure 3. Glass transition temperature T_g of polystyrene films of 2 kg mol^{-1} against film thickness (adapted from [21]).

mean strand length called *entanglement length* M_e . For PS, $M_c = 35 \text{ kg mol}^{-1}$ and $M_e = 17 \text{ kg mol}^{-1}$ is found [12]. According to the reptation model of de Gennes [14], the viscosity increases more strongly in the presence of chain entanglements and an algebraic behavior of $\eta \propto M_w^3$ is expected. Empirically, the linear regime below M_c is well reproduced, above M_c an exponent of 3.4 is experimentally found for different polymers. For a detailed description of chemical and physical properties of polymers, as well as for the Rouse or the reptation theory, we refer to the book *Polymer Physics* by Rubinstein and Colby [12].

2.1.2. Properties in confined geometries. In contrast to the bulk situation, where volume properties of the polymers are measured, liquids in confined geometries, such as a thin film, often show deviations from the behavior in the volume due to additional interface effects. One of these properties is the aforementioned glass transition temperature. It has been shown in numerous studies, that T_g changes with film thickness h . On the one hand, in cases of free-standing or supported films exhibiting no or repulsive interactions with the substrate, $T_g(h)$ decreases with decreasing film thickness [15–18]. On the other hand, Keddie and Jones have shown that an increase in the glass transition temperature with decreasing film thickness is possible for attractive interactions between the substrate and the polymer film [19]. The influence of the interfacial energy on the deviation of T_g from its bulk value has been studied and quantified by Fryer *et al* for different polymers [20]. In the case of PS on a solid support, a significant change of T_g is found for films thinner than 100 nm (see figure 3) [21]. For PS(2k) below 10 nm for instance, the glass transition temperature and the viscosity of the polymer film are affected such that these films are liquid at room temperature and may dewet spinodally.

Several attempts have been made to explain the change of T_g according to the film thickness. Besides interface-related effects such as reorientation of polymer chains or accumulation of chain-ends at the interface, finite-size effects

have been proposed to be responsible. Herminghaus *et al* discussed the strain relaxation behavior of thin viscoelastic polymer films with regard to surface melting and the shift of the glass transition temperature [21]. Kawana and Jones studied the thermal expansivity of thin supported polymer films using ellipsometry and attributed their results concerning T_g to a liquid-like surface layer [22], a result that was also found by other authors [23, 24]. Besides confinement effects on T_g , further interface-related phenomena have been studied: Si *et al* have shown that polymers in thin films are less entangled than bulk polymers and that the effective entanglement molecular weight M_e is significantly larger than the bulk value [25].

2.1.3. Viscosity and viscoelasticity. One of the major characteristics of a liquid in general, or a polymer in particular, is its viscosity η . Applying shear stress σ to a liquid usually causes it to react with a strain γ . If stress and strain rate $\dot{\gamma}$ are proportional, the fluid is called *Newtonian*. The constant of proportionality is identified as the viscosity η of the liquid.

$$\sigma = \eta \dot{\gamma}. \quad (2.2)$$

Liquids such as long-chained polymers show a shear-rate-dependent viscosity $\eta(\dot{\gamma})$ due to the fact that the liquid molecules are entangled. If the viscosity increases while shearing the liquid, we call this behavior *shear thickening*, whereas in case of lowered viscosity so-called *shear thinning* is responsible. In contrast to the elastic deformation of a solid, a deformation of a *viscoelastic* liquid might induce an additional flow and can relax on a specific timescale τ . On short timescales ($t < \tau$), the liquid behaves in an elastic, on long timescales ($t > \tau$) in a viscous manner. Strain γ is thereby connected to stress σ via the elastic modulus G of the liquid:

$$\sigma = G\gamma. \quad (2.3)$$

To cover the stress relaxation dynamics of a polymer film, several modeling attempts have been proposed. Mostly, so-called *Maxwell* or *Jeffreys* models are applied. The simplest model is the *Maxwell* model (see figure 4), which assumes a serial connection of a perfectly elastic element (represented by a spring) and a perfectly viscous one (represented by a dashpot). Consequently, the total shear strain γ is given by the sum of the corresponding shear strains γ_e and γ_v of both mechanisms:

$$\gamma = \gamma_e + \gamma_v. \quad (2.4)$$

With (2.3) and (2.2), we get

$$\sigma = G_M \gamma_e = \eta_M \dot{\gamma}_v \quad (2.5)$$

since both react on the same shear stress σ . Therefore, the ratio of viscosity of the viscous element to the elastic modulus of the elastic one can be identified with a specific timescale, the relaxation time τ_M :

$$\tau_M = \frac{\eta_M}{G_M}. \quad (2.6)$$

The relaxation of stress after a step strain γ leads to a time-dependent stress function $\sigma(t)$ for a viscoelastic liquid. Due

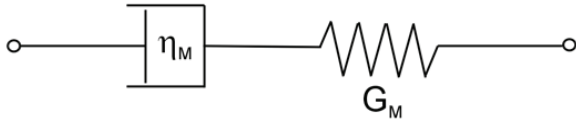


Figure 4. Maxwell model represented by a dashpot and a spring in a serial connection.

to the fact that the total strain γ is constant, a first order differential equation for the time-dependent strain $\gamma_v(t)$ is obtained:

$$\tau_M \dot{\gamma}_v = \gamma - \gamma_v(t). \quad (2.7)$$

Solving this differential equation using the initial condition $\gamma_v(t = 0) = 0$ gives a simple exponential decay of $\sigma(t)$ on the timescale of the stress relaxation time τ_M in the Maxwell model:

$$\begin{aligned} \gamma_e(t) &= \gamma \exp(-t/\tau_M), \\ \sigma(t) &= G_M \gamma_e(t) = G_M \gamma \exp(-t/\tau_M). \end{aligned} \quad (2.8)$$

A situation of special interest is the linear response region: for sufficiently small values of γ , the stress/strain-relation (2.3) is valid and the stress relaxation modulus $G(t)$ is independent of the strain γ . In this regime, a linear superposition of stresses resulting from an infinite number of strain steps can be used to model a steady, simple shear flow of a viscoelastic liquid. For larger applied shear rates, the linear response and the linear superposition fails. The viscosity is still defined as the ratio of stress and strain rate, but it has to be regarded as an apparent viscosity which differs from the above-described ‘zero shear rate’ viscosity. Polymers with *shear thinning* or *shear thickening* properties can be described by the function

$$\sigma \propto \dot{\gamma}^n, \quad (2.9)$$

where the exponent n can be extracted from experimental data. These type of fluids are also called ‘power law fluids’. Moreover, also other non-trivial stress–strain relations can be considered or alternatively non-linear extensions can be applied to the linear *Maxwell* models. In the case of the linear *Jeffreys* model, the stress tensor σ_{ij} relaxes according to the following constitutive relaxation equation:

$$(1 + \lambda_1 \partial_t) \sigma = \eta (1 + \lambda_2 \partial_t) \dot{\gamma}, \quad (2.10)$$

where the strain rate is given by the gradient of the velocity field $\dot{\gamma}_{ij} = \partial_j u_i + \partial_i u_j$. Thus, λ_1 governs the relaxation of stress, whereas λ_2 ($\lambda_2 < \lambda_1$) describes the relaxation of the strain rate, respectively. This model accounts for the viscous and the elastic properties of a fluid and was used by Blossey, Rauscher, Wagner and Münch as a basis for the development of a thin film equation that incorporates viscoelastic effects [26–28]. For a more elaborate description of non-Newtonian flows, we refer e.g. to the corresponding work of Te Nijenhuis *et al* [29].

2.1.4. Reynolds and Weissenberg number. The flow of a liquid can be characterized by specific numbers. One of these numbers is the so-called Reynolds number Re , which describes the ratio of inertia effects to viscous flow contributions. In the case of thin liquid films, Re can be written as

$$Re = \frac{\rho u h}{\eta}, \quad (2.11)$$

where ρ denotes the density of the liquid, u describes the flow velocity and h stands for the film thickness [30]. For thin dewetting polymer films, the Reynolds number is very small, i.e. $Re \ll 1$, and a low- Re lubrication theory can be applied. To quantify and to judge the occurrence of viscoelastic effects versus pure viscous flow, the Weissenberg number Wi has been introduced as

$$Wi = \tau \dot{\gamma}. \quad (2.12)$$

Here, τ denotes the relaxation time and $\dot{\gamma}$ the strain rate as introduced in section 2.1.3. If $Wi \ll 1$, an impact of viscoelasticity on flow dynamics can be neglected and viscous flow dominates.

2.2. Navier–Stokes equations

The Navier–Stokes equations for a Newtonian liquid mark the starting point for the discussion of fluid dynamics in confined geometries. According to conservation of mass, the equation of continuity can be formulated as

$$\partial_t \rho + \nabla \cdot (\rho \mathbf{u}) = 0, \quad (2.13)$$

where $\mathbf{u} = (u_x, u_y, u_z)$ is the velocity field of the fluid. For an incompressible liquid, which implies a temporally and spatially constant liquid density ρ , (2.13) can be simplified to

$$\nabla \cdot \mathbf{u} = 0. \quad (2.14)$$

With the conservation of momentum, the Navier–Stokes equations for an incompressible liquid can be written as

$$\rho (\partial_t + \mathbf{u} \cdot \nabla) \mathbf{u} = -\nabla p + \eta \Delta \mathbf{u} + \mathbf{f}, \quad (2.15)$$

with the pressure gradient ∇p and the volume force \mathbf{f} of external fields acting as driving forces for the liquid flow. We already stated that, for small Reynolds numbers, i.e. $Re \ll 1$, the terms on the left-hand side of (2.15) can be neglected as compared to terms describing the pressure gradient, external volume forces and viscous flow. With this, we can simplify (2.15) to the so-called Stokes equation

$$0 = -\nabla p + \eta \Delta \mathbf{u} + \mathbf{f}. \quad (2.16)$$

In section 2.5, we will demonstrate how these basic laws of bulk fluid dynamics can be applied to the flow geometry of a thin film supported by a solid substrate.

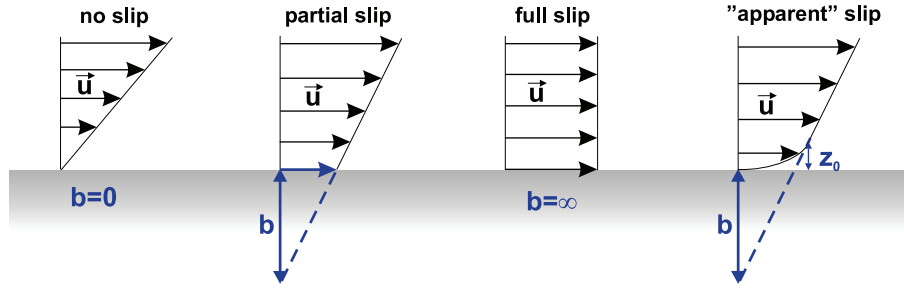


Figure 5. Different velocity profiles in the vicinity of the solid/liquid interface and illustration of the slip (extrapolation) length b . The situation of ‘apparent’ slip is illustrated on the right: according to a thin liquid layer of thickness z_0 that obtains a significantly reduced viscosity, the slip velocity $u_x|_{z=0}$ is zero, but a substantial slip length is measured.

2.3. Free interface boundary condition

At the free interface of a supported liquid film, i.e. at the liquid/gas or more typically the liquid/air interface, no shear forces can be transferred to the gas phase due to the negligible viscosity of the gas. In general, the stress tensor σ_{ij}^* is given by the stress tension σ_{ij} , see (2.2), and the pressure p :

$$\sigma_{ij}^* = \sigma_{ij} + p\delta_{ij} = \eta(\partial_j u_i + \partial_i u_j) + p\delta_{ij}. \quad (2.17)$$

The tangential \mathbf{t} and normal \mathbf{n} (perpendicular to the interface) components of the stress tensor are:

$$(\sigma^* \cdot \mathbf{n}) \cdot \mathbf{t} = 0 \quad (\sigma^* \cdot \mathbf{n}) \cdot \mathbf{n} = \gamma_{lv}\kappa, \quad (2.18)$$

where κ denotes the mean curvature and γ_{lv} the interfacial tension (i.e. the surface tension of the liquid) of the liquid/vapor interface. If the liquid is at rest, i.e. the stationary case $\mathbf{u} = 0$, the latter boundary condition gives the equation for the Laplace pressure p_L :

$$p_L = \gamma_{lv}\kappa = \gamma_{lv}\left(\frac{1}{R_1} + \frac{1}{R_2}\right). \quad (2.19)$$

R_1 and R_2 are the principal radii of curvature of the free liquid/gas boundary; the appropriate signs of the radii are chosen according to the condition that convex boundaries give positive signs. Such convex liquid/gas boundaries lead to an additional pressure within the liquid due to its surface tension. In the section 2.4, the solid/liquid boundary condition will be discussed, which yields a treatment of slip effects.

2.4. Slip/no-slip boundary condition

2.4.1. Navier slip boundary condition. In contrast to fluid dynamics in a bulk volume, where the assumption that the tangential velocity \mathbf{u}_{\parallel} at the solid/liquid interface vanishes (*no-slip boundary condition*), confined geometries require a more detailed investigation as slippage becomes important. In 1823, Navier [31] introduced a linear boundary condition: the tangential velocity \mathbf{u}_{\parallel} is proportional to the normal component of the strain rate tensor; the constant of proportionality is described as the so-called *slip length* b :

$$\mathbf{u}_{\parallel} = b\mathbf{n} \cdot \dot{\boldsymbol{\gamma}}. \quad (2.20)$$

In the case of simple shear flow in the x -direction, the definition of the slip length can be alternatively written as

$$b = \frac{u_x}{\partial_z u_x} \Big|_{z=0} = \frac{u_x \eta}{\sigma} = \frac{\eta}{\xi}, \quad (2.21)$$

where $\xi = \sigma/u_x$ denotes the friction coefficient at the solid/liquid interface. The xy -plane thereby represents the substrate surface. According to these definitions, the slip length can be illustrated as the extrapolation length of the velocity profile ‘inside’ the substrate, cf figure 5. Moreover, both limiting cases are included within this description: for $b = 0$, we obtain the *no-slip* situation, whereas $b = \infty$ characterizes a *full-slip* situation. The latter case corresponds to ‘plug-flow’, where the liquid behaves like a solid that slips over the support.

2.4.2. How can one measure the slip length? In recent years, numerous experimental studies have been published using diverse methods to probe the slip length at the boundary of different simple or complex liquids and solid supports. For details concerning these experimental methods, we refer to the review articles by Lauga *et al* [32], Neto *et al* [33] and Bocquet and Barrat [34] (and references therein). To probe the boundary condition, scientists performed either drainage experiments or direct measurements of the local velocity profile using e.g. tracer particles.

In the case of drainage experiments, the liquid is squeezed between two objects, e.g. a flat surface and a colloidal probe at the tip of an AFM cantilever, and the corresponding force for dragging the probe is measured (*colloidal probe AFM*). Alternatively, in a *surface force apparatus (SFA)*, two cylinders arranged perpendicular to each other are brought in closer contact and force/distance measurements are taken to infer the slip length.

The use of tracer particles as a probe of the local flow profile might bring some disadvantages. The chemistry of these particles is usually different from the liquid molecules and their influence on the results might not be negligible. A similar method is called *fluorescence recovery after photobleaching*. In this method, a distinct part of a fluorescent liquid is bleached by a laser pulse and the flow of non-bleached liquid into that part is measured. The disadvantage of this method is that diffusion might be a further parameter that

is difficult to control. Recently, Joly *et al* showed that also thermal motion of confined colloidal tracers in the vicinity of the solid/liquid interface can be used as a probe of slippage without relying on external driving forces [35].

2.4.3. Which parameters influence slippage? Of course, many interesting aspects in the field of micro- and nanofluidics are related to intrinsic parameters that govern slippage of liquid molecules at the solid/liquid interface. For simple liquids on smooth surfaces, the contact angle is one of the main parameters influencing slippage [36–39]. This originates from the effect of molecular interactions between liquid molecules and the solid surface: if the molecular attraction of liquid molecules and surface decreases (and the contact angle thereby increases), slippage is increased. Further studies aim to quantify the impact of roughness [37, 40–42] or topographic structure [43–47] of the surface on slippage. For different roughness length scales, a suppression (see e.g. [37, 40]) or an amplification (see e.g. [43]) of slippage can be observed. Moreover, the shape of molecular liquids itself has been experimentally shown to impact the boundary condition. Schmatko *et al* found significantly larger slip lengths for elongated linear molecules compared to branched molecules [48]. This might be associated with molecular ordering effects [49] and the formation of layers of the fluid in case of the capability of these liquids to align in the vicinity of the interface [50]. Cho *et al* identified the dipole moment of Newtonian liquids at hydrophobic surfaces as a crucial parameter for slip [51]. De Gennes proposed a thin gas layer at the interface of solid surface and liquid as a possible source of large slip lengths [52]. Recently, MD studies for water on hydrophobic surfaces by Huang *et al* revealed a dependence of slippage on the amount of water depletion at the surface and a strong increase of slip with increasing contact angle [53]. Such depletion layers for water in the vicinity of smooth hydrophobic surfaces have also been experimentally observed using scattering techniques [54–57]. Contamination by nanoscale air bubbles (so-called nanobubbles) and its influence on slippage has been controversially discussed in the literature (see e.g. [58–61]). In the case of more complex liquids, such as polymer melts, further concepts come into play. They will be illustrated in section 3.4.

2.5. Thin film equation for Newtonian liquids

2.5.1. Derivation. Confining the flow of a liquid to the geometry of a thin film, we can assume that the velocity contribution perpendicular to the substrate is much smaller than the parallel one. Furthermore, the lateral length scale of film thickness variations is much smaller than the film thickness itself. On the basis of these assumptions, Oron *et al* [62] developed a thin film equation from the rather complex equations of motion, (2.13) and (2.15). In cases of film thicknesses smaller than the capillary length $l_c = \sqrt{\gamma_V/\rho g}$, (which is typically on the order of magnitude of 1 mm) (2.16) can be written as

$$0 = -\nabla(p + \phi'(h)) + \eta\Delta\mathbf{u}. \quad (2.22)$$

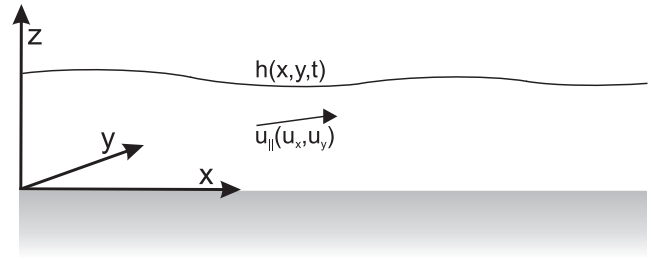


Figure 6. Illustration of the nomenclature of the thin film length scales (x and y are parallel to the substrate) and the velocity contribution $\mathbf{u}_{\parallel} = (u_x, u_y)$.

Additional external fields such as gravitation can be neglected, but a secondary contribution $\phi'(h)$, the *disjoining pressure*, has been added to the capillary pressure p . The disjoining pressure originates from molecular interactions of the fluid molecules with the substrate. The effective interface potential $\phi(h)$ summarizes the inter-molecular interactions and describes the energy that is required to bring two interfaces from infinity to the finite distance h . As already discussed in section 1, the stability of a thin liquid film is also governed by $\phi(h)$. For a further description of thin film stability, we refer to [8] and the references therein.

The derivation of a thin film equation for Newtonian liquids starts with the kinematic condition

$$\partial_t h = -\nabla_{\parallel} \int_0^h \mathbf{u}_{\parallel} dz, \quad (2.23)$$

i.e. the coupling of the time derivative of $h(x, y, t)$ to the flow field, where the index \parallel in general denotes the components parallel to the substrate ($\nabla_{\parallel} = (\partial_x, \partial_y)$ and $\mathbf{u}_{\parallel} = (u_x, u_y)$), as illustrated in figure 6.

For thin liquid films, film thickness variations on the lateral scale \mathbb{L} are much larger than the length scale of the film thickness \mathbb{H} . Introducing the parameter $\epsilon = \mathbb{H}/\mathbb{L} \ll 1$ yields the *lubrication approximation* and is used in the following to re-scale the variables to dimensionless values. In a first approximation, linearized equations are obtained while neglecting all terms of the order $O(\epsilon^2)$. For reasons of simplicity and due to translational invariance in the surface plane, a one-dimensional geometry is used:

$$\begin{aligned} \partial_x(p + \phi') &= \partial_z^2 u_x, & \partial_z(p + \phi') &= 0, \\ \partial_x u_x + \partial_z u_z &= 0. \end{aligned} \quad (2.24)$$

While the substrate is supposed to be impenetrable for the liquid, i.e. $u_z = 0$ for $z = 0$, friction at the interface implies a velocity gradient $\partial_z u_x = u_x/b$ for $z = 0$. Moreover, the tangential and normal boundary condition at the free interface, i.e. $z = h(x)$, can be simplified in the following manner:

$$\partial_x u_x = 0, \quad p + \partial_x^2 h = 0. \quad (2.25)$$

From (2.24) and the boundary conditions, the velocity profile $u_x(z)$ can be obtained. Using the kinematic

Table 1. Summary of lubrication models for Newtonian flow and different slip situations.

Model	Validity	Equation	Limiting cases	Reference
Weak-slip	$b \ll h$	(2.26), (2.27)	$b \rightarrow 0$ (no-slip) $b \rightarrow \infty$ (intermediate-slip)	[62]
Strong-slip	$b \gg h$	(2.28)	$\beta \rightarrow 0$ (intermediate-slip) $\beta \rightarrow \infty$ (‘free’-slip)	[63, 30]

condition (2.23), the equation of motion for thin films in three dimensions is derived:

$$\partial_t h = -\nabla[m(h)\nabla(\gamma_v \Delta h - \phi'(h))], \quad (2.26)$$

where $m(h)$ denotes the mobility given by

$$m(h) = \frac{1}{3\eta}(h^3 + 3bh^2). \quad (2.27)$$

2.5.2. Lubrication models including slippage. As discussed in section 2.5.1, the derivation of the thin film equation is based on the lubrication approximation and the re-scaling of relevant values in ϵ . As a consequence, the slip length b is supposed to obtain values smaller than the film thickness h , i.e. $b \ll h$. To extend this so-called *weak-slip* situation with regard to larger slip $b \gg h$, Münch *et al* [30] and Kargupta *et al* [63] independently developed *strong-slip* models. Therefore, the slip length is defined as $b = \beta/\epsilon^2$. The corresponding equation of motion together with the kinematic condition in one dimension for a Newtonian thin liquid film read as

$$u = \frac{2b}{\eta} \partial_x (2\eta h \partial_x u) + \frac{bh}{\eta} \partial_x (\gamma_v \partial_x^2 h - \phi'(h)) \quad (2.28)$$

$$\partial_t h = -\partial_x (hu).$$

In fact, a family of lubrication models, cf table 1, accounting for different slip situations have been derived. In the limit $b \rightarrow 0$, i.e. the *no-slip* situation, the mobility is given by $m(h) = h^3/3\eta$. If the slip length is in the range of the film thickness $b \sim h$, the mobility in the corresponding *intermediate-slip* model is $m(h) = bh^2/\eta$. Recently, Fetzer *et al* [64] derived a more generalized model based on the full Stokes equations, developed up to third order of a Taylor expansion. The authors were able to show that this model is in accordance with numerical simulations of the full hydrodynamic equations and is not restricted to a certain slip regime, like the aforementioned lubrication models.

2.5.3. Lubrication models including viscoelasticity. In the meantime, the derivation of a thin film equation for the weak-slip case including linear viscoelastic effects of Jeffreys type (such as described by equation (2.10) in section 2.1.3) has been achieved (see [26]). To cover relaxation dynamics of the stress tensor σ , an additional term $\nabla \cdot \sigma$ on the right-hand side of (2.22) has to be included to the aforementioned

model for Newtonian liquids. Furthermore, the treatment of linear viscoelastic effects was also achieved for the strong-slip situation by Blossey *et al* [27]. To summarize these extensions, the essential result is the fact that linear viscoelastic effects are absent in the weak-slip case and the Newtonian thin film model is still valid. The strong-slip situation, however, is more complicated. Slippage and viscoelasticity are combined and strongly affect the corresponding equations. In the meantime, the authors were able to fully incorporate the non-linearities of the co-rotational Jeffreys model for viscoelastic relaxation into their thin film model [28].

The extensions of the aforementioned thin film models for different slip conditions, with or without the presence of viscoelastic relaxation (Newtonian and non-Newtonian models), affect, on the one hand, the rupture conditions, but also on the other hand, the shape of a liquid ridge. These two phenomena will be discussed in the next two subsections. An elaborate description of these theoretical aspects can be found in a recent review article by Blossey [65].

2.5.4. Application I—spinodal dewetting. One of the main applications of the theoretical thin film models is the dewetting of thin polymer films. As introduced in section 1, and illustrated by figure 1, the stability of a thin liquid film is governed by the effective interface potential. Basically, long-range attractive van der Waals forces add to short-range repulsive forces. Due to the planar geometry of two interfaces of distance d , the van der Waals contribution to the potential is $\phi(d)_{\text{vdw}} \propto -A/d^2$, where A is the Hamaker constant. For the description of the explicit calculation of Hamaker constants from the dielectric functions of the involved materials, we refer to [8] and to the book by Israelachvili [66]. Experimental systems often exhibit multi-layer situations, cf figure 7. A hydrophobic film and/or an oxide layer of distinct thicknesses d_i exhibiting Hamaker constants A_i require a superposition of contributions to the potential:

$$\phi(d)_{\text{vdw}} = -\frac{A_1}{12\pi d^2} - \frac{A_2 - A_1}{12\pi(d + d_1)^2} - \frac{A_3 - A_2}{12\pi(d + d_1 + d_2)^2}. \quad (2.29)$$

Consequently, the shape of the effective interface potential (and thereby also the thin film stability) is governed by the set of Hamaker constants A_i and film thicknesses d_i . E.g. for a thin PS film of thickness h on a Si substrate with a native oxide layer of 2.4 nm, $\phi(h)$ shows a global minimum at an equilibrium film thickness h_{eq} (cf figure 8). Moreover, a local maximum at $h > h_{\text{eq}}$ is found.

If the PS film is sufficiently thin ($\phi''(h) < 0$), it may become unstable due to the amplification of thermally induced capillary waves. To track the evolution of small fluctuations of the film thickness h , i.e. $f(\mathbf{x}, t) = h(\mathbf{x}, t) - h$ with $f(\mathbf{x}, t) \ll h$, a Fourier transform of the linearized thin film equation (2.26) has to be performed. The amplitudes of the capillary waves grow exponentially in time. Their growth rate α can be calculated as a function of the wavenumber q and depends on the sign of the local curvature of the interface potential. If the second derivative of the effective interface potential ϕ'' at the film thickness h is positive, α is negative

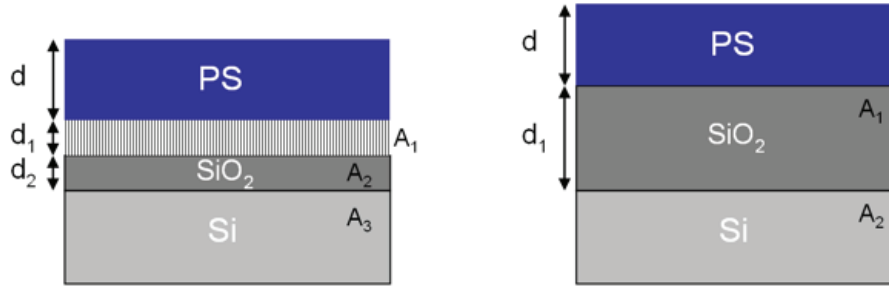


Figure 7. Two examples of polystyrene films prepared on multi-layer substrates. Left: silicon wafer with a native oxide layer covered with a hydrophobic layer (e.g. a self-assembled monolayer (SAM)). Right: silicon wafer with an increased (compared to a native silicon oxide) oxide layer thickness. A_1 denotes the Hamaker constant for the respective layer.

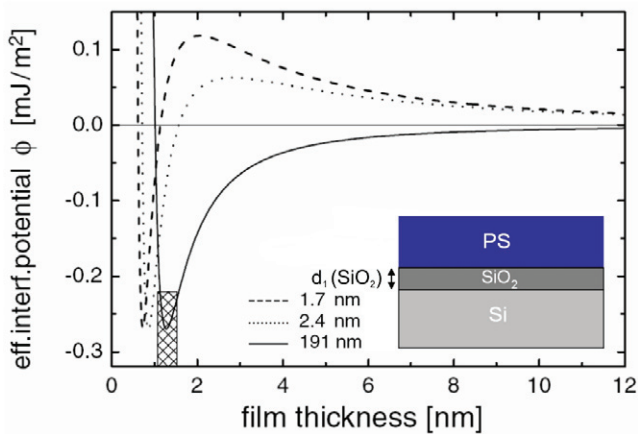


Figure 8. Effective interface potential $\phi(h)$, obtained from experimental data, plotted against the thickness h of a thin PS film prepared on silicon wafers with different oxide layer thicknesses d_1 (adapted from [7]). The cross-hatched rectangle marks the error for h_{eq} and the depth of the global minimum.

for all q and the amplitudes of the capillary waves are damped. If $\phi'' < 0$, the growth rate α is positive for a certain range of wavenumbers up to a critical wavenumber q_c and capillary waves are amplified. The wavenumber that corresponds to the maximum value of α , and therefore exhibits the fastest amplification, is called the preferred wavenumber q_0 and is connected to the preferred wavelength $\lambda_0 = 2\pi/q_0$. The latter is also called the spinodal wavelength and can be written as

$$\lambda_0 = \sqrt{\frac{8\pi^2\gamma_{lv}}{-\phi''(h)}}. \quad (2.30)$$

The spinodal dewetting process can be monitored, e.g. by atomic force microscopy (AFM), as shown in figure 9. By measuring λ_0 as a function of film thickness, $\phi''(h)$ can be inferred and conclusions can be drawn with regard to the effective interface potential $\phi(h)$ [7]. For further details concerning stability of thin films, we refer to [8] and references therein.

Using the strong-slip model while taking slip into account (2.28), Rauscher *et al* could theoretically show that slippage is supposed to influence the capillary wave spectrum

due to a different mobility at the solid/liquid interface [68]. The position of the maximum q_0 shifts to smaller wavenumbers and larger wavelengths for increasing slip length. As for today, to the best of our knowledge, experimental studies concerning the impact of slippage on the spinodal wavelength are not available.

The description of the influence of thermal noise on the temporal and spatial dynamics of spinodally dewetting thin polymer films has been recently achieved by Fetzer *et al* [69]. A stochastic Navier–Stokes equation, with an additional random stress fluctuation tensor that accounts for thermal molecular motion, is utilized to model the flow while assuming a no-slip boundary condition at the solid/liquid interface. The stochastic model matches the experimentally observed spectrum of capillary waves and thermal fluctuations cause the coarsening of typical length scales.

2.5.5. Application II—shape of a dewetting rim. Aside from the implications on spinodal dewetting, the one-dimensional thin film model has been successfully applied to the shape of the rim along the perimeter of e.g. nucleated holes. Experimentally, researchers have studied and observed different types of rim profiles [70–72]. As shown in figure 10, profiles either decay monotonically into the undisturbed film or they show a more symmetrical profile exhibiting a trough (termed ‘oscillatory shape’). If the depth of this trough is in the range of the film thickness, a ring of *satellite holes* can be generated [73, 74].

The shape of a dewetting rim can be understood by the aforementioned thin film theory for Newtonian liquids: introducing a small perturbation $\delta h(x, t) \ll h$ of the film thickness $h(x, t)$ and small velocities $u(x, t)$ leads to linearized thin film equations that describe the temporal and spatial evolution of δh . Therefore, the disjoining pressure $\phi'(h)$ can be neglected due to the fact that films thicker than 10 nm are considered. To obtain stationary solutions of the linearized equations, a frame that is co-moving with the rim $\zeta(x, t) = x - s(t)$ is introduced. Thus, $s(t)$ denotes the position of the three-phase contact line; \dot{s} stands for the dewetting velocity V as described in the next sections. Fetzer *et al* used a normal modes ansatz $\delta h(\zeta) = \delta h_0 \exp k\zeta$ and $u(\zeta) = u_0 \exp k\zeta$ in the linear stability analysis, which leads to a characteristic polynomial of third order. Depending on

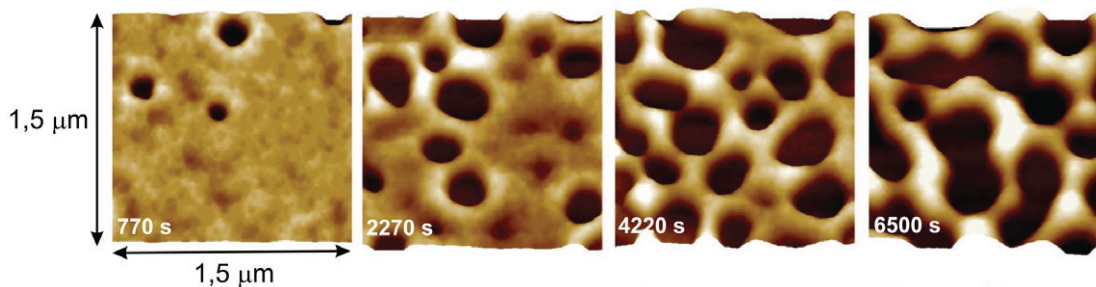


Figure 9. *In situ* atomic force microscopy (AFM) images of a spinodally dewetting 3.9(2) nm PS(2 kg mol⁻¹) film at elevated temperature of $T = 53\text{ }^{\circ}\text{C}$ (corresponding annealing times are given in the pictures) on a Si wafer with a thick (191 nm) oxide layer (adapted from [67]).

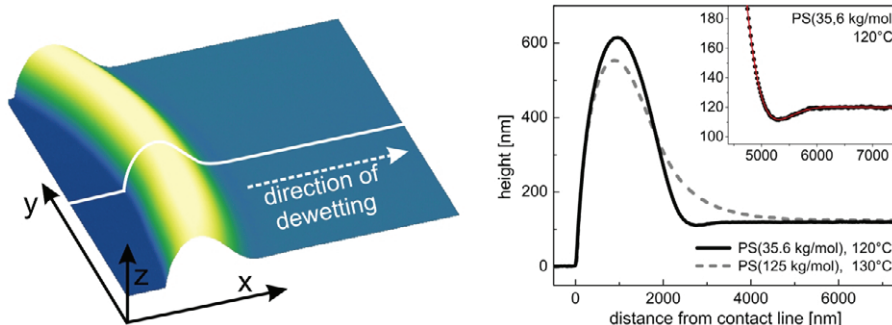


Figure 10. Left: $10\text{ }\mu\text{m} \times 10\text{ }\mu\text{m}$ AFM image of a liquid rim formed during hole growth in a PS film dewetting from a hydrophobic substrate, a Si wafer covered with a 21 nm hydrophobic Teflon coating (AF 1600). The solid white line exemplarily marks one AFM scan line. Right: AFM cross-sections of rims in PS films of different molecular weight on AF 1600: for PS(35.6 kg mol⁻¹) at 120 °C, a trough is observed (as can be clearly seen in the inset) and for PS(125 kg mol⁻¹) at 130 °C, a monotonically decaying rim is found.

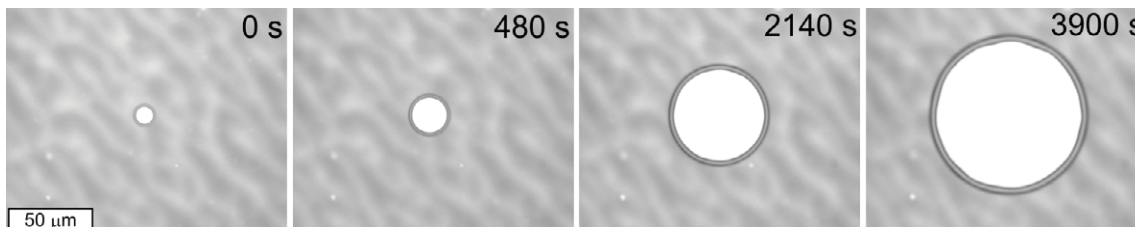


Figure 11. Temporal series of optical micrographs showing the growth of a hole in a 120 nm PS(13.7 kg mol⁻¹) film at $T = 120\text{ }^{\circ}\text{C}$ prepared on a Si wafer covered with a 21 nm hydrophobic Teflon[®] coating (AF1600). Note that the AF 1600 coating shows small thickness variations that have proved not to influence dewetting i.e. the curvature of the holes and the shape of straight fronts are not affected. In the last stage of hole growth (right image) perturbations of the three-phase contact line (according to the liquid rim instability) become visible.

the ratio of slip length to film thickness b/h and on the capillary number $Ca = \eta\dot{\gamma}/\gamma_{lv}$, the parameter k obtains complex or real solutions. Fetzer and co-workers successfully identified the morphological transition from oscillatory to monotonically decaying rims and were able to extract slip lengths and capillary numbers from diverse experiments on dewetting surfaces [75, 76, 64, 77].

3. Flow dynamics of thin polymer films—experimental studies and theoretical models

One of the main aspects of experimental studies concerning the flow dynamics of thin polymer films is to obtain a comprehensive view on the molecular mechanisms of slippage and on the responsible parameters. Although these insights are

rather indirect, several models have been proposed to explain diverse experimental results. In this section, we will focus on these studies, with special regard to the proposed mechanisms of slippage at the solid/polymer interface. In general, we have to distinguish two different dewetting geometries: growth of holes (cf figure 11) and receding straight fronts. In addition to driving forces, dissipation mechanisms have to be considered.

3.1. Dewetting dynamics—driving forces

According to the description of the effective interface potential in section 2.5.4, a global minimum of $\phi(h)$ occurs at h_{eq} in case of unstable or metastable films. This means that the film will thin out until a thickness of h_{eq} is reached. In other words, a thin wetting layer remains on top of the substrate, if $h_{eq} > 0$

and if h_{eq} has a size that is not below the size of the molecules¹. After dewetting has taken place (the dynamics of which are not covered by $\phi(h)$ but depend on viscosity, viscoelasticity, contact angle and the solid/liquid boundary condition), single droplets remain on top of the wetting layer. The droplets—in equilibrium—exhibit Young’s contact angle θ_Y . Parallel to Young’s equation that characterizes the contact angle via the involved surface tensions, another characteristic parameter can be defined to specify the wettability of a surface by a liquid. This is the so-called *spreading parameter* S given by

$$S = \gamma_{sv} - (\gamma_{sl} + \gamma_{lv} + \phi(h_{\text{eq}})), \quad (3.1)$$

where γ_{ij} denotes the interface tension of the solid (s), liquid (l) and the vapor (v) phase. S describes the energetic difference per unit area between a dry surface and a surface that is covered by a liquid layer. Consequently, if $S < 0$ the system can gain energy by reducing the contact area with the substrate. Hence, the liquid forms a dynamic contact angle $\theta_d = \theta_Y/\sqrt{2}$ at the three-phase contact line [81].

The link between the contact angle in equilibrium and the depth of the minimum of the effective interface potential becomes obvious, if the equation for Young’s contact angle is inserted into (3.1):

$$\phi(h_{\text{eq}}) = \gamma_{lv}(\cos \theta_Y - 1) = S. \quad (3.2)$$

Driving forces for wetting and dewetting are capillary forces (see [78]). The capillary force per unit length of the contact line is in general given by

$$\frac{F_c}{l} = \gamma_{lv}(\cos \theta_Y - \cos \theta_d). \quad (3.3)$$

As long as $\theta_d < \theta_Y$ remains valid, the capillary force is negative and the three-phase contact line recedes; the liquid film dewets. Dewetting ends as soon as droplets exhibit their Young’s contact angle θ_Y on the surface. During dewetting, a rim is formed from accumulated material and retracts from the substrate while growing further. De Gennes developed a theoretical description of the resulting driving force for dewetting [78].

On the ‘dry’ side of the rim, which denotes the side where the three-phase contact line is located, a negative capillary force pulls at the contact line:

$$\frac{F_c}{l} = S + \gamma_{lv}(1 - \cos \theta_d). \quad (3.4)$$

On the other side, where the rim decays into the liquid film (the ‘wet’ side of the rim), a positive capillary force occurs:

$$\frac{F_c}{l} = \gamma_{lv}(1 - \cos \theta_d). \quad (3.5)$$

We have to remark that in experimental systems, the Laplace pressure of course avoids edges and, therefore, forces the dry side of the rim to decay smoothly into the film. Summing up

¹ Note that the concept of the effective interface potential is a continuum approach. It may fail if molecular sized phenomena are to be captured, such as extremely thin films close to the size of the molecules.

both forces per unit length gives the effective driving force for retracting contact lines in dewetting systems:

$$\frac{F_c}{l} = |S| = \gamma_{lv}(1 - \cos \theta_Y) \simeq \frac{1}{2}\gamma_{lv}\theta_Y. \quad (3.6)$$

Therefore, it is assumed that the system is in a quasi-stationary state, which means that changes in the shape of the rim occur much more slowly than the dewetting velocity. All in all, this result implies that the driving force for dewetting is given by the absolute value of the spreading parameter, which solely depends on the surface tension γ_{lv} of the liquid (a property which is purely inherent to the liquid) and Young’s contact angle of the liquid on the surface. The same conclusion is drawn if considering energies instead of driving forces. The depth of the minimum of the effective interface potential $\phi(h)$ is equal to S and gives the energy per unit area that is set free during dewetting [79]. Consequently, S also stands for the force per unit length of the contact line (see (3.6)).

3.2. Dewetting dynamics—dissipation mechanisms

In section 3.1, we focused on the driving forces for dewetting. The experimentally observed dynamics represents a force balance of driving forces and friction forces. The resulting dewetting velocity V is connected to the spreading parameter S and the occurring energy dissipation mechanisms (F_i gives the friction force per unit length of the contact line) and their corresponding velocity contributions v_i via the power balance

$$|S|V = \sum_i F_i v_i. \quad (3.7)$$

In the case of dissipation due to viscous friction within the liquid (F_v) and dissipation due to friction of liquid molecules at the solid/liquid interface (F_s), i.e. slippage with a finite velocity $v_s = u|_{z=0}$, we end up with the following balance (the index v stands for ‘viscous’, s denotes ‘slip’):

$$|S|V = F_v v_v + F_s v_s. \quad (3.8)$$

3.2.1. Viscous friction. According to the work of Brochard-Wyart *et al* [80], the no-slip boundary condition for fluid flow implies a friction force that is proportional to the liquid viscosity and the dewetting velocity v , and means that the dissipation is solely due to viscous friction within the liquid. The largest strain rates occur in the direct vicinity of the three-phase contact line. The dissipation is therefore mainly independent from the size of the dewetting rim. However, the flow geometry (given by the dynamic contact angle θ_d) at the contact line influences viscous dissipation. In the case of pure viscous flow $V = v_v$, the following expression for the velocity contribution is obtained for viscous flow [80]:

$$v_v = C_v(\theta_d) \frac{|S|}{\eta}. \quad (3.9)$$

$C_v(\theta_d)$ denotes the constant of proportionality and displays a measurement for the flow field in the vicinity of the contact line. According to the description of Redon *et al* [81], the

velocity in case of viscous dissipation strongly depends on θ_Y and can also be written as

$$v_v \propto \frac{\gamma_{lv}}{\eta} \theta_Y^3, \quad (3.10)$$

where the constant of proportionality accounts for the flow singularity near the contact line. In detail, this constant represents a logarithmic factor that includes i.e. a short-distance cutoff and accounts for the fact that viscous dissipation diverges near the contact line. Moreover, a small impact of the slip length b on this logarithmic factor has been experimentally found [81] by variation of molecular weight M_w (cf (3.12)) by Redon [82]. Consequently, solely in the case of a no-slip boundary condition, the constant of proportionality in (3.10) and also $C_v(\theta_d)$ in (3.9) is purely independent of slip.

For growing holes of radius R and dewetting velocity $V = dR/dt$, integration of (3.9) gives a linear proportionality of the radius versus dewetting time t :

$$R \propto t. \quad (3.11)$$

3.2.2. Slippage—friction at the solid/liquid interface. Apart from viscous dissipation within the rim, de Gennes expected a long-chained polymer film to exhibit an exceptional amount of slippage. For entangled polymer melts on a non-adsorbing surface, de Gennes stated that the slip length should strongly increase with the chain length of the polymer [83]:

$$b = a \frac{N^3}{N_e^2}, \quad (3.12)$$

where a is the size of the monomer, N the polymerization index and N_e the entanglement length. In cases of dominating slippage, a minor contribution of viscous dissipation is expected due to very small stresses within the rim. The corresponding analytical model (see [80, 82]) is based on the linear friction force per unit length of the contact line given by $F_s \propto \xi v_s$. Dissipation occurs along the distance of the solid/liquid interface, where liquid molecules are moved over the substrate. In general, this distance is identified as the width w of the rim (cf figure 12).

Consequently, $F_s \propto w$ can be assumed. If the slip length is introduced according to Navier’s model by $b = \eta/\xi$ (see (2.21) in section 2.4), the slip velocity contribution v_s is given by

$$v_s = \frac{1}{3} \frac{|S|}{\eta} \frac{b}{w}. \quad (3.13)$$

Let us consider the conservation of mass for a growing hole of radius R ,

$$\pi(R + x_0)^2 h = 2\pi Q(R + w/2), \quad (3.14)$$

and for a straight dewetting front of dewetted distance D ,

$$(D + x_0)lh = Ql, \quad (3.15)$$

where x_0 stands for the distance as depicted in figure 12, Q denotes the cross sectional area of a rim (approximated as

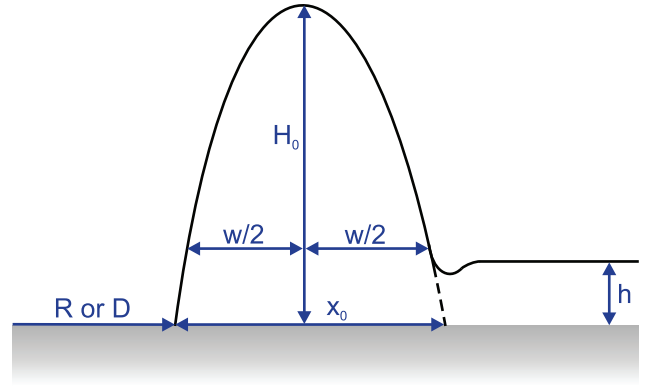


Figure 12. Schematic representation of a rim cross-section illustrating the rim width w (usually obtained as the distance between the three-phase contact line and the position where the rim height is dropped to $1.1h$), the distance x_0 for a given film thickness h and hole radius R (or dewetted distance D of a straight front). (The height scale in the sketch is exaggerated as compared to the lateral length scale.)

a half-circle², i.e. $Q = \pi(x_0/2)^2 \approx \pi(w/2)^2$, and l is the length of a straight front, which cancels out. Based on the assumption of self-similar growing rims and the fact that $x_0/R \ll 1$ and $x_0/D \ll 1$, the width of the rim $w \propto \sqrt{h}\sqrt{R}$ for both geometries. The constant of proportionality, however, which we name C_s in the following, depends on the shape of the rim and, furthermore, on the dewetting geometry itself:

$$w = C_s \sqrt{h}\sqrt{R}. \quad (3.16)$$

Values for C_s can be obtained collecting a temporal series of AFM snapshots of rim profiles and fitting (3.16) to the measured rim width w plotted versus the hole radius R . The initial film thickness h can also be measured by AFM. Of course, the validity of this simplified model, and especially the approximation $w \approx x_0$, becomes questionable for asymmetric rims and should lead to systematic differences in C_s . We point out that, as described in section 2.5.5, the degree of asymmetry of the cross-section of the rim is strongly correlated to the capillary number and the ratio of slip length to film thickness. Replacing the above-derived relation of rim width w and hole radius R in (3.13) gives the slip velocity contribution in terms of the hole radius R for purely slipping liquids:

$$v_s = \frac{1}{3} \frac{|S|}{\eta} \frac{b}{C_s \sqrt{h}\sqrt{R}}. \quad (3.17)$$

Via integration, a characteristic growth law for the radius R of a dewetting hole with time t is found (separation of variables),

$$R \propto t^{2/3}. \quad (3.18)$$

Using the lubrication models described in section 2.5, Münch compared numerical simulations of polymer melts

² Note that usually a dynamic contact angle $\theta_d < 90^\circ$ at the three-phase contact line is obtained in experiments. The difference between a segment of a circle and the half-circle approximation is marginal and contributes to the constant of proportionality C_s .

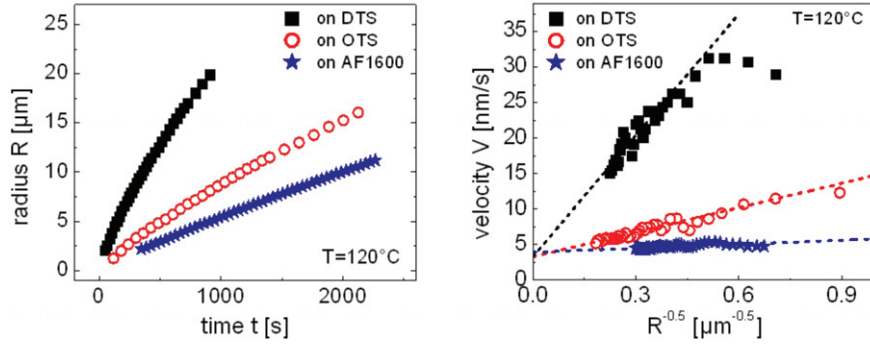


Figure 13. Left: optical measurement of the hole radius versus time in 130 nm PS (13.7 kg mol⁻¹) films on different substrates. Right: plot of the dewetting velocity V versus $1/\sqrt{R}$. Within the error bar, the y -axis intercept of the extrapolated experimental data points is identical for all substrates. The difference in the slope K indicates substantial differences in slip for dewetting PS (adapted from [86] and [87]).

dewetting from hydrophobized substrates to the above-described dewetting dynamics obtained from scaling arguments (based on energy balances) [84]: in the no-slip situation (mobility $m(h) \propto h^3$), an exponent $\alpha = 0.913$ is reported instead of one. The deviation is traced back to the fact that the logarithmic factor in the constant of proportionality of equation (3.10) also depends on the width of the rim (which evolves with time t). Numerical simulations of the slip-dominated case ($m(h) \propto h^2$) give $\alpha = 0.661$, which captures $\alpha = 2/3$ very well.

3.2.3. Models based on the superposition of dissipation mechanisms. Considering the models derived before for pure viscous flow and for pure slippage, a combination of these models seems to be reasonable for situations where viscous dissipation and dissipation at the solid/liquid interface act together. Jacobs *et al* proposed an additive superposition of the corresponding velocity contributions, i.e. $V = v_s + v_v$ [85], according to the fact that both mechanisms counteract the same driving force $|S|$. Separation of variables leads to the implicit function:

$$t - t_0 = \frac{K_v}{|S|} \left(R - 2 \frac{K_v}{K_s} \sqrt{R} + 2 \left(\frac{K_v}{K_s} \right)^2 \ln \left(1 + \frac{K_s \sqrt{R}}{K_v} \right) \right) \quad (3.19)$$

with

$$K_v = \frac{\eta}{C_v(\theta_d)}, \quad K_s = \frac{3\eta}{b} \frac{w}{\sqrt{R}}, \quad \frac{K_v}{K_s} \propto b\sqrt{R}. \quad (3.20)$$

In that notation, the velocity contributions are given by $v_v = |S|/K_v$ and $v_s = |S|/(\sqrt{R}K_s)$. One of the preconditions of this superposition was the successful inclusion of both border cases: for $b \rightarrow 0$, $R \propto t$ is obtained, whereas for $b \rightarrow \infty$, $R \propto t^{2/3}$ follows.

As a more practicable alternative for fitting this relation between radius R and time t to experimental data (typical data is shown in figure 13), Fetzer and Jacobs recently proposed a simpler way of visualizing slip effects [86]: according to the additive superposition, the dewetting velocity can be written in

terms of

$$V = v_v + \frac{K}{\sqrt{R}}, \quad K = \frac{1}{3} \frac{|S|}{\eta} \frac{b}{C_s \sqrt{h}} \quad (3.21)$$

which leads to a linear relationship when plotting the dewetting velocity v versus $1/\sqrt{R}$ (cf figure 13). Then, the y -axis intercept of the straight line can be identified as the viscous velocity contribution v_v , whereas the slope K is connected to the slip length, as illustrated in (3.21). The validity of this model, which assumes the linear superposition of velocity contributions, was checked by plotting the viscous velocity contribution v_v versus the reciprocal viscosity η . An excellent correlation has been demonstrated in view of melt viscosity data obtained from independent measurements. Moreover, the slope has been used to calculate the slip length b . In the experiments, substantial differences in slip lengths for different substrates (cf figure 13) at identical liquid properties were able to be detected [86].

3.2.4. Molecular-kinetic theory and further approaches. Besides theoretical models based on continuum hydrodynamics (see (3.2.1)), contact line dynamics, such as the spreading of a liquid droplet on a planar surface, has been analyzed according to the *molecular-kinetic theory* (MKT) [88–90]. The movement of a contact line is described as an activated rate process where the liquid molecules close to the substrate jump from one potential well to another. The resulting contact line friction coefficient is proportional i.a. to the viscosity η of the liquid and to the exponential of the reversible work of adhesion $\gamma_{lv}(1 + \cos \theta_Y)/k_B T$. As a consequence, increasing the temperature reduces the friction coefficient and increases the velocity. In the case of a squalane droplet spreading on gold surfaces covered with different self-assembled monolayers (SAM) of thiols, the corresponding contact line friction coefficient proves to increase linearly with the chain length of the SAM [91]. SAM surfaces have also been the subject of friction experiments using AFM tips. Barrena *et al* explained discrete changes in the frictional behavior with discrete molecular tilts of the chains of the SAM [92]. Viscoelastic deformation of the substrate at the contact line due to the normal component of the liquid surface tension has also attracted attention with

regard to fluid dynamics on the nanoscale and energy dissipation. The phenomenon of a reduced velocity of contact line displacements compared to a corresponding non-deformable substrate (termed ‘viscoelastic braking’) was extensively studied and described by Shanahan and Carré [93–97]. In this context, Long *et al* theoretically examined the static and dynamic wetting properties of liquids on thin rubber films [98] and grafted polymer layers [99]. To the best of our knowledge, there is, to date, no experimental evidence of deformations and tilting on the molecular scale in the case of SAM surfaces due to retracting contact lines of a dewetting polymer film. However, dewetting on soft deformable rubber surfaces has recently been shown to be influenced by viscoelastic deformations of the substrate [100]. In the case of non-volatile liquids such as polymers, evaporation into, and condensation from, the vapor phase can be excluded as the relevant mechanism of energy dissipation.

3.3. Dynamics of growing holes

Besides very early theoretical and experimental studies of thin film rupture [5, 101–106], one of the first studies concerning dewetting experiments had been published by Redon *et al* [81]. Films of alkanes and polydimethylsiloxane (PDMS) have been prepared on different hydrophobized silicon wafers. The authors observed a constant dewetting velocity, which was inversely proportional to the viscosity and very sensitive to the equilibrium contact angle of the liquid on a corresponding surface. In 1994, Redon *et al* investigated the dewetting of PDMS films of different thicknesses on silanized hydrophobic surfaces [82]. They found that, for films larger than 10 μm , a constant dewetting velocity is found, whereas $R(t) \propto t^{2/3}$ in films thinner than 1 μm is observed. These results corroborate the models represented by (3.11) and (3.18) and indicate that for sufficiently thick films ($h \gg b$) viscous dissipation dominates, whereas slippage becomes relevant in the case of thin films ($h < b$) [82].

3.3.1. Stages of dewetting. While studying the growth of holes, Brochard-Wyart *et al* proposed a set of subsequent stages that can be attributed to distinct growth laws [107]: starting with the birth of the hole, the radius of the hole is supposed to grow exponentially with time, i.e. $R(t) \propto \exp(t/\tau)$, as long as the radius R is smaller than $R_c \approx \sqrt{bh}$. Experimentally, Masson *et al* [108] found relaxation times orders of magnitude larger than the largest translational reptation times expected. For $R_c < R < R'_c \approx b$, the rim is formed and viscous dissipation dominates the hole growth dynamics, i.e. $R \propto t$. The special case of $R \gg R_c = \sqrt{bh}$ moreover gives an analytic expression for the hole growth:

$$R(t) \approx \frac{|S|}{\eta} \left(\frac{b}{h}\right)^{1/2} t. \quad (3.22)$$

During this linear regime, a dynamic (receding) contact angle $\theta_d = \theta_Y/\sqrt{2}$ is formed at the three-phase contact line. In the subsequent stage (for hole radii approximately larger than the slip length b), the rim is fully established and grows in a self-similar manner. As discussed in section 3.2.1, this

results in a characteristic $R \propto t^{2/3}$ growth law if large slip is present. That stage of self-similar growing rims is often called the ‘mature’ regime. These distinct regimes have been experimentally observed by Masson *et al* [108] and Damman *et al* [72]. Moreover, a dissipation dominated by slippage has been shown to be restricted to sufficiently small hole radii: if the rim has accumulated a very large amount of liquid (so that the height of the rim H_0 is much larger than the slip length b , i.e. $H_0 \gg b$), viscous dissipation dominates again. Consequently, this results in a transition to a linear growth law for the radius with respect to the dewetting time, i.e. $R \propto t$.

In this article, we mainly focus on dewetting phenomena in terms of growing holes or retracting straight fronts. Additionally, the subsequent regime influenced by the fingering instability has attracted the interest of researchers [109]. Therefore, facets such as the onset of the instability and the morphology of liquid profiles have also been shown to be sensitive to rheological properties of thin films and the hydrodynamic boundary condition at the solid/liquid interface [110–113].

3.3.2. ‘Mature’ holes. Recently, Fetzer *et al* experimentally studied the dewetting dynamics of ‘mature’ holes in thin PS films on two different types of hydrophobized surfaces. The aforementioned assumption of linear superposition of viscous dissipation and slippage (see section 3.2.3) was used to gain information about the slip contribution [86]. Hydrophobization was achieved by the preparation of a dense, self-assembled monolayer of silane molecules (silanization). In that case, two different silanes were utilized, octadecyltrichlorosilane (OTS) and dodecyltrichlorosilane (DTS). The slip length was shown to depend strongly on temperature (and, thereby, on the melt viscosity); in fact, the slip length decreased with increasing temperature. Furthermore, slippage was about one order of magnitude larger on DTS compared to OTS. The results are in accord with the results for the slip length gained by the analysis of the shape of rim profiles of the corresponding holes (see section 2.5.5). The molecular mechanisms of slippage are widely discussed and several models have been proposed with regard to different experimental conditions (shear rates, polymers, surfaces, etc). This will be discussed in section 3.4.

3.4. Molecular mechanisms of slippage

For small flow velocities, slip lengths lower than expected have been found (see e.g. [114]). This has been explained by the adsorption of polymer chains at the solid surface. These adsorbed chains are able to inhibit slippage due to entanglements with chains in the melt. At larger shear strains, disentanglement of adsorbed and melt chains occurs, the friction coefficient decreases rapidly and slippage is ‘switched on’ [115–118]. The authors interpret the results as follows: Strongly adsorbed chains stay at the solid/liquid interface followed by a coil-stretch transition of these tethered chains. Therefore, the interaction of anchored chains (which are stretched under high flow velocities) with the chains in the melt are reduced and slippage is enhanced. This has been experimentally observed by Migler *et al* [114] and Hervet *et al* [119]. Hence, the critical shear strain depends on the

molecular weight of chains attached to the surface and on their density [39]. This situation is also called ‘stick–slip transition’ and has, moreover, been reported for pressure-controlled capillary flow of polyethylene resins [120]. The authors find a characteristic molecular weight dependence of the slip length $b \propto M_w^{3.4}$, whereas the critical stress σ_c for the transition described before scales to $\sigma_c \propto M_w^{-0.5}$ [121]. Also, de-bonding of adsorbed chains might occur.

Molecular dynamics (MD) studies aiming to investigate the slip length in thin, short-chained polymer films subject to planar shear revealed a dynamic behavior of the slip length $b(\dot{\gamma})$ upon the shear rate according to $b = b^*(1 - \dot{\gamma}/\dot{\gamma}_c)^{-1/2}$, where $\dot{\gamma}_c$ represents a critical shear rate [122]. Slippage strongly increases as $\dot{\gamma}/\dot{\gamma}_c \rightarrow 1$. This relation was also found for simple liquids. Additionally, the authors studied the border case $\dot{\gamma} \rightarrow 0$ and especially the molecular parameters affecting the slip length.

Moreover, a special situation has been discussed in the literature: a thin polymer film prepared on a surface decorated with end-grafted polymer chains of the same species. Due to entropic reasons, an interfacial tension between identical molecules occurs and dewetting can take place. This phenomenon is called autophobicity or autophobic dewetting [123, 124]. Reiter and Khanna observed that PDMS molecules slipped over grafted PDMS brushes. They found a slip length on the order of 10 μm for film thicknesses between 20 and 850 nm of the dewetting PDMS film (high M_w of 308 kg mol^{-1} in most cases). For lower grafting densities, slippage is reduced, indicating a deeper interpenetration of free melt chains [123].

3.5. Impact of viscoelasticity and stress relaxation

As already introduced in section 2.1.3 and, furthermore, theoretically described in section 2.5, viscoelasticity can be included in the description of thin film dynamics. In the case of thin film flow with strong slippage, we have already mentioned that the impact of viscoelasticity might not be distinguishable from slippage effects. Numerous experimental studies have been published by Reiter, Damman and co-workers describing the influence of viscoelastic effects on the flow dynamics of thin polymer films. These studies have been supported with theories by Raphaël and co-workers. In the following, a snapshot of recent results in chronological order is presented. It reflects the progress from simple to increasingly more sophisticated models and experiments. Some of the results, however, may have a tentative character, as mentioned in a very recent manuscript by Coppée *et al* (cf section 3.7).

3.5.1. Thin film rupture. Reiter and de Gennes [125] pointed out that the usual spin-casting preparation (based on fast solvent evaporation) of thin, long-chained polymer films may induce a cascade of distinct states. Annealing the samples to high temperatures for annealing times longer than the reptation time of the polymer (depending on M_w and the temperature T) might induce a complete healing of the preparation effects. Non-equilibrated conformational states and residual stresses have been shown to be capable of causing the rupture of thin

films [126]. Therefore, the areal density of holes appearing at a certain temperature above T_g has been measured: after storage at elevated temperatures below T_g , an exponential reduction of the hole density can be observed. Vilmin and Raphaël were able to show that lateral stress reduces the critical value for surface fluctuations initiated by an anisotropic diffusion of polymer molecules to induce the formation of holes [127].

3.5.2. Stages of distinct dewetting dynamics—experimental results. Reiter and co-workers furthermore studied the temporal and spatial evolution of dewetting PS fronts on silicon wafers covered with a PDMS monolayer at times shorter than the relaxation (reptation) time τ_{rept} in equilibrated bulk samples [126]. At the beginning of their experiments, the dewetted distance and the rim width w increased in a logarithmic way with respect to the dewetting time t , consequently $V \propto t^{-1}$ is found. They correlated a maximum of the rim width w occurring at a distinct time t_1 (nearly independent on M_w and significantly shorter than τ_{rept}) of the experiment to a change in dewetting dynamics, namely $V \propto t^{-1/2}$ (i.e. $R \propto \sqrt{t}$).

Even before the aforementioned study, Damman *et al* compared the growth of a hole and the dynamics of a dewetting straight front [72]. Thus, the strong influence of the dewetting geometry on the dynamics of early stages became obvious. Moreover, the authors correlated their findings to the shape of the corresponding rim and clearly identified distinct dewetting stages: at the beginning of hole growth, capillary forces dominate the dynamics, and exponential growth is observed. In contrast to that, dewetting of a straight front at the beginning starts almost instantaneously at a high velocity and decreases as $V \propto t^{-1}$. As already observed by Redon *et al* [81], $V = \text{const}$ and $R \propto t$ due to viscous dissipation is found for growing holes. For both dewetting geometries, Damman *et al* find a maximum of the rim width w , which they interpret in terms of a transition of the shape of the rim from very asymmetric profiles towards more symmetric rims, while the volume still increases during dewetting. In the following dissipation-dominated regime, $V \propto t^{-1/3}$ and $R \propto t^{2/3}$ (slip boundary condition) or $V = \text{const}$ and $R \propto t$ (no-slip boundary condition) is found, depending on the boundary condition for the solid/liquid interface. Afterward, a constant dewetting velocity (until the ‘mature rim’ regime is reached and slippage dominates) is again obtained.

Recently, Damman and Reiter determined the strain γ from rim shapes of dewetting fronts, which can be written according to (2.3) as $\gamma = (S/h + \sigma_0)/G$, where σ_0 denotes residual stresses [128]. These values were one order of magnitude larger than for equilibrated PS films ($\gamma = S/(hG_{\text{bulk}})$) and increased with increasing M_w . Consequently, larger residual stresses σ_0 or smaller elastic moduli G can be responsible for this effect. Indeed, the elastic modulus of a thin film is supposed to be smaller than its bulk value, according to the fact that larger numbers for the entanglement length M_e (for larger M_w) are expected (see section 2.1.2). Additionally, instead of one transition time for both, two different transitions times t_w for the maximum of the rim width and t_v for the power law of the dewetting velocity (to $V \propto t^{-1/3}$) are

found for larger molecular weights. Time t_v is comparable to the reptation time t_{rept} (also for larger M_w). The authors interpret this as follows: after $t_v \sim t_{\text{rept}}$, the equilibrium entanglement conformation has been reached via interdiffusion and re-entangling of chains. Relaxation of stress, which is correlated to the rim shape transition and t_w , occurs at shorter times.

3.5.3. Stages of distinct dewetting dynamics—theoretical models. These observations have motivated a theoretical model by Vilmin and Raphaël [129] that takes viscoelastic properties of the liquid and slippage into account. The logarithmic increase of the dewetted distance with time can be explained if residual stress is regarded as an extra driving force for dewetting that has to be added to the capillary forces. Subsequent relaxation of the stress reduces this additional contribution. For times larger than the reptation time τ_{rept} , Vilmin and Raphaël predict a constant dewetting velocity and $V \propto t^{-1/3}$ as soon as the ‘mature regime’ is reached (and slippage becomes important). They consider a simple equation for a viscoelastic film, which includes one relaxation time τ_1 (and an elastic modulus G), but two distinct viscosities: η_0 is a short-time viscosity which describes the friction between monomers, and η_1 is the melt viscosity ($\eta_1 \ll \eta_0$) governed by disentanglements of polymer chains. Theoretically, three regimes of distinct time–response are expected: for $t < \tau_0 = \eta_0/G$, Newtonian flow accompanied by a small viscosity η_0 . Afterward ($\tau_0 < t < \tau_1 = \eta_1/G$), the elastic modulus governs the dynamics. For longer times, i.e. $t > \tau_1$, Newtonian flow is again obtained, but with a much larger viscosity η_1 . During the first and the last regime, asymmetric rims and constant velocities are predicted (the latter velocity, of course, is much smaller than the initial velocity). The intermediate regime, governed by viscoelastic behavior, is expected to show $V \propto t^{-1/2}$, according to the fact that the width of the rim w will increase proportionally to the dewetted distance D , i.e. $w \propto D$ (in contrast to the square-root dependence in cases of viscous flow). Including residual stresses into their model, Vilmin and Raphaël obtained the aforementioned experimentally observed $V \propto t^{-1}$ law instead of $V \propto t^{-1/2}$. Recently, Yang *et al* experimentally quantified the molecular recoiling force stemming from non-equilibrium chain conformations. They obtained values that are at least comparable to (or even larger than) the dispersive driving forces [130].

3.5.4. Further remarks. Concerning studies and models including viscoelastic effects, one has to bear in mind that stress relaxation dynamics and relaxation times in thin films have been shown to be different from bulk polymer reptation values. As mentioned in section 2.1.2 and indicated by the characteristic relaxation times τ_1 of elastic constraints being significantly shorter than bulk values, the entanglement length has been shown to be significantly higher in the case of thin films.

Recently, Reiter and co-workers extended their studies with regard to viscoelastic dewetting on soft, deformable substrates [100]. The essential result was that transient residual stresses can cause large elastic deformations in the

substrate which almost stop dewetting for times shorter than the relaxation time τ_{rept} of the polymer film. For times longer than τ_{rept} , the elastic behavior and the elastic trench in the deformable substrate vanishes.

Vilmin and Raphaël applied their model for viscoelastic liquids and residual stresses to the hole growth geometry [131] with regard to the early stage (exponential growth for Newtonian liquids). They discovered a very rapid opening regime followed by slow exponential growth of the radius of the holes.

3.6. Non-linear friction

With regard to energy dissipation at the solid/liquid interface, linear friction has been exclusively considered up to now. As described in section 3.4, often not only have smooth and passive (non-adsorbing) surfaces been experimentally considered, but grafted or adsorbed polymer layers are also used as a support for dewetting experiments. These systems motivate the theoretical treatment of non-linear friction, as described in section 3.6.1.

3.6.1. Theoretical model. To cover non-linear friction, Vilmin and Raphaël introduced a friction force per unit area that is linear below a certain transition velocity v_r and non-linear above [131]:

$$F_s = \xi v_r (v/v_r)^{1-r}, \quad v > v_r, \quad (3.23)$$

where r denotes a *friction exponent*. Consequently, the effective (velocity-dependent) friction coefficient ξ_{eff} can be written in terms of

$$\xi_{\text{eff}}(v) = \xi (v_r/v)^r \quad (3.24)$$

and a velocity-dependent slip length $b(v)$ can be defined as

$$b(v) = \eta/\xi_{\text{eff}}(v). \quad (3.25)$$

An increasing velocity leads to a decreasing friction coefficient and to pronounced slippage. The friction at the solid/liquid interface influences the power law of the velocity decrease. Assuming non-linear friction in the intermediate regime (which is governed by the viscoelastic behavior) gives (according to $w \propto D$) $V \propto t^{-1/(2-r)}$. Including residual stress σ_0 to this model leads to a formula for the maximum width of the rim (depending on r and σ_0). Experimentally, values for r between 0 (for low M_w) and 1 (for large M_w) have been found [128]. The dependence of the non-linearity of friction upon molecular weight M_w could be explained by the influence of chain length on slippage (see (3.12)).

3.6.2. Variation of substrate properties. Hamieh *et al* focused on the frictional behavior of dewetting viscoelastic PS films on PDMS-coated (irreversibly adsorbed) silicon wafers [132]. Thereby, thickness (via the PDMS chain length) and preparation of the PDMS support (via the annealing temperature) were varied. In summary, the observations are consistent with the aforementioned (section 3.5) experiments

by Reiter, showing a characteristic time t_1 for the change in dewetting dynamics and rim shape (from highly asymmetric towards a more symmetric equilibrated shape). Again, this transition is interpreted by the Laplace pressure that overcomes elastic effects. Probing the maximum rim width enables the authors to identify the impact of the friction coefficient or the friction exponent r : if they prepare thicker PDMS layers, the result is a larger maximum rim width. This result can be explained in terms of a small increase of r . Consequently, the velocity-dependent slip length $b(v)$ increases (see (3.25)): thicker PDMS layers lead to more slippage. Concerning the characteristic time for stress relaxation t_1 , no significant influence of the preparation procedure (annealing temperature of the PDMS coating) and thickness of the PDMS layer have been found.

3.7. Temporal evolution of the slip length

Most of the aforementioned dewetting experiments of thin (viscoelastic) PS films are based on supports consisting of a PDMS layer prepared onto a Si wafer. These PDMS surfaces, which were assumed to be impenetrable by PS chains, proved to be less ideal. Recently, the aforementioned fast decay of the dewetting velocity and the maximum of the rim width upon dewetting time (ascribed to relaxation of residual stresses, see section 3.5) has also been observed in the case of low molecular weight PS [133]. Furthermore, neutron reflectometry experiments revealed an interdiffusion of polymer chains at the PS-PDMS interface below the PS bulk glass transition temperature. The dewetting velocity accelerated as the brush thickness is increased. In view of energy dissipation due to brush deformation (pronounced by increasing thickness), this is in contradiction to the slower dewetting velocities expected in that case.

Ziebert and Raphaël recently investigated the temporal evolution of the energy balance (viscous dissipation and sliding friction) of thin film dewetting by numerical treatment, especially concerning non-linear friction [134]. They point out that both mechanisms have different time dependences and propose that simple scaling arguments, such as the mass conservation $w \propto D$, should be revisited. In cases of non-linear friction, viscous dissipation is even more important than sliding friction for times larger than τ_1 , whereas, for linear friction, both mechanisms are almost equally important. The stage of ‘mature’ rims afterward is again dominated by friction at the solid/liquid interface. Using scaling arguments and numerical solutions of the thin film model for viscoelastic liquids [129], they further showed that the aforementioned dewetting characteristics (fast decay of the dewetting velocity, maximum of the rim width in course of dewetting time) can be explained by the temporal decrease of the slip length during the experiment instead of stress relaxation [135]. Therefore, roughening of the PS-PDMS interface (as detected by neutron reflectometry) or potentially an attachment of very few PS chains to the silicon substrate might also be responsible if very low PDMS grafting densities are prepared.

The attachment of melt chains to the substrate has been recently considered by Reiter *et al* [136]. They pointed out

that the driving force is reduced by a certain pull-out force for molecules attached to the surface as they get stretched while resisting to be pulled out. Consequently, this force (per unit length of the contact line) can be written in terms of $F_p = \nu L f^*$, where ν represents the number of surface-connected molecules, L the length according to the stretching and f^* the pull-out force per chain.

4. Conclusions and outlook

To conclude, dewetting experiments can be regarded as a very powerful tool to probe rheological thin film properties and frictional mechanisms. The validity of the no-slip boundary condition at the solid/liquid interface, for a long period of time accepted as a standard approach in fluid dynamics, fails. Even for Newtonian liquids, such as polymers below their critical length for entanglements, substantial amounts of slippage have been found. For larger molecular weights, slippage can be even more pronounced if chain entanglements come into play.

We have reviewed in this article theories and experiments characterizing the statics and dynamics in thin liquid polymer films, focusing on energy dissipation mechanisms occurring during dewetting. Experiments are relatively easy to perform, since usually no very low or very high temperatures are needed, neither are high-speed cameras necessary. However, careful preparation, preferably in a clean-room environment, of thin films is inevitable. Concerning the experimental data, diligent interpretation and consideration of all relevant parameters are of essential importance: molecular weight, film thickness (also with regard to the molecular dimensions of a polymer coil in the respective melt), dewetting temperature, melt viscosity, dewetting velocity and capillary number, residual stresses, relaxation times and aging time represent parameters that are sometimes coupled and not easy to disentangle. Their unique impact on the friction coefficient or the slip length on a specific, ideally non-adsorbing and non-penetrable substrate (to reduce the number of parameters of the system) is not always easy to identify. In particular, the specific stage of dewetting (early or mature stage) and the dewetting geometry (holes or straight fronts) represent further facets and playgrounds for experimentalists and theoreticians that, under careful consideration, enable the gaining of insight into rheological or frictional mechanisms. The dynamics and the morphology of the fingering instability can provide additional access to the solid/liquid boundary condition and the rheology.

Obtaining a deeper understanding of the molecular mechanisms at the solid/liquid interface is one of the main tasks in micro- and nanofluidics. In this context, we would like to highlight two essential questions and possible pathways to answer them.

- (i) The liquid: what is the impact of the polydispersity of the liquid on dewetting? Dewetting studies of polymer melts by adding a second chemical component have been shown to influence slippage [137]. However, also the driving force is changed due to the difference in chemical composition for different species. To overcome this problem, the influence of chain length distribution on

dewetting can be probed by studying polymer mixtures instead of monodisperse polymer melts [138]. With regard to a theoretical approach to this question, dissipative particle dynamics (DPD) simulations enable the location of energy loss in the rim and reveal interesting results in the case of two immiscible fluids of different viscosities: in cases of a low-viscosity layer at the solid/liquid interface, faster dewetting dynamics are found that are attributed to a lubrication effect, i.e. the sliding of the upper high-viscosity layer [139]. Finally, these aspects lead to the fundamental discussion of whether ‘apparent’ slip, possibly induced by the formation of a short-chained layer of low viscosity, is present. In cases of entangled polymer melts, we very recently found evidence for a reduced entanglement density in the vicinity of the solid/liquid interface, which strongly affects the slippage properties of thin polymer films [140].

- (ii) The substrate: what is the impact of the molecular structure of the substrate? As indicated before, the set of parameters concerning the topographical and/or chemical structure of the support is large. Besides parameters such as surface roughness and surface energy, experiments can be performed on substrates, e.g. decorated with an amorphous coating, a self-assembled monolayer or even grafted polymer brushes of the same or different species. Scattering techniques (using neutrons or x-rays) provide access to the solid/liquid interface, complementing dewetting experiments and confirming proposed mechanisms of slippage. Simulations based on molecular dynamics (MD) of near-surface flows can help to compare experimental results from dewetting studies to molecular parameters, easily tunable in theoretical models, and structural changes [141, 142]. Moreover, the evolution of coarse-grained polymer brush/melt interfaces under flow has also been identified as a potential application of MD studies [143, 144]. In the end, all these facets help to obtain a universal picture of sliding friction which can potentially lead to surfaces precisely tailored to special microfluidic applications.

Acknowledgments

The authors acknowledge financial support from the German Science Foundation (DFG) under grant JA905/3 within the priority program 1165 ‘Micro- and nanofluidics’.

References

- [1] Squires T M and Quake S R 2005 Microfluidics: fluid physics at the nanoliter scale *Rev. Mod. Phys.* **77** 977
- [2] Thorsen T, Maerkl S J and Quake S R 2002 Microfluidic large-scale integration *Science* **298** 580
- [3] Leslie D C, Easley C J, Seker E, Karlinsey J M, Utz M, Begley M R and Landers J P 2009 Frequency-specific flow control in microfluidic circuits with passive elastomeric features *Nat. Phys.* **5** 231
- [4] Bear J 1972 *Dynamics of Fluids in Porous Media* (New York: Elsevier)
- [5] Vrij A 1966 Possible mechanism for the spontaneous rupture of thin, free liquid films *Discuss. Faraday Soc.* **42** 14
- [6] Herminghaus S, Jacobs K, Mecke K, Bischof J, Fery A, Ibn-Elhaj M and Schlagowski S 1998 Spinodal dewetting in liquid crystal and liquid metal films *Science* **282** 916
- [7] Seemann R, Herminghaus S and Jacobs K 2001 Dewetting patterns and molecular forces: a reconciliation *Phys. Rev. Lett.* **86** 5534
- [8] Jacobs K, Seemann R and Herminghaus S 2008 Stability and dewetting of thin liquid films *Polymer Thin Films* ed O K C Tsui and T P Russell (Singapore: World Scientific)
- [9] Seemann R, Herminghaus S and Jacobs K 2001 Gaining control of pattern formation of dewetting liquid films *J. Phys.: Condens. Matter* **13** 4925
- [10] Jacobs K, Seemann R and Mecke K 2000 Dynamics of structure formation in thin films: a special spatial analysis *Statistical Physics and Spatial Statistics (Springer Lecture Notes in Physics)* ed D Stoyan and K Mecke (Heidelberg: Springer)
- [11] Craster R V and Matar O K 2009 Dynamics and stability of thin liquid films *Rev. Mod. Phys.* **81** 1131
- [12] Rubinstein M and Colby R H 2003 *Polymer Physics* (New York: Oxford University Press)
- [13] Jones R A L and Richards R W 1999 *Polymers at Surfaces and Interfaces* (Cambridge: Cambridge University Press)
- [14] De Gennes P G 1971 Reptation of a polymer chain in the presence of fixed obstacles *J. Chem. Phys.* **55** 572
- [15] Keddie J L, Jones R A L and Cory R A 1994 Size-dependent depression of the glass transition temperature in polymer films *Europhys. Lett.* **27** 59
- [16] Mattsson J, Forrest J A and Börgesson L 2000 Quantifying glass transition behavior in ultrathin free-standing polymer films *Phys. Rev. E* **62** 5187
- [17] Dalnoki-Veress K, Forrest J A, de Gennes P-G and Dutcher J R 2000 Glass transition reductions in thin freely-standing polymer films: a scaling analysis of chain confinement effects *J. Physique* **10** 221
- [18] Herminghaus S, Jacobs K and Seemann R 2001 The glass transition of thin polymer films: some questions, and a possible answer *Eur. Phys. J. E* **5** 531
- [19] Keddie J L and Jones R A L 1995 Glass transition behavior in ultrathin polystyrene films *J. Isr. Chem. Soc.* **35** 21
- [20] Fryer D S, Peters R D, Kim E J, Tomaszewski J E, De Pablo J J and Nealey P F 2001 Dependence of the glass transition temperature of polymer films on interfacial energy and thickness *Macromolecules* **34** 5627
- [21] Herminghaus S, Jacobs K and Seemann R 2003 Viscoelastic dynamics of polymer thin films and surfaces *Eur. Phys. J. E* **12** 101
- [22] Kawana S and Jones R A L 2001 Character of the glass transition in thin supported polymer films *Phys. Rev. E* **63** 021501
- [23] Herminghaus S, Seemann R and Landfester K 2004 Polymer surface melting mediated by capillary waves *Phys. Rev. Lett.* **93** 017801
- [24] Seemann R, Jacobs K, Landfester K and Herminghaus S 2006 Freezing of polymer thin films and surfaces: the small molecular weight puzzle *J. Polym. Sci. B* **44** 2968
- [25] Si L, Massa M V, Dalnoki-Veress K, Brown H R and Jones R A L 2005 Chain entanglement in thin freestanding polymer films *Phys. Rev. Lett.* **94** 127801
- [26] Rauscher M, Münch A, Wagner B and Blossey R 2005 A thin-film equation for viscoelastic liquids of Jeffreys type *Eur. Phys. J. E* **17** 373
- [27] Blossey R, Münch A, Rauscher M and Wagner B 2006 Slip versus viscoelasticity in dewetting thin films *Eur. Phys. J. E* **20** 267
- [28] Münch A, Wagner B, Rauscher M and Blossey R 2006 A thin-film model for corotational Jeffreys fluids under strong slip *Eur. Phys. J. E* **20** 365
- [29] Te Nijenhuis K, McKinley G H, Spiegelberg S, Barnes H A, Aksel N, Heymann L and Odell J A 2007 Non-Newtonian flows *Springer Handbook of Experimental Fluid Mechanics* ed C Tropea, A L Yarin and J F Foss (Berlin: Springer)

- [30] Münch A, Wagner B A and Witelski T P 2005 Lubrication models with small to large slip lengths *J. Eng. Math.* **53** 359
- [31] Navier C L M H 1823 Mémoire sur les lois du mouvement des fluids *Mem. Acad. Sci. Inst. Fr.* **6** 389
Navier C L M H 1823 Mémoire sur les lois du mouvement des fluids *Mem. Acad. Sci. Inst. Fr.* **6** 432
- [32] Lauga E, Brenner M P and Stone H A 2007 Microfluidics: the no-slip boundary condition *Springer Handbook of Experimental Fluid Mechanics* ed C Tropea, A L Yarin and J F Foss (Berlin: Springer)
- [33] Neto C, Evans D R, Bonaccorso E, Butt H-J and Craig V S J 2005 Boundary slip in Newtonian liquids: a review of experimental studies *Rep. Prog. Phys.* **68** 2859
- [34] Bocquet L and Barrat J-L 2007 Flow boundary conditions from nano-to micro-scales *Soft Matter* **3** 685
- [35] Joly L, Ybert C and Bocquet L 2006 Probing the nanohydrodynamics at liquid/solid interfaces using thermal motion *Phys. Rev. Lett.* **96** 046101
- [36] Barrat J-L and Bocquet L 1999 Large slip effect at a nonwetting fluid-solid interface *Phys. Rev. Lett.* **82** 4671
- [37] Pit R, Hervet H and Léger L 2000 Direct experimental evidence of slip in hexadecane: solid interfaces *Phys. Rev. Lett.* **85** 980
- [38] Cottin-Bizonne C, Jurine S, Baudry J, Crassous J, Restagno F and Charlaix E 2002 Nanorheology: an investigation of the boundary condition at hydrophobic and hydrophilic interfaces *Eur. Phys. J. E* **9** 47
- [39] Leger L 2003 Friction mechanisms and interfacial slip at fluid–solid interfaces *J. Phys.: Condens. Matter* **15** S19
- [40] Zhu Y and Granick S 2002 Limits of the hydrodynamic no-slip boundary condition *Phys. Rev. Lett.* **88** 106102
- [41] Schmatko T, Hervet H and Léger L 2006 Effect of nano-scale roughness on slip at the wall of simple fluids *Langmuir* **22** 6843
- [42] Kunert C and Harting J 2007 Roughness induced boundary slip in microchannel flows *Phys. Rev. Lett.* **99** 176001
- [43] Cottin-Bizonne C, Barrat J-L, Bocquet L and Charlaix E 2003 Low-friction flows of liquid at nanopatterned interfaces *Nat. Mater.* **2** 237
- [44] Priezjev N V and Troian S M 2006 Influence of periodic wall roughness on the slip behaviour at liquid/solid interfaces: molecular-scale simulations versus continuum predictions *J. Fluid Mech.* **554** 25
- [45] Joseph P, Cottin-Bizonne C, Benoît J-M, Ybert C, Journet C, Tabeling P and Bocquet L 2006 Slippage of water past superhydrophobic carbon nanotube forests in microchannels *Phys. Rev. Lett.* **97** 156104
- [46] Ybert C, Barentin C, Cottin-Bizonne C, Joseph P and Bocquet L 2007 Achieving large slip with superhydrophobic surfaces: scaling laws for generic geometries *Phys. Fluids* **19** 123601
- [47] Steinberger A, Cottin-Bizonne C, Kleimann P and Charlaix E 2007 High friction on a bubble mattress *Nat. Mater.* **6** 665
- [48] Schmatko T, Hervet H and Léger L 2005 Friction and slip at simple fluid/solid interfaces: the roles of the molecular shape and the solid/liquid interaction *Phys. Rev. Lett.* **94** 244501
- [49] Priezjev N V, Darhuber A A and Troian S M 2005 Slip behavior in liquid films on surfaces of patterned wettability: comparison between continuum and molecular dynamics simulations *Phys. Rev. E* **71** 041608
- [50] Heidenreich S, Ilg P and Hess S 2007 Boundary conditions for fluids with internal orientational degrees of freedom: apparent velocity slip associated with the molecular alignment *Phys. Rev. E* **75** 066302
- [51] Cho J-H J, Law B M and Rieutord F 2004 Dipole-dependent slip of Newtonian liquids at smooth solid hydrophobic surfaces *Phys. Rev. Lett.* **92** 166102
- [52] De Gennes P G 2002 On fluid/wall slippage *Langmuir* **18** 3413
- [53] Huang D M, Sendner C, Horinek D, Netz R R and Bocquet L 2008 Water slippage versus contact angle: a quasiuniversal relationship *Phys. Rev. Lett.* **101** 226101
- [54] Steitz R, Gutberlet T, Hauss T, Klösgen B, Krastev R, Schemmel S, Simonsen A C and Findenegg G H 2003 Nanobubbles and their precursor layer at the interface of water against a hydrophobic substrate *Langmuir* **19** 2409
- [55] Doshi D A, Watkins E B, Israelachvili J N and Majewski J 2005 Reduced water density at hydrophobic surfaces: effect of dissolved gases *Proc. Natl Acad. Sci.* **102** 9458
- [56] Mezger M, Reichert H, Schröder S, Okasinski J, Schröder H, Dosch H, Palms D, Ralston J and Honkimäki V 2006 High-resolution *in situ* x-ray study of the hydrophobic gap at the water-octadecyl-trichlorosilane interface *Proc. Natl Acad. Sci.* **103** 18401
- [57] Maccarini M, Steitz R, Himmelhaus M, Fick J, Tatur S, Wolff M, Grunze M, Janeček J and Netz R R 2007 Density depletion at solid–liquid interfaces: a neutron reflectivity study *Langmuir* **23** 598
- [58] Tyrrell J W G and Attard P 2001 Images of nanobubbles on hydrophobic surfaces and their interactions *Phys. Rev. Lett.* **87** 176104
- [59] Trethewey D C and Meinhardt C D 2004 A generating mechanism for apparent fluid slip in hydrophobic microchannels *Phys. Fluids* **16** 1509
- [60] Poynor A, Hong L, Robinson I K, Granick S, Zhang Z and Fenter P A 2006 How water meets a hydrophobic surface *Phys. Rev. Lett.* **97** 266101
- [61] Hendy S C and Lund N J 2009 Effective slip length for flows over surfaces with nanobubbles: the effect of finite slip *J. Phys.: Condens. Matter* **21** 144202
- [62] Oron A, Davis S H and Bankoff S G 1997 Long-scale evolution of thin liquid films *Rev. Mod. Phys.* **69** 931
- [63] Kargupta K, Sharma A and Khanna R 2004 Instability, dynamics, and morphology of thin slipping films *Langmuir* **20** 244
- [64] Fetzer R, Münch A, Wagner B, Rauscher M and Jacobs K 2007 Quantifying hydrodynamic slip: a comprehensive analysis of dewetting profiles *Langmuir* **23** 10559
- [65] Blossey R 2008 Thin film rupture and polymer flow *Phys. Chem. Chem. Phys.* **10** 5177
- [66] Israelachvili J 1992 *Intermolecular and Surface Forces* 2nd edn (New York: Academic)
- [67] Becker J, Grün G, Seemann R, Mantz H, Jacobs K, Mecke K R and Blossey R 2003 Complex dewetting scenarios captured by thin-film models *Nat. Mater.* **2** 59
- [68] Rauscher M, Blossey R, Münch A and Wagner B 2008 Spinodal dewetting of thin films with large interfacial slip: implications from the dispersion relation *Langmuir* **24** 12290
- [69] Fetzer R, Rauscher M, Seemann R, Jacobs K and Mecke K 2007 Thermal noise influences fluid flow in thin films during spinodal dewetting *Phys. Rev. Lett.* **99** 114503
- [70] Seemann R, Herminghaus S and Jacobs K 2001 Shape of a liquid front upon dewetting *Phys. Rev. Lett.* **87** 196101
- [71] Reiter G 2001 Dewetting of highly elastic thin polymer films *Phys. Rev. Lett.* **87** 186101
- [72] Damman P, Baudelet N and Reiter G 2003 Dewetting near the glass transition: transition from a capillary force dominated to a dissipation dominated regime *Phys. Rev. Lett.* **91** 216101
- [73] Neto C, Jacobs K, Seemann R, Blossey R, Becker J and Grün G 2003 Correlated dewetting patterns in thin polystyrene films *J. Phys.: Condens. Matter* **15** 421

- [74] Neto C, Jacobs K, Seemann R, Blossey R, Becker J and Grün G 2003 Satellite hole formation during dewetting: experiment and simulation *J. Phys.: Condens. Matter* **15** 3355
- [75] Fetzer R, Jacobs K, Münch A, Wagner B and Witelski T P 2005 New slip regimes and the shape of dewetting thin liquid films *Phys. Rev. Lett.* **95** 127801
- [76] Fetzer R, Rauscher M, Münch A, Wagner B A and Jacobs K 2006 Slip-controlled thin film dynamics *Europhys. Lett.* **75** 638
- [77] Bäumchen O, Fetzer R, Münch A, Wagner B and Jacobs K 2009 Comprehensive analysis of dewetting profiles to quantify hydrodynamic slip *IUTAM Symp. on Adv. in Micro- and Nanofluidics* ed M Ellero, X Hu, J Fröhlich and N Adams (Berlin: Springer)
- [78] De Gennes P G 1985 Wetting: statics and dynamics *Rev. Mod. Phys.* **57** 827
- [79] Frumkin A N 1938 On the wetting phenomena and attachment of bubbles I *J. Phys. Chem. USSR* **12** 337
- [80] Brochard-Wyart F, De Gennes P-G, Hervet H and Redon C 1994 Wetting and slippage of polymer melts on semi-ideal surfaces *Langmuir* **10** 1566
- [81] Redon C, Brochard-Wyart F and Rondelez F 1991 Dynamics of dewetting *Phys. Rev. Lett.* **66** 715
- [82] Redon C, Brzoska J B and Brochard-Wyart F 1994 Dewetting and slippage of microscopic polymer films *Macromolecules* **27** 468
- [83] De Gennes P G 1979 Ecoulements viscométriques de polymères enchevêtrés *C. R. Acad. Sci. B* **288** 219
- [84] Münch A 2005 Dewetting rates of thin liquid films *J. Phys.: Condens. Matter* **17** S309
- [85] Jacobs K, Seemann R, Schatz G and Herminghaus S 1998 Growth of holes in liquid films with partial slippage *Langmuir* **14** 4961
- [86] Fetzer R and Jacobs K 2007 Slippage of newtonian liquids: influence on the dynamics of dewetting thin films *Langmuir* **23** 11617
- [87] Bäumchen O, Jacobs K and Fetzer R 2008 Probing slippage and flow dynamics of thin dewetting polymer films *Proc. Eur. Conf. on Microfluidics ((Bologna, Dec., 2008))*
- [88] Blake T D and Haynes J M 1969 Kinetics of liquid/liquid displacement *J. Colloid Interface Sci.* **30** 421
- [89] De Ruijter M J, Blake T D and De Coninck J 1999 Dynamic wetting studied by molecular modeling simulations of droplet spreading *Langmuir* **15** 7836
- [90] Blake T D and De Coninck J 2002 The influence of solid/liquid interactions on dynamic wetting *J. Adv. Colloid Interface Sci.* **96** 21
- [91] Voué M, Rioboo R, Adao M H, Conti J, Bondar A I, Ivanov D A, Blake T D and De Coninck J 2007 Contact-line friction of liquid drops on self-assembled monolayers: chain-length effects *Langmuir* **23** 4695
- [92] Barrena E, Kopta S, Ogletree D F, Charych D H and Salmeron M 1999 Relationship between friction and molecular structure: alkylsilane lubricant films under pressure *Phys. Rev. Lett.* **82** 2880
- [93] Shanahan M E R and Carré A 1994 Anomalous spreading of liquid drops on an elastomeric surface *Langmuir* **10** 1647
- [94] Shanahan M E R and Carré A 1995 Viscoelastic dissipation in wetting and adhesion phenomena *Langmuir* **11** 1396
- [95] Carré A and Shanahan M E R 1995 Influence of the 'wetting ridge' in dry patch formation *Langmuir* **11** 3572
- [96] Carré A, Gastel J-C and Shanahan M E R 1996 viscoelastic effects in the spreading of liquids *Nature* **379** 432
- [97] Shanahan M E R and Carré A 2002 Spreading and dynamics of liquid drops involving nanometric deformations on soft substrates *Colloids Surf. A* **206** 115
- [98] Long D, Ajdari A and Leibler L 1996 Static and dynamic wetting properties of thin rubber films *Langmuir* **12** 5221
- [99] Long D, Ajdari A and Leibler L 1996 How do grafted polymer layers alter the dynamics of wetting *Langmuir* **12** 1675
- [100] Al Akhrass S, Reiter G, Hou S Y, Yang M H, Chang Y L, Chang F C, Wang C F and Yang A C-M 2008 Viscoelastic thin polymer films under transient residual stresses: two-stage dewetting on soft substrates *Phys. Rev. Lett.* **100** 178301
- [101] Ruckenstein E and Jain R K 1974 Spontaneous rupture of thin liquid films *J. Chem. Soc. Faraday Trans. II* **132**
- [102] Brochard-Wyart F, Di Meglio J-M and Quéré D 1987 Dewetting *C. R. Acad. Sci. Paris II* **304** 553
- [103] Sharma A and Ruckenstein E 1989 Dewetting of solids by the formation of holes in macroscopic liquid films *J. Colloid Interface Sci.* **133** 358
- [104] Brochard-Wyart F and Daillant J 1990 Drying of solids wetted by thin liquid films *Can. J. Phys.* **68** 1084
- [105] Brochard-Wyart F, Redon C and Skykes C 1992 Dewetting of ultrathin liquid films *C.R. Acad. Sci. Paris II* **314** 19
- [106] Reiter G 1992 Dewetting of thin polymer films *Phys. Rev. Lett.* **68** 75
- [107] Brochard-Wyart F, Debregeas G, Fondecave R and Martin P 1997 Dewetting of supported viscoelastic polymer films: birth of rims *Macromolecules* **30** 1211
- [108] Masson J-L and Green P F 2002 Hole formation in thin polymer films: a two-stage process *Phys. Rev. Lett.* **88** 205504
- [109] Brochard-Wyart F and Redon C 1992 Dynamics of rim instabilities *Langmuir* **8** 2324
- [110] Reiter G and Sharma A 2001 Auto-optimization of dewetting rates by rim instabilities in slipping polymer films *Phys. Rev. Lett.* **87** 166103
- [111] Münch A and Wagner B 2005 Contact-line instability of dewetting thin films *Physica D* **209** 178
- [112] Gabriele S, Sclavons S, Reiter G and Damman P 2006 Disentanglement time of polymers determines the onset of rim instabilities in dewetting *Phys. Rev. Lett.* **96** 156105
- [113] King J R, Münch A and Wagner B 2009 Linear stability analysis of a sharp-interface model for dewetting thin films *J. Eng. Math.* **63** 177
- [114] Migler K B, Hervet H and Leger L 1993 Slip transition of a polymer melt under shear stress *Phys. Rev. Lett.* **70** 287
- [115] Brochard F and de Gennes P G 1992 Shear-dependent slippage at a polymer/solid interface *Langmuir* **8** 3033
- [116] Ajdari A, Brochard-Wyart F, De Gennes P-G, Leibler L, Viovy J-L and Rubinstein M 1994 Slippage of an entangled polymer melt on a grafted surface *Physica A* **204** 17
- [117] Gay C 1999 New concepts for the slippage of an entangled polymer melt at a grafted solid interface *Eur. Phys. J. B* **7** 251
- [118] Tchesnokov M A, Molenaar J, Slot J J M and Stepanyan R 2005 A molecular model for cohesive slip at polymer melt/solid interfaces *J. Chem. Phys.* **122** 214711
- [119] Hervet H and Leger L 2003 Flow with slip at the wall: from simple to complex fluids *C. R. Physique* **4** 241
- [120] Drda P P and Wang S-Q 1995 Stick-slip transition at polymer melt/solid interfaces *Phys. Rev. Lett.* **75** 2698
- [121] Wang S-Q and Drda P A 1996 Stick-slip transition in capillary flow of polyethylene. 2. Molecular-weight dependence and low-temperature anomaly *Macromolecules* **29** 4115
- [122] Priezjev N V and Troian S M 2004 Molecular origin and dynamic behavior of slip in sheared polymer films *Phys. Rev. Lett.* **92** 018302
- [123] Reiter G and Khanna R 2000 Kinetics of autophobic dewetting of polymer films *Langmuir* **16** 6351
- [124] Reiter G and Khanna R 2000 Negative excess interfacial entropy between free and end-grafted chemically identical polymers *Phys. Rev. Lett.* **85** 5599
- [125] Reiter G and De Gennes P-G 2001 Spin-cast, thin, glassy polymer films: highly metastable forms of matter *Eur. Phys. J. E* **6** 25

- [126] Reiter G, Hamieh M, Damman P, Sclavons S, Gabriele S, Vilmin T and Raphaël E 2005 Residual stresses in thin polymer films cause rupture and dominate early stages of dewetting *Nat. Mater.* **4** 754
- [127] Vilmin T and Raphaël E 2006 Dynamic instability of thin viscoelastic films under lateral stress *Phys. Rev. Lett.* **97** 036105
- [128] Damman P, Gabriele S, Coppée S, Desprez S, Villers D, Vilmin T, Raphaël E, Hamieh M, Al Akhrass S and Reiter G 2007 Relaxation of residual stress and reentanglement of polymers in spin-coated films *Phys. Rev. Lett.* **99** 036101
- [129] Vilmin T and Raphaël E 2005 Dewetting of thin viscoelastic polymer films on slippery substrates *Europhys. Lett.* **72** 781
- [130] Yang M H, Hou S Y, Chang Y L and Yang A C-M 2006 Molecular recoiling in polymer thin film dewetting *Phys. Rev. Lett.* **96** 066105
- [131] Vilmin T and Raphaël E 2006 Dewetting of thin polymer films *Eur. Phys. J. E* **21** 161
- [132] Hamieh M, Al Akhrass S, Hamieh T, Damman P, Gabriele S, Vilmin T, Raphaël E and Reiter G 2007 Influence of substrate properties on the dewetting dynamics of viscoelastic polymer films *J. Adhes.* **83** 367
- [133] Coppée S, Gabriele S, Jonas A M, Jestin J and Damman P 2009 Influence of chain interdiffusion between immiscible polymers on dewetting dynamics arXiv:0904.1675v1
- [134] Ziebert F and Raphaël E 2009 Dewetting dynamics of stressed viscoelastic thin polymer films *Phys. Rev. E* **79** 031605
- [135] Ziebert F and Raphaël E 2009 Dewetting of thin polymer films: influence of interface evolution *Europhys. Lett.* **86** 46001
- [136] Reiter G, Al Akhrass S, Hamieh M, Damman P, Gabriele S, Vilmin T and Raphaël E 2009 Dewetting as an investigative tool for studying properties of thin polymer films *Eur. Phys. J.* **166** 165 Special Topics
- [137] Besancon B M and Green P F 2007 Dewetting dynamics in miscible polymer-polymer thin films mixtures *J. Chem. Phys.* **126** 224903
- [138] Fetzer R 2006 *Einfluss von Grenzflächen auf die Fluidik dünner Polymerfilme* (Berlin: Logos)
- [139] Merabia S and Avalos J B 2008 Dewetting of a stratified two-component liquid film on a solid substrate *Phys. Rev. Lett.* **101** 208304
- [140] Bäumchen O, Fetzer R and Jacobs K 2009 Reduced interfacial entanglement density affects the boundary conditions of polymer flow *Phys. Rev. Lett.* at press
- [141] Servantie J and Müller M 2008 Temperature dependence of the slip length in polymer melts at attractive surfaces *Phys. Rev. Lett.* **101** 026101
- [142] Müller M, Pastorino C and Servantie J 2008 Flow, slippage and a hydrodynamic boundary condition of polymers at surfaces *J. Phys.: Condens. Matter* **20** 494225
- [143] Pastorino C, Binder K, Kreer T and Müller M 2006 Static and dynamic properties of the interface between a polymer brush and a melt of identical chains *J. Chem. Phys.* **124** 064902
- [144] Pastorino C, Binder K and Müller M 2009 Coarse-grained description of a brush/melt interface in equilibrium and under flow *Macromolecules* **42** 401

3 Preparative and Experimental Techniques

As substrates for the dewetting experiments described in this thesis, smooth hydrophobized silicon wafers were utilized. The preparation of these surfaces and their characterization is highlighted in the first part of the following chapter. Aside from macroscopic contact angle measurements, two main experimental techniques were utilized: atomic force microscopy (AFM) and ellipsometry. The AFM technique was realized for the first time by Binnig, Quate and Gerber in 1986 [35]. In the meanwhile, AFM is a common method in diverse disciplines of natural and life sciences to study not only the topography of a surface on the nanometer scale, but also to gain information about e.g. elasticity, adhesion and tribological properties. A detailed description of the functional principles and work modes can be found for example in the nanotechnology handbook edited by B. Bhushan [36]. The general working principle of ellipsometry and the various modes of operation (including the single wavelength null-ellipsometry which was utilized in the case of this study) can be found for example in the books by H.G. Tompkins [37] or R.M.A. Azzam [38]. Spin-coating is, among similar preparative methods such as dip-coating or spray-coating, a fundamental technique to realize uniform thin polymer films. In this thesis, spin-coating was utilized to coat silicon substrates with hydrophobic Teflon[®] layers, but also for the preparation of thin polymer films on top of these substrates. The latter aspect is specified in the second part of this chapter.

3.1 Substrate Preparation

Besides the silanization of Si wafers with dodecyl-trichlorosilane (DTS) and octadecyl-trichlorosilane (OTS) forming hydrophobic self-assembled monolayers (see [39] for details concerning the surface properties and the sophisticated preparation based on a procedure proposed in [40, 41]), a thin amorphous Teflon[®] layer (termed AF 1600¹) on Si wafers was used as a novel type of substrate. This material has extraordinary optical and mechanical properties²: Besides the low absorption of light from UV to a portion of the IR range, which results in optical clarity and high transmission, AF 1600 exhibits a low refractive index of 1.305. Concerning the mechanical properties, the material shows a dynamic elastic modulus between 0.9 and 0.6 GPa for temperatures between 100 °C and 150 °C (satisfying typical experimental dewetting temperatures). Due to their extraordinary low surface energy², Teflon[®] coatings are utilized to fabricate low-adhesion surfaces and are of outstanding importance in everyday life (e.g. as a coating for frying pans) and for a set of technological applications. This material was used

¹The term Teflon[®]AF is used by the company DuPont for a family of amorphous fluoropolymers. The grade 1600 indicates the glass transition temperature of 160 °C.

²For further details concerning handling, preparation, applications and performance see: Product Information of Teflon[®]AF (www.dupont.com), DuPont Fluoroproducts, P.O. Box 80711, Wilmington, DE, USA.

to study dewetting morphologies and dynamics of thin PS film on the basis of several aspects: First, as a dielectric layer with a large elastic modulus, deformation of the substrate can be neglected as an additional energy dissipation mechanism during dewetting. Consequently, established theoretical models can be applied. Second, its unique wetting properties and its hydrophobicity result in even larger driving forces for dewetting compared to silanized substrates. Third, its amorphous structure differs from the regular structure of a self-assembled monolayer formed at the surface of a Si wafer decorated with a native oxide layer. Finally, Teflon[®] can be prepared as a coating via different techniques and is therefore of enormous technological and practical relevance. The preparation procedure via spin-coating and the characterization of the resulting thin layers with respect to their roughness, thickness and wetting properties will be described in detail in the following sections.

3.1.1 Materials and Preparation

To prepare AF 1600 layers as a uniform thin film, the fluoropolymer can be dissolved in certain perfluorinated solvents. For this study, 0.5 and 1 w/v% solutions of AF 1600 (Poly[4,5-difluoro-2,2-bis(trifluoromethyl)-1,3-dioxane-co-tetrafluoroethylene, Aldrich, 469610-1G, CAS: 37626-13-4) dissolved in Perfluoro-compound FC-75[®] ($C_8F_{16}O$, Acros Organics, CAS: 335-36-4) were prepared. As soon as the fluoropolymer was fully dissolved³, thin AF1600 layers can be prepared by spin-coating (see section 3.2) the solution on freshly cleaned pieces of Si wafers⁴ (Wacker Siltronic, Burghausen, Germany). Before processing, the coated samples are stored in a laminar flow bench for at least one day to ensure complete solvent evaporation. To accelerate the solvent evaporation, it is recommended to heat the coated sample above its glass transition temperature². An improvement of the coating's adhesion to the substrate can be achieved if the Si or glass substrate is decorated with fluorosilanes before preparation of the film, followed by a specific annealing procedure (above the boiling point of the solvent and the glass transition of the fluoropolymer) after film preparation².

3.1.2 Characterization by AFM and Ellipsometry

Samples were characterized by atomic force microscopy (AFM, Multimode and Dimension 3100, Veeco, Santa Barbara, CA, USA) in tapping-modeTM and by ellipsometry (EP³, Nanofilm, Göttingen, Germany).

Ellipsometry was used to determine the thickness of the AF 1600 layer d_{AF1600} and, if simultaneously possible, to measure its index of refraction n . Measurements with fixed wavelength of

³Mixing can be enhanced by placing the solution in e.g. an ultrasonic bath.

⁴Cleaning of the Si wafers (polished, crystal orientation 1-0-0 or 1-1-1, thickness: $525 \pm 20 \mu\text{m}$, specific resistance 10-20 Ωcm , boron (B) doping) was performed by exposure to air plasma (for about 10 min, low power) or by keeping the Si pieces for about 30 min in a freshly prepared "piranha solution" (a 1:1 mixture of concentrated sulfuric acid H_2SO_4 and unstabilized hydrogen-peroxide H_2O_2). In case of wet chemical cleaning, samples have to be repeatedly rinsed in hot MilliQTM water (Milli-Q synthesis system, Millipore, USA, organic impurities < 6 ppb, resistance at 25 °C: 18.2 $M\Omega\text{cm}$) to avoid residues of the "piranha solution". After this (preferentially used) chemical cleaning, Si samples were exposed to a "Snow-Jet", i.e. a focused jet of CO_2 crystals capable to mechanically remove particles adhering to the surface [42].

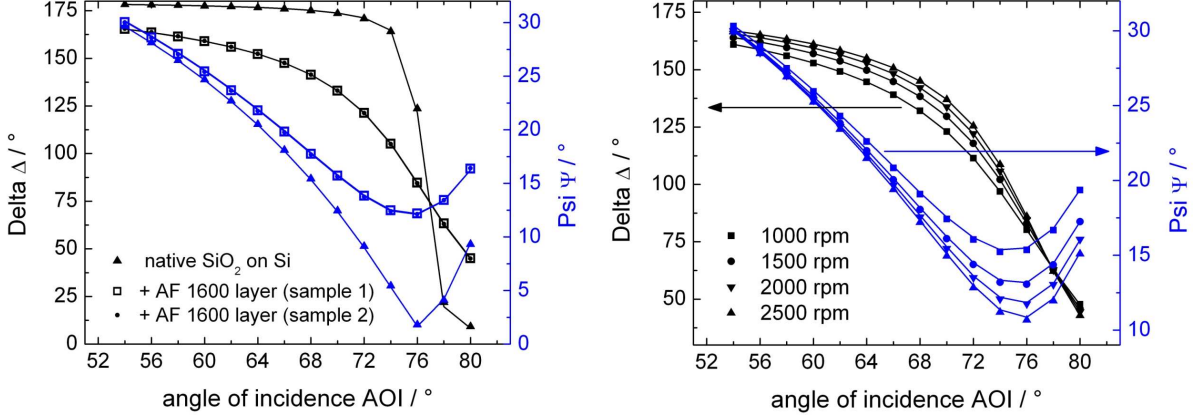


Figure 3.1: Ellipsometric measurements of bare (filled triangles) and spin-coated (open squares) samples (left). The reproducibility was checked by a measurement on a second spot of the AF 1600 sample (filled circles). Variation of spinning velocity ω results in a shift of the corresponding $\Psi(\text{AOI})$ and $\Delta(\text{AOI})$ curves (right). Solid lines represent the modelling of the experimental data points.

Table 3.1: Spin-coating parameters (ω : spinning velocity) and mean thicknesses d_{AF1600} of a series of AF 1600 layers (from two measurements on different spots of the sample) on Si wafers for two different concentrations c . The fit model is based on the following parameters: $d_{SiO_2} = 1.7$ nm, $n_{SiO_2} = 1.4605$, $k_{SiO_2} = 0$, $n_{Si} = 4.131$, $k_{Si} = 0.022$. As an additional fit parameter, the index of refraction $n_{AF1600} = 1.300(5)$ of the AF 1600 layer is obtained for sufficiently large film thicknesses.

c (w/v%)	ω (rpm)	d_{AF1600} (nm)
1	1000	69(1)
1	2000	49(1)
0.5	1000	27.2(2)
0.5	1500	22.3(2)
0.5	2000	19.6(3)
0.5	2500	17.6(4)

the laser light ($\lambda=532$ nm, green laser) and variable angle of incidence (AOI, usually between 54° and 80°) for different polarisator, compensator and analyser configurations (4-zones measurement) give mean values for the ellipsometric angles Ψ and Δ as a function of the AOI (see Fig. 3.1). Results for the AF 1600 layer thickness d_{AF1600} are shown in Tab. 3.1 for various concentrations and spin-coating parameters. Modelling of $\Psi(\text{AOI})$ and $\Delta(\text{AOI})$ requires the knowledge of the dielectric properties of the Si (bulk) and the SiO_2 layer located underneath the AF 1600. The thickness of the oxide layer $d_{SiO_2} = 1.7(1)$ nm was determined by a corresponding ellipsometric measurement after cleaning of the Si wafer (before coating with the AF 1600). For sufficiently large layer thicknesses, the index of refraction n can be fitted

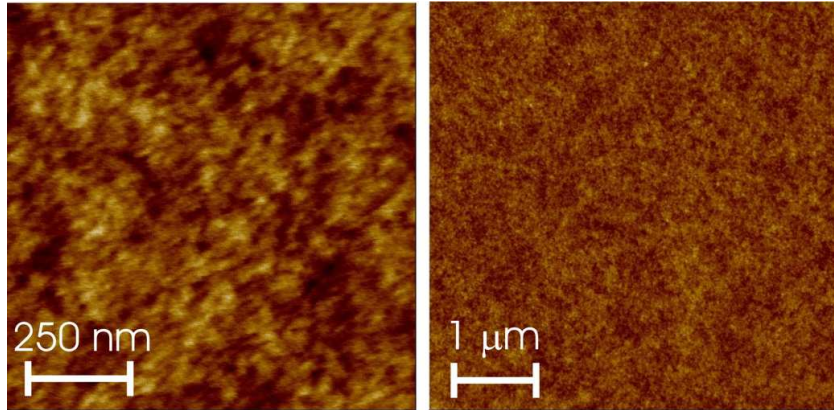


Figure 3.2: AFM image of a Si wafer coated with an AF 1600 layer. Left: Typical image to determine the surface roughness on a scale of $1 \mu\text{m}^2$. Right: Image size of $5 \times 5 \mu\text{m}^2$. The height scale (white to black) is 3 nm (left) and 5 nm (right), respectively.

simultaneously in combination with the AF 1600 layer thickness. From these measurements $n=1.300(5)$ is obtained, in good agreement with the manufacturer information². For small layer thicknesses of a dielectric material, the thickness and the index of refraction are usually coupled in ellipsometric measurements. If simultaneous modelling resulted in significant deviations from $n=1.300(5)$, n was kept constant for reasons of comparability while solely fitting d_{AF1600} . Moreover, the reproducibility of the experimentally measured AF 1600 layer thicknesses is excellent for different solutions of the fluoropolymer. Annealing of the AF 1600 layer above its glass transition temperature of 160°C did not result in any changes of the ellipsometric data and, thus, identical layer thicknesses compared to the as-cast samples were obtained. For the dewetting experiments, the 0.5 w/v% solution was prepared on freshly cleaned Si wafers at a spinning velocity of 2000 rpm, resulting in a AF 1600 thickness of $20(2)$ nm.

AFM was used to characterize the surface of the amorphous fluoropolymeric AF 1600 layer with regard to its roughness. A typical AFM image used for roughness analysis is shown in Fig. 3.2 left. The *rms* roughness of the surface was found to be $0.30(3)$ nm as an average of different samples and different spots⁵. On larger lateral scales periodic film thickness variations can be found potentially originating from the spin-coating process (see Fig. 4.1). The undulations have proven not to influence dewetting, i.e. the curvature of holes or the shape of straight fronts are not affected⁶.

⁵The AFM images (512×512 data points) for the roughness analysis were taken in tapping-modeTM on a scale of $1 \mu\text{m}^2$.

⁶The periodicity of these structures is approx. $15 \mu\text{m}$, whereas the peak-to-valley distance was found to be in the range of 5-8 nm (for an average layer thickness of 20 nm resulting from spin-coating a 0.5 w/v% solution at 2000 rpm).

3.1.3 Wetting Properties

To characterize the wettability of the prepared AF 1600 samples, two types of experiments were performed: First, the wetting properties are characterized in terms of dynamical water contact angle measurements. Therefore, the advancing and the receding contact angle of MilliQTM water were measured via the sessile drop method: An advancing contact angle of 128(2)^o and a receding contact angle of 118(2)^o was found. Second, apolar liquids (in this case 1-bromonaphthalene and bicyclohexyl) are utilized to determine the surface energy γ_{sv} of the AF 1600 samples via the Good-Girifalco [43] equation

$$\gamma_{sl} = \gamma_{sv} + \gamma_{lv} - 2\sqrt{\gamma_{sv}\gamma_{lv}}. \quad (3.1)$$

γ_{ij} denotes the interfacial tension for the different phases, i.e. the solid (*s*), the liquid (*l*) and the vapor (*v*) phase. In combination with the Young's equation [44] for the contact angle θ_Y of a liquid droplet on top of a substrate

$$\cos \theta_Y = \frac{\gamma_{sv} - \gamma_{sl}}{\gamma_{lv}}, \quad (3.2)$$

the surface energy of the substrate γ_{sv} can be calculated via

$$\gamma_{sv} = \frac{1}{4}\gamma_{lv}(1 + \cos \theta_Y)^2. \quad (3.3)$$

The static contact angle θ_Y of bicyclohexyl (Acros Organics, 99%, $\gamma_{lv} = 32.8$ mN/m) was found to be 69(2)^o, for 1-bromonaphthalene (Fluka, >95%, $\gamma_{lv} = 44.6$ mN/m) 81(3)^o was obtained. To conclude, the surface energy $\gamma_{sv} = 15.0$ mN/m is in good agreement with the expectation from literature² of 15.7 mN/m and significantly lower than for OTS and DTS (see Tab 3.2). Compared to the silanized Si wafers, the water contact angles (yet also the contact angle hysteresis) on the AF 1600 substrate are higher (see Tab 3.2).

The driving force for dewetting is the capillary force. For its calculation via the spreading parameter S , it is necessary to know the surface tension of the liquid γ_{lv} (a property purely inherent to the liquid, $\gamma_{lv}(\text{PS}) = 30.8$ mN/m, [45]) and the Young's contact angle θ_Y of the polystyrene melt on top of the AF 1600 surface:

$$S = \gamma_{lv}(\cos \theta_Y - 1). \quad (3.4)$$

To determine the static contact angle θ_Y of PS, AFM measurements of sufficiently large⁷ PS(13.7k) droplets, resulting from dewetting experiments, were performed. The contact angle of $\theta_Y = 88(2)$ ^o was measured by fitting a tangent to a close-up view of the three-phase contact

⁷Note that besides contributions from interfacial tension to the static contact angle of a liquid drop, according to the Young's equation, for very tiny droplets on the nanometer scale a further contribution comes into play: The line tension [46, 47] acts as an additional force to reduce the length of the three-phase contact line and, hence, enlarges the contact angle.

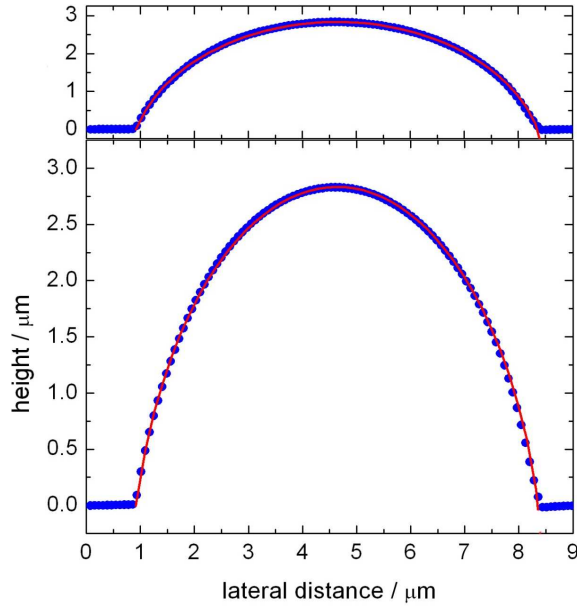


Figure 3.3: *Ex situ* AFM cross-section (filled circles) of a PS(13.7k) droplet on AF 1600. The lower representation exhibits an exaggerated height-scale. The line represents the fit of a portion of a circle to the experimental data.

line avoiding tip-shape induced artifacts⁸. Using the standard AFM tapping-modeTM technique makes the measurement of contact angles larger than 90° impossible. To assure that the contact angle of PS is indeed below 90° , AFM data of the whole drop shape could be fitted by a portion of a circle (see Fig. 3.3). The dynamic (receding) contact angle $\theta_{rec} = 68(2)^\circ$ of PS on AF 1600 was determined likewise with AFM measurements of the three-phase contact line of a growing hole in a PS(13.7k) film.

A detailed comparison of the properties of AF 1600 and silanized (OTS and DTS) substrates is given in Tab. 3.2.

Table 3.2: Properties of AF 1600, OTS and DTS substrates: layer thickness d , *rms* roughness, advancing water contact angle θ_{adv} , water contact angle hysteresis $\Delta\theta$, surface energy γ_{sv} and static contact angle of PS. Data for OTS and DTS was taken from [39].

layer	d (nm)	<i>rms</i> (nm)	θ_{adv} ($^\circ$)	$\Delta\theta$ ($^\circ$)	γ_{sv} (mN/m)	$\theta_Y(\text{PS})$ ($^\circ$)
AF 1600	20(2)	0.30(3)	128(2)	10	15.0	88(2)
OTS	2.3(2)	0.09(1)	116(1)	6	23.9	68(2)
DTS	1.5(2)	0.13(2)	114(1)	5	26.4	66(2)

⁸The measurement was performed on the tip-allocated side of the droplet. According to the slight tilt of the AFM tip (Olympus OMCL- AC160-TS), the data obtained from the "retrace" direction of the scan was used for evaluation.

3.2 Preparation of Thin Polymer Films

Polymers, in this case polystyrene (PS) and poly(methyl methacrylate) (PMMA), were obtained from PSS (Mainz, Germany). Thin PS and PMMA films were prepared by *spin-coating*, a standard thin film preparation technique: A droplet of the polymer solution is put on a substrate⁹ that is fixed on a rotating sample holder. As a solvent for the PS, toluene (Selectipur[®] or LiChrosolv[®], Merck, Darmstadt, Germany) was used in this study. The fast rotation of the substrate causes the solution to spread all over the substrate's surface while the solvent rapidly evaporates. In the end, a thin uniform polymer film remains. The resulting film thickness h_0 is mainly determined by the concentration c of the polymer solution, the spinning velocity ω of the substrate, the acceleration of the spin-coater and the molecular weight M_w of the polymer. For a given molecular weight, the film thickness h_0 scales with $\sqrt{c^3/\omega}$.

Tab. 3.3 gives a survey of various preparation parameters used in this study. Film thicknesses were determined by ellipsometry of PS films prepared on small pieces of cleaned Si wafers (with a native oxide layer) or by AFM measurements of the step height in the vicinity of the three-phase contact line. Depending on the handling of the solution and the adjustment of the spinning acceleration, values for the film thicknesses might vary. For the dewetting experiments, in this study usually polymer film thicknesses between 90 and 140 nm were used. Smaller film thicknesses were prepared for deuterated polymers utilized in neutron scattering experiments (see section 6.1).

As a hydrophilic substrate for spin-coating, freshly-cleaved mica sheets were utilized. To remove dust particles resulting from the cleavage of the mica, the substrate is blown clear with a jet of pure nitrogen prior to further preparation. To transfer the PS film to a hydrophobic substrate, i.e. in this case a small piece of a Si wafer covered with a OTS, DTS or a AF 1600 layer, a further preparation step is essentially necessary: the *floating* procedure. Thereby, the PS film is bloated on a clean MilliQTM water surface and subsequently skimmed by a freshly cleaned hydrophobic substrate. The entire thin film preparation is performed in a laminar flow bench providing a class 100 clean-room atmosphere.

Prior to the floating step, PS films with molecular weights above the critical molecular weight for chain entanglements M_c ($= 35$ kg/mol, see [48]) were usually annealed on the mica substrate on a heating plate under ambient air pressure conditions. The aim of this procedure is to ensure relaxation of residual stresses by transferring the film in the liquid state (without enabling dewetting from the substrate). The pre-annealing was consistently performed at 140 °C for 3 hours (as described in [39] for the highest molecular weight of PS(390k)). This value was chosen according to the study by Podzimek *et al.* investigating the reduction of the density of nucleated holes in view of the pre-annealing time period and the link between nucleation via stress centers and stress relaxation [49]. Residual stresses are supposed to originate from the fast solvent evaporation during spin-coating. The next chapter, dealing with the temporal and spatial evolution of holes during dewetting, starts with a consideration of relevant shear rates

⁹Note that the substrate has to be wettable by the solvent. Spin-coating on hydrophobic substrates such as OTS, DTS or AF 1600 would, therefore, cause the solution to vanish and would not result in the formation of a thin film.

and polymer relaxation times (calculated from the respective viscosities and the elastic modulus of PS). The resulting Weissenberg numbers clearly indicate that non-Newtonian behavior originating from viscoelastic effects by stress relaxation can be safely excluded.

Table 3.3: Film thickness h_0 as obtained by spin-coating (Laurell Technologies Cooperation, at max. acceleration) for various molecular weights M_w from the concentration c of the polymer solution (in toluene) and spinning velocity ω . The polydispersity index M_w/M_n (according to the manufacturer) of the respective polymer is also given in the table. Deuterated polymer melts were prepared to study monodisperse polymer films (see section 5.3) and polymer mixtures by neutron scattering experiments (see section 6.1). A PMMA/toluene solution was prepared to test the impact of the polymer species itself (see section 6.2).

M_w (kg/mol)	M_w/M_n	c (w/v%, mg/ml)	ω (rpm)	h_0 (nm)
PS(5.61k)	1.06	33.8	2500	130
PS(13.7k)	1.03	30.0	2500	130
PS(18k)	1.04	27.8	2000	130
PS(35.6k)	1.03	25.8	2000	120
PS(51.5k)	1.03	23.1	2050	110
PS(65k)	1.02	28.9	3000	130
PS(65k)	1.02	44.1	2000	230
PS(81k)	1.03	25.2	2350	120
PS(101k)	1.03	25.5	2600	130
PS(125k)	1.02	25.4	2800	120
PS(186k)	1.02	20.9	2200	110
PS(271k)	1.02	16.7	1400	120
PS(271k)	1.02	28.4	2000	260
PS(390k)	1.09	19.9	2700	100
d-PS(12.3k)	1.05	16.1	3000	50
d-PS(60.7k)	1.02	13.0	3000	50
80% d-PS(60.7k) + 20% PS(1.97k)	1.02, n.a.	11.6, 2.9	3000	50
80% PS(51.5k) + 20% d-PS(2.32k)	1.03, 1.05	11.5, 2.8	1000	90
80% PS(51.5k) + 20% d-PS(2.32k)	1.03, 1.05	11.5, 2.8	3000	50
PMMA(14k)	1.03	29.9	2500	100

4 Hole Growth Dynamics in Metastable Thin Polymer Films

Fig. 4.1 depicts a typical distribution of heterogeneously nucleated holes in a PS(65k) film on the AF 1600 substrate and a temporal series of optical micrographs illustrating the growth of a hole. Aside from analyzing liquid rim profiles (see Chapter 5) to gain information about the hydrodynamic boundary condition at the solid/liquid interface, the hole growth dynamics as captured by optical microscopy additionally offers a pathway to obtain a good estimation of the slip length b . The following sections are organized as follows: As described in ADDENDUM V, a proper estimation of relaxation times, shear rates and Weissenberg numbers for the dewetting experiments investigated in this study is inevitable to exclude the influence of viscoelastic effects causing non-Newtonian flow behavior. In the following sections, series of hole growth data on AF 1600 substrates for diverse molecular weights and dewetting temperatures are presented and analyzed. The first parameter to be investigated is the dynamics exponent α denoting the temporal evolution of the hole radius, i.e. $R \propto t^\alpha$. Subsequently, the data is evaluated according to the analytical model and analysis technique presented in ADDENDUM III. A discussion of the viscous friction and the slippage velocity contribution, in particular in view of the molecular weight of the polymer melt, completes this chapter. The comparison of dewetting experiments below the critical molecular weight for chain entanglements on different substrates, i.e. DTS, OTS and AF 1600, is discussed in detail in ADDENDUM III: Dewetting is much faster on DTS as compared to OTS substrates. Although the driving force is significantly larger, the slowest hole growth is found on AF 1600 substrates. This phenomenon can be explained by substantial differences in slip properties, as described in ADDENDUM III.

4.1 Estimation of Relaxation Times, Shear Rates and Weissenberg Numbers

An important issue of this study concerns the estimation of relaxation times τ (see Tab. 4.1), via the viscosity η obtained from the Williams-Landel-Ferry (WLF) equation ([50], see section 5.2.4) and the shear modulus G of the polymer melt, the shear rates $\dot{\gamma}$ and the Weissenberg numbers Wi of experiments performed for diverse system parameters (substrate, temperature, viscosity, molecular weight). Weissenberg numbers Wi smaller than 1 assure that viscoelastic effects originating from stress relaxation of the polymer melt can be neglected. For dewetting experiments of PS films up to a typical M_w of 390 kg/mol and typical dewetting temperatures of 105-155 °C on OTS and DTS, the corresponding Weissenberg numbers do not exceed a value of 0.5 [39]. As indicated in Tab. 4.1, Weissenberg numbers (with regard to the molecular weight M_w and the dewetting temperature T) calculated from experiments on the AF 1600

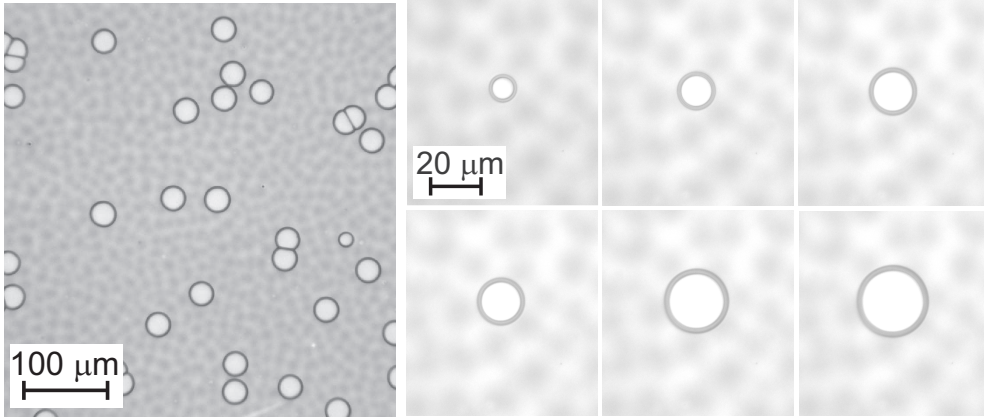


Figure 4.1: Left: Optical micrograph of a PS(65k) film dewetting at 140°C. A typical distribution of nucleated holes is observed. Prior to the preparation on the hydrophobic AF1600 substrate and subsequent dewetting, the sample was pre-annealed for 3 hours at 140°C on the mica substrate. Right: Temporal series of optical close-up images of a growing hole of the same experiment. The time interval between two subsequent images is $\Delta t=100$ s.

Table 4.1: Calculated relaxation times $\tau = \eta/G$ and Weissenberg numbers Wi for diverse temperatures T and molecular weights M_w of the PS melt dewetting from the AF1600 substrate. The viscosity η was obtained from the WLF equation (see section 5.2.4); $G \approx 0.2$ MPa was taken from literature [48]. The maximum shear rates $\dot{\gamma}_{max}$ and the maximum values for corresponding Weissenberg numbers Wi were calculated as described in ADDENDUM V.

M_w	T (°C)	τ (s)	$\dot{\gamma}_{max}$ (1/s)	Wi	M_w	T (°C)	τ (s)	$\dot{\gamma}_{max}$ (1/s)	Wi
35.6k	120	11.55	0.0045	0.052	125k	130	57.5	0.0003	0.019
35.6k	130	0.81	0.0546	0.044	125k	150	1.39	0.0167	0.023
51.5k	125	9.75	0.0023	0.022	186k	130	222	0.0002	0.052
51.5k	130	2.81	0.0065	0.018	186k	140	28.05	0.0012	0.034
51.5k	140	0.36	0.0863	0.031	186k	150	5.4	0.0072	0.039
65k	130	6.5	0.0074	0.048	271k	140	100.5	0.0006	0.057
65k	140	0.8	0.0368	0.029	271k	150	19.35	0.0040	0.077
81k	130	13.15	0.0092	0.121	271k	155	9.55	0.0041	0.039
81k	140	1.66	0.0647	0.108	390k	150	66.5	0.0004	0.029
101k	130	27.8	0.0037	0.103	390k	155	32.9	0.0018	0.058
101k	140	3.52	0.0197	0.069					

substrate do not exceed a value of 0.1 (see ADDENDUM V for details concerning the calculation of shear rates). Consequently, the occurrence of non-Newtonian effects resulting from stress relaxation are not expected for the examined molecular weights and the low shear rates (see Tab. 4.1) in such dewetting experiments. A further discussion concerning the presence of residual stresses caused by the preparation process is included in section 5.3.

4.2 Evaluation of the Dewetting Exponent

While performing hole growth measurements of thin polymer films in the mature stage of a fully developed rim (see section 5.1), the first result that can be extracted from an experiment like the one shown in Fig. 4.1 right is the dewetting exponent α . Fitting an algebraic power law, i.e. $R \propto (t - t_0)^\alpha$, or alternatively plotting the data in a double-logarithmic representation and fitting a straight line represent reliable ways to determine α . Figs. 4.2 and 4.3 exemplarily illustrate a set of typical measurements of the temporal evolution of the radius of holes nucleated in diverse PS films supported by AF 1600 substrates. Note that $t = 0$ marks the time where the hole was detected by optical microscopy.

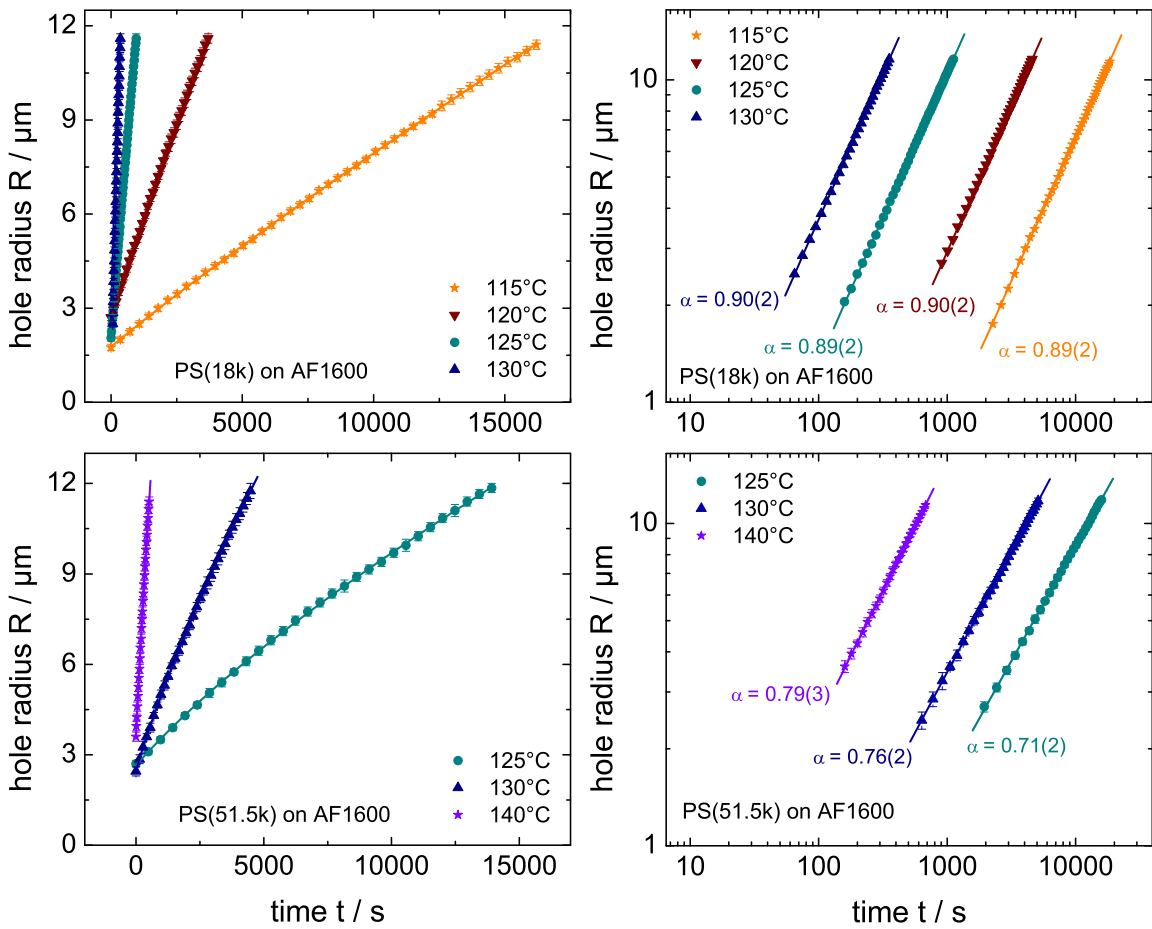


Figure 4.2: Hole radius R versus time t (in linear and logarithmic representation) obtained from optical micrographs for PS(18k) and PS(51.5k) films at different dewetting temperatures. Solid lines represent fit curves of an algebraic growth function, i.e. $R \propto (t - t_0)^\alpha$, to the experimental data. Note that it is necessary to shift the time scale (to match the condition $R(t = 0) = 0$) to obtain a linear relation in the double logarithmic representation.

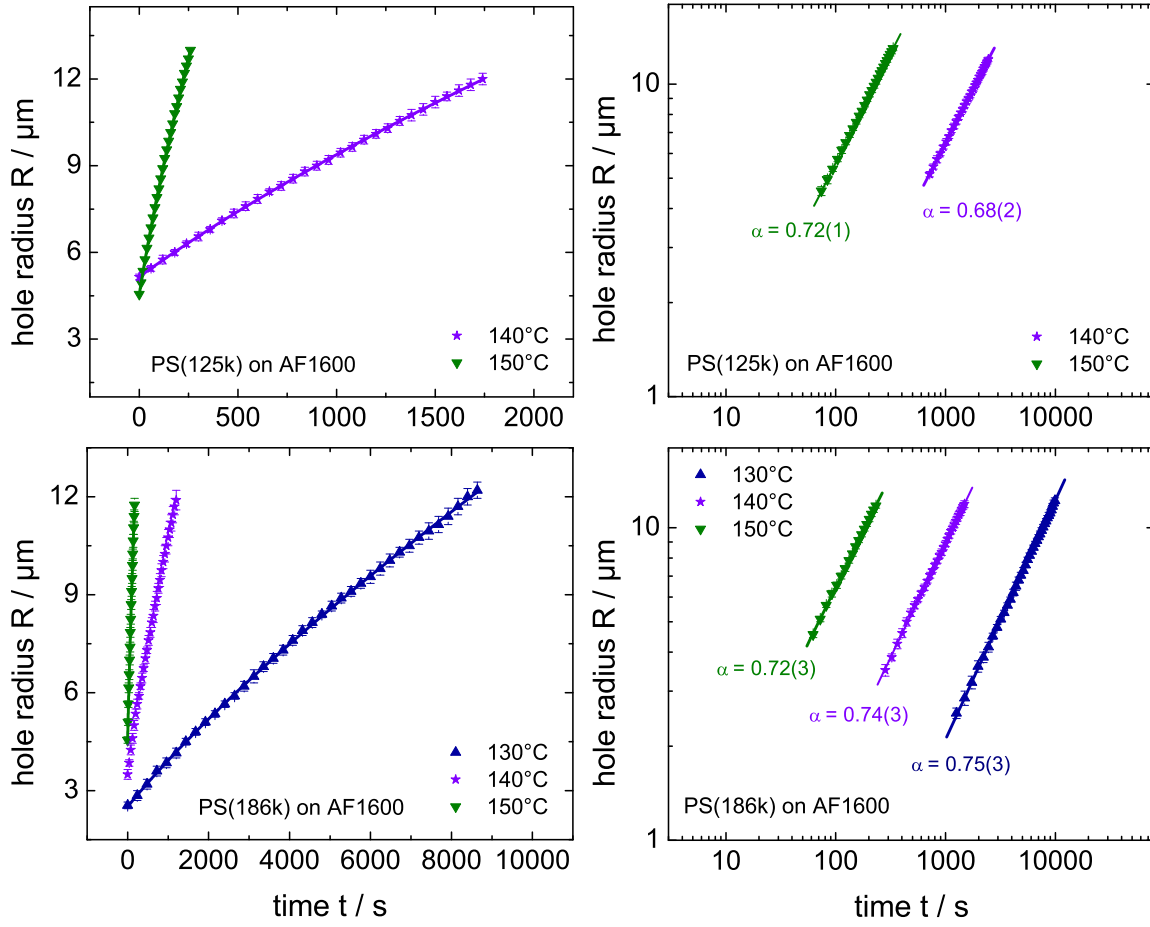


Figure 4.3: Hole radius R versus time t (in linear and logarithmic representation) obtained from optical micrographs for PS(125k) and PS(186k) films at different dewetting temperatures. Solid lines represent fit curves of an algebraic growth function, i.e. $R \propto (t - t_0)^\alpha$, to the experimental data.

A long-term hole growth measurement in the case of a PS(13.7k) film at 120 °C on the AF 1600 substrate and its data evaluation is shown in Fig. 4.4. At this point it should be pointed out that, for the dynamics and rim profile analysis, the experiment was usually stopped at a hole radius of approximately 12 μm to ensure that approximately the same amount of liquid is accumulated in the rim while analyzing its shape. The dewetting experiment analyzed in Fig. 4.4 was stopped due to the occurrence of the liquid rim instability (see e.g. [51]) that manifests itself by periodic undulations of the three-phase contact line and the formation of (optically visible) liquid bulges and valleys (see Fig. 4.5). Moreover, hole-hole coalescence, as depicted in Fig. 4.5, and the coalescence of holes and receding straight fronts (entailed by the presence of floating gaps due to the preparation process) in this stage of dewetting handicaps the recording of further hole growth data. In case of the experiment depicted in Fig. 4.4, $\alpha = 0.90(1)$ is constant over the whole range of experimental data points (see Fig. 4.4 right).

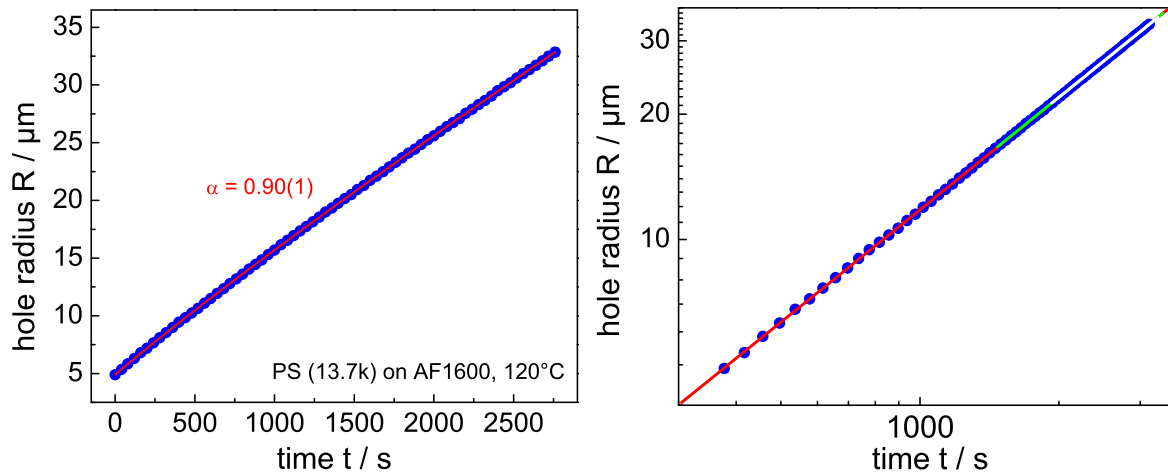


Figure 4.4: Left: Hole growth dynamics captured by optical microscopy of a PS(13.7k) film on AF 1600 at 120 °C. The solid (red) line represents a fit of an algebraic growth function, i.e. $R \propto (t - t_0)^\alpha$, to the experimental data. Right: Double-logarithmic representation of the same data: Different parts of this curve were selected for fitting, showing no significant differences in their slope. Note that it is necessary to shift the time scale (to match the condition $R(t = 0) = 0$) to obtain a linear relation in this representation.

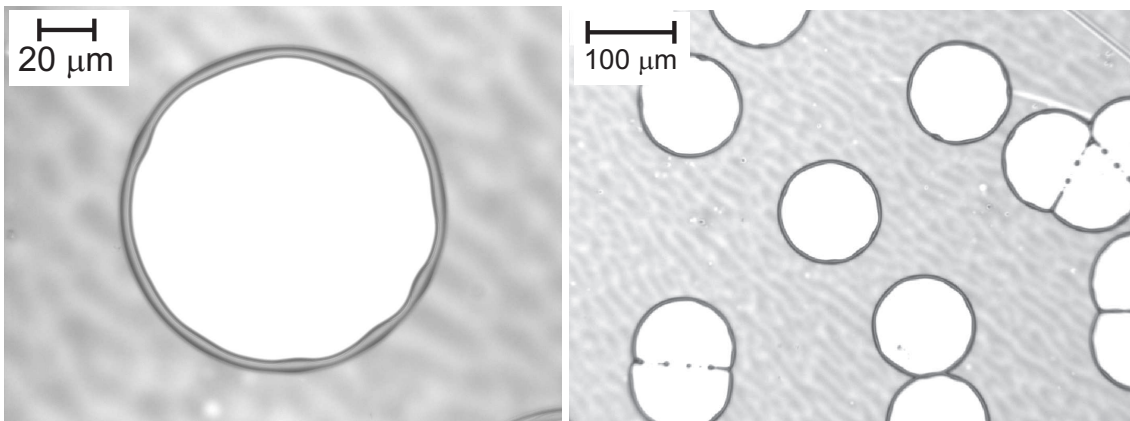


Figure 4.5: Optical micrographs illustrating the late stage of hole growth for a PS(13.7k) film on AF 1600 at 120 °C. The left image shows a large hole in the PS film exhibiting undulations of the rim shape along the perimeter of the hole according to a liquid rim instability. This instability also causes liquid cylinders, formed via the coalescence of holes (as depicted in the right image), to decay into droplets.

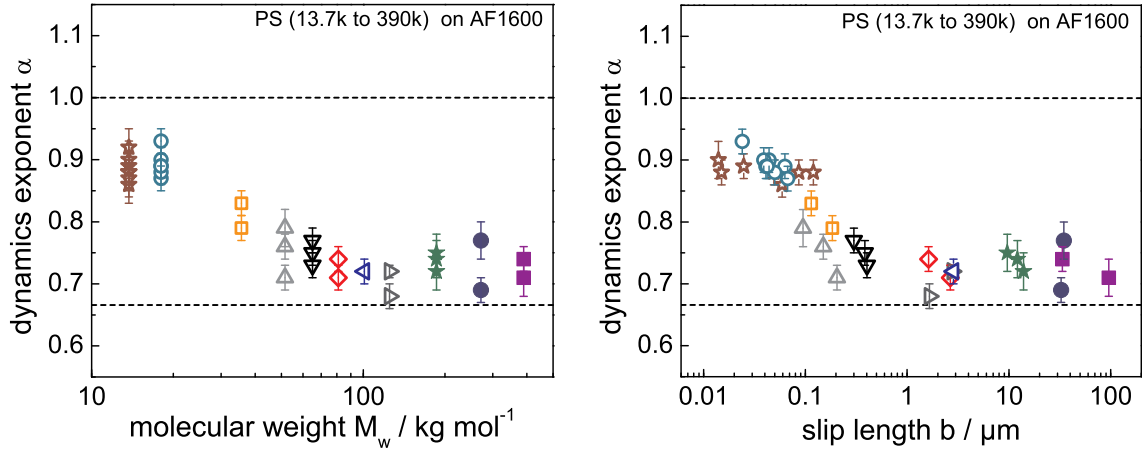


Figure 4.6: Left: Dewetting exponent α for a series of dewetting experiments using different molecular weights M_w . Right: Dewetting exponent α versus the slip length b as obtained from the hole growth analysis (see section 4.4). The color code (symbols) for different molecular weights M_w corresponds to the colors (symbols) used in the graph on the left.

To study the impact of polymer chain length and, especially, of chain entanglements, the molecular weight M_w was systematically varied in dewetting experiments from PS(5.61k) up to PS(390k). While no significant temperature dependency of α could be detected for a certain molecular weight¹, Fig. 4.6 illustrates a significant decrease that is found by increasing the molecular weight (above the critical molecular weight M_c for chain entanglements). Thus, the molecular weight is correlated to the slip length b (as e.g. obtained from the analysis of hole growth dynamics, cf. section 4.4): For $M_w < M_c$ a dynamics exponent $\alpha \approx 0.9$ is measured, whereas $\alpha \approx 0.7$ is found for $M_w > M_c$. As soon as chain entanglements become considerable and slippage starts to increase, the dewetting exponent changes significantly. This finding is consistent with the theoretical expectation obtained from simple energetic considerations (see ADDENDUM II), which predict $R \propto t$ and $R \propto t^{2/3}$ in the border cases of no-slip and full-slip, respectively. The experimental result, however, visualizes at the same time the limitations of this rather naive approach: Although the slip length varies orders of magnitude, α does not show significant variations except for the transition from weak to strong slip (note that the slip length is orders of magnitude larger as compared to the typical film thickness). Consequently, drawing further conclusions solely from measurements of the dewetting exponent α with regard to slippage and the slip length in particular is hardly practicable.

¹Besides the aforementioned correlation between α and the slip length b , a significant deviation is found for the smallest molecular weight, i.e. PS(5.61k): α decreases as the dewetting temperature increases (mean values for at least two independent experiments at fixed temperature: $\alpha = 0.86(4)$ at 105 °C, $\alpha = 0.82(4)$ at 110 °C and $\alpha = 0.77(4)$ at 115 °C). The experimental results for the slip lengths of PS(5.61k) films (shown in section 5.2.2) indicate that this singular dependence of α on the dewetting temperature is not connected to a systematic enhancement of slippage.

4.3 Evaluation of the Viscous Velocity Contribution

Separating viscous velocity contribution v_v and slip velocity contribution v_s is feasible by plotting the dewetting velocity V (given by the first derivative dR/dt of the hole radius $R(t)$) versus $1/\sqrt{R}$ (as described in detail in ADDENDUM III):

$$V = v_v + v_s = C_v(\theta) \frac{|S|}{\eta} + \frac{|S|b}{3\eta} \frac{1}{w}, \quad (4.1)$$

$$w = C_s \sqrt{h_0} \sqrt{R}. \quad (4.2)$$

This was extensively done for dewetting experiments of thin PS films below and above the critical entanglement length (molecular weight M_c) of the polymer on the AF 1600 substrate. By plotting $v_0/|S|$ versus $1/\eta$ for different $M_w < M_c$, as shown in Fig. 4.7 left, the predicted linear relationship between the viscous velocity contribution $v_v = v_0$ and the reciprocal viscosity $1/\eta$ is reproduced. The spreading coefficient $S = \gamma_{lv}(\cos\theta_Y - 1) = -0.0297 \text{ N/m}$ quantifies the driving force of the dewetting process of PS on the AF 1600 substrates ($S = -0.0188 \text{ N/m}$ is found on OTS and DTS substrates [34]). Consequently, the constant of proportionality $C_v(\theta) = \text{const.} = 0.039$ can be calculated from this master-curve for the AF 1600 substrate.

Comparing these results (see Fig. 4.7) to corresponding data for PS(13.7k) dewetting from OTS and DTS substrates (see [39]), significant deviations from this relation are found². The absolute value of the deviation increases for decreasing dewetting temperature and is significantly pronounced on DTS as compared to OTS. These observations suggest a correlation to the slip length b (as described in ADDENDUM III) which is in turn also connected to the shape of rim profiles: more asymmetric ones in the case of pronounced slip compared to symmetric profiles in the case of dominating viscous dissipation, see Chapter 5 and ADDENDUM IV. With regard to the work by Redon *et al.* (see also ADDENDUM II), a logarithmic factor L is introduced that accounts for the divergence of the viscous dissipation near the three-phase contact line of a liquid wedge [19, 22]: This factor is written as $L \approx \ln(x_{max}/x_{min})$, where x_{min} corresponds to a short-distance cutoff for the flow field and x_{max} is attributed to the maximum width of the rim. Moreover, the authors identify x_{min} with the slip length b and, thus, they expect L to decrease as the slip length increases. This is in qualitative accordance with their experimental observation for increasing molecular weight [19], corresponding to an amplification of slippage ($b \propto M_w^3$, see [52]).

Aside from this interpretation of the experimental data, additional energy dissipation mechanisms can be taken into consideration: These processes are mainly located at the three-phase contact line and, therefore, are independent of the size of the rim. Referring to the corresponding discussion in ADDENDUM II, the molecular kinetic theory (MKT) describes the motion of single molecules, in contrast to the aforementioned hydrodynamic (continuum) approach to energy dissipation. For decreasing temperatures, however, the MKT predicts increasing friction

²Note that using the same viscosities (from the Williams-Landel-Ferry equation) for the calculation of $C_v(\theta)$ on different substrates assures that the deviations can not be attributed to the limited accuracy of the viscosity data.

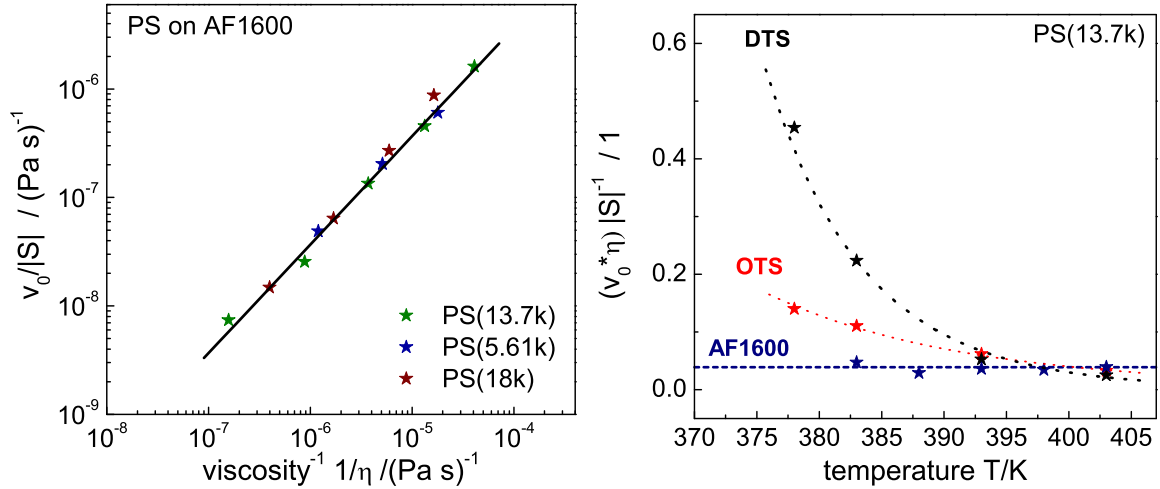


Figure 4.7: Left: Double-logarithmic representation of the y-axis intercept $v_0/|S|$, normalized by the absolute value of the spreading coefficient S , versus the reciprocal viscosity $1/\eta$ (from the WLF equation, see 5.2.4 for further details). Mean values of different experiments are plotted for different molecular weights M_w below the critical molecular weight M_c for chain entanglements. Right: $C_v(\theta) = (v_0\eta)|S|^{-1}$ versus the dewetting temperature T : For decreasing temperature, the experimental data for OTS and DTS (adapted from [39], dotted lines represent a guide to the eye) significantly deviates from the constant value obtained for the AF 1600 substrate (dashed line).

coefficients and, consequently, decreasing velocities of the three-phase contact line. In other words, for decreasing temperatures it becomes more difficult for the liquid molecules to overcome the potential barrier. This is, however, in contradiction to the experimental observation for OTS and DTS substrates: v_0 and, consequently, $C_v(\theta) = (v_0\eta)|S|^{-1}$ increase significantly (up to roughly one order of magnitude for DTS as compared to AF 1600) as the dewetting temperature decreases (see Fig. 4.7 right). Further potential mechanisms acting at the three-phase contact line of a liquid volume on a surface and impacting its movement are presented and discussed in ADDENDUM II.

To conclude, it can be stated that the formerly described correlation between the viscous velocity contribution v_0 and the slip length b is supposed to be responsible for the deviations occurring on OTS and DTS as compared to the AF 1600 substrate. No evidence is found for the presence of additional dissipation mechanisms in the case of growing holes in thin polymer films. The friction force F_v describing viscous dissipation within the rim is inversely proportional to $C_v(\theta)$. An increase in $C_v(\theta)$ is linked to the reduction of shear strain within the rim (to be more precise: in the vicinity of the three-phase contact line) indicating the presence of slippage at the solid/liquid interface. Consequently, it has to be emphasized that the viscous velocity contribution in the analytical model based on the superposition of energy dissipation mechanisms, as presented in ADDENDUM III, still contains a minor but nevertheless observable dependency on slippage.

For polymer melts above M_c , slippage dramatically increases with increasing molecular weight ($b \propto M_w^3$, see [52]). Due to the fact that the slip length for this experimental configuration was found to be not systematically depending on the dewetting temperature³, $C_v(\theta)$ is expected to be a function of the molecular weight M_w according to the previous discussion. As shown in Tab. 4.2, a clear increase in $C_v(\theta)$ is found on the AF1600 substrate⁴, even despite the limited accuracy of the experimental data. To finally conclude, this result corroborates the aforementioned description of the impact of slippage (via a logarithmic pre-factor) on the viscous velocity contribution.

Table 4.2: $C_v(\theta)$ and C_s for diverse molecular weights. $C_v(\theta)$ was determined from the y-axis intercept v_0 and the viscosity η given by the WLF equation (see section 5.2.4). In case of several measurements at different temperatures, the average value is given in conjunction with the standard deviation given in brackets. C_s is given as mean value of at least two independent measurements at different temperatures (standard deviation of different measurements is given in brackets) and was calculated via $C_s = w/\sqrt{h_0 R}$, where w and h_0 are measured by AFM and the hole radius R is measured by optical microscopy after quenching the sample to room temperature (see section 4.4 for further details).

M_w	5.61k	13.7k	18k	35.6k	51.5k	65k
$C_v(\theta)$	0.012(3)	0.038(15)	0.031(7)	0.031(2)	0.011(6)	0.028(3)
C_s	2.4(1)	2.1(1)	2.2(1)	2.0(1)	2.2(1)	2.2(1)
M_w	81k	101k	125k	186k	271k	390k
$C_v(\theta)$	0.06(3)	0.09	0.03(1)	0.5(3)	0.74(72)	0.78(3)
C_s	2.4(1)	2.7(1)	3.3(3)	4.2(3)	6.0(2)	8.8(4)

4.4 Evaluation of the Slip Length

Aside from the evaluation of the viscous velocity contribution, the determination of the slope of the $V(1/\sqrt{R})$ data (see Eqs. (4.1) and (4.2)) representation enables to quantify the slip length b (as described in ADDENDUM III). Again, viscosity data extracted from the WLF equation are utilized (see section 5.2.4). C_s is calculated from AFM measurements of the rim width w (see Tab. 5.1) and the film thickness h_0 in combination with an optical measurement of the hole radius R after quenching the sample to room temperature⁵. Values for C_s on the AF1600 substrate with regard to the molecular weight are shown in Tab. 4.2 in the previous section.

Fig. 4.8 exemplarily illustrates a set of typical $V(1/\sqrt{R})$ curves for diverse dewetting experiments: Fig. 4.8 left shows three data sets for hole growth experiments on PS(65k) films of

³Consequently the slip length does not significantly depend on the viscosity for a fixed M_w .

⁴Note that this was also found for OTS and DTS substrates, see [39].

⁵Note that C_s can also be quantified by *in situ* AFM measurements if the hole radius R and the rim width w are recorded simultaneously. The temporal resolution of AFM imaging and piezo drifts correlated to the high-temperature environment, however, restrict this pathway to retarded dewetting velocities especially at temperatures close to T_g of the polymer melt. An example of an *in situ* AFM measurement of the growth of the rim and the temporal evolution of the rim width w is presented in section 5.1.

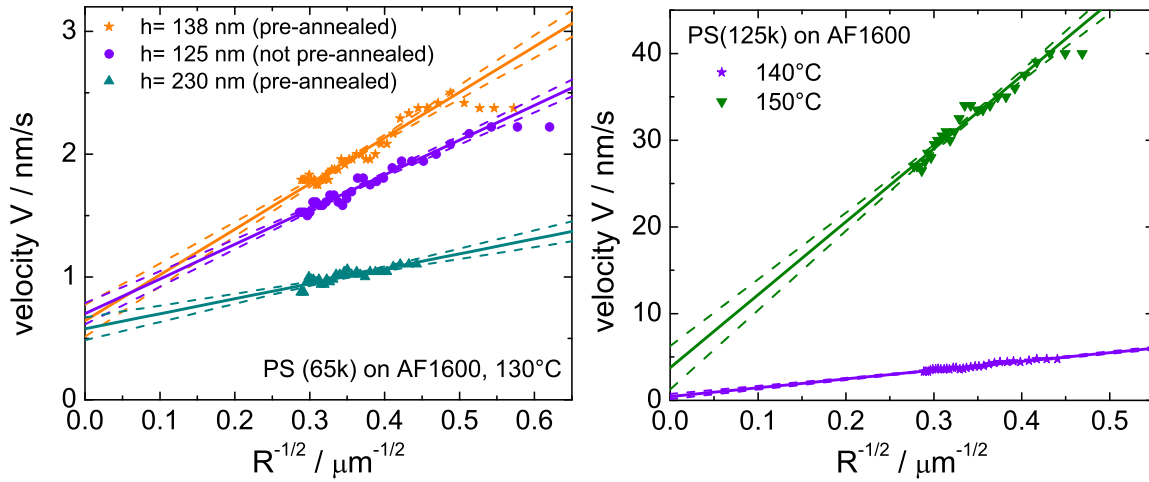


Figure 4.8: Dewetting velocity plotted versus the reciprocal square root of the corresponding hole radius, i.e. $V(1/\sqrt{R})$. Left: Experiments of PS(65k) dewetting from AF 1600 for different film thicknesses at an identical dewetting temperature of 130 °C and, consequently, identical viscosities. Different slopes of the linear fit curves (solid lines) can be found, the y-axis intercept, however, is identical within the experimental error for all experiments. The dashed lines illustrate the corresponding 95% confidence bands of the fit curves. Right: Effect of varying melt viscosities via different dewetting temperatures for the same molecular weight, i.e. PS(125k), on AF 1600. The y-axis intercept is significantly larger for the larger dewetting temperature and, consequently, smaller melt viscosity.

different film thicknesses of PS(65k) films dewetting from AF 1600 substrates. The film thickness impacts the slope of the curves, but does not act on the position of the y-axis intercept of the extrapolated linear fit to the experimental data. The figure on the right depicts different data sets for different dewetting temperatures and, therefore, different melt viscosities which impacts the y-axis intercept (as evaluated in the previous section) as well as the slope of the curve.

For small hole radii, i.e. for large $1/\sqrt{R}$, data points deviating from the linear regime are usually found. This deviation can be attributed to the presence of the pre-mature stage of hole growth, where the rim of the hole is not fully developed. According to the description of Brochard-Wyart *et al.* (see ADDENDUM II for further details), the transition to the mature stage of a fully developed rim is determined by the slip length [53]. The latter correlation, however, was not systematically studied due to the fact that the initial hole size at the time of the first images captured by the microscope did slightly vary for diverse experiments.

The slip length b is evaluated with regard to the molecular weight of the polymer melt: Below the critical molecular weight M_c for chain entanglements, slip lengths roughly between 10 and 100 nm are found. Above M_c , the slip length increases with $M_w^{2.9(2)}$ and values for b are systematically lowered compared to the expectation by de Gennes (i.e. $b = aN^3/N_e^2$, see [52]) based on bulk literature values for a and N_e . These results are in good agreement with

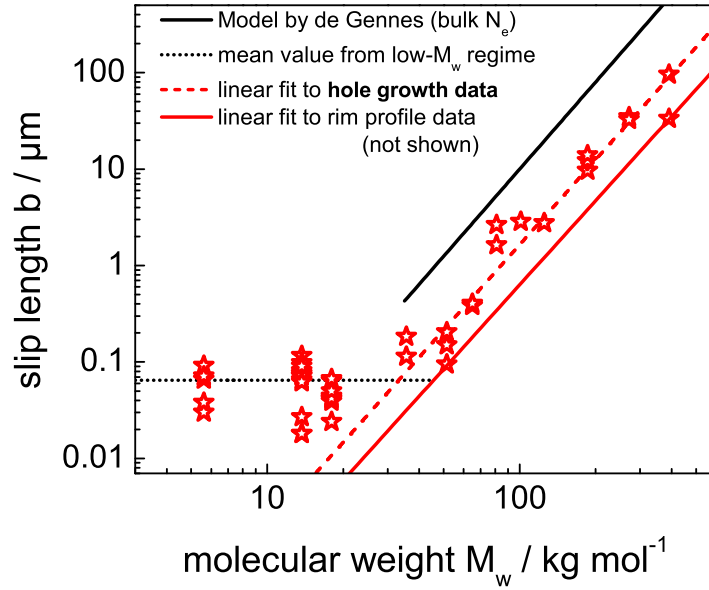


Figure 4.9: Double-logarithmic plot of the slip length b as function of the molecular weight M_w of the PS melt; b is obtained from hole growth analysis for single experiments (stars) with PS dewetting from AF 1600 substrates. The solid black line represents the model by de Gennes [52] using bulk $N_e=163$, whereas the dashed red line is a fit to the experimental data. For reasons of comparison, the solid red line represents the fit to the slip length data (not shown) obtained from the rim profile analysis (see section 5.2.2).

the corresponding data obtained from the quantitative analysis of the rim profiles from the identical holes (see ADDENDUM V and section 5.2.2). Consequently, this independent technique based on comparatively simple arguments concerning energy dissipation and capillary driving forces corroborates the observation of a reduced entanglement density in the vicinity of the solid/liquid interface (as described in ADDENDUM V and section 5.2.2). A direct comparison of both techniques determining the slip length in view of the molecular weight of the polymer melt and a detailed discussion of the processes on the molecular scale is presented in section 5.3.

4.5 Summary

- The Weissenberg numbers Wi are in the range of 0.1 at maximum for the relevant shear rates and relaxation times for PS dewetting from AF 1600. Hence, Newtonian flow can be assumed.
- Dewetting is much slower on the AF 1600 substrate (compared to OTS and DTS) below the critical molecular weight of chain entanglements, although the driving force for dewetting is larger on AF 1600 (see ADDENDUM III).
- Hole growth data obtained for the AF 1600 substrate for diverse temperatures and molec-

ular weights of the PS melt was analyzed according to established models and compared to the corresponding data for OTS and DTS (see ADDENDUM III).

- Below the critical molecular weight for chain entanglements, AF 1600 exhibits slip lengths between 10 and 100 nm, whereas a substantial amount of slippage is found for OTS and DTS (see ADDENDUM III).
- The dewetting exponent α on AF 1600 is sensitive to the transition from weak slip to strong slip (occurring in the range of the critical molecular weight for chain entanglements M_c). The exponent, however, does not change significantly by a further increase in the slip length and is, therefore, no appropriate measure for the slip length.
- The viscous velocity contribution on AF 1600 for PS films below M_c is proportional to the reciprocal viscosity $1/\eta$. Deviations from this behavior on OTS and DTS are assigned to the substantial amount of slippage present on these surfaces.
- The slip length strongly increases for increasing molecular weights above the critical molecular weight for chain entanglements. The data shows excellent agreement with the corresponding quantitative analysis of rim profiles. Further details, results and their implications are discussed in section 5.3.

Addendum III - Probing Slippage and Flow Dynamics of Thin Dewetting Polymer Films

Proceedings of the 1st European Conference on Microfluidics - Microfluidics 2008, Bologna, December 10-12, 2008, μ Flu08-194, ISBN 2-906831-76-X (2008).

Authors: O. BÄUMCHEN¹, R. FETZER², and K. JACOBS¹

¹ Department of Experimental Physics, Saarland University, 66123 Saarbrücken, Germany.

² Present address: Ian Wark Research Institute, University of South Australia, Mawson Lakes, SA 5095, Australia.

Author contributions: K. Jacobs designed research. Experiments were performed by O. Bäumchen (experiments on the AF 1600 substrate) and R. Fetzer (experiments on OTS and DTS). The article was written by O. Bäumchen. Writing was supervised by R. Fetzer and K. Jacobs.

Abstract - The control of hydrodynamic boundary conditions has become more and more important for confined geometries such as lab-on-a-chip devices. Probing the boundary conditions at the solid/liquid interface is therefore of essential interest. In this article we study the dewetting dynamics of thin polymer film flow on smooth hydrophobic surfaces and present a method to extract hydrodynamic boundary conditions, i.e. the slip length. It has been shown that different energy dissipation mechanisms occur in such systems. Viscous dissipation and friction at the solid/liquid interface counteract the capillary driving force. Silicon wafers with three different hydrophobic surface coatings, an amorphous Teflon[®] coating (AF 1600) and self-assembled monolayers of octadecyltrichlorosilane (OTS) and dodecyltrichlorosilane (DTS) exemplarily show the applicability of the proposed model. By superposing both dissipation mechanisms and plotting hole growth dynamics data in a special way, we are able to identify viscous part and slippage part. Thereby we manage to extract the slip length for our systems. Concerning the silane layer surfaces we find values in the range of microns that decrease with increasing temperature. Especially on DTS slippage is pronounced; the slip lengths are about one order of magnitude larger than on OTS. In case of the AF 1600 coating, viscous dissipation dominates and we obtain slip lengths roughly between 10 to 100 nm. Additionally, further potential dissipation mechanisms will be briefly discussed.

PROBING SLIPPAGE AND FLOW DYNAMICS OF THIN DEWETTING POLYMER FILMS

Oliver Bäumchen¹, Karin Jacobs

Department of Experimental Physics, Saarland University, D-66123 Saarbrücken, Germany
o.baumchen@physik.uni-saarland.de, k.jacobs@physik.uni-saarland.de

Renate Fetzer

Present address: Ian Wark Research Institute, University of South Australia, Mawson Lakes SA5095,
Australia
renate.fetzer@unisa.edu.au

KEY WORDS

Slippage, Dewetting, Polymer Flow, Thin Films

ABSTRACT

The control of hydrodynamic boundary conditions has become more and more important for confined geometries such as lab-on-a-chip devices. Probing the boundary conditions at the solid/liquid interface is therefore of essential interest. In this article we study the dewetting dynamics of thin polymer film flow on smooth hydrophobic surfaces and present a method to extract hydrodynamic boundary conditions, i.e. the slip length. It has been shown that different energy dissipation mechanisms occur in such systems. Viscous dissipation and friction at the solid/liquid interface counteract the capillary driving force. Silicon wafers with three different hydrophobic surface coatings, an amorphous Teflon[®] coating (AF 1600) and self-assembled monolayers of octadecyltrichlorosilane (OTS) and dodecyltrichlorosilane (DTS) exemplarily show the applicability of the proposed model. By superposing both dissipation mechanisms and plotting hole growth dynamics data in a special way, we are able to identify viscous part and slippage part. Thereby we manage to extract the slip length for our systems. Concerning the silane layer surfaces we find values in the range of microns that decrease with increasing temperature. Especially on DTS slippage is pronounced; the slip lengths are about one order of magnitude larger than on OTS. In case of the AF 1600 coating, viscous dissipation dominates and we obtain slip lengths roughly between 10 to 100 nm. Additionally, further potential dissipation mechanisms will be briefly discussed.

1. INTRODUCTION

Up to now various methods have been developed to characterize whether a liquid is able to slip in the vicinity of the solid/liquid interface. In most of these studies fluid flow is induced externally, either by shearing two parallel plates and probing the flow profile of the liquid in between (particle imaging velocimetry (PIV) [1, 2, 3], fluorescence recovery after photobleaching (FRAP) [4, 5]), or by squeezing liquid out from between two curved interfaces and measuring the interfacial friction of drainage (colloidal probe atomic force microscopy (AFM) [6, 7], surface force apparatus (SFA) [8, 9]). To avoid side effects generated by external driving forces, new techniques are put forward to probe the interfacial dissipation (e.g., particle diffusion close to the interface [10]).

To date, there seems to be a common agreement that, in the case of simple liquids, slippage depends on the strength of the interaction between the liquid molecules and the surface of the substrate. However, in case of other liquids such as polymers, the description might be more complex. In many studies, further parameters such as surface roughness, shear rate, polarizability or interfacial layers of reduced viscosity have been shown

¹ Corresponding author

to strongly influence slippage. Recent review articles give an overview concerning many results obtained by different methods for different liquid/substrate combinations and properties [11, 12, 13].

Polymers, in our case polystyrene, are very common model liquids due to the fact that their viscosity and their dynamics can be easily controlled via temperature or their chain length. To induce flow, we make use of an internal driving force, the dewetting process of thin films. Dewetting takes place if the system can gain energy by minimizing the contact area with the substrate [14, 15]. In our case, hydrophobic substrates are only partially wetted by the polystyrene melt and are ideal smooth model substrates. The relevant driving forces for dewetting can be inferred from the effective interface potential [16]. Additionally, friction forces have to be taken into account. These are on the one hand viscous dissipation within the liquid (see section 3.1) and on the other hand dissipation due to friction at the solid/liquid interface (see section 3.2).

In this article, we present a how-to manual to obtain values for the slip length. Thereby, the velocity of the dewetting front is analyzed, permitting the distinction of energy dissipation due to viscous flow from the dissipation due to interfacial friction with the result that the slip length can be extracted (see section 3.3). Further potential energy dissipation mechanisms are briefly discussed in section 3.4.

2. PREPARATION

Silicon wafers (2.1 nm native oxide layer, Siltronic AG, Germany) have been carefully cleaned by standard procedures and hydrophobized by octadecyltrichlorosilane (OTS) or dodecyltrichlorosilane (DTS) monolayers using standard silanization methods [17]. To obtain a Teflon[®] coating on top of the silicon, we directly spin-coat a solution of AF 1600 (purchased from Aldrich) in a perfluorinated solvent (FC-75, purchased from Acros Organics). Polystyrene (PS, obtained by PSS, Mainz, Germany) films of 13.7 kg/mol (termed "PS13.7k") molecular weight, low polydispersity (1.03) and thickness of either about 130 nm or 230 nm have been prepared by spin-coating a toluene solution on mica, transferring the films onto a Millipore water surface and picking them up with the substrates. Heating the samples above the glass transition temperature of the polymer initiates the dewetting process.

The substrates are characterized by the surface energy γ_{sv} , determined via measuring the Young's contact angle with non-polar liquids [18]. Additionally, the substrates show large advancing contact angles and small contact angle hysteresis of Millipore water. The (static) receding contact angle θ of polystyrene (which has also polar contributions) droplets was 67(3)[°] on the silanized substrates, whereas we find 88(2)[°] for AF 1600 surfaces. These data were measured with the help of scans of the proximity of the three phase contact line by atomic force microscopy (AFM, Multimode by Veeco, Santa Barbara, CA, USA). Roughness measurements (on a 1 μm^2 area) have as well been performed using AFM; the thickness of the hydrophobic coatings has been controlled by ellipsometry (EP³ by Nanofilm, Göttingen, Germany). All results regarding wetting and structure properties of the samples are summarized in table 1.

hydrophobic layer	thickness (nm)	roughness (nm)	θ_{adv} (°)	$\Delta\theta$ (°)	γ_{sv} (mN/m)
AF 1600	21(1)	0.30(3)	128(2)	10	15.0
OTS	2.3(2)	0.09(1)	116(1)	6	23.9
DTS	1.5(2)	0.13(2)	114(1)	5	26.4

Table 1: Summary of substrate properties concerning wettability, roughness and thickness of the hydrophobic layers. (Numbers in brackets give the error of the last digit.)

3. HOLE GROWTH

The first optically visible sign of dewetting is the appearance of circular holes that slowly (\sim nm/s) grow in size. The removed material is collected in a so-called rim (see fig. 1). Cross sections of such rims can be measured by in situ AFM scans. These experiments reveal that the dynamic (receding) contact angle stays constant during dewetting. Measuring the radii of growing holes within the thin liquid film by optical microscopy, we find that the dewetting velocity at a certain temperature strongly depends on the type of substrate. The experiments

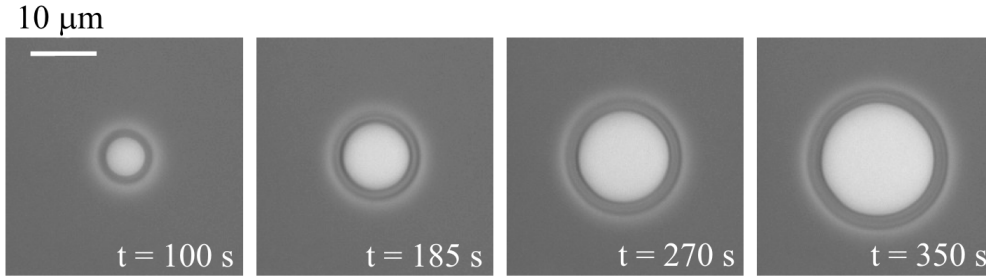


Figure 1: Optically obtained images of growing holes in a thin dewetting PS film on DTS at 120°C.

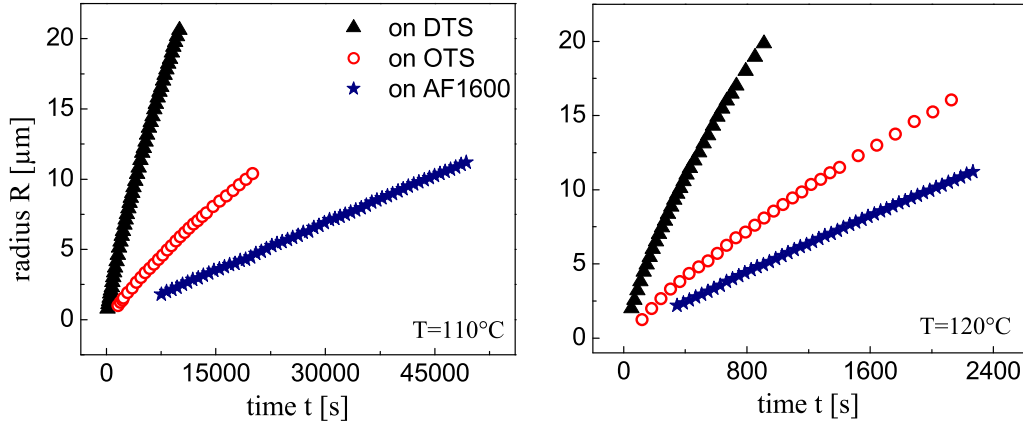


Figure 2: Hole growth dynamics on AF 1600, OTS and DTS at 110°C and 120°C.

show that dewetting proceeds slowest on the AF 1600 substrate and fastest on DTS (the shorter silane). These findings are remarkable since the driving force for dewetting, described by the spreading parameter S ,

$$S = \gamma_{lv}(\cos\theta - 1), \quad (1)$$

actually is identical on the silane monolayers and even larger on AF 1600. γ_{lv} describes the surface tension of the liquid (30.8 mN/m for PS).

This indicates that dissipation is different on both substrates. In the following sections, we present different energy dissipation models first developed by Brochard-Wyart et al. [19] and proceed in illustrating a way to determine the slip length b . As will be shown, the difference in dissipation on the three surfaces can be attributed to different slippage.

3.1 No-Slip Limit

Assuming a vanishing flow velocity at the solid/liquid interface (no-slip), dissipation is of purely viscous nature. Because the shear rate is highest in the vicinity of the three-phase contact line, viscous friction is localized along this line and, thus, independent of the width of the rim. If the flow field (which depends only on the dynamic contact angle θ_{dyn}) at the contact line is not affected by the rim size, a dependency of the viscous dissipation on dewetting time is not expected. In this case, we stay with a friction force which is proportional to the viscosity η of the liquid and the following velocity contribution:

$$v_{visc} = C_v(\theta_{dyn}) \frac{|S|}{\eta}. \quad (2)$$

$C_v(\theta_{dyn})$ is a constant that characterizes the flow-field in the vicinity of the three-phase contact line. In summary, this model describes the so-called no-slip boundary condition. The velocity of the traveling rim does not depend on the holes radius R and by that, we stay with holes that grow linearly in time:

$$R \propto t. \quad (3)$$

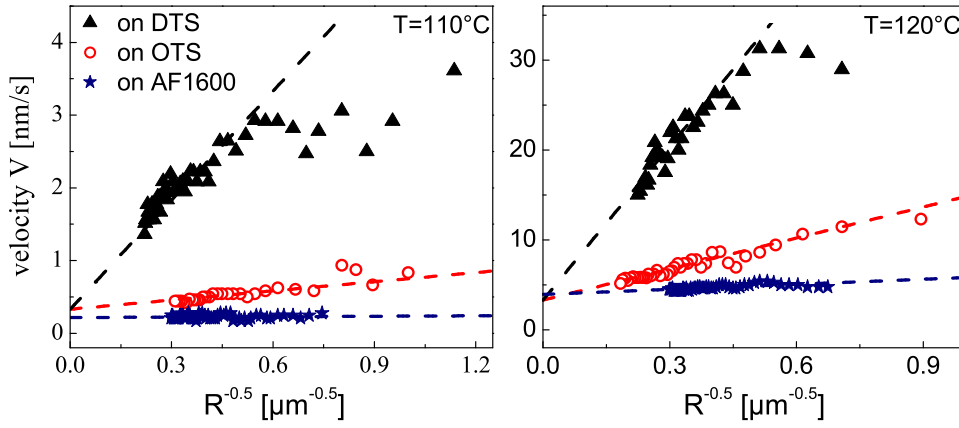


Figure 3: Dewetting velocity plotted versus the inverse square root of the hole radius for OTS and DTS.

3.2 Plug-Flow Limit

In contrast to the previously described model, Redon et al. observed remarkably large slip for long entangled polymer melts [20]. In this so-called plug-flow situation, energy dissipation takes place at the solid/liquid interface of the moving liquid. Thus, a reliable definition of the amount of slipping fluid has to be found. This is usually estimated as the width of the rim w . Hence, the friction force is proportional to the friction coefficient κ at the interface and the width of the rim. Using Navier's description of the slip length b

$$b = \frac{\eta}{\kappa} \quad (4)$$

the corresponding velocity contribution can be written as follows:

$$v_{slip} = \frac{|S|b}{3\eta} \frac{1}{w}. \quad (5)$$

If the rim grows in a self-similar way, conservation of mass leads to the assumption that the width of the rim is proportional to \sqrt{R} . In case of a thin film of thickness h_0 this leads to

$$w = C_s \sqrt{h_0} \sqrt{R} \quad (6)$$

with C_s being a proportionality constant. For this slip situation, integration leads to an algebraic power law for hole growth:

$$R \propto t^{2/3}. \quad (7)$$

3.3 Partial Slip Regime

Our experiments have shown that the hole radius grows with an exponent of 0.82(5) in case of the silane layers (see [21]) and 0.88(1) in case of AF 1600, i.e., between the limiting cases of 2/3 for plug-flow and 1 for no-slip. This corroborates the hypothesis that both mechanisms contribute to the flow dynamics and that the energy gained in the dewetting process (per unit time), Sv , is dissipated by both viscous friction and sliding friction (dissipated power P).

$$|S|v = P_{visc} + P_{slip}. \quad (8)$$

Here, the overall dewetting velocity v is given by the sum of shear flow (with no-slip boundary condition) and sliding velocity, $v = v_{visc} + v_{slip}$. Further, the viscous dissipation is independent of the sliding velocity, which does not contribute to the shear flow, whereas the interfacial dissipation depends only on the slip velocity. Thus, we assume that the respective velocity contributions v_{visc} and v_{slip} are still given by Eqs. (2) and (5) which leads to an overall dewetting velocity of

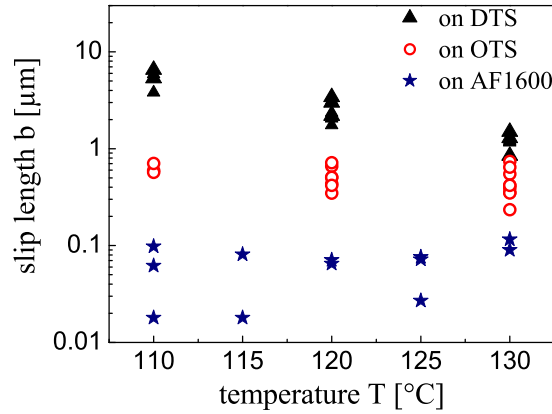


Figure 4: Slip length b plotted versus dewetting temperature T on DTS, OTS and AF 1600.

$$v = C_v(\theta) \frac{|S|}{\eta} + \frac{|S|b}{3\eta} \frac{1}{w}. \quad (9)$$

Including equation (6) leads to

$$v = v_0 + \frac{K}{\sqrt{R}} \quad (10)$$

with

$$v_0 = v_{visc} = C_v(\theta) \frac{|S|}{\eta} \quad (11)$$

and

$$K = \frac{|S|b}{3\eta C_s \sqrt{h_0}}. \quad (12)$$

The differential equation for the radius R of the growing holes (note that $v = dR/dt$), equation (10), can be solved by separation of variables [22]. This solution is implicit and rather cumbersome and therefore not very beneficial to draw further conclusions. In the following, an alternative pathway is presented.

According to equation (10), plotting the velocity of the growing holes versus the inverse square root of the radius allows to distinguish between radius-independent contributions, i.e., viscous dissipation and other friction mechanisms located at the three-phase contact line (see section 3.4), and radius-dependent contributions, i.e. friction at the interface (see fig. 3). Solely in case of very small holes on DTS we observe a deviation from linear behavior. This is due to the fact that the rims are not yet in the mature regime (self-similar growth of the rim) and we therefore neglect these data points in terms of further analysis.

The slope is connected to the slip length b and allows its determination due to the fact that spreading parameter S , viscosity η and film thickness h_0 can be independently determined. The results are shown in fig. 4. The geometrical constant C_s can be extracted from in situ AFM experiments of the growing rim (see [21]). Plotting the width of the rim versus the hole radius and fitting equation (6), we obtain $C_s = 2.1(1)$ for DTS and $C_s = 1.96(5)$ for OTS.

3.4 Further Potential Dissipation Mechanisms

There is a number of various mechanisms proposed in literature concerning flow of liquids over smooth surfaces, especially if a three-phase contact line is involved. First of all, evaporation into or condensation from the vapor phase might occur. For liquids with low vapor pressure, such as polymer melts, these effects can be excluded. Further, induced by the shear stress transferred to the solid when a liquid flows over its surface, the substrate might be elastically deformed. Indeed, elastic deformation of the substrate has shown to influence flow dynamics (Carré and Shanahan [23, 24]). In our experiments, we deal with silicon wafers coated with self-assembled monolayers of OTS and DTS. In the case of these short silane brushes of high packing density it is

quite unlikely that the polystyrene flow can induce significant deformation and structural changes of the silane molecules. The AF 1600 coating exhibits a large elastic modulus and is therefore also not likely to deform during dewetting [25].

For systems of simple liquids on solid substrates, Blake and Haynes proposed a molecular kinetic theory for the motion of a three-phase contact line [26]. Up to now, we considered only continuum descriptions of thin film flow, i.e., hydrodynamics. However, close to the three-phase contact line the continuum approach might fail and one might have to consider the motion of single molecules. In the molecular kinetic model, liquid molecules are assumed to displace adsorption sites by thermally activated jumps, which gives rise to a so-called contact line friction. The corresponding dissipation is localized at the three-phase contact line and, thus, independent of the rim size. Therefore, even if the contact line friction described by the molecular kinetic approach is relevant in our system, its contribution is included in the radius-independent term v_0 and does not affect our data analysis and results for the slip length.

4. DISCUSSION

Now the question arises whether the proposed model of combined friction mechanisms and the extraction of slip lengths based on this model give reasonable and consistent results. Recently, a complementary method to quantify slippage was developed. Depending on the solid/liquid boundary condition of flow, the rim of a moving liquid film exhibits either an oscillatory or a monotonically decaying profile towards the film. From the exact shape of this rim, characterized for instance by atomic force microscopy, the slip length can be determined quite accurately. For detailed review of this method we refer to previous publications [27, 28, 29, 30]. For the same experimental system of polystyrene films on OTS or DTS coated wafers, we achieve consistent values for the slip lengths. In addition, the evaluation of profiles on AF 1600 also provides nearly vanishing slip lengths [31]. This corroborates the model and analysis presented in this article.

In the work shown here, we concentrated on and extensively studied the growth of holes in dewetting films. While dewetting proceeds, however, these holes meet and coalesce and in the end a set of droplets remains on the substrate. The latter occurs due to an instability of the rim similar to the well-known Rayleigh instability of a liquid cylinder, i.e. in our case the rim of a straight front or surrounding a hole. In combination with theoretical simulations, we could show that the morphology of this instability is also sensitive to slippage. By that it is even possible to visualize slip properties of a liquid on a solid substrate and distinguish, even by eye, different boundary situations [32].

The comparatively small slip lengths in case of the AF 1600 substrate are in good agreement with molecular dynamic simulations for a simple Newtonian liquid that predict slip lengths exceeding 30 times the molecular diameter of the liquid molecules [33]. If we estimate this with the radius of gyration R_g of the polymer chains ($R_g = 3.2$ nm for PS13.7k), we would expect slip lengths up to roughly 100 nm.

This raises the question of the underlying molecular mechanism of slippage. Our findings that slip is substantially different on OTS, DTS and AF 1600 might be explained by various scenarios. Besides some concepts like structural changes of the self-assembled monolayer or roughness effects, we can safely exclude ideas such as penetration of polymer melt chains between the silane molecules. To date we propose that the origin of the very large slip lengths is a so-called lubrication layer. That is a layer of reduced viscosity close to the solid/liquid interface. Final clarification of this scenario might be delivered by X-ray and neutron scattering experiments which are under way.

5. CONCLUSIONS

In summary, we have shown that in our system of thin polymer films on hydrophobic substrates viscous dissipation as well as slippage are relevant. We presented a way to obtain slip lengths from dewetting experiments simply from optical studies of radii of growing holes. Results of this analysis clearly show that slippage at the solid/liquid interface is pronounced on DTS compared to OTS and that slip lengths in the range of microns are obtained. For the AF 1600 substrate we observe a nearly vanishing slippage contribution (slip lengths in the range of 10 to 100 nm) and a dominance of energy dissipation via viscous friction.

ACKNOWLEDGEMENTS

This work was financially supported by DFG grants JA 905/3 within the priority program SPP 1164, the European Graduate School GRK 532 and the Graduate School 1276. We acknowledge the generous support of Si wafers from Siltronic AG, Burghausen, Germany.

REFERENCES

- [1] Tretheway, D.C., & Meinhard, C.D. (2002). Apparent fluid slip at hydrophobic microchannel walls. *Phys. Fluids*, 14, L9-L12.
- [2] Tretheway, D.C., & Meinhard, C.D. (2004). A generating mechanism for apparent fluid slip in hydrophobic microchannels. *Phys. Fluids*, 16, 1509-1515.
- [3] Lumma, D., Best, A., Gansen, A., Feuillebois, F., Rädler, J.O., & Vinogradova, O.I. (2003). Flow profile near a wall measured by double-focus fluorescence cross-correlation. *Phys. Rev. E*, 67, 056313.
- [4] Pit, R., Hervet, H., & Léger, L. (2000). Direct experimental evidence of slip in hexadecane: Solid interfaces. *Phys. Rev. Lett.*, 85, 980-983.
- [5] Schmatko, T., Hervet, H., & Léger, L. (2005). Friction and slip at simple fluid-solid interfaces: The roles of the molecular shape and the solid-liquid interaction. *Phys. Rev. Lett.*, 94, 244501.
- [6] Craig, V.S.J., Neto, C., & Williams, D.R.M. (2001). Shear-dependent boundary slip in an aqueous newtonian liquid. *Phys. Rev. Lett.*, 87, 054504.
- [7] Vinogradova, O.I., & Yakubov, G.E. (2003). Dynamic effects on force measurements. 2. Lubrication and the atomic force microscope. *Langmuir*, 19, 1227-1234.
- [8] Cottin-Bizonne, C., Jurine, S., Baudry, J., Crassous, J., Restagno, F., & Charlaix, E. (2002). Nanorheology: An investigation of the boundary condition at hydrophobic and hydrophilic interfaces. *Eur. Phys. J. E*, 9, 47-53.
- [9] Zhu, Y., & Granick, S. (2002). No-slip boundary condition switches to partial slip when fluid contains surfactant. *Langmuir*, 18, 10058-10063.
- [10] Joly, L., Ybert, C., & Bocquet, L. (2006). Probing the nanohydrodynamics at liquid-solid interfaces using thermal motion. *Phys. Rev. Lett.*, 96, 046101.
- [11] Neto, C., Evans, D.R., Bonaccorso, E., Butt, H.-J., & Craig, V.S.J. (2005). Boundary slip in Newtonian liquids: a review of experimental studies. *Rep. Prog. Phys.*, 68, 2859-2897.
- [12] Lauga, E., Brenner, M.P., & Stone, H.A. (2007). Microfluidics: The no-slip boundary condition. In: Tropea, C., Yarin, A.L., Foss, J.F. (eds) *Springer Handbook of Experimental Fluid Mechanics*. Springer, Berlin Heidelberg New York.
- [13] Bocquet, L., & Barrat, J.-L. (2007). Flow boundary conditions from nano- to micro-scales. *Soft Matter*, 3, 685-693.
- [14] Ruckenstein, E., & Jain, R.K. (1974). Spontaneous rupture of thin liquid films. *J. Chem. Soc. Faraday Trans. II*, 70, 132-147.
- [15] Reiter, G. (1992). Dewetting of thin polymer films. *Phys. Rev. Lett.*, 68, 75-78.
- [16] Seemann, R., Herminghaus, S., & Jacobs, K. (2001). Dewetting patterns and molecular forces: A reconciliation. *Phys. Rev. Lett.*, 86, 5534-5537.
- [17] Wasserman, S.R., Tao, Y.-T., & Whitesides, G.M. (1989). Structure and reactivity of alkylsiloxane monolayers formed by reaction of alkyltrichlorosilanes on silicon substrates. *Langmuir*, 5, 1074-1087.
- [18] Good, R.J., & Girifalco, L.A. (1960). A theory for estimation of surface and interfacial energies. III. Estimation of surface energies of solids from contact angle data. *J. Phys. Chem.*, 64, 561-565.
- [19] Brochard-Wyart, F., De Gennes, P.-G., Hervet, H., & Redon C. (1994). Wetting and slippage of polymer melts on semi-ideal surfaces. *Langmuir*, 10, 1566-1572.
- [20] Redon, C., Brzoska, J.B., & Brochard-Wyart, F. (1994). Dewetting and slippage of microscopic polymer films. *Macromolecules*, 27, 468-471.
- [21] Fetzer, R., & Jacobs, K. (2007). Slippage of newtonian liquids: Influence on the dynamics of dewetting thin films. *Langmuir*, 23, 11617-11622.
- [22] Jacobs, K., Seemann, R., Schatz, G., & Herminghaus, S. (1998). Growth of holes in liquid films with partial slippage. *Langmuir*, 14, 4961-4963.
- [23] Shanahan, M.E.R., & Carré, A. (1994). Anomalous spreading of liquid drops on an elastomeric surface. *Langmuir*, 10, 1647-1649.

- [24] Shanahan, M.E.R., & Carré, A. (1995). Viscoelastic dissipation in wetting and adhesion phenomena. *Langmuir*, 11, 1396-1402.
- [25] Kostourou, K., & Seemann, R. (2008). Private Communication.
- [26] Blake, T.D., & Haynes, J.M. (1969). Kinetics of liquid/liquid displacement. *J. Colloid Interface Sci.*, 30, 421-423.
- [27] Münch, A., Wagner, B., & Witelski, T.P. (2005). Lubrication models with small to large slip lengths. *J. Eng. Math.*, 53, 359-383.
- [28] Fetzer, R., Jacobs, K., Münch, A., Wagner, B., & Witelski, T.P. (2005). New slip regimes and the shape of dewetting thin liquid films. *Phys. Rev. Lett.*, 95, 127801.
- [29] Fetzer, R., Rauscher, M., Münch, A., Wagner, B.A., & Jacobs, K. (2006). Slip-controlled thin film dynamics. *Europhys. Lett.*, 75, 638-644.
- [30] Fetzer, R., Münch, A., Wagner, B., Rauscher, M., & Jacobs, K. (2007). Quantifying hydrodynamic slip: A comprehensive analysis of dewetting profiles. *Langmuir*, 23, 10559-10566.
- [31] Bäumchen, O., Fetzer, R., & Jacobs, K. (2008) to be published.
- [32] Marquant, L., Bäumchen, O., Mainka, J., Münch, A., Wagner, B., & Jacobs, K. (2008) to be published.
- [33] Barrat, J.-L., & Bocquet, L. (1999). Large slip effect at a nonwetting fluid-solid interface. *Phys. Rev. Lett.*, 82, 4671-4674.

5 Morphological Characterization and Analysis of Liquid Rim Profiles

Based on the rim profile analysis explained in detail in ADDENDUM IV (for PS films dewetting from OTS and DTS substrates), experiments were performed and evaluated for various molecular weights on the AF 1600 substrate (see Fig. 5.1). The first part of the present chapter covers the investigation of the temporal and spatial evolution of the shape of a liquid front by *in situ* AFM measurements. The second part deals with the evaluation and interpretation of *ex situ* liquid rim profiles captured at a fixed hole radius. The resulting findings concerning slip length, capillary number and viscosity are compared and discussed in view of parameters such as temperature and molecular weight of the polymer. Special attention will be paid to the link between the slip length, the viscosity and the friction coefficient at the solid/liquid interface. The chapter finally concludes by drawing a picture of the formation of chain entanglements in the vicinity of the solid/liquid interface and throughout the polymer film. Moreover, the results concerning in particular the slip length are compared to the results obtained from the analysis of the hole growth dynamics (Chapter 4) and discussed in view of the available literature.

5.1 *In situ* Measurement of the Evolution of the Rim Shape

Fig. 5.1 shows the portion of a hole in a 130 nm thick PS(13.7k) film as seen by AFM. To probe the temporal and spatial growth of the liquid rim, subsequent *in situ* AFM images during dewetting on a high-temperature heating plate were recorded in tapping modeTM. Cross-sections obtained from a temporal series of AFM scans (for a time interval $\Delta t = 640$ s) for PS(13.7k) dewetting from AF 1600 at 115 °C are shown in Fig. 5.2 left. The rim clearly grows in height and width as the dewetting time proceeds. Nevertheless, the form of the profiles at different times (and therefore different volumes) is very similar. All profiles exhibit a substantial trough (see inset of Fig. 5.2) on the "wet" side of the rim (where the height profile merges into the unperturbed film).

As illustrated in Fig. 5.2 right, plotting the rim width w versus the maximum rim height H can be identified with a linear increase with a slope of 3.75(6) and a y-axis intercept of 0.35(3) μm . This linear relationship indicates the presence of a self-similar growth of the rim, i.e. $w \propto \sqrt{R}$ (where R denotes the radius of the hole), as obtained from the conservation of volume for growing holes (see ADDENDUM II). The self-similar growth of the liquid rim (see also [34, 54]) or in general a retracting liquid front is a strong criteria for the presence of the "mature stage" of hole growth in dewetting polymer films and, consequently, the applicability of the analysis technique of hole growth data presented in ADDENDUM III. The following section represents the main part of this chapter and deals with rim profiles obtained from *ex situ* AFM measurements.

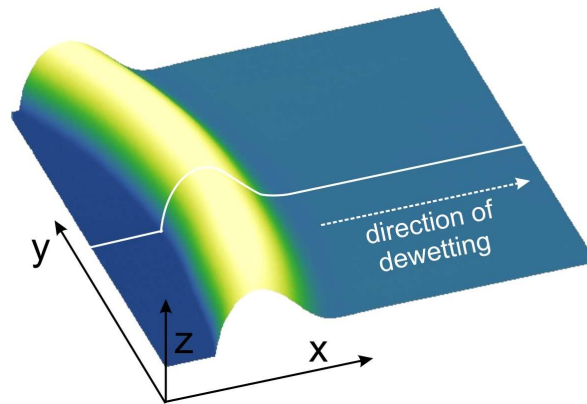


Figure 5.1: PS film on AF 1600: $10\ \mu\text{m} \times 10\ \mu\text{m}$ AFM image of a portion of a liquid rim surrounding a hole in the polymer film. The solid white line exemplarily marks one AFM scan line.

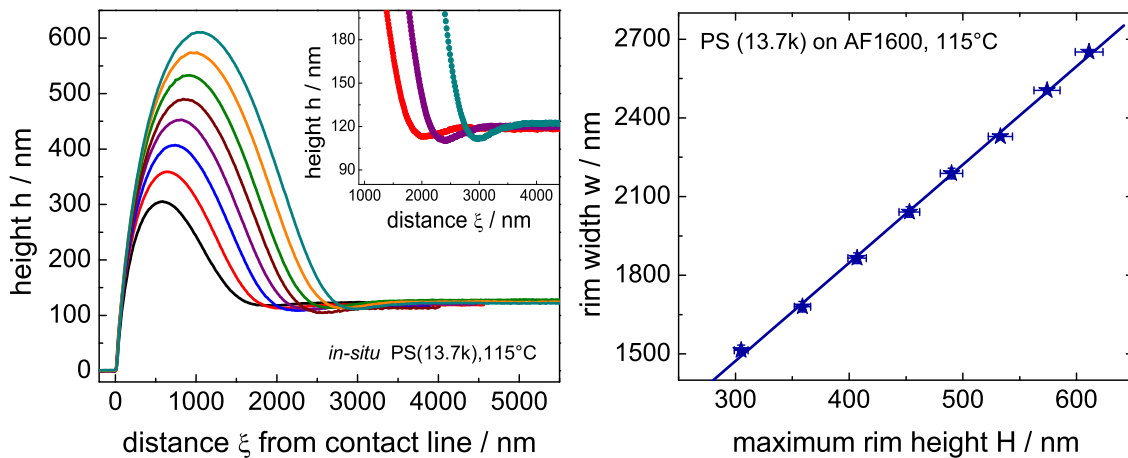


Figure 5.2: Left: *In situ* measurement of the temporal evolution ($\Delta t = 640\ \text{s}$) of the rim growth of a 120 nm PS(13.7k) film at $115\ ^\circ\text{C}$ on AF 1600. All profiles clearly exhibit an oscillatory rim shape on the "wet" side of the rim (illustrated by a selection of close-up views shown in the inset). Right: Evaluation of the corresponding rim profiles with regard to the rim width w (the distance between three-phase contact line and the point, where the rim height has dropped to 110% of the initial film thickness) and the maximum rim height H .

5.2 *Ex situ* Measurement and Analysis of the Rim Shape at fixed Hole Radii

As described in ADDENDUM IV, the analysis of rim profiles according to thin film models allows for gaining access to the flow properties of thin liquid films. *Ex situ* AFM measurements after quenching the samples to room temperature are analyzed according to the techniques and fit functions presented in ADDENDUM IV: More precisely, the third-order Taylor expanded model based on the full Stokes equations was utilized since it applies to a non-restricted range of slip lengths (in contrast to e.g. the strong-slip lubrication model). For reasons of comparability, profiles were recorded at fixed hole radii ($12\ \mu\text{m}$) to ensure that approximately the same amount of liquid forms the rim profiles.

5.2.1 *Ex situ* AFM Measurements of Rim Profiles

Rim profiles exhibit two distinct morphological shapes: The "oscillatory" decay is characterized by a significant trough where the rim merges into the unperturbed film ("wet side") as illustrated in Fig. 5.3a. In some cases, the experimental data for this part of the rim profile even exhibits a slight overshoot as compared to initial film thickness (see inset of Fig. 5.3a). For increasing M_w , the trough becomes progressively smaller (see Fig. 5.3b). Finally, it vanishes and the rim exhibits a monotonically decaying profile (see Fig. 5.3c). Exemplarily, Fig. 5.3 shows typical portions of oscillatory and monotonically decaying rim shapes and the corresponding fit functions to the experimental data. Monotonically decaying rim profiles can be analyzed by fitting a single exponential decay or a superposition of two distinct exponential decays. The latter, however, is not applicable for all rim profiles due to the fact that both exponential functions, in particular characterized by their decay lengths k_1 and k_2 , have to be clearly distinguishable. If two exponential decays can be separated from each other, the quantification of the slip length b and of the capillary number Ca (and also the viscosity η by measuring the current dewetting velocity \dot{s} prior quenching the sample to room temperature) is possible. The determination of b in the case of a single exponential decay, however, necessitates the knowledge of Ca and, therefore, also of the viscosity η (see section 5.2.2). The theoretical models and the application of the fit functions to the rim profile data are discussed in detail in ADDENDUM IV.

The region of the transition from oscillatory to monotonically decaying rims is non-trivial concerning the fit function to be applied. As discussed in detail in the work by Fetzner *et al.* [29], the local minimum of the height data (called "trough") can be fitted either by a damped oscillation or by a superposition of two exponential decays with one of the amplitudes being negative. However, Fetzner *et al.* have proven in their study that one major criterion of the application of the theoretical model to the experimental data is not fulfilled in the case of two exponential decays with one positive and one negative amplitude: The slip length extracted from this fit is not independent of the hole radius anymore. Fitting a damped oscillation, however, still leads to a radius-independent result. Consequently, rim profiles exhibiting a trough on the wet side of the rim were fitted with a damped oscillation and slip length and the

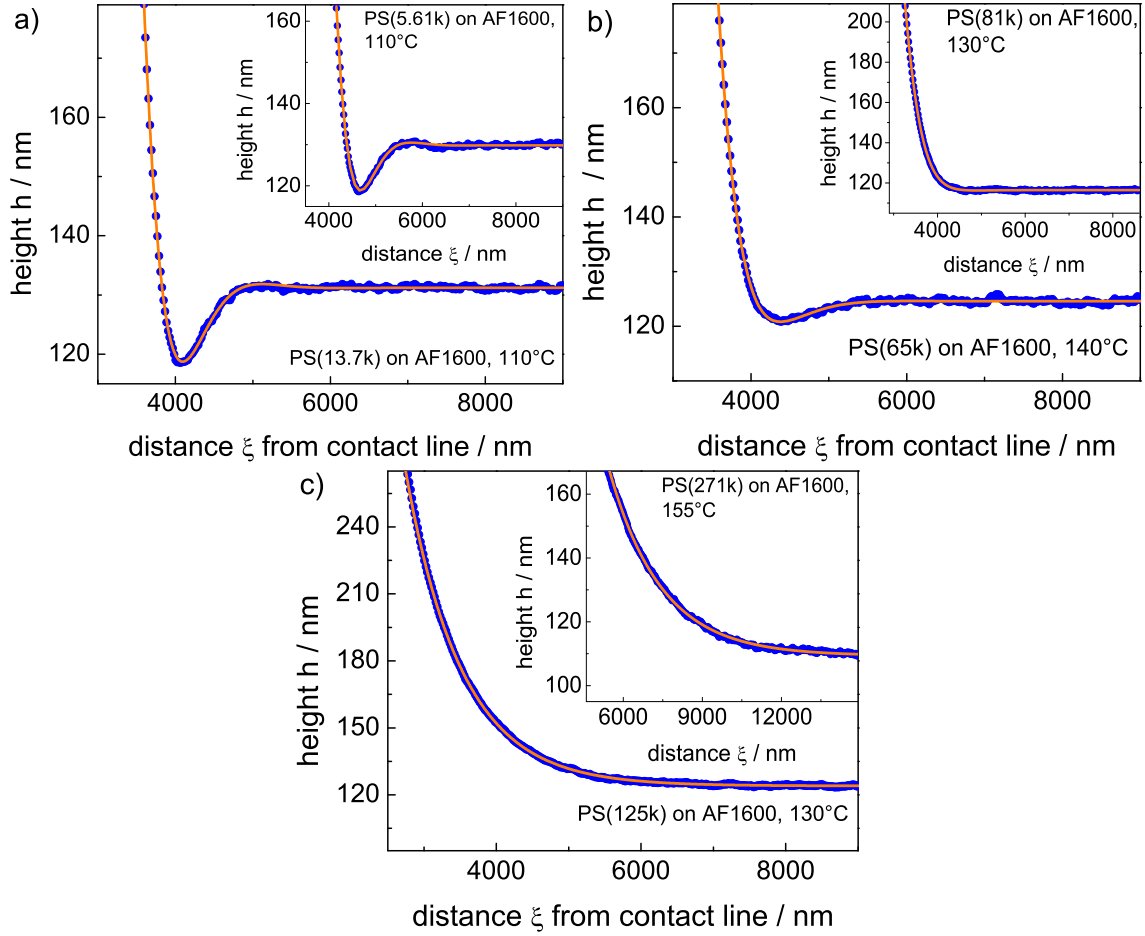


Figure 5.3: Experimentally obtained AFM images of the "wet side" of rim profiles for thin PS films of different molecular weight on AF 1600. a) PS(13.7k) and PS(5.61k) (see inset) at 110 °C represent typical rim shapes below the critical molecular weight M_c for chain entanglements. b) PS(65k) at 140 °C and PS(81k) at 130 °C (see inset) are clearly above M_c . c) PS(125k) at 130 °C and PS(271k) at 155 °C (see inset). The solid red lines indicate the fits to the experimental data according to a damped oscillation or a single monotonic decay.

capillary number could be extracted. Further details concerning the region of the morphological transition can be found in [29].

As illustrated in Fig. 5.4a, profiles show progressively shallower declines for increasingly larger molecular weights M_w : The rim height decreases while the rim gets significantly broadened (data for the rim width w is given in Tab. 5.1). For a given M_w , however, no systematic dependency on the dewetting temperature and, thus, on the viscosity of the polymer melt can be recorded (see Fig. 5.4b and Fig. 5.5). To check the influence of possible internal stress in the polymer film due to the preparation process [49, 55, 56, 57], the films prepared on mica were annealed prior to the transfer to the AF 1600 substrate. A comparison of profiles with

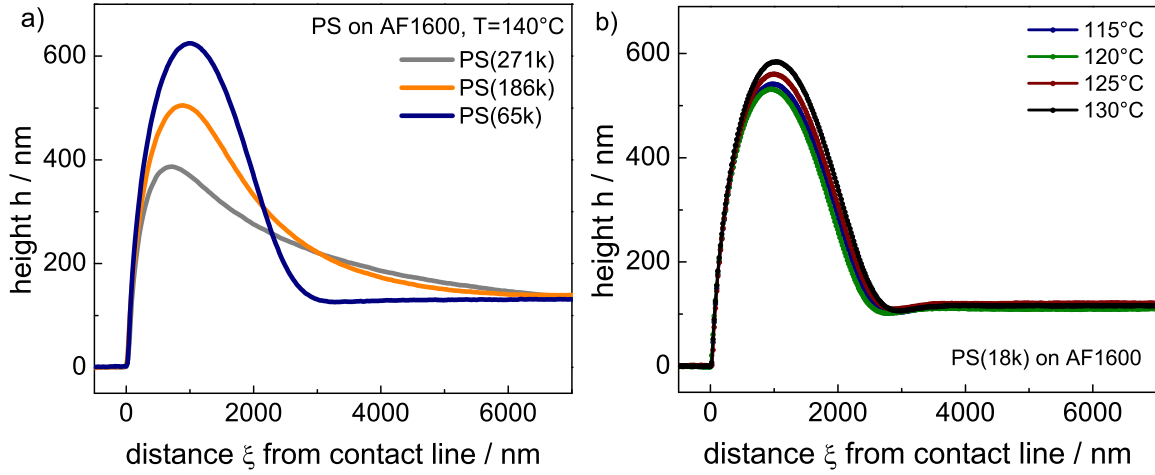


Figure 5.4: a) Examples of rim profiles on AF 1600 for different molecular weights M_w . Increasing M_w results in a transition from oscillatory to monotonically decaying rims and to successively less steep decays into the unperturbed film. b) Rim profiles for PS(18k) as a representative for the typical situation below the critical chain length for the formation of entanglements. Dewetting temperature and, thus, viscosity of the polymer film have no significant impact on the rim profiles (see also Fig. 5.5).

Table 5.1: PS on AF 1600: Molecular weight M_w , dewetting temperature T and measured rim width w (determined from rim profiles at fixed hole radii of $12(1) \mu\text{m}$). According to our definition, w is taken as the lateral displacement between the three-phase contact line and the distance, where the rim height has dropped to 1.1 times the initial film thickness h_0 .

M_w	T (°C)	w (μm)	M_w	T (°C)	w (μm)
35.6k	120	2.44(4)	125k	130	4.06(4)
35.6k	130	2.48(4)	125k	150	4.30(4)
51.5k	125	2.56(4)	186k	130	5.02(4)
51.5k	130	2.34(4)	186k	140	4.86(4)
51.5k	140	2.40(4)	186k	150	5.29(4)
65k	130	2.73(4)	271k	140	7.47(6)
65k	140	2.81(4)	271k	150	6.83(6)
81k	130	2.97(4)	271k	155	7.12(6)
81k	140	2.93(4)	390k	150	10.04(8)
101k	130	3.26(4)	390k	155	10.20(8)
101k	140	3.54(4)			

and without the pre-annealing is shown in Fig. 5.5 for two molecular weights, PS(65k) and PS(125k). Again, no systematic influence was detected for a fixed molecular weight (see also section 5.2.2).

The following subsections present the detailed results of the analysis of the rim profiles according to the Taylor-expanded Stokes model as described in ADDENDUM IV. Slip lengths as well as capillary numbers are calculated for a broad set of molecular weights and dewetting temperatures.

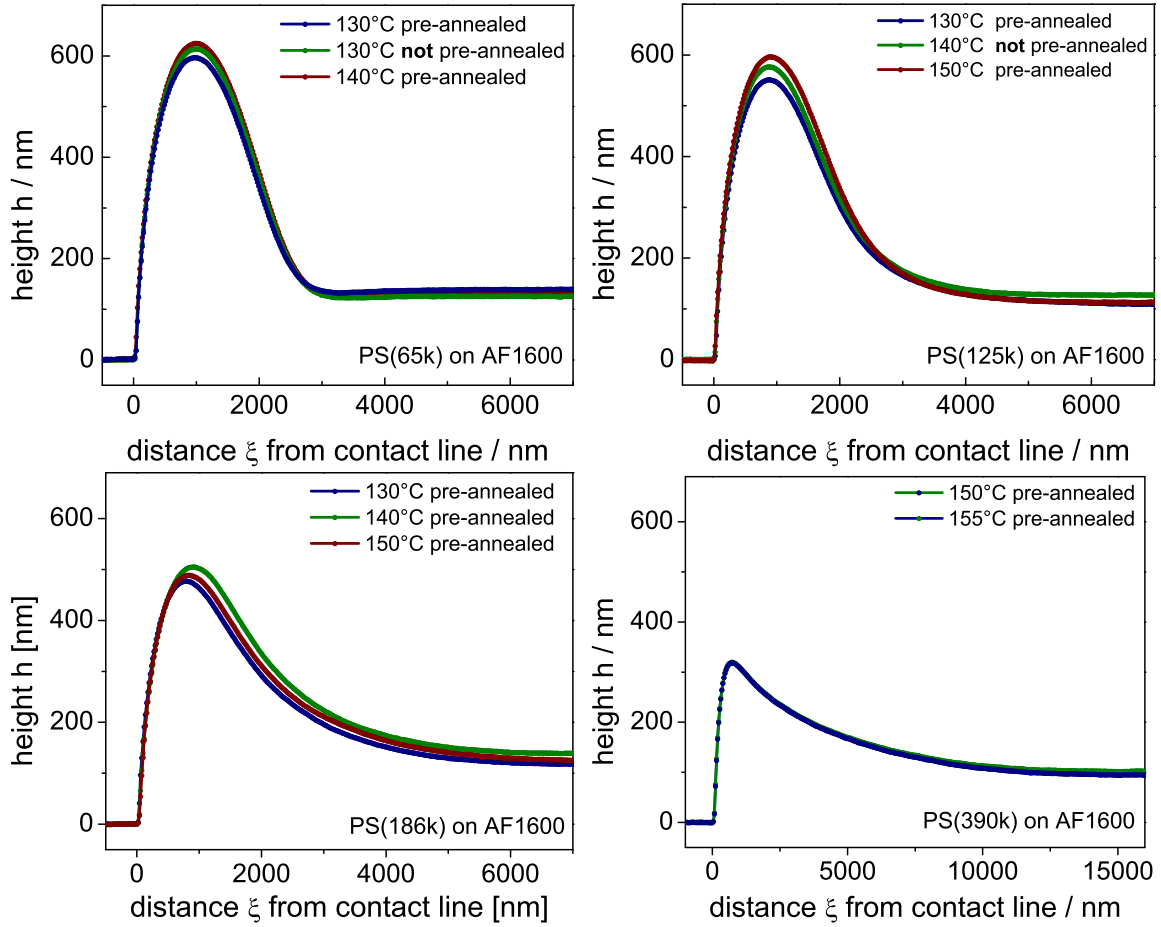


Figure 5.5: Testing the role of pre-annealing and dewetting temperature for the shape of the rim profile on AF 1600 for PS(65k), PS(125k), PS(186k) and PS(390k). Note that differences in rim shape for a specific M_w can be attributed to small variations of the prepared film thickness and differences in hole radius which lead to small variations of the volume of the rim.

Short Summary

- Two distinct rim morphologies were recorded for PS dewetting from AF 1600 substrates: oscillatory (showing a trough on the wet side of the rim, for $M_w \leq 81$ kg/mol) and

monotonically decaying rim shapes (for $M_w \geq 101$ kg/mol).

- Rim profiles show progressively shallower declines for increasingly larger molecular weights M_w .
- Rim profiles could be fitted by a damped oscillation (oscillatory decaying rims) or by an exponential decay (monotonically decaying rims).
- Dewetting temperature T and melt viscosity η (for a fixed molecular weight M_w) have no systematic impact on the rim shape.
- PS films above the critical molecular weight for chain entanglements were pre-annealed on the mica substrate prior transferring them to AF 1600: Omitting the pre-annealing step does also not show any systematic effect concerning the shape of the rims.

5.2.2 Evaluation of the Slip Length

In the previous subsection, a variety of rim profiles of PS films dewetting from AF 1600 substrate is shown and discussed in view of the dewetting temperature and the molecular weight of the polymer film. As mentioned before, the rim profiles are analyzed according to thin film models to extract the slip length and, if possible, the capillary number (see ADDENDUM IV for a detailed description of this technique). Fig. 5.3 depicts several examples of rim profiles for various molecular weights in conjunction with the corresponding fits to the experimental data. The evaluation of the slip length according to the theoretical model is the subject of this subsection (and ADDENDUM V).

Fig. 5.6 depicts the results of the slip length b in view of the molecular weight M_w in a double-logarithmic representation: Below the critical molecular weight for chain entanglements M_c , the slip length reaches values up to 150 nm^1 . For $M_w > M_c$, the slip length strongly increases with the molecular weight and the length of the polymer chain, respectively. To be more precisely, a scaling exponent of 2.9(2) between the slip length and the molecular weight, i.e. $b \propto M_w^{2.9}$, is found. This result is in excellent agreement with the outcome of the hole growth dynamics (see section 4.4). Again, values for b are systematically lowered compared to the expectation by de Gennes (i.e. $b = aN^3/N_e^2$, see [52]) based on literature values for the molecular size a and the bulk entanglement length N_e . The pre-factor a/N_e^2 is obtained from the linear fit to the experimental data in the double-logarithmic representation: The rim profile analysis leads to $N_e = 517$ which is a factor of 3.2 compared to the bulk entanglement length². A direct comparison of both techniques determining the slip length (i.e. hole growth dynamics and rim profile analysis) in view of the molecular weight of the polymer melt and a detailed interpretation and discussion of the processes on the molecular scale is presented in section 5.3.

The general consistency of this method to extract the slip length and the capillary number from liquid rim profiles was checked by Fetzer *et al.* for PS(13.7k) dewetting from OTS and

¹The experimental data usually fluctuates between 0 and 150 nm at maximum. In some individual cases slightly negative slip lengths were obtained for PS(5.61k), PS(13.7k) and PS(18k).

²To the best of our knowledge, a smaller value for the molecular size than $a = 3\text{\AA}$, [22], is not reasonable for a polymer melt. The lowered slip lengths give, thus, rise to an increased entanglement length N_e .

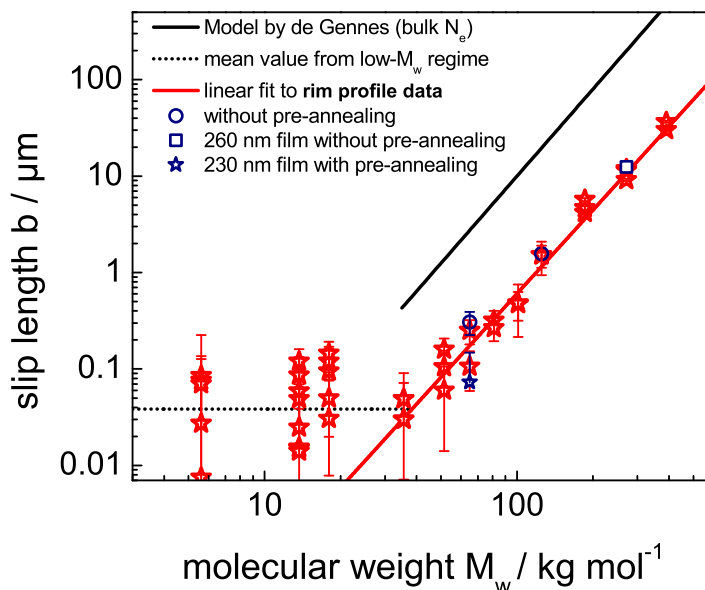


Figure 5.6: Double-logarithmic representation of the slip length b as a function of molecular weight M_w . b is obtained from the analysis of rim profiles for single experiments (symbols) with PS dewetting from AF 1600 substrates. The solid black line represents the model by de Gennes [52] using bulk $N_e=163$, whereas the solid red line is a fit to the experimental data. Additionally, film thickness and pre-annealing conditions were varied.

DTS substrates [58]: The viscosity (which was determined from the capillary number and the dewetting velocity) turned out to be in excellent agreement with independent (bulk) viscosimeter data (see ADDENDUM IV). *In situ* measurements did prove that the slip length was independent of the radius of the holes (the range between 2.5 and 17 μm was tested). Dewetting experiments for various film thicknesses (between 50 and 230 nm) also lead to consistent results. The method, consequently, yields reliable results for the slip length and the viscosity of dewetting thin polymer films.

In the following paragraphs, two particular aspects in view of the experimental results on AF 1600 substrates are discussed: First, the impact of the pre-annealing conditions is tested by comparing the results of the rim profile analysis of as-cast (not pre-annealed) to pre-annealed polymer films. Second, the impact of the film thickness is studied. Here, the question is addressed whether the reduction of the entanglement density is exclusively governed by the solid/liquid interface or whether the slip length is correlated to the thickness of the film.

Impact of the Pre-Annealing Conditions In the context of the results of this dewetting study concerning the flow dynamics of thin polymer films, a discussion of the influence of potential viscoelastic effects becomes inevitable. As considered before (see section 4.1), the occurrence of polymer relaxation processes and their impact on the flow dynamics can be excluded for the present experimental configuration (dewetting temperatures, shear rates,

molecular weights, relaxation times and Weissenberg numbers resulting from that). A source of viscoelastic effects are residual stresses caused by the fast solvent evaporation during the spin-coating process. To safely exclude this issue, dewetting experiments were usually performed after a pre-annealing step on the mica substrate (see section 3.2): The films were annealed at 140 °C for a time duration of 3 hours (see [39, 49]). However, to test the influence of this procedure, experiments were carried out without annealing prior dewetting. Corresponding rim profiles were analyzed and compared to pre-annealed samples: No systematic influence of the pre-annealing step is found for the typical molecular weights of PS(65k) and PS(125k) used in this study (see Fig. 5.5). The slip lengths determined from these experiments are still roughly one order of magnitude lower than expected from literature values for N_e (see Fig. 5.6).

Impact of the Film Thickness A further important question arises with regard to the aforementioned results concerning the reduced entanglement density affecting slippage of thin polymer films: Is this effect located in the vicinity of the solid/liquid interface or is it caused by a confinement effect given by the thickness of the polymer film? A reduced entanglement density is correlated to a reduced viscosity. Close to the solid/liquid interface, this results in a reduced slip length (compared to the prediction by the model of de Gennes using the bulk entanglement length). To test the effect of the film thickness on the slip length, a dewetting experiment (without pre-annealing) was performed using PS(271k) at 140 °C with a film thickness of 260 nm. The experiment was stopped at a hole radius of 12.8 μm . The analysis of the rim profile of this hole gave (using the current dewetting velocity obtained from the evolution of the hole radius) a slip length of 12.4 μm . This is (within the experimental error) in very good agreement with the corresponding slip length of 11.8 μm for a 115 nm thick PS(271k) film. A further hole growth experiment of a 230 nm PS(65k) film (with pre-annealing for 3 hours at 140 °C on mica) at 130 °C was stopped at a hole radius of 12.1 μm . The analysis of the corresponding rim profile exhibited a slip length of 73 nm. Both experiments using thicker films do not show a significant increase in the slip length (see Fig. 5.6) and, thus, corroborate the hypothesis that the reduced entanglement density is restricted to the direct vicinity of the solid/liquid interface. Note that the model of de Gennes using bulk literature values for the entanglement length N_e predicts slip length of roughly one order of magnitude larger than what is found in these experiments. The effect can not be correlated to the fact that specific parameters such as the radius of gyration R_g compare to the film thickness h_0 : We could not expect to reproduce the $b \propto M_w^3$ law in that case due to the fact that the ratio R_g/h_0 increases as the molecular weight M_w (and, thus, the chain length N and the radius of gyration R_g) increases. An estimation of the extent of the layer of reduced entanglement density in the direction perpendicular to the substrate is given and discussed in section 5.3.

To conclude, we have strong evidence that the reduced entanglement density is located in the vicinity of the solid/liquid interface causing a significant reduction of the slip length by approximately one order of magnitude.

Short Summary

- Below the critical molecular weight for polymer chain entanglements M_c , slip lengths b up to approx. 150 nm are found on the AF 1600 substrate.

- On AF 1600, the slip length is not significantly depending on dewetting temperature, but is strongly correlated to the molecular weight, i.e. the chain length of polymer molecules in the melt.
- The relation $b \propto N^3$ of slip length b and chain length N (or alternatively the molecular weight M_w), as predicted by de Gennes, is well reproduced on the AF 1600 substrate.
- The absolute values of the slip lengths obtained from the rim profile analysis on AF 1600 are approximately one order of magnitude lower than what is expected from the model by de Gennes using bulk literature values for the entanglement length N_e . Determining N_e from the relation between slip length and molecular weight gives $N_e = 517$, which is 3.2 times larger than the bulk entanglement length. Consequently, the density of inter-chain entanglements is reduced at the solid/liquid interface.
- Omitting the pre-annealing step of the PS film did not exert significant influence on the value of slip length. Thicker PS films also lead to consistent results.

5.2.3 Evaluation of the Capillary Number vs. the Ratio of Slip Length to Film Thickness

The calculation of capillary numbers from the rim profile analysis requires an appropriate fit to the experimental data by the full fit functions³ (see section 5.2.1). The results for the AF 1600 substrate are shown in Fig. 5.7 and corroborate the experimental data obtained for DTS and OTS (see ADDENDUM IV): The capillary number increases as the ratio of slip length to film thickness increases. In the oscillatory regime (for small Ca and small b/h_0) the data points for $M_w > M_c$ fall on a curve (dashed grey line in Fig. 5.7 right) that originates from a constant shift of a series of numerical hydrodynamic simulations⁴ depicted as the solid blue line in Fig. 5.7 right. In the monotonic regime (for large Ca and large b/h_0), the values for Ca could not be obtained from the analysis of rim profiles due to the fact that only a single exponential decay could be fitted to the experimental data for $M_w \geq 101$ kg/mol. In this case, the capillary number $Ca = \eta \dot{s} / \gamma_{lv}$ was determined via the viscosity (calculated from the WLF equation, see section 5.2.4), the dewetting velocity \dot{s} as obtained from the hole growth dynamics immediately before quenching the sample (see Tab. 5.2) and the surface tension γ_{lv} of the PS. The data still follow the trend of increasing capillary numbers Ca for enhanced slippage, i.e. an increasing ratio b/h_0 of slip length b to film thickness h_0 . Note that the error bars for Ca (for $M_w \geq 101$ kg/mol) were calculated from the error given by the dewetting velocity measurement and do not include the uncertainty of the viscosity data taken from the WLF equation as illustrated in section 5.2.4.

The following subsection describes the calculation of the viscosity from the capillary numbers determined by the analysis of the rim profiles. Subsequently, these results will be compared to the theoretical expectation given by the WLF equation.

³It should be emphasized that this requires a fit of a damped oscillation or, in the case of a monotonic decay, a superposition of two clearly distinguishable exponential decays (see ADDENDUM IV).

⁴Further details concerning the model and possible explanations for the systematic shift of the experimental data compared to the results of the hydrodynamic simulation by A. Münch and B. Wagner can be found in the publication by R. Fetzer *et al.* [29].

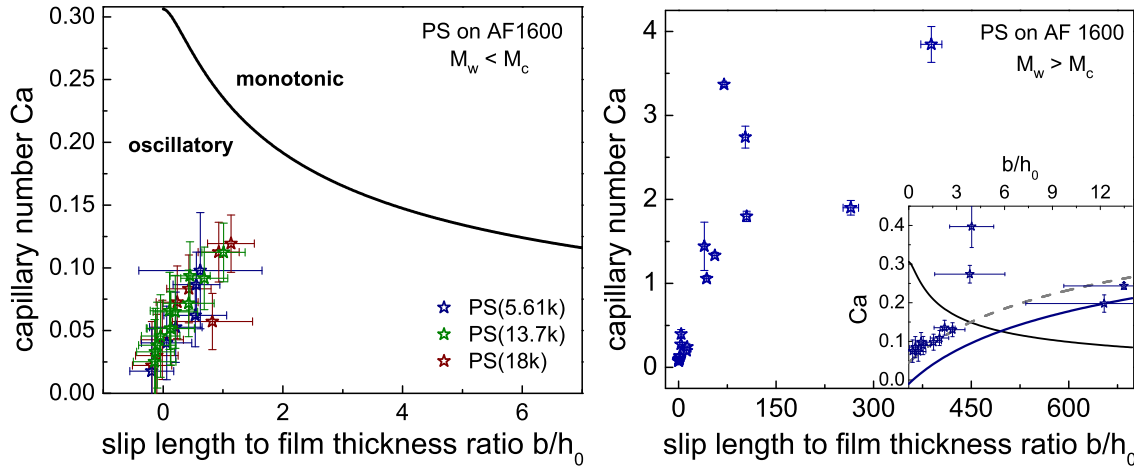


Figure 5.7: Capillary number Ca versus the ratio of slip length b to film thickness h_0 for diverse molecular weights $M_w < M_c$ (left) and $M_w > M_c$ (right). The solid black line represents the transition from "oscillatory" to "monotonic" solutions of the Taylor-expanded Stokes model (see ADDENDUM IV). For monotonic profiles, i.e. $M_w \geq 101$ kg/mol, Ca was determined from viscosity data (as calculated from the WLF equation, see section 5.2.4) and the dewetting velocity \dot{s} (from hole growth analysis). The inset (right) depicts a close-up view of the region of the morphological transition of the rim shape. The dashed grey line results from a constant shift of a series of numerical hydrodynamic simulations (solid blue line).

Short Summary

- Capillary numbers Ca for the dewetting experiments could be determined from the analysis of rim profiles (for $M_w \leq 81$ kg/mol) using dewetting velocities \dot{s} from optical measurements. For $M_w \geq 101$ kg/mol, values for the viscosity (from the WLF equation) have to be used to obtain an estimation of Ca .
- Ca increases as the ratio of slip length b to film thickness h_0 increases for various molecular weights and dewetting temperatures.

5.2.4 Evaluation of the Viscosity from the Rim Profile Analysis

If the capillary number Ca can be extracted from the analysis of the experimentally recorded rim profiles, the knowledge of the surface tension of the polymeric liquid ($\gamma_{lv}(\text{PS}) = 30.8$ mN/m, [45]) and the experimental determination of the actual dewetting velocity \dot{s} (from optical hole growth measurements, see Tab. 5.2) enable the calculation of the viscosity η of the polymer melt via $Ca = \eta\dot{s}/\gamma_{lv}$ for a given dewetting temperature. Dewetting experiments were performed for diverse molecular weights M_w of PS melts below and above the critical molecular weight M_c for entanglements. As given in Fig. 5.8 and Tab. 5.3, results show, within the experimental error, good agreement with independent viscosimeter measurements⁵ and the extrapolation of

⁵The viscosimeter data was measured by R. Seemann for PS(12.5k) and PS(65k) at diverse temperatures [39].

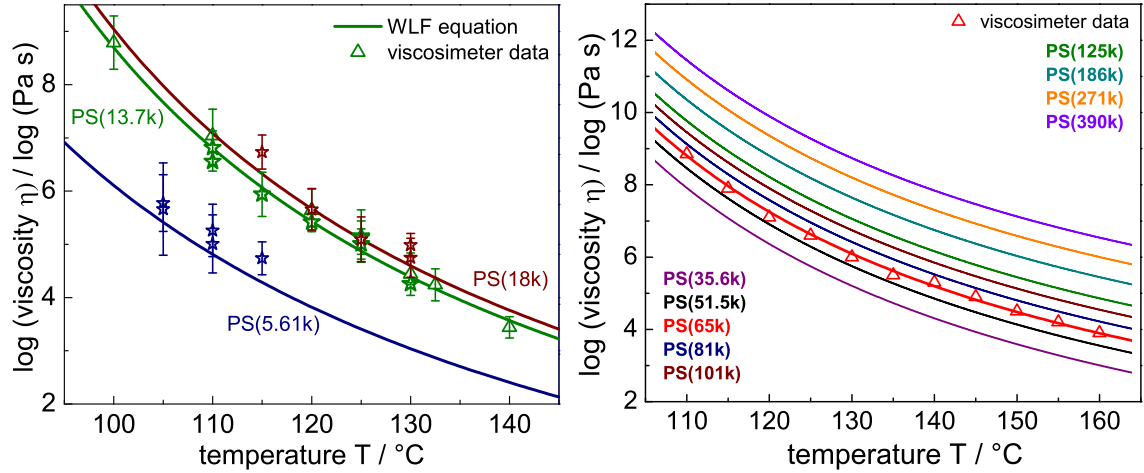


Figure 5.8: Semi-logarithmic plots of viscosity η versus temperature T for PS melts of various molecular weights $M_w < M_c$ (left) and $M_w > M_c$ (right). The viscosity data for $M_w < M_c$ (left) was obtained from rim profile analysis (via the model based on the Taylor-expansion of the full Stokes equations, see ADDENDUM IV) of PS(5.61k), PS(13.7k) and PS(18k) films on AF 1600. The solid curves are based on the extrapolation of a fit to experimental viscosimeter data for PS(12.5k) (left) and PS(65k) (right) according to the WLF equation.

a fit to this data according to the Williams-Landel-Ferry (WLF) equation⁶ [50].

The capillary number and, thus, the viscosity could not be extracted from monotonically decaying rims, i.e. for PS(101k) and larger M_w , on the AF 1600 substrate. As discussed in section 5.2.2 the determination of the slip length from a fit by a single exponential decay, however, necessitates a value for the viscosity of the polymer film. Fig. 5.8 illustrates the extrapolation of the viscosity data for diverse molecular weights above the critical chain length for entanglements (as used in the hole growth and the rim profile analysis). It should be emphasized that the functional form of the plotted graphs of the WLF equation was obtained by the assumption of a scaling exponent of 3.4 (usually found in experimental viscosimeter measurements), i.e. $\eta \propto M_w^{3.4}$ and bulk properties (see ADDENDUM II and [48]). This approach is applicable to the polymer films in this study according to the fact that film thicknesses significantly larger than 50 nm were investigated. Thinner films have proven to exhibit a reduction of the glass transition temperature (see e.g. [59, 60]). A detailed discussion concerning the impact of the polymer film thickness on the glass transition temperature is given in ADDENDUM II.

⁶The reconstruction of the viscosity η as function of temperature T according to the WLF equation requires the knowledge of the glass transition temperature $T_g = T_g(\infty) - C/M_w$ for the corresponding M_w , the Vogel temperature T_{Vogel} and the ratio of the parameters B/f_g (see ADDENDUM II and [48]): For PS melts T_{Vogel} (in Kelvin units) is given by $T_{Vogel} = T_g - 48$ K. $B/f_g = 30.3$ is found according to literature [48]. Data for T_g was obtained by R. Fetzer from ellipsometric determination of the change of the thermal expansion coefficient of the PS films prepared on mica surfaces [39]: $C = 70$ K kg mol⁻¹ and $T_g(\infty) = 372$ K is found.

Table 5.2: PS on AF 1600: Dewetting velocity \dot{s} (at fixed hole radii of 12(1) μm just before quenching the sample to room temperature) as determined from optical hole growth measurements (see Chapter 4).

M_w	T ($^{\circ}\text{C}$)	\dot{s} (nm/s)	M_w	T ($^{\circ}\text{C}$)	\dot{s} (nm/s)
35.6k	120	0.76(3)	125k	130	0.53(6)
35.6k	130	8.3(4)	125k	150	27(1)
51.5k	125	0.5(1)	186k	130	1.0(2)
51.5k	130	1.7(1)	186k	140	5.8(2)
51.5k	140	13.8(7)	186k	150	38(1)
65k	130	1.80(5)	271k	140	4.2(2)
65k	140	14(1)	271k	150	27(1)
81k	130	4.0(2)	271k	155	29(1)
81k	140	25(3)	390k	150	4.4(2)
101k	130	2.2(3)	390k	155	18(1)
101k	140	12(1)			

Table 5.3: PS on AF 1600: Quantitative comparison of viscosities η_{Stokes} determined from capillary numbers which were obtained by the analysis of rim profile to viscosities η_{WLF} calculated from the WLF equation.

M_w	T ($^{\circ}\text{C}$)	η_{WLF} (Pa s)	η_{Stokes} (Pa s)
35.6k	120	2.31×10^6	$3.5(13) \times 10^6$
35.6k	130	1.61×10^5	$2.8(11) \times 10^5$
51.5k	125	1.95×10^6	$5.5(26) \times 10^6$
51.5k	130	5.62×10^5	$1.8(5) \times 10^6$
51.5k	140	7.11×10^4	$1.6(6) \times 10^5$
65k	130	1.30×10^6	$1.7(4) \times 10^6$
65k	140	1.60×10^5	$2.4(6) \times 10^5$
81k	130	2.63×10^6	$1.0(2) \times 10^6$
81k	140	3.32×10^5	$1.7(5) \times 10^5$

Short Summary

- The viscosity η of the polymer could be calculated from the capillary number Ca (obtained from the rim profile analysis) and the dewetting velocity \dot{s} for molecular weights $M_w \leq 81$ kg/mol.
- The values for η are, within the experimental error, in good agreement with corresponding values obtained from the (bulk) WLF equation.

5.2.5 Correlation of Slip Length, Viscosity and Friction Coefficient

In this section the link between the slip length, the viscosity of the polymer melt and the friction coefficient at the solid/liquid interface is studied to reveal the nature of slippage on AF 1600 substrates. Aside from the dependency on the temperature, the viscosity of a polymer melt is also a function of the molecular weight, especially as soon as chain entanglements have to be considered. According to the linear model by Navier [24], the slip length b is a function of the viscosity η and the friction coefficient κ at the solid/liquid interface:

$$b = \frac{\eta}{\kappa}. \quad (5.1)$$

The results presented in section 5.2.1 allow the conclusion that rim profiles on the AF 1600 substrate are independent of the temperature and, thus, of the viscosity for a given molecular weight M_w (see Fig. 5.5). The slip length for a certain M_w , which is determined from these profiles (see section 5.2.2), is also independent of the temperature and the viscosity (as shown in Fig. 5.9 left). For molecular weights exceeding the critical value for chain entanglements M_c , however, experiments exhibit a clear dependency on the chain length, i.e. the molecular weight M_w , rather than on the viscosity (see section 5.2.2 and ADDENDUM V).

M. Müller [61] proposed to test the aforementioned correlations by a separation (factorisation) of both dependencies of the viscosity as

$$\eta = \xi(T)f(M_w), \quad (5.2)$$

where $\xi(T)$ denotes the functional (local microscopic) dependency of the viscosity on the temperature and $f(M_w)$ stands for the (polymer-specific) dependency on the chain length or the molecular weight, respectively. The friction coefficient κ at the solid/liquid interface is supposed to be proportional to the friction $\xi(T)$ between monomers in the volume⁷ and independent of the molecular weight, i.e.

$$\kappa \propto \xi(T). \quad (5.3)$$

Consequently, the first condition to be tested consists in the fact that the slip length b should be proportional to $f(M_w)$ and independent of the dewetting temperature T . The results of the slip lengths, as previously mentioned, show no systematic dependency on the temperature. Below the critical molecular weight for chain entanglements M_c , the slip length is supposed to be proportional to the molecular weight M_w , i.e. $b \propto f(M) \propto M_w$ (see e.g. [48]). The fluctuations of the slip length of different measurements below M_c , however, are quite large and make the verification of $b \propto M_w$ very difficult or even impossible. Above M_c , the correlation between slip length and chain length, i.e. $b \propto f(M) \propto M_w^3$ (reptation model [62, 63]) and the impact of chain entanglements are clearly evidenced (see section 5.2.2 and Fig. 5.6).

⁷De Gennes expects the friction coefficient κ in ideal conditions (passive and smooth solid surface, no attachment of chains) to be comparable to the friction coefficient within a fluid of monomers $\kappa_m = \eta_m/a$, where η_m denotes the monomer viscosity and a the molecular size [52].

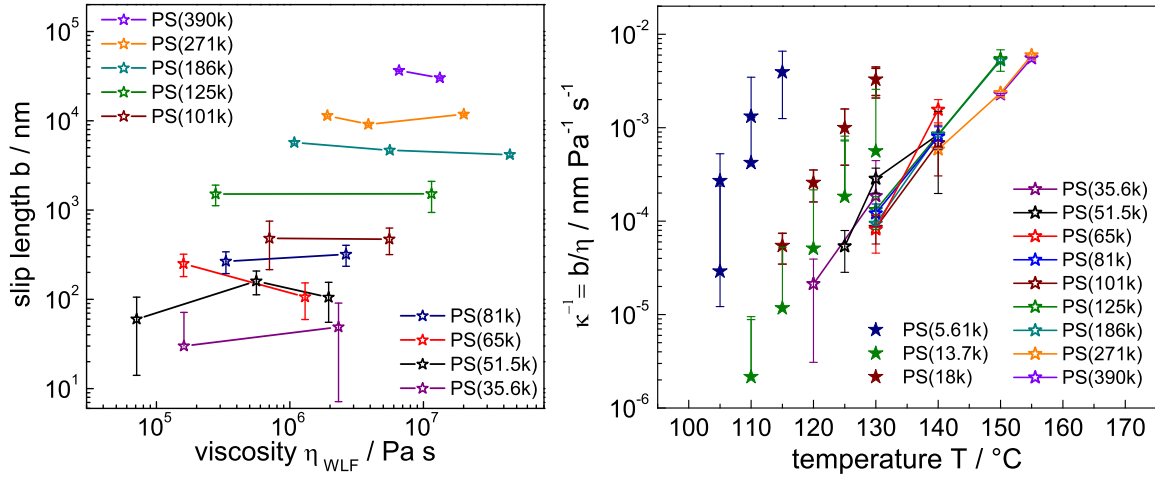


Figure 5.9: Left: Double-logarithmic representation of the slip length b , obtained from the rim profile analysis, and the viscosity η of the PS melt (as calculated from the WLF equation, see section 5.2.4) for diverse molecular weights $M_w > M_c$. Right: Semi-logarithmic representation of $b/\eta = \kappa^{-1}$ in view of the dewetting temperature T . Filled symbols mark data points for $M_w < M_c$, open symbols stand for $M_w > M_c$.

The second condition to be tested consists in the fact that $1/\kappa = b/\eta$ should be proportional to $1/\xi(T)$ and independent of molecular weight M_w . As illustrated in Fig. 5.9, the data for the reciprocal friction coefficient for molecular weights above M_c indeed does not, within the experimental error, show any systematical dependency on the molecular weight. Consequently, the interaction of the polymer chains with the substrate at the solid/liquid interface is governed by a single (monomeric) friction coefficient.

Below M_c , however, deviations from the aforementioned behavior are found. For PS(18k), PS(13.7k) and, especially, for PS(5.61k), systematically larger values for b/η , i.e. smaller values for the friction coefficient $\kappa = \eta/b$, are experimentally obtained. It should be noticed, however, that the data for the viscosity was taken from the WLF equation (see section 5.2.4). Deviations such as observed for PS(5.61k) potentially result from uncertainties of the WLF data (e.g. from the glass transition temperature measurement). The test of this condition could also be affected by the fact that a reduced viscosity at the solid/liquid interface should be taken into consideration. In this case, the b/η data for molecular weights above M_c is systematically too low due to the fact that the viscosity at the solid/liquid interface is reduced. Probably both effects hold responsible for the deviations of the reciprocal friction coefficient $1/\kappa$ illustrated in Fig. 5.9. A discussion concerning the local viscosity at the solid/liquid interface in view of the previously described experimental results is led in the following section.

Short Summary

- The slip length b , the viscosity η of the polymer and the friction coefficient κ are correlated via the linear model by Navier.

- Above the critical molecular weight M_c for chain entanglements, the interactions of the polymer chains with the substrate at the solid/liquid interface is governed by a single (monomeric) friction coefficient.
- Below M_c , smaller values for the friction coefficient $\kappa = \eta/b$ are obtained.

5.3 Results and Discussion

The quantitative comparison of both methods that enable the determination of the slip length, i.e. the hole growth dynamics (see Chapter 4 and ADDENDUM III) and the rim profile analysis (see ADDENDUM IV and V), lead to consistent results. Below the critical molecular weight for chain entanglements M_c , slip lengths up to approx. 150 nm are obtained on the AF 1600 substrate. In literature, slip lengths determined from molecular dynamics (MD) simulations in non-wetting conditions are reported to be in the range of 15 molecular diameters [64]. Approximating the molecular diameter of a polymer coil by two times its radius of gyration R_g , $R_g = 3.2$ nm for PS(13.7k) results in values for the slip length of up to 100 nm. From this point of view, the experimental results for the slip length on AF 1600 below M_c are in good accordance with the expectation.

5.3.1 Reduced Interfacial Entanglement Density and its Implications

With regard to the molecular weight of the polymer above M_c , the experimental data for the slip length follows an algebraic power law with an exponent of 2.9(2) for both methods. This is in excellent accordance with the scaling law $b \propto M_w^3$ predicted by de Gennes [52]. The pre-factor a/N_e^2 is obtained from the linear fit to the experimental data in the double-logarithmic representation: As described in detail in ADDENDUM V and section 5.2.2, the rim profile analysis leads to $N_e = 517$ which is a factor of 3.2 larger compared to the bulk entanglement length. The lowered slip lengths give, therefore, rise to a **significantly increased entanglement length** N_e . This fact will be discussed in the following paragraphs.

The diffusive motion of polymer chains in a melt was successfully described by the reptation model [62, 63] (as e.g. described in the book by Rubinstein and Colby [48]). A polymer chain can diffuse within a tube, defined by the entanglement length N_e , and performs a snakelike motion along its contour. The entanglement length is of extraordinary importance for many properties of polymers. The motion of chains shorter than N_e can be described by the Rouse model [48]. Polymer chain entanglements and hence the entanglement length of the polymer, are related to the packing of the polymer chains in the bulk. Close to an interface, however, the chains pack differently. The reduced entanglement density in the vicinity of the solid/liquid interface (see Fig. 5.10 for an illustration of the possible situation on the molecular level) results from a reduction in the volume pervaded by a polymer chain at an interface as described by Brown and Russell [65]: The polymer coil cannot cross the boundary at the interface or wall that acts as a reflecting plane. Chain segments fold back on the same chain and, thus, the degree of coil-coil interpenetration decreases. The reflection process causes a decrease of the radius of gyration normal to the plane, but does not affect the radius of gyration parallel to the

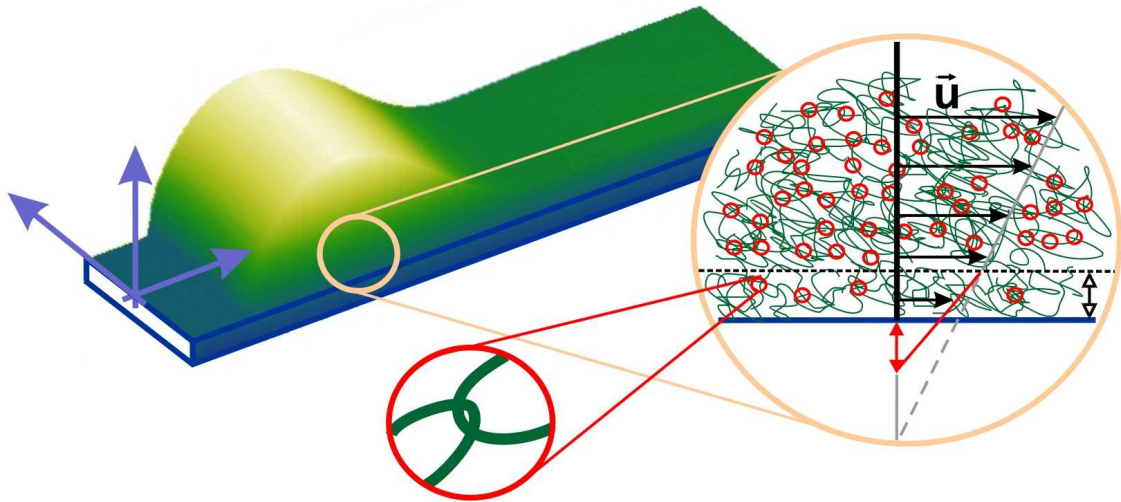


Figure 5.10: Illustration of the molecular situation for entangled polymer thin films. Interpenetrating polymer coils form a network of entanglements. The density of inter-chain entanglements is reduced in the vicinity of the solid/liquid interface. This phenomenon affects the hydrodynamic boundary condition of polymer flow as concluded from the dewetting dynamics and the morphology of thin polymer films.

plane. The polymer coil can be imagined having an ellipsoidal rather than a spherical shape [66]. Close to the interface or the wall, the volume pervaded by a given chain length is smaller than in the bulk. Brown and Russell [65] suggest that the vertical distance affected by this phenomenon can be approximated at most by the radius of gyration of the polymer. Hence, the normal bulk entanglement density is expected to be recovered. They analytically calculate a reduction of the entanglement density or, analogous to that, an increase of the entanglement length by approximately a factor of 4 which is in accordance with the experimental results presented here.

The effect of an altered entanglement network and, in particular, a **reduced entanglement density at interfaces** is of extraordinary importance in view of sliding friction of thin polymer films, but also impacts other interfaces (where the hypothesis of the reflection of polymer segments is applicable) such as polymer/polymer (and their interdiffusion) or polymer/air interfaces. Recent experimental studies probing the effect of polymer chains in confined geometries such as thin films have also provided strong evidence of deviations from polymer bulk properties and a reduced entanglement density: Si *et al.* report a decrease of the entanglement density in thin freestanding films compared to the bulk polymer [67]. They conclude that the total entanglement density is constant, but due to the reduced chain overlap near interfaces, the proportion of self-entanglements increase versus inter-chain entanglements. Rowland *et al.* recently studied the squeeze flow of entangled polymers in confined conditions of films thinner than the size of the bulk macromolecule [68]. Their experiments reveal a reduced interpenetration of neighboring chains in favor of self-penetration leading to a weakening of the polymer

network and a decreased resistance to melt flow due to the presence of less inter-chain entanglements. Barbero and Steiner studied the mobility at the surface, i.e. at the liquid/air interface of thin polymer films by an electric field technique. They attributed the reduced effective viscosity in the case of as-cast films compared to annealed ones to a reduced, non-equilibrium entanglement density resulting from preparation [69]. Molecular dynamics simulations and corresponding primitive path analysis for polymers studying chain conformations and local dynamics corroborate the occurrence of a reduced entanglement density near a wall [70, 71].

The unique feature of the experimental results presented in this thesis consist in the fact that sliding friction is sensitive to the proximate properties of the polymer at the solid/liquid interface, though the residual film is not necessarily affected by confinement. The previously discussed experimental studies relate their findings to the confinement given by the film thickness (and its ratio to the spatial dimensions of the polymer chains therein). Here, however, the direct and unique impact of the solid/liquid interface upon chain conformations and rheological properties of the polymers in its vicinity is revealed. Even far from confinement conditions for the entire film, slippage is highly affected by this phenomenon: The **thickness of the layer** affected by the reduced entanglement density at the solid/liquid interface is supposed to be at most in the range of the radius of gyration R_g [65]. R_g depends on the chain length of the polymer and varies for typical PS molecular weights $M_w > M_c$ used in this study from 5.2 nm for PS(35.6k) up to 17.1 nm for PS(390k)⁸. Moreover, the polymer/air interface might also cause a reduced entanglement density that, potentially, propagates the same distance away from the interface into the polymer film. Due to the fact that the polymer films exhibit thicknesses of at least 100 nm, the latter is, even for the largest M_w , still about 3 times larger than the superposition of both effects (layers).

The decrease of the entanglement density at the solid/liquid interface is, as described before, inferred from the determination of the entanglement length $N_e = 517$. This value corresponds to a molecular weight of the polymer strand between two entanglements of $M_e = 53.8$ kg/mol. Thus, being significantly larger than the **critical molecular weight** M_c found for bulk situations, this consideration suggest that the formation of entanglements at the interface starts at a higher molecular weight as compared to the upper residual (bulk-like) polymer film⁹.

5.3.2 Quantitative Comparison of Slip Lengths: Rim Profile Analysis vs. Hole Growth Dynamics

Slip lengths obtained from hole growth analysis (see Chapter 4) are usually larger compared to those gained from the analysis of rim profiles. The corresponding linear fit to the experimental data from hole growth leads to $N_e = 345$ (still roughly a factor of 2.1 compared to the bulk entanglement length). The systematic difference between both pathways to access the slip length is depicted in Fig. 5.11 and discussed in the following paragraphs.

⁸ R_g is calculated via $\langle R_g^2 \rangle = N_K b_K^2 / \sqrt{6}$, where b_K denotes the Kuhn length and N_K the number of Kuhn monomers. For PS, $b_K = 1.8$ nm and $N_K = M_N / (720 \text{ g mol}^{-1})$ is found according to [48].

⁹The critical molecular weight M_c for polymer chain entanglements (in the case of bulk PS) is given by approx. 2 times the entanglement length M_e [48].

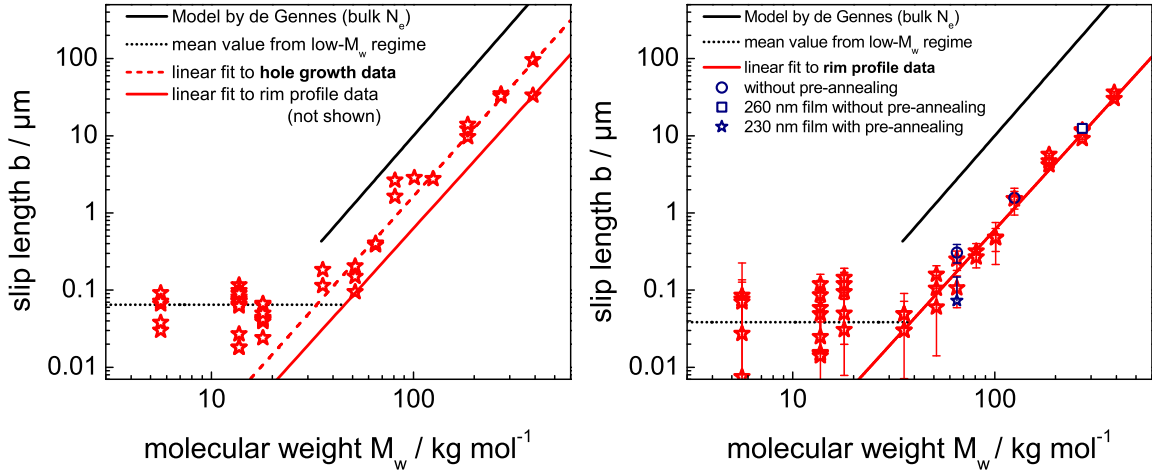


Figure 5.11: Double-logarithmic representation of the slip length b as a function of molecular weight M_w : a comparison of hole growth (left, Fig. 4.9) and rim profile (right, Fig. 5.6) analysis for PS dewetting from AF 1600 substrates. The solid black line represents the model by de Gennes [52] using the PS bulk entanglement length $N_e=163$.

The systematically larger slip lengths originating from the hole growth analysis, which result in a smaller N_e as compared to the rim profile analysis, is potentially caused by an inevitable assumption included in the energy dissipation model of sliding friction: In the two dimensional representation of the rim, the **lateral extent of slippage** in the x-direction, i.e. the direction of dewetting, is approximated by the rim width w . The latter is again connected to the slip length: Increasingly larger slip lengths are correlated to more smoothly decaying rims. Following the applied definition of the rim width, i.e. the distance between the three-phase contact line and the x-coordinate where the rim height has dropped to 1.1 times the initial film thickness h_0 , larger slip lengths consequently lead to broader rims. If, however, the "true" lateral extent of slippage is significantly larger than the rim width w , slip lengths obtained from the combined model for the hole growth analysis (assuming a superposition of viscous flow and slippage) would be systematically too large¹⁰. This view is supported by the dewetting experiments on the AF 1600 substrate below the critical chain length for entanglements: In case of these solely weakly slipping PS films, no significant difference between slip lengths obtained from rim profiles and hole growth dynamics is found. Consequently, the significant shift between the results of the two methods is either correlated to the change of the rim profile, in combination with the definition of the rim width, or, and that is the second possibility to be discussed, to the change of the velocity profile according to the presence of slippage.

To gain information about the extent of slippage is difficult. For block-copolymer films it can be estimated by the area within the rim of a dewetted hole in which the shear has oriented the cylindrical micro-domains [55]. By detaching the film from the substrate and imaging

¹⁰Note that for dewetting experiments on OTS and DTS below the critical entanglement length of PS also systematically larger values for the slip length are obtained as compared to corresponding values from the rim profile analysis [39].

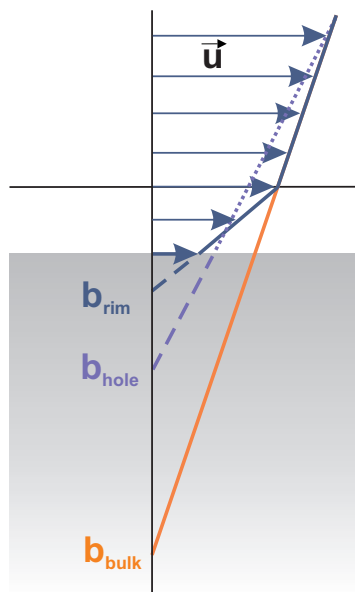


Figure 5.12: Illustration of the velocity profile and the hypothesis explaining the discrepancy between slip lengths as determined by the evaluation of the hole growth dynamics (b_{hole} , light blue) and the rim profile analysis (b_{rim} , dark blue). The solid blue line includes the reduction of the entanglement density in the vicinity of the solid/liquid interface. The dotted blue line represents an average of reduced and bulk-like entanglement density. The solid orange line illustrates the slip length b_{bulk} as expected from pure bulk polymer properties.

the rim from underneath with the AFM, differences in the orientational structure of the two phases become visible for different lateral displacements related to the three-phase contact line. Unfortunately, the method is not applicable for homopolymer melts. Second, dewetting of polymer films on elastic substrates (such as e.g. PDMS supports) affects and deforms the elastic substrate [72]. The spatial dimensions of the elastic deformation can be quantified again by detaching the polymer film and imaging the spot on the elastic substrate that correlates to the former position of the rim [73]. However, viscoelastic deformation of the substrate, especially at the three-phase contact line where the substrate surface is pulled upwards [73], represents an additional energy dissipation mechanism which complicates the interpretation of the substrate deformation in view of slippage.

Besides the aforementioned methodical issue of the differences concerning the determination of slip lengths from the hole growth dynamics and the analysis of rim profiles, a further explanation might be hypothesized: Rim profiles and hole growth dynamics are governed by **different physical properties of sliding friction**. Their analysis, therefore, yield different boundary conditions. At first, there is the option that the rim profile analysis is sensitive to the local hydrodynamic boundary condition *on the lateral scale* at the section of the solid/liquid interface where the rim decays into the unperturbed film, whereas the hole growth analysis is, as discussed before, sensitive to the entire extent of the rim width w (as already proposed in

[39]). The second option is the following: Since the entanglement density defines the viscosity of a long-chained polymer melt, a reduced entanglement density at the solid/liquid interface is correlated to a reduced viscosity (compared to the residual upper part of the film). Consequently, a modification of the velocity profile towards a *non-linear* behavior *on the vertical scale* within the rim could be expected. This is our present **hypothesis**: Compared to the usual assumption of an entirely linear velocity profile, the question arises as to whether the evaluation of the hole growth dynamics and the rim profile analysis probe this *non-linear* and, thus, more sophisticated situation in the same manner (as illustrated in Fig. 5.12): The dewetting dynamics may provide an averaging (based on the velocity profile on the vertical scale, i.e. the z-direction) of the reduced slip length, originating from a reduced number of entanglements and a reduced viscosity, and the rest of the film exhibiting a larger, bulk-like entanglement density. The shape of a liquid rim and consequently the quantitative analysis of such profiles potentially, however, relies on the "true" hydrodynamic boundary condition exhibiting a reduced slip length. The latter is defined via the velocity of the first polymer molecules and the viscous stress at the solid/liquid interface (at $z = 0$). Thus, the rim profile analysis is sensitive to the very few polymer molecules adjacent to the solid/liquid interface, whereas the analysis of the dewetting velocity takes the entire film into account. This issue will be furthermore discussed in the following subsection in particular in view of the experimental results for the polymer viscosity obtained from the determination of capillary numbers.

5.3.3 Viscosity of Thin Polymer Films at the Solid/Liquid Interface

As mentioned at the end of the previous subsection, the question arises as to whether the rim profile analysis is sensitive to the reduced interfacial viscosity η_i directly at the solid/liquid interface or whether it is governed by the bulk-like viscosity η_{bulk} throughout the residual film. Since $\eta \propto M_e^{-2}$ [48], an increase of the entanglement length by a factor 3.2 would result in a reduction of the interfacial viscosity η_i by roughly one order of magnitude¹¹ as compared to η_{bulk} .

However, the simultaneous determination of the capillary number Ca gives values for the viscosity (using the actual dewetting velocity as determined from the hole growth dynamics) that are, within the experimental error, in good agreement with the (bulk) viscosity obtained from the WLF equation. Unfortunately, the calculation of Ca from monotonically decaying rim profiles ($M_w \geq 101$ kg/mol) could not be achieved. The temperature-dependence of the inverse friction coefficient $1/\kappa = b/\eta$ (taking η from the bulk WLF equation) gives rise to the presence of a consistent (monomeric) friction coefficient at the solid/liquid interface for the dewetting experiments above M_c (see Fig. 5.9 in section 5.2.5). The corresponding data for molecular weights below M_c , however, deviates from this behavior. This discrepancy might be

¹¹The calculation of the slip length obtained from fitting the experimental rim profile data with a single exponential decay necessitates, as mentioned before, the knowledge of the viscosity (to determine the capillary number). Assuming reduced (by a factor of 10) viscosities and re-calculating the slip lengths from these values, however, leads to unreasonable large negative slip length for PS(101k) and PS(125k) and deviations from the former slip lengths of less than 7% for PS(271k) and PS(390k). Thus, calculating the slip length using bulk viscosities is appropriate. Artifacts resulting from a low viscosity layer at the solid/liquid can be safely excluded.

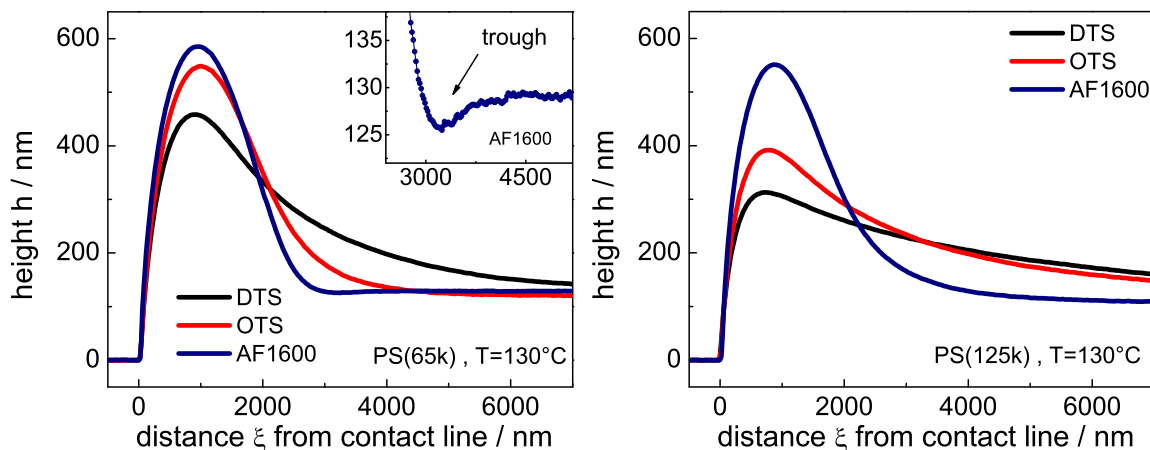


Figure 5.13: Influence of the substrate: Comparison of rim profiles on AF 1600, OTS and DTS. Profiles on the silanized surfaces are taken from [39]. Left: PS(65k) at 130 °C (the inset depicts the trough that is observed on the AF 1600 substrate). Right: PS(125k) at 130 °C.

attributed to a reduced interfacial viscosity η_i (compared to η_{bulk}) for the experiments above M_c .

To conclude, a direct evidence for a reduction of the viscosity cannot be inferred from the experimentally accessible capillary numbers. However, a reduced viscosity η_i at the solid/liquid interface would explain noticeable differences in friction coefficients. A region of a reduced entanglement density (and reduced viscosity) at the solid/liquid interface could, moreover, have implications in view of the molecular mechanism of slippage for PS melts on silanized surfaces such as OTS and DTS. A comparison of the results on AF 1600 with previously obtained results on OTS and DTS (see ADDENDUM IV) is the subject of the following subsection.

5.3.4 Comparison with Previous Results on OTS and DTS Substrates

Comparison of Rim Profiles Comparing the rim profiles for PS(65k) (see Fig. 5.13 left) dewetting from silanized and from AF 1600 surfaces, one finds a trough on the wet side of the rim on AF 1600 and a smooth monotonic decay on DTS. Dewetting from OTS results in a monotonic decrease, but with a steeper slope as compared to DTS. Fig. 5.13 right shows a direct comparison of rim profiles for PS(125k). In all cases monotonically decaying rims are recorded corroborating the same trend as for PS(65k): The profile on AF 1600 exhibits the steepest slope on the wet side of the rim, whereas on OTS and DTS shallower declines are observed. These observations indicate clear differences concerning the slip length on the three substrates. Moreover, the different rim profiles (on different substrates but for the same preparation and properties of the polymer film above the entanglement length) impressively visualize that viscoelastic effects can be excluded as the source of distinct rim morphologies. In diverse publications (see ADDENDUM II), the occurrence of monotonically decaying rims was attributed to viscoelastic stress relaxation.

Comparison of Slip Lengths Compared to the AF 1600 substrate, the slip length for the identical molecular weight below M_c is substantially larger on OTS and DTS substrates. As shown in ADDENDUM IV, slippage decreases for increasing temperature and the slip length is significantly larger (roughly one order of magnitude) on DTS as compared to OTS. These findings are corroborated by the results obtained from the analysis of the corresponding hole growth dynamics (see ADDENDUM III). Above M_c , diverse experiments were performed on OTS and DTS by R. Fetzer [39]: The hole growth analysis indicates an increase of the slip length on OTS from $b \approx 1 \mu\text{m}$ for PS(51.5k) to $b \approx 100 \mu\text{m}$ for PS(390k) with $b \propto M_w^{2.1}$ being independent of the temperature and of pre-annealing procedures. The discrepancy to the results for the AF 1600 substrate, which are in excellent accordance with theoretical expectation $b \propto M_w^3$, is potentially correlated to the unique mechanism at the SAM/polymer interface. In the following paragraph, experimental results on OTS and DTS are interpreted in terms of different hypotheses concerning possible interactions on the molecular level of the polymer with the self-assembled silane monolayer.

Potential Molecular Mechanism of Slippage on OTS and DTS The fact that the slip length increases less strongly in view of the molecular weight $M_w > M_c$ than expected (and experimentally found on the AF 1600 substrate) might be interpreted as a hint concerning the **presence of surface-anchored polymer chains or chain-ends**. The more such chains are entangled with chains from the melt (for larger molecular weights), the more strongly they are able to constrain slippage (see [74] and ADDENDUM II). This hypothesis is supported by the experimental observation that holes nucleated at a later time exhibited slower dewetting dynamics [39]. In this case, the chains have more time to attach to the substrate and, thus, the initial density of anchored chains is higher. The hypothesis of anchoring of melt chains at or in between silane molecules in the case of OTS and DTS substrates and the formation of entanglements above M_c contains a further aspect that is worth considering: At a certain critical shear rate, anchored chains and free melt chains can disentangle which results in a decrease of the friction coefficient and in an increase in the slip length. Consequently, a shear-rate dependent slip length would be expected (see ADDENDUM II). A correlation between this hypothesis and the potential formation of a lubricant layer, also called "slip plane" (see also ADDENDUM II), or an alignment of polymer chains at the SAM/polymer interface (as evidenced by X-ray scattering in the case of a silicon substrate and PDMS at high shear rates [75]) is still under debate and not clear to date. The amorphous AF 1600 substrate obviously represents a non-adsorbing, passive surface with a very low surface energy.

The analysis of rim profiles for PS melts on OTS and DTS entails the following results [39]: For a given molecular weight, the slip length and also the **friction coefficient** $\kappa = \eta/b$ decrease as the temperature increases. With regard to the formerly proposed attachment and anchoring of polymer melt chains at the surface, this result was interpreted by R. Fetzer as follows: With increasing thermal energy, the number of attaching polymer chains decreases and the rate of the desorption increases respectively. Consequently, the density of polymer chains anchored to the substrate decreases with increasing temperature. Above M_c , the friction coefficient increases for a given temperature with the length of the polymer chains, i.e. the molecular weight. Entanglements between anchored and free melt chains are supposed to hinder slippage and, consequently, could cause the increase in the friction coefficient.

The seemingly exponential decrease of the slip length below M_c on OTS and DTS in view of the temperature is a unique feature. It is still unclear how the **temperature-dependency** of the slip length is exactly correlated to the molecular mechanism. In recent numerical simulations, Lichter *et al.* treated liquid slip in nanochannels as a rate process [76]: The slip length is found to increase exponentially with the reciprocal temperature and sliding is considered as hopping of liquid molecules into molecular-sized vacancies. However, clear evidence for a correlation between slippage of PS in the case of OTS and DTS substrates and the discreteness of the SAM molecules (as compared to the random-like roughness structure of the amorphous AF 1600 substrate) is to date not given.

In connection with the molecular mechanism of slippage of polymer melts on SAM surfaces in general, the **discrepancy between OTS and DTS** is of special interest: On both substrates, identical Young's contact angles for PS are found, but the solid/vapor interfacial (surface) tension is smaller on OTS compared to DTS. This gives rise to a smaller solid/liquid interfacial tension on OTS compared to DTS. The OTS surface is, thus, less attractive for the PS film or PS molecules than the DTS. A further discrepancy between OTS and DTS layers potentially consists in their bending properties upon lateral forces due to the difference in the length of the silane molecules. The shorter DTS brush could be less stiff than the longer and potentially more crystalline-like OTS layer. However, no evidence is given corroborating the relevance of this hypothesis in dewetting experiments and in the range of temperatures usually used for these studies. To date, a direct proof for the molecular mechanism of slippage is still lacking. First experimental results originating from scattering studies are presented in the following paragraph.

Neutron and X-ray Scattering Studies The most direct experimental access to the molecular level is provided by neutron and X-ray scattering experiments (performed in collaboration with the groups of Prof. Dr. Hartmut Zabel and Prof. Dr. Andreas Magerl). First results of **neutron scattering experiments** of deuterated polystyrene films that were prepared and subsequently annealed on OTS and DTS surfaces show a significant increase in the scattering length density of the silane layer [77]. This increase is more pronounced on DTS as compared to OTS for the identical annealing time and polymer chain length. The scattering length density of the silane layer exhibits a negative value, whereas polystyrene features a positive one. These findings suggest a penetration of polymer chains or chain ends into the silane layer. For both substrates, the increase in the scattering length density is found to be more pronounced for d-PS(12.3k), annealed for 30 s at 120 °C, as compared to d-PS(60.7k) that was annealed for 40 s at the identical temperature: Either the penetration into the silane layer is faster due to the higher mobility of the d-PS(12.3k) chains, or the larger number of chain ends (approx. 5 times compared to d-PS(60.7k)) causes a higher density of attached chains. The pronounced penetration and anchoring of chains from the melt in between the DTS molecules is also in accordance with the fact that the attraction for PS chains is pronounced on DTS compared to OTS substrates (as argued from the lower surface energy in the case of OTS).

These preliminary results could, moreover, explain dewetting experiments of **polystyrene mixtures of different chain length** by R. Fetzer [39]: Pre-annealing on the hydrophobic substrate (at temperatures slightly below the glass transition temperature to avoid early dewet-

ting) showed reduced slippage, whereas pre-annealing on the hydrophilic mica substrate and subsequent "floating" (and flipping) of the film lead to enhanced slippage. Annealing could have caused a migration of the short-chained species towards the surface, i.e. the polymer/air interface, of the polydisperse polymer film (see also section 6.1). In the case of transferring the film on the hydrophobic substrate, this short-chained PS layer is in contact with the solid/liquid interface impacting the molecular mechanism of slippage. It can be speculated that these short chains hinder the long melt chains to form entanglements with surface anchored chains and could, consequently, enhance slippage. Further complementary studies utilizing dewetting experiments and scattering techniques are very promising.

The **quality and perfectness of the SAM** might also be a crucial parameter especially in connection to its surface energy or the density of potentially anchored polymer chains from the melt. **X-ray scattering experiments** (in collaboration with Volker Schön and Dr. Patrick Huber from Saarland University and the groups of Prof. Dr. Andreas Magerl from Erlangen and Prof. Dr. Hartmut Zabel from Bochum), however, show a high density self-assembled monolayer that exhibits a very low surface roughness indicating the absence of defects or island-formation within the monolayer [78]. However, the quality of the SAM might vary for different preparations. Thus, more experiments are necessary focussing on relating differences in sliding properties of polymers on OTS and DTS to different SAM qualities. Further experimental pathways to access the molecular mechanism of slippage are discussed in the following paragraph.

Further Experiments To verify the potential presence of polymer chains or molecular aggregates remaining attached to dewetted patches of the substrate and within the holes, further studies were initiated: First **AFM** experiments in dewetted holes on DTS show a distribution of objects accompanied with a slight increase in the surface roughness. Corresponding ellipsometry measurements detecting the layer thickness and optical properties of thin layers likewise do not provide conclusive results due to technical restrictions: **Spatially-resolved single wavelength ellipsometry** relies on a variation of the angle of incidence hindering the data collection for large angles and small holes. In case of receding straight fronts generated by floating gaps, dewetted patches did not show any change in ellipsometric measurements. Further studies and corresponding experiments will be necessary to obtain conclusive results. Further experimental techniques from **nonlinear optical spectroscopy** such as second harmonic generation (SHG), sensitive to the anisotropy caused by shearing the liquid, and sum frequency generation (SFG), probing vibrational modes and sensitive to orientation distributions at interfaces, were also considered to study the molecular conformations at the solid/polymer interface. However, these techniques are not offhand applicable without changing the system [79]: Marker molecules are necessary in the case of SHG, whereas transparent substrates would be required for SFG. Moreover, the presence of two interfaces (solid/liquid and liquid/air) is supposed to cause experimental problems.

5.3.5 Viscoelastic Effects

The analysis of the dewetting experiments presented in this study is based on the assumption of Newtonian flow. At this point, the question arises as to whether the obtained results may have implications on the estimation of the **Weissenberg numbers**. As described in section 4.1, the Weissenberg number is given by the product of relaxation time and shear rate. At first, let us consider the relaxation times: According to the previous discussion of the experimental results, the viscosity is reduced due to the reduced entanglement density at the interface(s). Consequently, relaxation times are supposed to be even shorter compared to the numbers utilized for the calculation of Wi . Second, the estimation of shear rates requires an estimation of the lateral extent of slippage (identified as the rim width w) and a vertical range (identified as the sum of the film thickness h_0 and the slip length b obtained from the rim profile analysis). Following the hypothesis of a lateral extent of slippage larger than w causing larger slip lengths in the case of the hole growth analysis as compared to the rim profile analysis, the resulting shear rate would be even lower. The same is valid for the direction perpendicular to the substrate plane: Using the slip lengths from the hole growth analysis or even taking bulk literature values to calculate slip lengths, lower numbers of the corresponding shear rate are obtained. To conclude this debate, it can be stated that the experimental results imply no restrictions concerning the analysis due to possible viscoelastic effects since the Weissenberg numbers Wi for the PS in the vicinity of the interface are even lower than estimated before in section 4.1. The estimation of Wi in section 4.1, thus, represents the "worst case" and Newtonian flow can be safely assumed.

Samples were exposed to elevated temperature on hydrophilic mica substrates prior to the dewetting experiments (see section 3.2). The **annealing** time and the annealing temperature were chosen according to experimental investigations of the density of nucleated holes in thin polymer films [49]: Stresses might act as nuclei for the generation of holes and their relaxation is correlated to a significant reduction of the hole density, i.e. the number of holes per area. At a distinct annealing time, no further reduction of the density of nucleated holes can be detected. Barbero and Steiner recently reported a reduction of the entanglement density, and thus also of the viscosity, of thin polymer films due to non-equilibrium chain conformations after spin-coating [69]. Samples that were annealed for long annealing times at high temperatures, however, showed bulk rheology. To safely exclude an impact of modifications of the polymer conformations and the rheological properties of the films after such long time annealing procedures on the formerly presented results, further experiments might shed light on this issue. While performing dewetting experiments, holes taken for the analysis of the dewetting dynamics and the evaluation of corresponding rim profiles were chosen randomly in this study. The nucleation of different holes usually starts at different times after exposing the sample to a temperature above the glass transition temperature T_g of the polymer film. This additional pre-annealing time on the hydrophobic substrate can be varied if holes are studied that were nucleated at an advanced stage. Such holes might be investigated in further studies in comparison to early nucleated holes. However, viscoelastic effects are not expected to occur during dewetting as discussed before.

5.4 Summary

In this chapter, liquid rim profiles of thin PS films dewetting from AF 1600 substrates are experimentally recorded by AFM and analyzed according to thin film models. A number of conclusions can be drawn which are summarized below.

- By *in situ* AFM experiments, the hole growth dynamics in the mature stage of a rim can be characterized and reveals a self-similar rim growth.
- *Ex situ* rim profiles are recorded on AF 1600 and their analysis by theoretical thin film models gives the capillary number Ca (for $M_w \leq 81$ kg/mol) and the slip length b .
- Below the critical molecular weight for polymer chain entanglements M_c , slip lengths b up to approx. 150 nm are found on the AF 1600 substrate.
- On AF 1600, the slip length is not significantly depending on dewetting temperature (and thus on the viscosity for a fixed M_w), but is strongly correlated to the molecular weight for $M_w > M_c$, i.e. the chain length of polymer molecules in the melt.
- The correlation between slippage and chain length is corroborated by the fact that a difference in the slip length of two orders of magnitude is obtained for the same viscosity but different chain length of the polymer (PS(51.6k) vs. PS(271k)) on AF 1600.
- The relation $b \propto N^3$ of slip length b and chain length N (or alternatively the molecular weight M_w), as predicted by de Gennes, is well reproduced on the AF 1600 substrate by the rim profile analysis as well as by hole growth measurements (Chapter 4).
- The absolute values of the slip lengths obtained from the rim profile analysis on AF 1600 are approx. one order of magnitude lower than what is expected from the model by de Gennes using bulk literature values for the entanglement length N_e . Determining N_e from the relation between slip length and molecular weight gives $N_e = 517$, which is 3.2 times larger than the bulk entanglement length. A decrease of the density of inter-chain entanglements caused by geometric restrictions for the polymer conformation at the solid/liquid interface is evident.
- Studying as-cast PS films (not pre-annealed prior to dewetting) and analyzing rim profiles of PS films exhibiting significantly larger film thicknesses leads to consistent slip lengths.
- For PS on AF 1600, Ca increases as the ratio of slip length and polymer film thickness increases.
- Values for the viscosity η of the polymer melt can be extracted from the measured capillary numbers (for $M_w \leq 81$ kg/mol) by taking the current dewetting velocity prior quenching. The viscosity data is in good agreement with independent (bulk) viscosity data.
- Above the critical molecular weight for chain entanglements, the interaction between polymer chains and the solid substrate can be described by a singular (monomeric) friction coefficient κ (independent of the molecular weight).

- Previously obtained results for the slip lengths on OTS and DTS (from the strong-slip lubrication model) below M_c were evaluated according to the Taylor-expanded model based on the Stokes equations (see ADDENDUM IV). This model is not restricted to the strong-slip regime and, therefore, leads to more reliable results for smaller slip lengths.
- Morphological differences of the rim profiles for DTS, OTS and AF 1600 at an identical temperature and molecular weight (below and above the critical molecular weight for entanglements) clearly indicate that the slippage properties of the substrate, and not viscoelastic effects, govern the rim shape (see ADDENDUM V).

Addendum IV - Comprehensive Analysis of Dewetting Profiles to Quantify Hydrodynamic Slip

IUTAM Symposium on Advances in Micro- and Nanofluidics, IUTAM Bookseries, Vol. 15, pages 51-65, Ed. by M. Ellero, X. Hu, J. Fröhlich, N. Adams, Springer, ISBN 978-90-481-2625-5 (2009).

Authors: O. BÄUMCHEN¹, R. FETZER², A. MÜNCH³, B. WAGNER⁴ and K. JACOBS¹

¹ Department of Experimental Physics, Saarland University, 66123 Saarbrücken, Germany.

² Present address: Ian Wark Research Institute, University of South Australia, Mawson Lakes, SA 5095, Australia.

³ School of Mathematical Sciences, University of Nottingham, University Park, Nottingham, NG7 2RD, UK.

⁴ Weierstrass Institute for Applied Analysis and Stochastics (WIAS), Mohrenstrasse 19, 10117 Berlin, Germany.

Author contributions: K. Jacobs designed research. Experiments were performed by R. Fetzer. Models were developed by A. Münch and B. Wagner. The analysis of the experimental results according to the "Stokes model" was performed by O. Bäumchen. The article was written by O. Bäumchen. Writing was supervised by R. Fetzer, A. Münch, B. Wagner and K. Jacobs.

Abstract - Hydrodynamic slip of Newtonian liquids is a new phenomenon, the origin of which is not yet clarified. There are various direct and indirect techniques to measure slippage. Here we describe a method to characterize the influence of slippage on the shape of rims surrounding growing holes in thin polymer films. Atomic force microscopy is used to study the shape of the rim; by analyzing its profile and applying an appropriate lubrication model we are able to determine the slip length for polystyrene films. In the experiments we study polymer films below the entanglement length that dewet from hydrophobized (silanized) surfaces. We show that the slip length at the solid/liquid interface increases with increasing viscosity. The correlation between viscosity and slip length is dependent on the type of silanization. This indicates a link between the molecular mechanism of the interaction of polymer chains and silane molecules under flow conditions that we will discuss in detail.

Comprehensive Analysis of Dewetting Profiles to Quantify Hydrodynamic Slip

Oliver Bäümchen¹, Renate Fetzner^{1,2}, Andreas Münch³, Barbara Wagner⁴, Karin Jacobs¹

¹ Department of Experimental Physics, Saarland University, 66123 Saarbruecken, Germany. o.baemchen@physik.uni-saarland.de

² Present address: Ian Wark Research Institute, University of South Australia, Mawson Lakes, SA 5095, Australia.

³ School of Mathematical Sciences, University of Nottingham, University Park, Nottingham, NG7 2RD, UK.

⁴ Weierstrass Institute for Applied Analysis and Stochastics (WIAS), Mohrenstrasse 19, 10117 Berlin, Germany.

Summary. Hydrodynamic slip of Newtonian liquids is a new phenomenon, the origin of which is not yet clarified. There are various direct and indirect techniques to measure slippage. Here we describe a method to characterize the influence of slippage on the shape of rims surrounding growing holes in thin polymer films. Atomic force microscopy is used to study the shape of the rim; by analyzing its profile and applying an appropriate lubrication model we are able to determine the slip length for polystyrene films. In the experiments we study polymer films below the entanglement length that dewet from hydrophobized (silanized) surfaces. We show that the slip length at the solid/liquid interface increases with increasing viscosity. The correlation between viscosity and slip length is dependent on the type of silanization. This indicates a link between the molecular mechanism of the interaction of polymer chains and silane molecules under flow conditions that we will discuss in detail.

1 Introduction

1.1 Slippage at Solid/Liquid Interfaces

The control of the flow properties at the solid/liquid interface is important for applications ranging from microfluidics, lab-on-chip devices to polymer melt extrusion. Slippage would, for instance, greatly enhance the throughput in lab-on-chip devices and extruders. Usually slippage is characterized by the so-called slip length which is defined as the distance between the solid/liquid interface and the point within the solid where the velocity profile of the liquid extrapolates to zero. During the last years, several different techniques have

M. Ellero et al. (eds.), *IUTAM Symposium on Advances in Micro- and Nanofluidics*, IUTAM Bookseries 15,

© Springer Science + Business Media B.V. 2009

been established to probe the slip length of different systems. These methods can be classified into two groups, direct and indirect measurements of the flow velocity at the solid/liquid interface. Direct measurements are based on particle imaging velocimetry techniques [1–3] that utilize tracer particles or fluorescence recovery after photobleaching [4, 5]. Colloidal probe atomic force microscopy [6, 7] and surface forces apparatuses [8, 9] are more indirect techniques to probe slippage. Detailed information concerning slippage and techniques to measure liquid velocities in the vicinity of solid/liquid interfaces are reviewed in recent articles by Neto et al. [10], Lauga et al. [11] and Boquet and Barrat [12].

1.2 Dewetting Dynamics of Polymer Films

Dewetting takes place whenever a liquid layer can reduce energy by retracting from the contacting solid [13]. Dewetting starts by the birth of holes, which can be generated by three different mechanisms, spinodal dewetting, homogeneous and heterogeneous nucleation [14]. The holes grow in size, cf. Fig. 1, until neighboring holes touch. The quasi-final state is a network of droplets [15]. The equilibrium state would be a single droplet, yet this state is usually not awaited since it may take years for viscous liquids such as our polystyrene. Since we are only interested in the growth of holes and their rim morphology, the underlying mechanism of their generation is irrelevant. However, the most likely process in our system is nucleation. The type of nucleus is unclear and also of no relevance for our studies. It can be a dust particle or a heterogeneity in the film or on the substrate. After holes are generated, they instantly start to grow until they touch neighboring holes and coalesce. We study the flow dynamics of thin polymer films on smooth hydrophobic substrates. The driving force for the dewetting process can be characterized by the spreading parameter S , which depends on the surface tension of the liquid γ_{lv} (30.8 mN/m for polystyrene) and the Young’s contact angle Θ of the liquid on top of the solid surface:

$$S = \gamma_{lv}(\cos \Theta - 1). \quad (1)$$

The system also dissipates energy, namely by viscous friction within the liquid and sliding friction at the solid/liquid interface. A force balance between driving forces and dissipation determines the dewetting rate. Conservation of mass leads to a rim that surrounds each hole. We show that the shape of this rim is not only sensitive to the chain length of the polymer melt [16] but is also to the underlying substrate. The use of recently developed models [17] enables us to extract the slip length b as well as the capillary number Ca from the rim profiles. The latter is given by

$$Ca = \frac{\eta \dot{s}}{\gamma_{lv}}. \quad (2)$$

Here, \dot{s} is the current dewetting velocity, which can be obtained by a series of optical images of the hole growth before the sample is quenched to

room temperature and imaged by atomic force microscopy (AFM). From the capillary number, the viscosity η of the melt can be calculated and compared to independent viscosity measurements, cf. Sect. 3.4.

2 Experimental Section

2.1 Our System

Atactic polystyrene (PS) obtained from PSS Mainz with a molecular weight of 13.7 kg/mol ($M_w/M_n = 1.03$) was used as a liquid in our experiments. As substrates, we used Si wafers (Siltronic AG, Burghausen, Germany) that were hydrophobized by two different types of silanes following standard methods [18]. Thin PS films were prepared by spin coating a toluene solution of PS onto mica, floating the films onto Millipore water, and then picking them up with the silanized silicon wafers. The floating step is necessary since on the spin coater, a drop of toluene solution would just roll off the hydrophobized surface. All PS films in this study have a thickness of 130(5) nm. We utilized two different silane coatings on the Si wafer (2.1 nm native oxide layer): octadecyltrichlorosilane (OTS) and the shorter dodecyltrichlorosilane (DTS), respectively. The thicknesses of these self-assembled monolayers are $d_{\text{OTS}} = 2.3(2)$ nm and $d_{\text{DTS}} = 1.5(2)$ nm as determined by ellipsometry (EP³ by Nanofilm, Goettingen, Germany). The contact angle hysteresis of water is very low (6° in case of OTS and 5° in case of DTS), while the advancing contact angles are $116(1)^\circ$ (OTS) and $114(1)^\circ$ (DTS). Surface characterization by AFM (Multimode by Veeco, Santa Barbara, CA, USA) revealed RMS roughnesses of 0.09(1) nm (OTS) and 0.13(2) nm (DTS) on a $1 \mu\text{m}^2$ area, and an (static) receding contact angle of polystyrene droplets of $67(3)^\circ$ on both substrates.

Surface energies cannot be determined directly from contact angle measurements of PS only, due to the fact that polystyrene has polar contributions. The advancing contact angles of apolar liquids like bicyclohexane vary slightly on both coatings. We find $45(3)^\circ$ on OTS and $38(4)^\circ$ on DTS. The surface energy of the substrate is linked to the contact angle of apolar liquids via the Good-Girifalco equation [19]. Consequently, we find a slightly larger surface energy for DTS ($\gamma_{\text{DTS}} = 26.4$ mN/m) than for OTS ($\gamma_{\text{OTS}} = 23.9$ mN/m) substrates. Identical contact angles of PS on both substrates therefore lead to different energies at the OTS/PS and DTS/PS interface due to Young's equation.

2.2 Hole Growth Dynamics

To induce dewetting, the films were heated to different temperatures above the glass transition temperature of the polymer. After a short time circular holes appear and instantly start to grow (see Fig. 1).

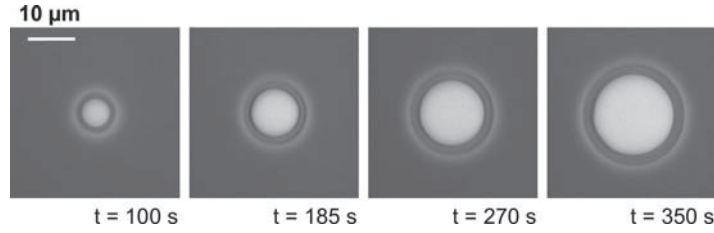


Fig. 1. Series of optical images of a growing hole in a PS film on DTS at 120°C.

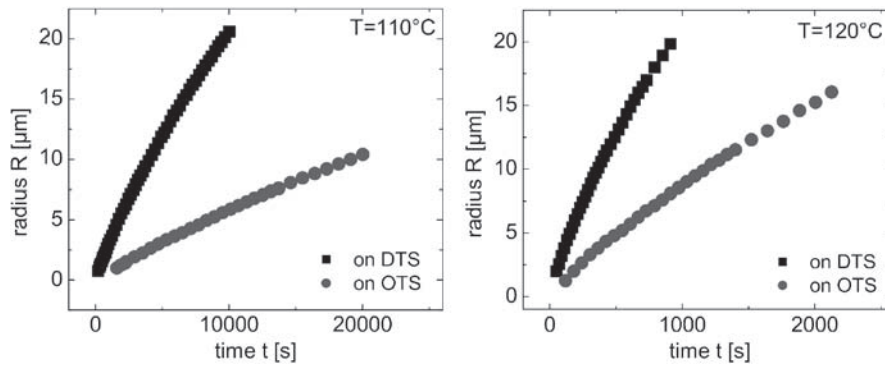


Fig. 2. Hole radius versus time on OTS and DTS at 110°C and 120°C.

Holes in the PS film were imaged by optical microscopy captured by an attached CCD camera, and hole radii were measured. As shown in Fig. 2, dewetting progresses much faster on DTS than on OTS coated substrates.

We explain these results as follows: At the same temperature, the liquids on both samples have exactly the same properties: the viscosity as well as the surface tension do not depend on the substrate underneath. Additionally, the contact angle of polystyrene on both surfaces is the same within the experimental error. Therefore, the spreading coefficient S , that is the driving force of the dewetting process, is identical on both substrates. Hence, the different dewetting velocities observed on OTS and DTS indicate different energy dissipation pathways on these coatings. Viscous friction within the liquid is expected to be identical for both surfaces since we compare liquids of the same viscosity and with the same dynamic contact angle [20]. The latter can be probed by AFM scans in the vicinity of the three-phase contact line. In situ imaging reveals that the dynamic contact angle stays constant at $56(2)^\circ$ during hole growth. Consequently, friction at the solid/liquid interface and therefore slippage must be different on OTS and DTS. In the next section we show that not only the hole growth dynamics but also the shape of rims is affected by the underlying substrate.

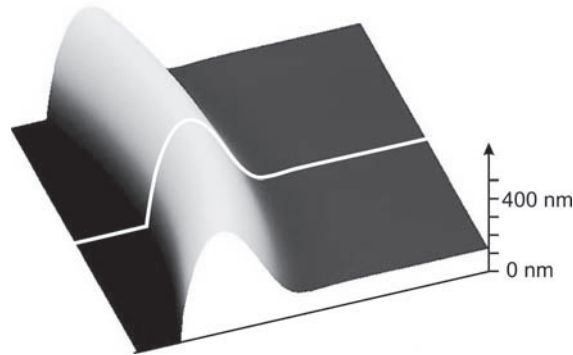


Fig. 3. AFM image of a rim on OTS: scan size $10 \times 10 \mu\text{m}^2$. The dewetting was performed at 130°C . The white line represents a single scan line of the rim perpendicular to the three-phase contact line.

2.3 Rim Shapes

For the characterization of the shape of the rims surrounding the holes, the samples were quenched to room temperature after the holes have reached a diameter of $12 \mu\text{m}$. AFM scans were then taken in the glassy state of PS. An example is shown in Fig. 3.

Figure 4 demonstrates that the type of substrate affects the rim profile: On OTS covered substrates, the rim of the dewetting PS film exhibits an oscillatory shape, whereas on DTS covered surfaces, at the same temperature, a monotonically decaying function is observed. The insets to Fig. 4 shall clarify the term “oscillatory rim shape” on OTS. Furthermore, Fig. 4 shows that temperature influences the shape of the profile: the higher the temperature the more pronounced are the oscillations on OTS and even on DTS, an oscillatory shape is recorded for $T = 130^\circ\text{C}$. Comparing the impact of the substrate on the rim morphology to the hole growth experiments in the previous section, we observe a correlation between the dewetting velocity and the shape of corresponding rims: high dewetting velocities lead to monotonic rim profiles while lower dewetting speeds tend to result in oscillatory rim shapes. In the previous section we argued that different sliding friction at the solid/liquid interface might be responsible for the different dewetting speeds on OTS and DTS. In the next section, the theoretical expectation of the influence of slippage on the rim shapes will be explained. Moreover, the experimental results are compared to theoretical predictions.

3 Theoretical Models and Data Analysis

3.1 Lubrication Model

The theoretical description is based on a lubrication model developed by Münch et al. [21] for systems showing strong slip at the solid/liquid inter-

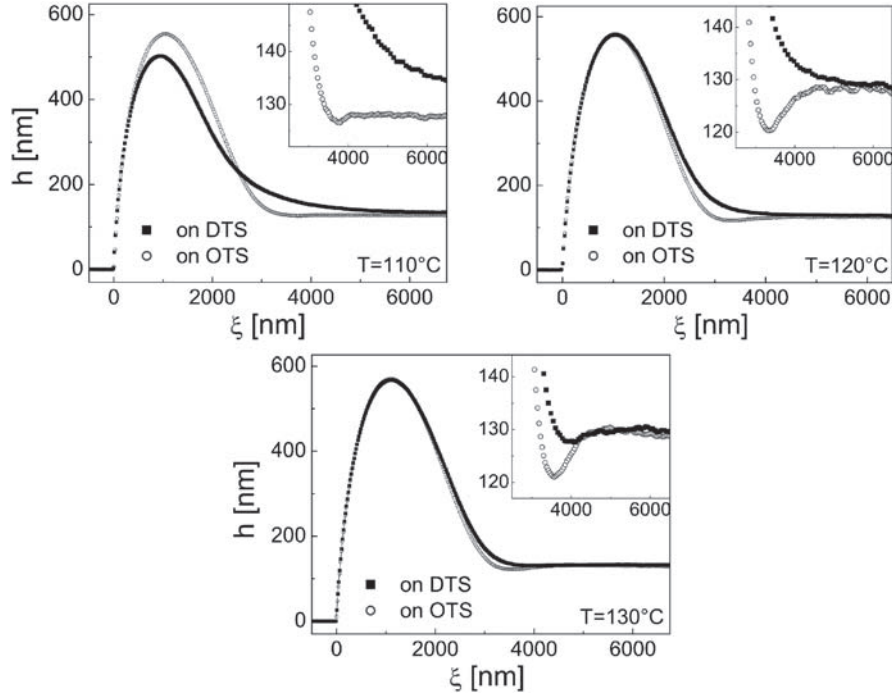


Fig. 4. Rim profiles on OTS and DTS at 110°C, 120°C and 130°C.

face. Starting point for this description are the Navier-Stokes equations in two dimensions for a viscous, incompressible Newtonian liquid:

$$-\nabla[p + \phi(h)] + \eta \nabla^2 \mathbf{u} = \rho(\partial_t \mathbf{u} + \mathbf{u} \cdot \nabla \mathbf{u}), \quad \nabla \cdot \mathbf{u} = 0, \quad (3)$$

with pressure p , disjoining pressure $\phi(h)$, viscosity η , density ρ and the velocity $\mathbf{u} = (u, w)$ of the liquid.

By applying the Navier slip boundary condition

$$b = \frac{u}{\partial_z u} \Big|_{z=0} = \frac{\eta}{\kappa}, \quad (4)$$

where η is the viscosity of the melt and κ the friction coefficient at the solid/liquid interface, and using a lubrication approximation (which assumes that the typical length scale on which variations occur is much larger in lateral direction than in vertical direction) we get the following equations of motion:

$$u = \frac{2b}{\eta} \partial_x (2\eta h \partial_x u) + \frac{bh}{\eta} \partial_x (\gamma \partial_x^2 h - \phi'(h)), \quad (5)$$

$$\partial_t h = -\partial_x (hu). \quad (6)$$

Here, the slip length b is assumed to be much larger than the average film thickness H (i.e., for $b/H \gg 1$). In order to perform a linear stability analysis

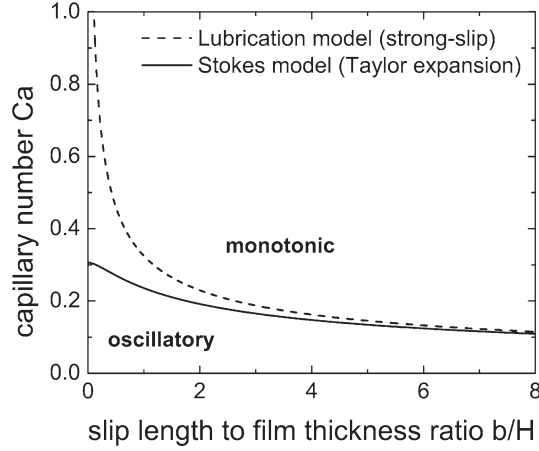


Fig. 5. Comparison of the theoretically expected transition from oscillatory profiles to monotonic ones for the strong-slip lubrication model (dashed line) and the third-order Taylor expanded Stokes model (solid line).

of the flat film of thickness H we introduce a small perturbation $\delta h \ll H$ traveling in the frame of the moving rim

$$h(x, t) = H + \delta h \exp(k\xi) \quad (7)$$

with

$$\xi = x - s(t) \quad (8)$$

where $s(t)$ is the position of the three-phase contact line. This ansatz leads to the characteristic polynomial of third order in k :

$$(Hk)^3 + 4Ca(Hk)^2 - Ca\frac{H}{b} = 0. \quad (9)$$

One of the three solutions for k is real and positive and therefore does not connect the solution to the undisturbed film for large ξ . Hence, this solution is not taken into account any further. The remaining two solutions k_1 and k_2 are either a pair of complex conjugate numbers with negative real part or two real numbers < 0 . These two different sets of solutions correspond to two different morphologies of the moving rim, i.e., either an oscillatory (k_1 and k_2 are complex conjugate) or a monotonically decaying (k_1 and k_2 are real) shape. These morphologies are separated by a distinct transition as indicated by the dashed line in Fig. 5. If both the capillary number Ca and the slip length b are given for a certain film thickness H , it is possible to qualitatively predict the shape of the rim. This is in good agreement with our experimental observations: On DTS we observe fast dewetting and expect large slip lengths, and we indeed observe mainly monotonically decaying rims; on OTS we find

slower dewetting and expect comparatively small slip lengths, and, again in agreement with the theoretical prediction, we observe oscillatory profiles.

Furthermore, if two solutions k_1 and k_2 are known (or extracted from experimentally obtained rim profiles), the characteristic polynomial can be solved for the unknown slip length b and the capillary number Ca . By that we obtain the solution for b and for Ca from the strong-slip lubrication model:

$$b_{lub} = \frac{1}{4H} \frac{k_1^2 + k_1 k_2 + k_2^2}{k_1^2 k_2^2}, \quad (10)$$

$$Ca_{lub} = -\frac{H}{4} \frac{k_1^2 + k_1 k_2 + k_2^2}{k_1 + k_2}. \quad (11)$$

Besides this strong slip model, further lubrication models have been developed [17, 21]. The corresponding weak slip (i.e., for $b/H < 1$) model always leads to complex solutions for k_1 and k_2 and therefore predicts only oscillatory rim shapes.

3.2 Stokes Model

As already mentioned, the former introduced lubrication model is just valid for large slip lengths compared to film thickness. To handle smaller slip lengths it is necessary to use a more recently developed model [17] which is a third-order Taylor expansion of the characteristic equation gained by linear stability analysis of a flat film using the full Stokes equations:

$$\left(1 + \frac{H}{3b}\right)(Hk)^3 + 4Ca\left(1 + \frac{H}{2b}\right)(Hk)^2 - Ca\frac{H}{b} = 0. \quad (12)$$

This equation again predicts a transition between oscillatory and monotonically decaying rims. In Fig. 5, the respective transition line (solid line) is compared to the one of the strong-slip lubrication model (dashed line). As expected, significant deviations between the two models occur for moderate and weak slippage, while good agreement is given for strong slippage. As shown in [17], the transition line for the Taylor expansion is, even for small slip lengths, quite close to the one predicted by the full Stokes equations. Solving (12) for b and Ca leads to additional contributions compared to the strong-slip lubrication model, (10) and (11):

$$b_{Taylor} = \frac{1}{4H} \frac{k_1^2 + k_1 k_2 + k_2^2}{k_1^2 k_2^2} - \frac{H}{2}, \quad (13)$$

$$Ca_{Taylor} = -\frac{H}{4} \frac{k_1^2 + k_1 k_2 + k_2^2}{k_1 + k_2} + \frac{H^3}{6} \frac{k_1^2 k_2^2}{k_1 + k_2}. \quad (14)$$

Note that the slip length obtained from the third-order Taylor expansion of the characteristic equation of the full Stokes model equals the slip length

obtained from the strong-slip lubrication model minus a shift of half of the film thickness.

We like to point out that, in contrast to previous publications [22, 23], all data sets presented in the following sections were evaluated by applying the third-order Taylor expanded Stokes model, i.e., (13) and (14). This enables us to exclude deviations that occur from the strong-slip lubrication model, which is not valid for smaller slip lengths.

3.3 Method to Extract Slip Length and Capillary Number

To fit the profile of a rim obtained by AFM we choose data points on the “wet” side of the rim ranging from about 110% of the film thickness to the film thickness itself (see Fig. 6). Oscillatory profiles are fitted by a damped oscillation as described by (15) with δh_0 , k_r , k_i and ϕ as fit parameters:

$$\delta h_{osci} = \delta h_0 \exp(k_r \xi) \cos(k_i \xi + \phi) \quad (15)$$

k_r is the real part and k_i the imaginary part of k_1 and k_2 :

$$k_{1,2} = k_r \pm ik_i. \quad (16)$$

In case of monotonically decaying rims we deal with a superposition of two exponential decays given by (17):

$$\delta h_{mono} = \delta h_1 \exp(k_1 \xi) + \delta h_2 \exp(k_2 \xi). \quad (17)$$

Here we obtain the amplitudes $\delta h_{1,2}$ and the decay lengths $k_{1,2}$ as fit parameters. In some cases, the fitting procedure may not be able to distinguish between two decaying exponentials, leading to two identical decay lengths. In

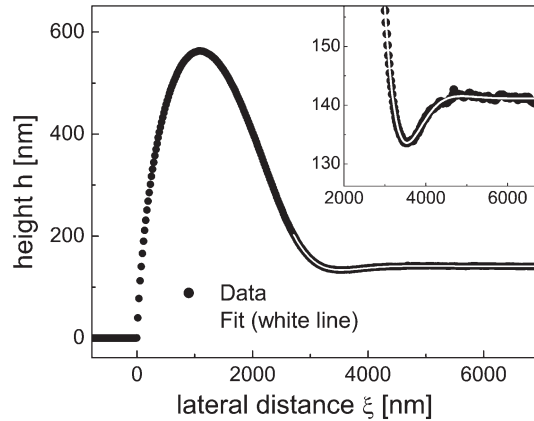


Fig. 6. AFM cross-section of a rim profile of a hole (about 12 μm radius) in a PS(13.7k) film on OTS dewetted at 120°C and corresponding fit.

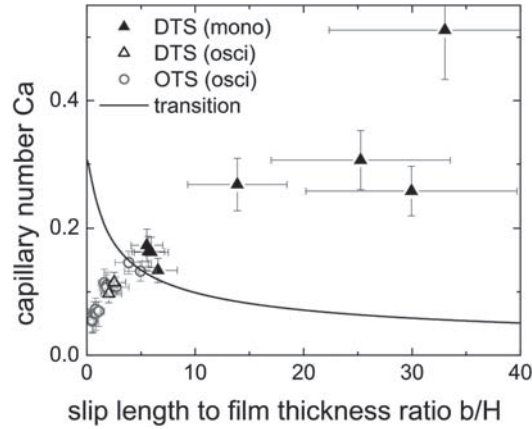


Fig. 7. Capillary number Ca versus the ratio of slip length b and film thickness H on OTS and DTS obtained from the third-order Taylor expanded Stokes model.

that case, an independent calculation of b and Ca is not possible. However, if the capillary number Ca is known (for example if the viscosity is known and the capillary number was calculated via (2)), one decay length is sufficient to extract the slip length.

From the parameters k_1 and k_2 gained by fitting the respective function (15) or (17) to the rim profiles, we determined slip lengths via (13) and capillary numbers via (14) for the PS films on our substrates at different temperatures, i.e., for different melt viscosities. As shown in Fig. 7, the capillary number clearly increases non-linearly with the slip length. In the transition region from oscillatory profiles to monotonic decaying rims, we have to deal with the fact that profiles with just one clear local minimum, but no local maximum in between the minimum and the undisturbed film, can be fitted by (17) as well as by (15). In the first case, this corresponds to one of the amplitudes $\delta h_{1,2}$ being negative. We emphasize that exclusively (15) leads to slip lengths that do not depend on the hole radius R , cf. the recent study [17]. This criterion enables us to justify the choice of (15) as the appropriate fitting function in this region.

3.4 Experimental Tests

The independent extraction of capillary number Ca and slip length b from the rim profiles allows us to check the consistency of the applied model. Comparing for instance the viscosities gained by rim shape analysis (via the calculated capillary numbers, the dewetting velocities \dot{s} from hole growth experiments and (2)) to independent viscosimetry measurements shows excellent agreement for both types of substrates, cf. Fig. 8.

Furthermore we evaluated certain rim shapes of the same hole but at different hole radii, cf. [23]. Although the rim grows in size during dewetting,

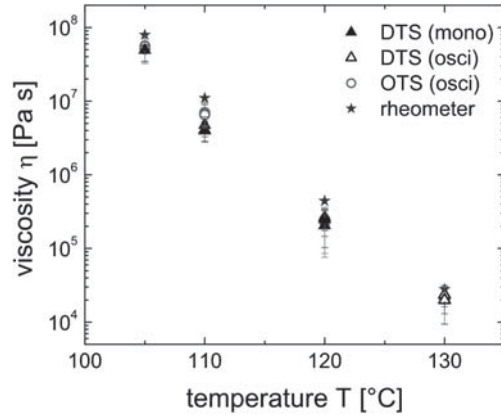


Fig. 8. Viscosities obtained from rim profile analysis and the third-order Taylor expanded Stokes model compared to viscosimetry data.

the extracted slip length stays constant within the range of our variation of rim size. The extracted capillary number, however, decreases for increasing hole radius. On the other hand, dewetting slows down with increasing rim size, cf. Fig. 2. The ratio of the measured dewetting velocities \dot{s} and the extracted capillary numbers gives viscosity data independent of the hole size, which again is in agreement with the expectation. To conclude, all these tests underline the applicability of the former introduced models to our system.

4 Results and Discussion

Analysis of rim shapes for different temperatures above the glass transition temperature gives slip lengths ranging from less than 100 nm up to about 5 microns.

As shown in Fig. 9, the slip length on DTS is about one order of magnitude larger than on OTS. On both substrates, the slip length decreases for higher temperatures. These results are in good agreement with slip lengths obtained by hole growth analysis studies [24]. Plotting the slip length versus melt viscosity, determined by rim analysis, shows non-linear behavior (see Fig. 10). This is at variance with the Navier slip condition (4), where a linear dependency of slip length on viscosity is expected. To evaluate this discrepancy, experiments were performed with polymer melts of different molecular weights below the entanglement length. The results are shown in Fig. 10. Variation of molecular weight of the melt gives data that fall on a master curve for each substrate. This means that friction has to be stronger for higher viscosities. This fact is possibly a valuable hint to the molecular mechanism of friction and slippage at the solid/liquid interface and will be further discussed in the following.

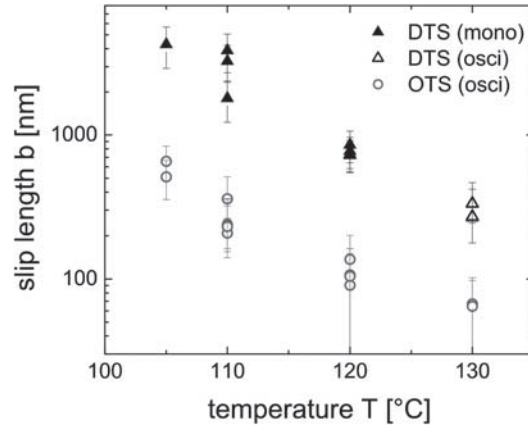


Fig. 9. Slip length b on OTS and DTS versus the dewetting temperature. Rim profile analysis was performed by applying the third-order Taylor expansion of the Stokes model on holes of 12 μm radius in a 130 nm PS(13.7k) film.

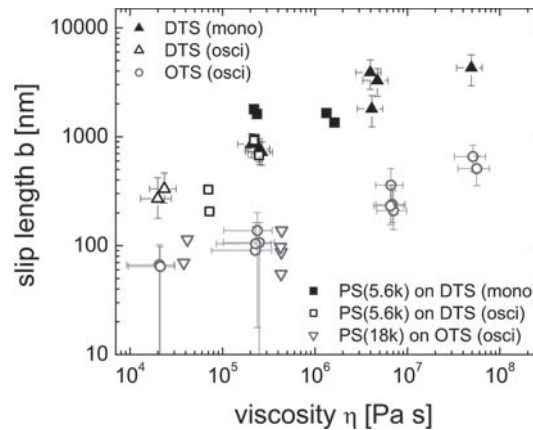


Fig. 10. Slip length data from Fig. 9 versus the respective film viscosity in logarithmic scale.

A scenario described in literature [25–27] for similar systems concerns melt chains penetrating between silane molecules and adhering to the underlying high-energy silicon substrate. This may lead to polymer chains slipping over grafted polymer chains of the same polymer. For this situation it is reported that flow is expected to be strongly dependent on shear rate and grafting density. The density of adhered chains is assumed to be dependent on the perfectness of the monolayer of the silane molecules. From the surface energies we obtained for OTS and DTS, we might expect OTS to build up a denser layer compared to DTS. Higher shear rates obtained for larger dewetting rates i.e. temperatures may lead to a dynamic desorption of adhered chains and, thus,

change friction at the interface. Molecular dynamics simulations of flowing polymer chains interacting with grafted chains of the same polymer by Pastorino et al. [28] have shown that interpenetration and subsequent anchoring as well as the grafting density influences slippage. They observe pronounced slippage for lower density of anchored chains.

Our further studies concerning the molecular mechanism of slippage focus on X-ray and neutron reflectivity experiments of (deuterated) polystyrene melts on Si substrates covered with self-assembled monolayers. These techniques are known to be very sensitive on changes at the solid/liquid interface. First X-ray reflectivity measurements on bare silanized wafers show that the silane molecules form very dense monolayers and stand upright on top of the underlying Si substrate [29]. Therefore, the previously discussed explanation of interdigitation does not seem to be very likely. Other explanations assuming structural changes of the substrate, such as bending or tilting of silane molecules, producing a temperature-dependent slip length also seem not to be a major issue in the temperature range of our experiments, though we can not absolutely exclude them. Further, roughness has been shown in miscellaneous studies to influence slippage [27, 30]. However, due to the fact that our surfaces are extremely smooth, cf. Sect. 2.1, the influence of roughness might be safely excluded. Other parameters such as the polarizability of the liquid have been shown to influence slippage dramatically. Cho et al. [31] observed lower slip length for higher polarizable liquid molecules. In addition, the shape of the liquid molecules can also be relevant for differences in slip lengths [5]. Using the same liquid, the latter two aspects can not be responsible for the different slip length on OTS and DTS.

The most probable scenario concerning the origin of the huge slip lengths is the formation of a so-called lubrication layer, i.e., a liquid layer of reduced viscosity close to the substrate, that may build up due to migration of low molecular-weight species to the solid/liquid interface or an alignment of liquid molecules at the interface. This slip plane could cause large apparent slip lengths. Systematic ellipsometry measurements on spots where a film front has passed the substrate and potentially left a remaining liquid layer, may corroborate this point of view. If lubrication layers are important, then polydispersity of the liquid should play a crucial role on slippage. Dewetting experiments dealing with mixtures or double-layers of polymers with different chain lengths are planned. At last, this argument cannot yet afford explaining the difference in slippage on OTS and DTS of about one order of magnitude. Nevertheless, we can speculate that the formation of this lubrication layer may depend on the interfacial energies of PS and silane brushes, $\gamma_{\text{PS/OTS}}$ and $\gamma_{\text{PS/DTS}}$, which are known to be slightly different, cf. Sect. 2.1.

5 Conclusion

We could show that slippage may strongly affect profiles of moving rims surrounding growing holes in thin liquid films. Furthermore, the connection of

fitting parameters concerning the shape of the rims and system parameters as slip length b and capillary number Ca via a theoretical model allows us to quantify slippage. We observe a slip length which is about one order of magnitude larger on DTS than on OTS and which decreases with increasing temperature. Moreover, we record experimentally a non-linear dependency of the viscosity on the slip length, which is at variance with the expectation due to the Navier-slip condition. Friction at the solid/liquid interface has to be enhanced for higher viscosity of the melt. From variation of the molecular weight we know that temperature can be assumed to be an indirect parameter in our system influencing slippage via the direct parameter viscosity. To conclude, we have presented a method to extract slip lengths from the analysis of rim profiles of dewetting polymer films. This method is a powerful tool to characterize slippage of dewetting liquid films. Further studies will focus on the variation of substrate and liquid properties. Viscoelastic properties of the liquid, i.e., high molecular-weight polymer chains above the entanglement length, may be topic of future research.

Acknowledgments

This work was financially supported by DFG grants JA 905/3 and MU 1626/5 within the priority program SPP 1164, the European Graduate School GRK 532 and the Graduate School 1276. We acknowledge the generous support of Si wafers from Siltronic AG, Burghausen, Germany.

References

1. Tretheway DC, Meinhart CD (2002) *Phys Fluids* 14:9–12
2. Tretheway DC, Meinhart CD (2004) *Phys Fluids* 16:1509–1515
3. Lumma D, Best A, Gansen A, Feuillebois F, Rädler JO, Vinogradova OI (2003) *Phys Rev E* 67:056313
4. Pit R, Hervet H, Léger L (2000) *Phys Rev Lett* 85:980–983
5. Schmatko T, Hervet H, Léger L (2005) *Phys Rev Lett* 94:244501
6. Craig VSJ, Neto C, Williams DRM (2001) *Phys Rev Lett* 87:054504
7. Vinogradova OI, Yakubov GE (2003) *Langmuir* 19:1227–1234
8. Cottin-Bizonne C, Jurine S, Baudry J, Crassous J, Restagno F, Charlaix E (2002) *Eur Phys J E* 9:47–53
9. Zhu Y, Granick S (2002) *Langmuir* 18:10058–10063
10. Neto C, Evans DR, Bonaccorso E, Butt H-J, Craig VSJ (2005) *Rep Prog Phys* 68:2859–2897
11. Lauga E, Brenner MP, Stone HA (2007) *Microfluidics: The no-slip boundary condition*. In: Tropea C, Yarin AL, Foss JF (eds) *Springer handbook of experimental fluid mechanics*. Springer, Berlin, Heidelberg, New York
12. Bocquet L, Barrat J-L (2007) *Soft Matter* 3:685–693
13. Ruckenstein E, Jain RK (1974) *J Chem Soc Faraday Trans II* 70:132–147

14. Seemann R, Herminghaus S, Jacobs K (2001) *Phys Rev Lett* 86:5534–5537
15. Reiter G (1992) *Phys Rev Lett* 68:75–78
16. Seemann R, Herminghaus S, Jacobs K (2001) *Phys Rev Lett* 87:196101
17. Fetzer R, Münch A, Wagner B, Rauscher M, Jacobs K (2007) *Langmuir* 23:10559–10566
18. Wasserman SR, Tao Y-T, Whitesides GM (1989) *Langmuir* 5:1074–1087
19. Good RJ, Girifalco LA (1960) *J Phys Chem* 64:561–565
20. Brochard-Wyart F, De Gennes P-G, Hervet H, Redon C (1994) *Langmuir* 10:1566–1572
21. Münch A, Wagner BA, Witelski TP (2005) *J Eng Math* 53:359–383
22. Fetzer R, Jacobs K, Münch A, Wagner B, Witelski TP (2005) *Phys Rev Lett* 95:127801
23. Fetzer R, Rauscher M, Münch A, Wagner BA, Jacobs K (2006) *Europhys Lett* 75:638–644
24. Fetzer R, Jacobs K (2007) *Langmuir* 23:11617–11622
25. Migler KB, Hervet H, Léger L (1993) *Phys Rev Lett* 70:287–290
26. Hervet H, Léger L (2003) *C R Phys* 4:241–249
27. Léger L (2003) *J Phys: Condens Matter* 15:S19–S29
28. Pastorino C, Binder K, Kreer T, Müller M (2006) *J Chem Phys* 124:064902
29. Magerl A (2007) Personal communication
30. Cottin-Bizonne C, Barrat J-L, Boquet L, Charlaix E (2003) *Nat Mater* 2:237–240
31. Cho JJ, Law BM, Rieutord F (2004) *Phys Rev Lett* 92:166102

Addendum V - Reduced Interfacial Entanglement Density Affects the Boundary Conditions of Polymer Flow

Physical Review Letters **103**, 247801 (2009).

Authors: O. BÄUMCHEN¹, R. FETZER², and K. JACOBS¹

¹ Department of Experimental Physics, Saarland University, D-66041 Saarbrücken, Germany.

² Present address: Ian Wark Research Institute, University of South Australia, Mawson Lakes, SA 5095, Australia.

Author contributions: K. Jacobs designed research. The experiments were performed by O. Bäumchen (except the rim profiles on OTS and DTS which were measured by R. Fetzer). Quantitative analysis was done by O. Bäumchen. The article was written by O. Bäumchen. Writing was supervised by R. Fetzer and K. Jacobs.

Abstract - Hydrodynamic boundary conditions play a crucial role in the flow dynamics of thin films and can be probed by the analysis of liquid front profiles. For long-chained polymer films it was reported that a deviation from a symmetric profile is a result of viscoelastic effects. In this Letter, however, evidence is given that merely a slip-boundary condition at the solid-liquid interface can lead to an asymmetric profile. Variation of molecular weight shows that slippage is directly linked to chain entanglements. We find a reduced entanglement density at the solid-liquid interface (factors 3 to 4), which stresses the importance of considering nonbulk polymer properties in the vicinity of an interface.

Reduced Interfacial Entanglement Density Affects the Boundary Conditions of Polymer Flow

O. Bäumchen, R. Fetzer,^{*} and K. Jacobs[†]

Department of Experimental Physics, Saarland University, D-66041 Saarbrücken, Germany.

(Received 10 July 2009; published 8 December 2009)

Hydrodynamic boundary conditions play a crucial role in the flow dynamics of thin films and can be probed by the analysis of liquid front profiles. For long-chained polymer films it was reported that a deviation from a symmetric profile is a result of viscoelastic effects. In this Letter, however, evidence is given that merely a slip-boundary condition at the solid-liquid interface can lead to an asymmetric profile. Variation of molecular weight shows that slippage is directly linked to chain entanglements. We find a reduced entanglement density at the solid-liquid interface (factors 3 to 4), which stresses the importance of considering nonbulk polymer properties in the vicinity of an interface.

DOI: [10.1103/PhysRevLett.103.247801](https://doi.org/10.1103/PhysRevLett.103.247801)

PACS numbers: 68.15.+e, 47.61.-k, 83.50.Lh, 83.80.Sg

The controlled manipulation of small liquid volumes is one of the main tasks in the field of micro- and nanofluidics. In this context, the role of hydrodynamic slippage has attracted much attention due to its enormous relevance for applications such as lab-on-chip devices. A variety of experimental methods exist to characterize slippage. The large number of techniques and results is summarized and discussed in recent review articles [1–3].

If a thin liquid film on top of a solid substrate can gain energy by minimizing its interfacial area, the film ruptures and holes occur (see [4,5], and references therein). These dry circular patches grow with time, and the removed liquid accumulates in a rim surrounding the holes along their perimeter. Dewetting of thin liquid films on solid substrates is a result of internal capillary forces, which can be inferred from the effective interface potential [6,7]. Viscous dissipation within the liquid, which mainly occurs at the three-phase contact line [8], and friction at the solid-liquid interface (slippage) counteract these driving forces. Concerning the characteristic dynamics of hole growth (hole radius R versus time t), Brochard-Wyart and colleagues [8] proposed a sequence of different stages starting with the birth of a hole, which is characterized by an exponential increase of the dewetting velocity. It is followed by a regime that is governed by the formation of the rim and dominated by viscous flow ($R \propto t$), followed by a stage of a “mature” rim, where surface tension rounds the rim and slippage might be involved. In case of full slippage, a growth law $R \propto t^{2/3}$ is expected. This view was supplemented by an experimental study by Damman and colleagues, who associated different dewetting regimes with corresponding rim shapes in case of viscoelastic fluids [9]. Vilmin *et al.* presented a theoretical approach taking viscoelastic properties and slippage into account [10]. In our earlier studies, we examined rim profiles of dewetting long-chained PS films on hydrophobized Si wafers and attributed the transition from symmetric to increasingly asymmetric shapes with the molecular weight of the polymer to viscoelastic effects [11]. These results go along with

a phenomenological model that predicts a phase diagram for rim morphologies [12].

These previous studies, however, lack one facet, which by now has been identified as one of the major issues influencing dewetting dynamics and profiles: hydrodynamic slippage [13–15]. In this Letter, we study the very nature of slippage in a molecular weight regime where chain entanglements can make an impact on the solid-liquid interface friction. Entanglements, however, might involve new challenges related to non-Newtonian behavior due to viscoelastic flow and stress relaxation. The latter has been reported to cause polymer thin film rupture [16,17] and to impact the early stage of dewetting [17]. As will be shown in the following for the mature stage, residual stress and viscoelastic properties have no impact on the shape of dewetting rims, if low shear rates are involved. It will be demonstrated that in that stage, asymmetric rim profiles are caused by slippage only.

Films of atactic polystyrene (PSS Mainz, Germany) with molecular weights ranging from 5.61 to 390 kg/mol [termed, e.g., PS(390k)] and low polydispersity ($M_w/M_n = 1.02$ – 1.09) were spin cast from toluene solutions on freshly cleaved mica sheets and transferred to smooth hydrophobized Si wafers with a native oxide layer (obtained from Siltronic, Burghausen, Germany) by floating them on a MilliporeTM water surface. To avoid residual stresses in films above the entanglement length of PS, the films were preannealed on the mica substrate well above their glass transition temperature (up to 3 h at 140 °C) [16]. The prepared film thicknesses h_0 varied between 100 and 140 nm. Hydrophobization was either achieved through standard silanization techniques [18] using self-assembled monolayers of octadecyltrichlorosilane (OTS) and dodecyltrichlorosilane (DTS) or by preparing a thin amorphous Teflon layer (AF 1600) using the spin coating technique. The thickness d and the root-mean-square (rms) roughness of the hydrophobic layers (see Table I) were measured via ellipsometry (EP³, Nanofilm, Göttingen, Germany) and atomic force microscopy (AFM, Multimode, Veeco

TABLE I. Substrate properties.

Layer	d (nm)	rms (nm)	θ_{adv} ($^\circ$)	$\Delta\theta$ ($^\circ$)	γ_{sv} (mN/m)
AF 1600	21(1)	0.30(3)	128(2)	10	15.0
OTS	2.3(2)	0.09(1)	116(1)	6	23.9
DTS	1.5(2)	0.13(2)	114(1)	5	26.4

Instruments, Santa Barbara, CA, USA). Additionally, substrates are characterized in terms of their wetting properties by their contact angles (advancing θ_{adv} , and contact angle hysteresis $\Delta\theta$) of MilliporeTM water and their surface energy γ_{sv} (via measuring the contact angles of apolar liquids).

Nucleation and subsequent growth of holes starts after heating the samples above the glass transition temperature of the PS melt. In the following, optical microscopy is utilized to dynamically monitor the size of growing holes. At a certain hole radius (about 12 μm) in the mature regime, the experiment is stopped by quenching the sample to room temperature. The profile of the rim is then imaged by AFM [19]. As shown in Fig. 1(a), comparing rim profiles of PS films for the same molecular weight, film thickness and viscosity [approximately 120 nm thick PS(65k) at 130 $^\circ\text{C}$] clearly exhibits strong differences that can exclusively be ascribed to the different substrates: Close to the three-phase contact line of the liquid, i.e., on the “dry side” of the rim (at $\xi = 0$), the rim shape is dominated by the receding contact angle of the liquid. On the “wet” side of the rim, however, where the profile connects to the undisturbed thin film, the rim shapes on the three different substrates deviate significantly: AF1600 exhibits the steepest and DTS the most shallow decline. Looking closely, on AF1600 [cf. inset of Fig. 1(a)], a “trough” can be observed (termed “oscillatory” profile), while in case of OTS and DTS rims are found to decay monotonically into the unperturbed polymer film. In Fig. 1(b), experimental profiles are shown for the AF 1600 substrate, where the molecular weight of the polymer melt is varied. In case of PS(65k), an oscillatory

profile is observed, whereas for, e.g., PS(186k) or higher molecular weights, monotonic rim morphologies are recorded. Hence, an increase in M_w on the identical substrate provokes the same morphological differences in rim shapes as before [Fig. 1(a)] the variation of the substrate. To probe whether or not the effect is merely a result of the melt viscosity, the dewetting temperature on AF 1600 (see Table II) was additionally varied. Yet, no systematic influence of the viscosity on the rim profiles is found for this substrate, as exemplarily shown for PS(186k) in the inset of Fig. 1(b). The observed marginal differences of the rim profiles can be related to small variations of accumulated material (via slightly different hole radii and film thickness in different experiments).

Summarizing the qualitative observations, we find that an increase in molecular weight strongly amplifies the asymmetry of the profiles in the same manner as a change of substrate is capable of causing. According to our previous studies on OTS and DTS concerning nonentangled PS melts, asymmetric rims are related to slippage [13–15]. For DTS, slip lengths b of up to 5 μm were obtained, for OTS, values are about 1 order of magnitude smaller. The question now arises as to the manner in which slippage correlates to the molecular weight and the number of entanglements in the AF 1600 system. To quantify slippage there, rim profiles will be analyzed.

As shown recently, lubrication models for Newtonian flow and different slip conditions (no-slip, weak-slip, intermediate-slip, and strong-slip [21]) and a more generalized model based on the full Stokes equations [14] can be applied to thin dewetting films with the important result that values for the slip length b can be obtained.

The theoretical description of the model for Newtonian liquids presented in [14] is derived from the full Stokes equations in two dimensions for a viscous, incompressible liquid including the Navier slip-boundary condition $b = u_x / \partial_z u_x|_{z=0}$, where u_x denotes the velocity in the direction of dewetting (x direction) and z the vertical scale with the substrate at $z = 0$. This leads to the equations of motion for a flat liquid film. Then, a linear stability analysis is applied

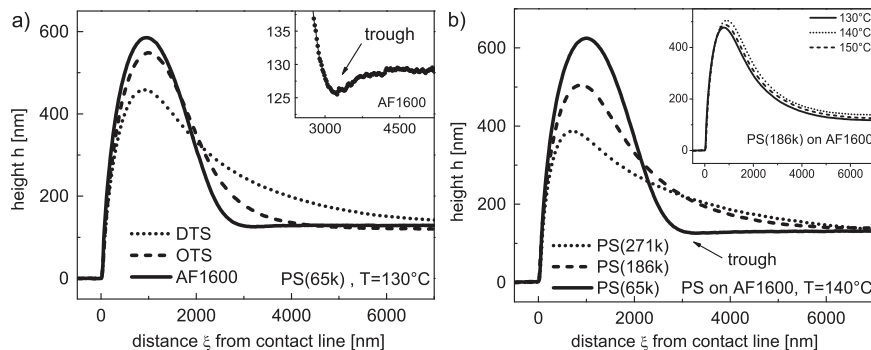


FIG. 1. (a) Rim profiles of PS(65k) on DTS (dotted), OTS (dashed), and AF 1600 (solid line) at 130 $^\circ\text{C}$. The inset illustrates the oscillatory behavior on AF 1600. (b) Rim shapes on AF 1600 for different molecular weights [140 $^\circ\text{C}$, PS(65k), PS(186k), PS(271k)]. Inset: Variation of viscosity via different temperatures for the same molecular weight (see Table II) shows insignificant influence on rim profiles.

TABLE II. Comparison of viscosities (obtained from the Williams-Landel-Ferry equation [20]), calculated relaxation times τ and measured rim widths w (on AF 1600) given for a selection (see Fig. 1) of dewetting temperatures T and molecular weights M_w .

M_w	T ($^{\circ}\text{C}$)	η (Pa s)	τ (s)	w (μm)
65k	130	1.3×10^6	6.5	2.73
65k	140	1.6×10^5	0.8	2.81
186k	130	4.4×10^7	222	5.02
186k	140	5.6×10^6	28.1	4.86
186k	150	1.1×10^6	5.4	5.29
271k	140	2.0×10^7	100.5	7.47

by introducing a small perturbation $\delta h = h(x, t) - h_0$ and velocity $u_x(x, t)$ to the undisturbed state $h = h_0$ and $u_x = 0$. In the comoving frame $\xi = x - s(t)$, where $s(t)$ is the position of the rim, a quasistationary profile evolves. Solving the linear equation using the normal modes ansatz $\delta h = \delta h_0 \exp(k\xi)$ and $u_x = u_{x,0} \exp(k\xi)$ gives a characteristic equation for k which is expanded up to third order according to the Taylor series expansion:

$$\left(1 + \frac{h_0}{3b}\right)(h_0 k)^3 + 4\text{Ca}\left(1 + \frac{h_0}{2b}\right)(h_0 k)^2 - \text{Ca}\frac{h_0}{b} = 0, \quad (1)$$

where Ca denotes the capillary number given by $\text{Ca} = \eta\dot{s}/\gamma_{lv}$. Hence, rim profiles depend on the capillary number Ca and the ratio of slip length b to film thickness h_0 . Equation (1) implies that a morphological transition from oscillatory (complex conjugate solutions for k) to monotonically (real k values) decaying rim shapes occurs if $\text{Ca}^2 > (3^3(b/h_0 + 1/3)^2)/(4^4(b/h_0 + 1/2)^3)$ on slippery substrates (large b/h_0) and for large capillary numbers Ca [14,15]. Furthermore, Eq. (1) predicts progressively asymmetric rims for increasing values of b/h_0 .

To assess whether these models might be used to analyze the experimental data, the impact of viscoelasticity on fluid flow needs to be estimated: The Weissenberg number $\text{Wi} = \tau\dot{\gamma}$ relates the time scale of stress relaxation τ with the time scale of applied shear $\dot{\gamma}$. Relaxation times are determined from the corresponding viscosities η and the shear modulus $G \approx 0.2$ MPa (for PS, [22]) via $\tau = \eta/G$ (see Table II). In order to evaluate the shear rate, it is necessary to estimate the dominating shear component, which in our case is the x direction, since $u_x \gg u_z$ applies to the velocity field (u_x, u_z) within the rim. Furthermore, we approximate u_x by \dot{s} , which is experimentally accessible by measuring the hole growth. An upper estimate for $\dot{\gamma}$ is given by $\dot{\gamma} = \max(\partial_x u_x, \partial_z u_x) \approx \max(\dot{s}/\Delta x, \dot{s}/\Delta z)$. Hereby, the lateral displacement Δx can be taken as the width w of the rim; w is defined as the distance between the three-phase contact line and the position at the wet side of the rim where the rim height has dropped to 110% of the prepared film thickness h_0 , i.e., $h(w) = 1.1h_0$. The vertical displacement Δz is given by $\Delta z = h_0 + b$, where b denotes the slip length as determined by the quantitative rim

analysis described in the last part of this Letter. The described estimation leads to values for Wi between 0.01 and 0.1 (on AF 1600) and 0.5 (on OTS/DTS). An influence of viscoelastic effects on flow dynamics is expected for Weissenberg numbers of 1 and larger. In that case, a model including viscoelasticity has to be used [23]. Low shear rates as described above and the preannealing step after spin coating allow us to safely exclude viscoelastic effects as the source of different rim morphologies. This consideration justifies the assumption of Newtonian flow, on which the following data analysis for PS melt films on the AF 1600 substrate is based.

Rim profiles are evaluated by fitting the wet side of the rim with a damped oscillation [oscillatory profiles, up to PS(81k)] or a simple exponential decay [monotonic rims, for PS(101k) and above]. In the case of an exponential decay, a single value for k is gained from the experimental data. Knowing the film thickness h_0 and the capillary number Ca (from independent rim velocity data), this k value allows us to calculate the respective slip length via Eq. (1). For oscillatory profiles, k is a pair of complex conjugate numbers. From these two independent solutions, both the capillary number and the slip length can be extracted via Eq. (1) at the same time. Viscosity data calculated from these Ca values showed excellent agreement with theoretical values (from the Williams-Landel-Ferry equation [20]) and demonstrate the consistency of the applied model. For further details concerning the fitting procedure and data evaluation we refer to previous publications [13–15].

The slip lengths b of a set of experiments, i.e., different dewetting temperatures and viscosities, are shown in Fig. 2 as a function of molecular weight M_w of the PS melt. Two distinct regimes can clearly be seen: constant slip lengths in the order of 10 to 100 nm at small M_w and slip lengths that increase with the power of 2.9(2) in case of larger M_w . The transition between both regimes occurs at 37 kg/mol, which is consistent with the critical value M_c of entanglement effects ($M_c = 35$ kg/mol for PS according to [22]). For the same viscosity (e.g., 2×10^6 Pa s) in case of, e.g., PS(51.5k) and PS(271k), an enormous difference in slippage of 2 orders of magnitude solely due to the difference in chain length is obtained. We therefore state that slippage is directly related to entanglements rather than viscosity. Besides the fact that an influence of the melt viscosity (via temperature variation) for a certain molecular weight could not be detected, even experiments omitting the preannealing step after preparation on mica do not show significant impact. Additionally, we want to emphasize that careful analysis of the dewetting velocity data from hole growth dynamics (of the identical samples), according to the model presented in [24], confirmed the $b(M_w)$ behavior obtained from rim analysis [25].

For long polymer chains, described by the reptation model, de Gennes predicts a scaling of $b \propto N^3$ [26], where N denotes the number of monomers, which corroborates the experimental exponent of 2.9(2) for experiments with

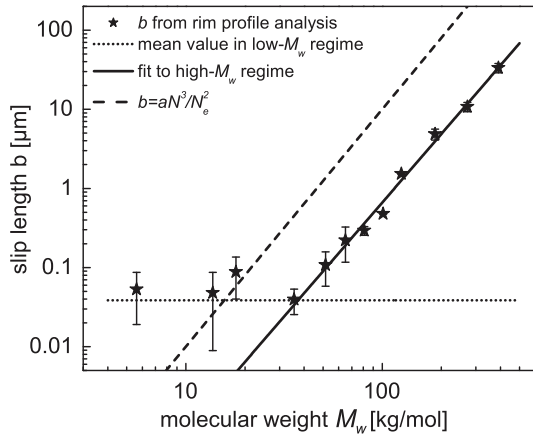


FIG. 2. Slip lengths of PS films on AF 1600 obtained from rim profile analysis. Each data point represents the average value of different measurements (2–3 measurements for each M_w value above 35.6k and 5 or more below). The solid line represents a fit to the experimental data from PS(35.6k) to PS(390k), the dashed line visualizes $b = aN^3/N_e^2$ using values for a and N_e given in the literature [22]. The dotted line represents the average of slip lengths for melts from PS(5.61k) to PS(18k).

$M_w > 35$ kg/mol as depicted in Fig. 2. According to the model [26], $b = aN^3/N_e^2$, where N_e is the bulk entanglement length (number of monomers in an entanglement strand) and a a polymer specific molecular size, and is plotted in Fig. 2 as the dashed line for the literature values of $N_e = 163$ [22] and $a = 3 \text{ \AA}$ [27] for PS. From the linear fit to our experimental data (solid line in Fig. 2), we obtain $a/N_e^2 = 1.12(7) \times 10^{-5} \text{ \AA}$, which is 1 order of magnitude smaller than expected by using the literature values given above. Keeping a from the literature, a significantly larger entanglement length of $N_e = 517$ results from the linear fit. This is an indication for a significantly lowered effective entanglement density in the vicinity of the substrate compared to the bulk and is in line with recent studies of thin polymer films [28–30]. According to Brown and Russell, N_e of a polymer melt near an interface is expected to be about 4 times that in the bulk [31], which corroborates our experimental results.

To conclude, entanglements can strongly amplify slippage as deduced from dewetting experiments. Assigning asymmetric profiles exclusively to non-Newtonian effects such as viscoelasticity therefore turns out to be invalid. On the contrary, the hydrodynamic boundary condition, i.e., slippage, can dramatically provoke morphological changes in rim shape such as transitions from oscillatory to monotonic profiles. The onset of slippage correlates to the critical chain length for entanglements. The dependence of the slip length on molecular weight corroborates the description by de Gennes. Conversely, to derive slip lengths solely from de Gennes' theory entails that bulk values for a and N_e (from literature) have to be used that might not appropriately describe polymer melts next to an interface. The method described here, however, represents

a powerful tool to gain experimentally access to liquid flow properties at the solid-liquid interface and to quantify slip lengths.

We gratefully acknowledge financial support from German Science Foundation DFG under Grant No. Ja 905/3 within the priority program 1164 and support of Si wafers by Wacker Siltronic AG, Burghausen, Germany.

*Present address: Ian Wark Research Institute, University of South Australia, Mawson Lakes, SA 5095, Australia.

†k.jacobs@physik.uni-saarland.de

- [1] C. Neto *et al.*, Rep. Prog. Phys. **68**, 2859 (2005).
- [2] E. Lauga *et al.*, in *Springer Handbook of Experimental Fluid Mechanics*, edited by C. Tropea, A.L. Yarin, and J.F. Foss (Springer, Berlin, Heidelberg, New York, 2007).
- [3] L. Bocquet and J.-L. Barrat, Soft Matter **3**, 685 (2007).
- [4] G. Reiter, Phys. Rev. Lett. **68**, 75 (1992).
- [5] K. Jacobs, R. Seemann, and S. Herminghaus, in *Polymer Thin Films*, edited by O.K.C. Tsui and T.P. Russell (World Scientific, New Jersey, London, Singapore, 2008).
- [6] A. Vrij, Discuss. Faraday Soc. **42**, 23 (1966).
- [7] R. Seemann, S. Herminghaus, and K. Jacobs, Phys. Rev. Lett. **86**, 5534 (2001).
- [8] F. Brochard-Wyart *et al.*, Langmuir **10**, 1566 (1994).
- [9] P. Damman, N. Baudalet, and G. Reiter, Phys. Rev. Lett. **91**, 216101 (2003).
- [10] T. Vilmin *et al.*, Europhys. Lett. **72**, 781 (2005).
- [11] R. Seemann, S. Herminghaus, and K. Jacobs, Phys. Rev. Lett. **87**, 196101 (2001).
- [12] S. Herminghaus, R. Seemann, and K. Jacobs, Phys. Rev. Lett. **89**, 056101 (2002); Eur. Phys. J. E **12**, 101 (2003).
- [13] R. Fetzer *et al.*, Phys. Rev. Lett. **95**, 127801 (2005); Europhys. Lett. **75**, 638 (2006).
- [14] R. Fetzer *et al.*, Langmuir **23**, 10559 (2007).
- [15] O. Bäümchen *et al.*, in *Proceedings of the IUTAM Symposium on Advances in Micro- and Nanofluidics*, edited by M. Ellero, X. Hu, J. Fröhlich, and N. Adams (Springer, New York, 2009).
- [16] D. Podzimek *et al.*, arXiv:cond-mat/0105065v1.
- [17] G. Reiter *et al.*, Nature Mater. **4**, 754 (2005).
- [18] S.R. Wassermann *et al.*, Langmuir **5**, 1074 (1989).
- [19] Quenching the sample to room temperature does not influence the shape of the rim profile, c.f. [13].
- [20] M.L. Williams *et al.*, J. Am. Chem. Soc. **77**, 3701 (1955).
- [21] A. Münch *et al.*, J. Eng. Math. **53**, 359 (2005).
- [22] M. Rubinstein and R. Colby, *Polymer Physics* (Oxford University Press, Inc., New York, 2003).
- [23] R. Blossey *et al.*, Eur. Phys. J. E **20**, 267 (2006).
- [24] R. Fetzer and K. Jacobs, Langmuir **23**, 11617 (2007).
- [25] O. Bäümchen and K. Jacobs (to be published).
- [26] P.-G. de Gennes, C.R. Seances Acad. Sci., Ser. B **288**, 219 (1979).
- [27] C. Redon *et al.*, Macromolecules **27**, 468 (1994).
- [28] L. Si *et al.*, Phys. Rev. Lett. **94**, 127801 (2005).
- [29] D.R. Barbero and U. Steiner, Phys. Rev. Lett. **102**, 248303 (2009).
- [30] H.D. Rowland *et al.*, Science **322**, 720 (2008).
- [31] H.R. Brown and T.P. Russell, Macromolecules **29**, 798 (1996).

6 Continuative Experimental Studies

In the previous chapters it was shown that the slip length strongly increases as soon as polymer chain entanglements become relevant for the dynamics of thin polymer films. In case of AF 1600 substrates, the entanglement density has shown to be reduced by a factor 3 to 4 in the vicinity of the solid/liquid interface. Consequently, the slip length is reduced by approximately one order of magnitude, as obtained by the analysis of rim profiles, compared to bulk values. This chapter contains additional experiments with the goal to gain more information concerning the link between slippage and the properties of the polymer itself. Up to this point, PS melts with a nearly monodisperse chain length distribution were utilized. In the first part of this chapter, the role of the polydispersity of the polymer melt is investigated by dewetting experiments with mixtures of PS melts of two distinct chain lengths. The second part deals with first results originating from dewetting experiments of a different polymer species, namely poly(methyl methacrylate) (PMMA). The experiments presented in this chapter can be considered as cutting-edge investigations that might be continued and expanded in further studies.

6.1 Impact of Polydispersity - Chain Length Specific Polymer Mixtures

With regard to the experimental results described in the previous chapters, the interesting question now arises to what extent the addition of a significant amount of short polymer chains influences the flow dynamics: Will these chains migrate towards an interface and influence the boundary condition?

Neutron scattering studies (in collaboration with the groups of Prof. Dr. Andreas Magerl and Prof. Dr. Hartmut Zabel) of thin films of polymer mixtures on bare silicon wafers with a native oxide layer were launched to investigate the first part of this question. The second part, i.e. the question whether the slip length is affected by the addition of short chains, is studied by complementary dewetting experiments.

First Neutron Scattering Studies Polymer mixtures of two distinct chain lengths were prepared as a thin homogeneous PS films on bare silicon wafers, subsequently annealed and were studied with neutron scattering techniques¹: Mixtures of 80% hydrogenated long-chained polystyrene PS(51.5k) and short-chained 20% deuterated d-PS(2.32k) showed a significant modification of the scattering length density at the polymer/air interface of the film [77]. To

¹Prepared film thickness: approx. 50 nm. Samples were annealed for 15 minutes at 120 °C. See section 3.2 for further preparative details.

Table 6.1: Slip lengths b on AF 1600: Comparison between a pure PS(51.5k) film and a film consisting of mixture of 80% PS(51.5k) and 20% d-PS(2.32k). T : dewetting temperature, H : the maximum rim height of the hole, h_0 : film thickness.

M_w	T	H	h_0	b
PS(51.5k)	140 °C	~ 500 nm	100 nm	60(46) nm
80% PS(51.5k) + 20% PS(2.32k)	115 °C	~ 400 nm	88 nm	51(22) nm
80% PS(51.5k) + 20% PS(2.32k)	140 °C	~ 600 nm	87 nm	81(32) nm

probe whether this is due to a de-mixing effect according to the slight difference in surface tension of deuterated and hydrogenated PS (as reported e.g. in [80]), the complementary mixture (80% d-PS(60.7k) and 20% PS(1.97k)) was prepared and investigated. However, the results for this system also suggest a migration of the short-chained species towards the liquid/air interface [77]. In both experimental conditions, a migration of short chains towards at the solid/polymer interface could not be probed.

First Dewetting Experiments According to the neutron scattering results discussed in the previous paragraph, pre-annealing on a hydrophilic support and subsequent transfer of the polymer film to the hydrophobic substrate (which includes flipping of the film) would lead to an accumulation of short polymer chains at the solid/liquid interface. To determine the slip length, rim profiles of holes in thin films of mixtures of 80% hydrogenated long-chained polystyrene PS(51.5k) and 20% short-chained deuterated d-PS(2.32k) were evaluated (see Chapter 5). Samples were pre-annealed for 3 hours at 140 °C (on mica under ambient conditions) prior to dewetting from AF 1600 substrates. For the first sample dewetting was induced at 140 °C : The rim profile of a hole (maximum rim height of approx. 600 nm, film thickness: 87 nm) exhibited a clear trough on the wet side of the rim and was, thus, fitted with a damped oscillation. The corresponding slip length b obtained from the Taylor-expanded Stokes model was 81 nm. A second polymer film dewetted at 115 °C: In this case, the rim profile analysis of a hole (maximum rim height of approx. 400 nm, film thickness: 88 nm) gave $b = 51$ nm. In Tab. 6.1, these results are summarized and compared to a corresponding monodisperse PS film.

Conclusion To conclude first neutron scattering studies after annealing of polymer films on bare Si wafers indicate that short polymer species in a mixture of long and short chains migrate towards the liquid/air interface. Consequently, flipping the polymer film after annealing on the hydrophilic support should lead to an accumulation of short chains at the solid/liquid interface after transferring the film to the hydrophobic substrate. Reviewing the aforementioned results from dewetting experiments on AF 1600, it can be concluded that the presence of short polymer chains did not lead to a significant modification of slippage. However, it is not clear yet whether the annealing on the hydrophobic substrate while dewetting again modifies the distribution of short chains.

Table 6.2: Summary of results from dewetting experiments of PMMA(14k) on AF 1600, OTS and DTS substrates.

Substrate	Slip length b	Capillary number Ca	film thickness h_0
AF 1600	74(47) nm	0.08(3)	101 nm
OTS	139(52) nm	0.09(2)	104 nm
DTS	218(66) nm	0.08(2)	105 nm

Further systematic dewetting experiments are necessary to gain more information about polymer mixtures in dewetting situations. Utilizing a long chain component with even larger molecular weights might give new insights towards the interaction of a certain amount of short chains with longer chains at the solid/liquid interface in view of slippage.

6.2 Dewetting Experiments of PMMA Melts

Most experiments probing the dewetting of thin polymer films were performed with polystyrene (PS, e.g. [39]). The reason for this is that PS is an excellent model liquid as it can be fabricated in a very pure and nearly monodisperse manner and it moreover does not uptake water [45]. To judge whether the analytical methods, as described in this study, can also be applied to further polymeric liquids, a "proof-of-concept" experiment was performed: Thin poly(methyl methacrylate) (PMMA) films were used for dewetting studies on AF 1600, OTS and DTS substrates. PMMA(14k) films were prepared by spin-coating a PMMA/toluene solution analogous to the preparation of PS films². PMMA has a low polydispersity ($M_w/M_n = 1.03$) and was also purchased from PSS (Mainz, Germany). Film thicknesses of approx. 100 nm were prepared by spin-coating (at 2500 rpm) the polymer solution on a mica substrate and by subsequently "floating" the films onto the hydrophobic substrates.

Dewetting experiments were performed at 150 °C. Hole growth was recorded with optical microscopy and stopped at approx. 12 μm hole radius by quenching the sample to room temperature. Then, the rim of the hole was imaged by AFM and profiles were analyzed according to the thin film model (third-order Taylor expansion of the full Stokes model, see ADDENDUM IV). The profiles exhibited in the case of all substrates (AF 1600, OTS and DTS) "oscillatory decays" with a trough on the wet side of the rim. Results are summarized in Tab. 6.2: The slip length follows the same trend as compared to PS(13.7k) films: The largest slip length is found on DTS. The results corroborate the observation that dewetting was faster on DTS as compared to OTS. Slowest dewetting and the smallest slip length was recorded on the AF 1600 substrate.

Conclusion To conclude, the dewetting experiments presented in this section show that the analysis of liquid rim profiles is also applicable to further polymers such as PMMA. Qualitatively, the slip lengths follow the same trend as in the case of PS melts of similar molecular

²See section 3.2 for further preparative details.

weight. Quantitatively, the slip length on AF 1600 is in good agreement with the results obtained for PS. In case of OTS and DTS, a series of experiments for different dewetting temperatures and PMMA melt viscosities is necessary to give a quantitative comparison to the corresponding (temperature-dependent) slip lengths for PS.

Systematic variation of molecular weight and dewetting temperature of PMMA melts on DTS, OTS and AF 1600 substrates might provide further insights towards the molecular mechanism of slippage on silanized surfaces and the role of chain entanglements at the solid/liquid interface. Obtaining a general and unified picture of polymer flows and conformations in the vicinity of the solid/liquid interface is of enormous fundamental and practical interest.

7 Summary and Outlook

The challenge of explaining facets such as sliding friction and the fluid dynamics of polymers at the solid/liquid interface on the molecular level is a main task in the field of micro- and nanofluidics. The aim of this thesis was the characterization of the flow dynamics of thin polymer films in view of the hydrodynamic boundary condition at the solid/liquid interface.

Dewetting experiments are a powerful tool to study the mechanisms of friction and the rheological properties of polymers. Variation of the substrate showed enormous influence on the flow properties for the identical viscosity and chain length of the polymer molecules. The role of entanglements of polymer chains and the link between slippage and entanglements was of special interest. A new type of substrate for polymer dewetting experiments was introduced, AF 1600, and turned out to be perfectly suited.

The results presented in this thesis are of extraordinary importance in view of the rheological and sliding properties of polymers concerning a series of applications such as e.g. polymer extruders or, in general, microfluidic devices. One should bear in mind that the mean velocity of a pressure drop flow in a cylindrical channel is increased by a factor $1 + 8b/h$ as compared to the classical no-slip boundary condition, where b is the slip length and h the thickness of the channel [81]. Thus, the permeability of channels and also of porous media is highly increased by slippage. An increase in the slip length for longer polymer chains by two orders of magnitude, as presented in this study, would also impact the mean velocity in sub-micron channels by orders of magnitude. A further aspect applies to the hydrodynamic dispersion of molecules or particles transported in such a channel which is quantified by the velocity difference in the middle and at the walls of the channel. Slippage reduces this velocity difference; its impact is again given by the ratio b/h [81]. Gaining control on the sliding properties of fluids, as described in this thesis for polymer melts, by tailoring the substrate properties or the characteristics of the fluid (e.g. the chain length in the case of polymers) is of major benefit for micro- and nanofluidics.

7.1 Summary

Analysis of the Hole Growth Dynamics

Analyzing the hole growth dynamics, neither pure viscous flow, i.e. $R \propto t$, nor pure slippage, i.e. $R \propto t^{2/3}$, can be detected. It is shown that the linear superposition of both mechanisms, as proposed by Jacobs *et al.* [33], and a specific data evaluation method, as proposed by Fetzer and Jacobs [34], can be applied: Plotting the dewetting velocity V versus $1/\sqrt{R}$ instead of plotting R versus the time t , enables the separation of radius-dependent (slippage) and radius-independent (viscous flow) velocity contributions. In conjunction with measurements of the

width of the rim surrounding the hole according to conservation of volume, the slip length can be extracted. Three types of hydrophobic coatings on Si wafers (with native oxide layer) were used: self-assembled monolayers of two types of silanes, dodecyl-trichlorosilane (DTS) and octadecyl-trichlorosilane (OTS), and an amorphous Teflon[®] coating (AF 1600).

Below the critical molecular weight for chain entanglements Comparing the dewetting velocities of PS films of identical viscosity and molecular weight on different hydrophobic substrates clearly reveals enormous differences. For PS(13.7k) at a fixed temperature, dewetting is significantly faster on DTS as compared to OTS (see ADDENDUM III). The driving force on both surfaces is the same and is a result of the identical Young's contact angle of PS on both substrates [34]. The viscosity of the polymer melt is also identical and, hence, the dissipation by viscous friction within the liquid counteracting the driving force is essentially the same. As a consequence, the mechanism of sliding friction has to play a more significant role on DTS. This conclusion is corroborated by the fact that, as presented in Chapter 4 and ADDENDUM III of this thesis, hole growth for the same liquid parameters on AF 1600 is significantly slower than for the equivalent dewetting scenario on OTS. The contact angle of PS is even larger than on the silanized substrates and, hence, the driving force for dewetting is larger on AF 1600. Nevertheless, a considerably larger friction coefficient causes less slippage and slower dewetting.

Quantitative evaluation of the experimental data (i.e. the slope in the representation of V as a function of $1/\sqrt{R}$) provides clear evidence for a weak-slip situation on the AF 1600 substrate, which is characterized by a slip length in the range of 10 to 100 nm. This is considerably lower (orders of magnitude, depending on the dewetting temperature) compared what is found for the OTS and DTS substrates [34]. This result illuminates the enormous impact of slippage on the fluidics of liquids on the micro- and nanoscale.

The viscous (radius-independent) velocity contribution on the AF 1600 substrate is found to be in excellent agreement with the theoretical expectation: A proportionality of the viscous velocity contribution to the reciprocal viscosity of the polymer melt is evidenced. Systematic deviations from this behavior are found on OTS and DTS when comparing these results to the results on AF 1600. As reported by Redon *et al.*, non-vanishing slippage contributions exert an influence on the flow field in the vicinity of the three-phase contact line and, thus, also affect the viscous flow velocity contribution [19, 22]. Hence, a correlation between the slip length (especially in cases of huge slip lengths as found for DTS at temperatures close to the glass transition temperature) to the viscous velocity contribution is evident.

Above the critical molecular weight for chain entanglements Subsequently, experiments were extended to diverse molecular weights and chain lengths above the corresponding critical values for the occurrence of chain entanglements. Again, the aforementioned model and data evaluation technique was applied. To exclude viscoelastic effects originating from the preparation process, samples were pre-annealed to avoid the relaxation of residual stresses during the experiment. For the chosen molecular weights and the shear rates present in the corresponding dewetting scenarios, the Weissenberg numbers are in the range of 0.1 at maximum.

Therefore, viscoelastic effects causing non-Newtonian behavior can be safely excluded. Entanglements, however, are expected to have a strong impact on the slip length of polymer flows on non-adsorbing substrates: De Gennes predicted an increase in the slip length b proportional to N^3 according to scaling arguments, where N denotes the number of monomers [52]. Indeed, a strong correlation between slip length and the molecular weight M_w (which is proportional to the chain length N of the polymer) and an excellent agreement of the experimentally obtained scaling exponent, i.e. $b \propto N^{2.9} \propto M_w^{2.9}$, is found.

Analysis of Liquid Rim Profiles

In the context of the experiments on hole growth dynamics, the self-similar evolution of the rims marks an essential precondition for the applicability of the evaluation technique for the hole growth data. This technique was used, as described in the first part of this summary, to calculate the slip length from hole growth experiments. *In situ* atomic force microscopy (AFM) experiments on the AF 1600 substrate were carried out to confirm the self-similar growth of the rim; the spatial and temporal evolution of the rim was probed and the proportionality between the maximum rim height and the width of the rim was confirmed.

Ex situ AFM imaging of the rim profiles of formerly analyzed holes was carried out by quenching the samples to room temperature at constant hole radius. The morphology of the section of the rim where the height profile merges the unperturbed film has shown to be sensitive to the hydrodynamic boundary condition at the solid/liquid interface (as given by the slip length) [28, 58]. The strong-slip lubrication model, to which the aforementioned studies refer to is, however, limited in its applicability to slip lengths b which are much larger than the film thickness h_0 , i.e. $b \gg h_0$. Therefore, parallel to the experimental studies, a more generalized model based on the full Stokes equations was developed according to a Taylor expansion [29]. The decisive advantage of this new model lies in its unlimited applicability independent of the slip length. Compared to the strong-slip lubrication model, this model exhibited similar characteristics, i.e. in particular a transition from oscillatory to monotonic solutions (see ADDENDUM IV). Fitting an exponentially damped oscillation (to profiles exhibiting a trough) or a superposition of two exponential decays (to monotonically decaying profiles) allows to extract the slip length b , but also to extract the capillary number Ca .

Below the critical molecular weight for chain entanglements *Ex situ* AFM measurements of the rim shape were performed after quenching the samples to room temperature. The morphology of the rim profiles of thin PS films on DTS, OTS and AF 1600 substrates is different: For PS(13.7k) at an identical dewetting temperature, the rim profile on the OTS substrate exhibits a "trough" where the rim merges the unperturbed film (called oscillatory profile), whereas on the DTS substrate, a monotonic decay of the rim can be found. This aspect is described in detail in ADDENDUM IV in conjunction with the evaluation of the data for DTS and OTS according to the new thin film model. Substantial differences in the slip length on the different substrates are found: As first reported by R. Fetzer [58] and recalculated according to the more generalized new "Stokes model" (see ADDENDUM IV), the slip length b on DTS is found to be in the range of up to 5 μm . On OTS, the slip length is about one

order of magnitude smaller compared to DTS. For both substrates, the slip lengths decrease as the dewetting temperature increases. For the AF 1600 substrate, exclusively oscillatory profiles are obtained below the critical molecular weight for chain entanglements: Slip lengths up to 150 nm are found, independent of the dewetting temperature and in good agreement with results from the hole growth analysis.

Aside from the determination of the slip length, also the capillary number can be extracted. Taking the current dewetting velocity from the corresponding hole growth experiment enables the calculation of the viscosity. The good agreement of the viscosity data, as obtained from the rim profile analysis, to independent viscosimeter results demonstrates an important consistency check for the theoretical model.

Above the critical molecular weight for chain entanglements As shown in previous studies [39, 54], increasing the molecular weight of the polymer melt leads to less steep decays of the rim into the unperturbed film. The quantification of slippage in view of the variation of the molecular weight on the AF 1600 substrate is described in ADDENDUM V. Again, a strong correlation between the slip length and the molecular weight is found (corroborating the previously described result from the hole growth analysis): The slip length increases with $b \propto N^{2.9} \propto M_w^{2.9}$, reproducing the prediction by de Gennes' reptation theory of entangled polymer melt dynamics. A variation of the dewetting temperature does not exert a significant influence on the shape of the rim profile. Preparing the identical viscosity for different molecular weights and different temperatures shows a remarkable result: The slip length is found to be (for the example studied here) two orders of magnitude larger for longer polymer chains (the larger molecular weight). Consequently, slippage is found to be directly correlated to the polymer chain entanglements rather than to the viscosity of the melt.

Special attention is drawn to the fact that, in this thesis, evidence for a reduced interfacial entanglement density is found in the vicinity of the solid/liquid interface. The model by de Gennes predicts a correlation between the slip length and the entanglement length N_e , i.e. $b \propto N_e^{-2}$. The entanglement length N_e describes the number of monomers between two entanglements. Comparing the experimental results to the model by de Gennes using bulk (literature) values for N_e features a systematic discrepancy between the experiment and the bulk model: The slip length is roughly one order of magnitude smaller as compared to the model based on the bulk entanglement length. This result suggests an increase of the entanglement length by a factor of 3.2 and, thereby, a decrease of the *effective* entanglement density. Brown and Russell [65] use rather simple geometric arguments to predict an increase of N_e by roughly a factor of 4 in the vicinity of the solid/liquid interface, which corroborates the experimental finding. Moreover, it has to be emphasized that the reduction of the entanglement density is caused by the presence of the wall and its impact on the formation of inter-chain entanglements in the vicinity of the solid/liquid interface and not by the confinement given by the film thickness: Thicker PS films do not exhibit significantly larger slip lengths.

In particular, the comparison of rim profiles for the identical molecular weight (above the critical entanglement length of the polymer), temperature and preparation of the polymer film on different substrates impressively visualizes the impact of slippage on the shape of liquid

rims. The morphological differences can, consequently, certainly not be related to viscoelastic effects.

Continuative Studies

First experimental studies were extended to polymer mixtures of two distinct molecular weights instead of monodisperse polymer melts and to thin poly(methyl methacrylate) (PMMA) films instead of PS. By adding 20% short PS chains to a polymer melt, neutron scattering experiments (in collaboration with the groups of Prof. Dr. Andreas Magerl and Prof. Dr. Hartmut Zabel) of a thin film supported by a bare Si wafer suggest a migration of the short species towards the liquid/air interface. Consequently, annealing the as-cast films and transferring them to the hydrophobic AF 1600 substrate should lead to an accumulation of short polymer chains at the solid/liquid interface. The slip length did not show significant deviations from the purely long-chained polymer melt yet. Consequently, the presence of short polymer chains did not lead to a modification of slippage. In the second part of this chapter, the dewetting of PMMA(14k) melts was studied. First experiments show that the rim profile analysis is also applicable to this system. In agreement with the results for PS, a weak-slip situation is present in the case of AF 1600 substrates.

These cutting-edge experiments represent starting points for future investigations and can be extended to gain further remarkable information about the link between polymer properties and slippage of polymer chains at the solid/liquid interface.

7.2 Outlook

Impact of Surface Properties on Slippage

The methods presented in this thesis can be applied to further polymer/solid configurations in view of distinct properties of the polymer melt and/or the solid substrate:

The influence of the **surface roughness** might be systematically studied by the analysis of dewetting experiments on substrates with variable roughness values or types of roughness. Initial studies were started using mesoporous silicon wafers (in collaboration with Dr. Patrick Huber from Saarland University) that were silanized with a hydrophobic OTS layer [82]. Etching techniques also allow a controlled roughening of intrinsically smooth silicon wafers in the range of a few nanometers (avoiding the generation of pores in the material).

Aside from the topographical structure, the chemical composition of the substrates utilized for dewetting experiments can also be systematically varied. Physical chemistry, thus, provides a variety of techniques to chemically modify surfaces in view of their **surface energy** and their **wettability**. For simple liquids such as water, a correlation between the slip length and the wettability was recently reported [83].

Liquid Properties and the Role of Polymer Chain Entanglements

As described in ADDENDUM II, a variety of parameters are supposed to have an impact on the slip length. Dewetting studies of further polymeric liquids might shed light on the link between slippage and these parameters (such as e.g. the **dipole moment** [84]) of the polymer. In this study, first dewetting experiments and a proof-of-concept concerning the applicability of the experimental techniques were accomplished for **poly(methyl methacrylate) (PMMA)**. Systematic studies (variation of the molecular weight, temperature, etc.) are promising and might result in new insights concerning the role of the **monomeric structure** of the polymer and its impact on slippage.

Thin films of PMMA show differences compared to PS films concerning their interaction with solid substrates as evidenced in diverse studies investigating the **glass transition temperature** (see ADDENDUM II). Forrest, Dalnoki-Veress and Dutcher could show that the polymer-substrate interaction is the dominant effect in determining the glass transition temperature as a function of PS film thickness supported by SiO surfaces [85]. For the surface of polystyrene films, i.e. the liquid/air interface, Fakhraai and Forrest recently reported an enhanced surface mobility compared to the bulk [86]. In view of the mobility of polymer chains and the role of chain entanglements at the solid/liquid interface, experiments using PMMA melts could additionally contribute further important results to the debate concerning the glass transition temperature of thin polymer films. In view of the impact of **confinement** on the glass transition temperature, dewetting experiments of polymer films in the range of the spatial dimensions of the polymer (e.g. given by $2 \times R_g$) might provide interesting findings and insights.

Viscoelastic Effects and Slippage

Weissenberg numbers for dewetting experiments using considerably longer polymer chains than PS(390k) close to their glass transition temperature could potentially exceed the critical value of 1. Such experiments are expected to show **non-Newtonian flow behavior** in terms of viscoelastic stress relaxation. Viscoelastic effects are theoretically covered by corresponding models developed by Dr. Markus Rauscher, Dr. Andreas Münch, Dr. Barbara Wagner and Prof. Dr. Ralf Blossey for different slip conditions [87, 88]. In case of substantial slip present in the system, however, slip effects are supposed to be not distinguishable from viscoelastic effects. Additionally, a controlled variation of stress is experimentally difficult to realize. Taking these facts together, studying the interplay of viscoelastic effects and slippage quantitatively through the analysis of rim profiles seems to be not practicable.

Molecular Mechanism of Slippage on OTS and DTS

One of the main tasks for future studies is to accomplish a direct proof of the molecular mechanism of slippage on the silanized substrates, i.e. OTS and DTS. Direct experimental access to the molecular level is provided by **neutron and X-ray scattering techniques**. Additional experiments are planned in collaboration with the groups of Prof. Dr. Hartmut Zabel and Prof. Dr. Andreas Magerl. In parallel to these scattering studies, further pathways are

currently followed to explore the molecular interactions of polymer chains and self-assembled silane monolayers:

Comparing OTS and DTS, only very few parameters show significant differences: The **length of the silane molecules** (thickness of the monolayer) and the **surface energy** of the silanized surfaces are different and could potentially exert an influence on the spatial dimension or conformations of polymer chains and, thus, on the flow properties. Dewetting experiments using **hexadecyl-trichlorosilane (HTS)**, exhibiting 16 carbon atoms in its backbone (compared to 12 for DTS and 18 for OTS), were started to clarify the role of the length of the molecules forming the SAM [89]. Self-assembled monolayers of **perfluoro-silanes** will be used as substrates for corresponding dewetting experiments to study the impact of the surface energy (which is supposed to be in the range of the AF 1600 substrate due to the similar chemical composition) on slippage.

Simulation Studies

The interaction of polymer chains with the self-assembled monolayer and the reduction of inter-chain entanglements, as evidenced for the AF 1600 substrate, are of enormous fundamental interest. **Molecular dynamic (MD) simulations**, performed in the group of Prof. Marcus Müller, could help to gain new insights concerning the structure of the solid/liquid interface and near-surface flows [90, 91]. **Dissipative particle dynamics (DPD) simulations**, performed in the group of Prof. Ignacio Pagonabarraga and by Dr. Samy Merabia, show interesting results concerning dewetting of immiscible fluids exhibiting two different viscosities: An upper high-viscosity layer can slide on a lower low-viscosity layer at the solid/liquid interface leading to a faster dynamics attributed to this lubrication effect [92].

Slippage and the Liquid Rim Instability

Aside from the aforementioned techniques to analyze and quantify frictional and rheological properties of polymers, it was experimentally and theoretically shown in collaboration with Dr. Andreas Münch and Dr. Barbara Wagner that the liquid rim instability (see e.g. [51]) is also an indicator for the slip/no-slip boundary condition [93, 94, 95, 96]. This instability is comparable to the Rayleigh-Plateau instability emerging on a surface of a cylindrical jet of water flowing off a tap. The resulting surface corrugations can be optically observed and the jet finally decays into discrete droplets [13, 14]. The **morphology of the instability** of retracting straight fronts in thin liquid films is governed by the hydrodynamic boundary condition [94, 96]: While under no-slip conditions symmetric liquid bulges (co-moving with the front) are found, slippage causes the formation of asymmetric finger-like structures (see Fig. 7.1). This phenomenon can be optically observed and represents a further way to access slippage in thin polymer films. Further characteristics of the instability such as the evolution of the wavelength of the instability along the receding front (on lateral scale and perpendicular to the surface plane) are subject of ongoing investigations [96].

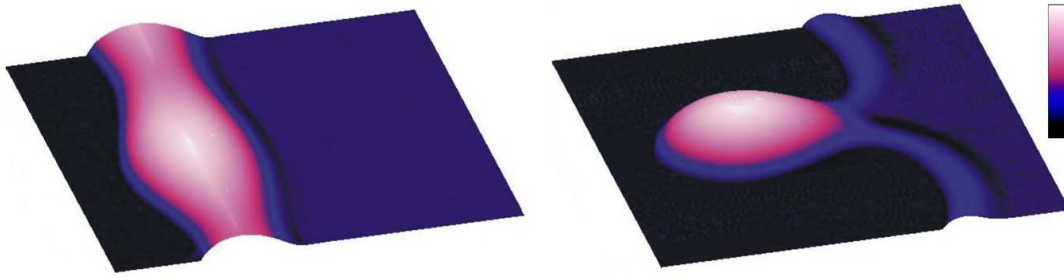


Figure 7.1: AFM height data visualizing the liquid rim instability of a 130 nm PS(13.7k) film at 120 °C dewetting from different substrates [94]. Left: PS on AF 1600 after 91 minutes (lateral scale: 20 μm). The rim exhibits a rather symmetric representation of the instability. Right: PS on DTS after 50 minutes (lateral scale: 25 μm). The instability is asymmetric and a liquid finger is formed. The height scale of 5 μm is indicated by the color code.

Slippage and Spinodal Dewetting

In a recent theoretical work by Dr. Markus Rauscher, Prof. Dr. Ralf Blossey, Dr. Andreas Münch and Dr. Barbara Wagner [97], the wavelength of spinodally dewetting thin polymer films is shown to be influenced by slippage. Up to now, studies of spinodal dewetting of polymer films were mainly performed on hydrophilic substrates (usually silicon wafers with different oxide layer thicknesses, see ADDENDUM I and II). Recently, the preparation of thin PS(2k) films (in the range of 3 to 4 nm) on **hydrophobic DTS and OTS substrates** was achieved. This project will focus on two aspects: First, the spinodal wavelength (which can be determined via AFM experiments) and its correlation to the effective interface potential $\phi(h)$. By adding a hydrophobic layer (with a certain layer thickness) to the hydrophilic SiO_2 surface, however, additional contributions to $\phi(h)$ have to be considered. Moreover, the short-range interactions are varied. Experimental studies will show whether these effects can be separated from an effect originating from the slip-boundary condition. The second aspect concerns the dynamics of the instability: As described in ADDENDUM I, the time constant of the evolution of the amplitudes of the instability (again measured with AFM) depends on certain parameters such as the viscosity and the film thickness. First results from spinodal dewetting on DTS, however, suggest significantly faster dewetting dynamics than expected [89].

Bibliography

- [1] P.G. de Gennes, F. Brochard-Wyart and D. Quéré, *Capillarity and Wetting Phenomena - Drops, Bubbles, Pearls, Waves* (Springer: New York, 2004).
- [2] W. Barthlott and C. Neinhuis, *Planta* **202**, 1 (1997).
- [3] C. Neinhuis and W. Barthlott, *Annals of Botany* **79**, 667 (1997).
- [4] T.M. Squires and S.R. Quake, *Rev. Mod. Phys.* **77**, 977 (2005).
- [5] T. Thorsen, S.J. Maerkl and S.R. Quake, *Science* **298**, 580 (2002).
- [6] D.C. Leslie, C.J. Easley, E. Seker, J.M. Karlinsey, M. Utz, M.R. Begley, and J.P. Landers, *Nature Physics* **5**, 231 (2009).
- [7] A. Vrij, *Discuss. Faraday Soc.* **42**, 23 (1966).
- [8] J. Israelachvili, *Intermolecular and Surface Forces* 2nd ed. (Academic Press Inc.: New York, 1992).
- [9] S. Herminghaus, K. Jacobs, K. Mecke, J. Bischof, A. Fery, M. Ibn-Elhaj, and S. Schlagowski, *Science* **282**, 916 (1998).
- [10] R. Seemann, S. Herminghaus and K. Jacobs, *Phys. Rev. Lett.* **86**, 5534 (2001).
- [11] R. Seemann, S. Herminghaus and K. Jacobs, *J. Phys.: Condens. Matter* **13**, 4925 (2001).
- [12] K. Jacobs, R. Seemann and S. Herminghaus, *Stability and Dewetting of Thin Liquid Films in Polymer Thin Films* ed. by O.K.C. Tsui and T.P. Russell (World Scientific: Singapore, 2008).
- [13] J. Plateau, *Statique expérimentale et théorique des liquides soumis aux seules forces moléculaires* (Gauthiers-Villars: Paris, 1873).
- [14] Lord Rayleigh, *Scientific Papers* (Cambridge University Press: Cambridge, 1899): *Proc. London Math. Soc.* **10**, 4 (1878); *Proc. R. Soc. London* **29**, 71 (1879); *Philos. Mag.* **34**, 145 (1873).
- [15] E. Ruckenstein and R.K. Jain, *J. Chem. Soc. Faraday Trans.* **II**, 132 (1974).
- [16] F. Brochard-Wyart, J.-M. di Meglio and D. Quéré, *C. R. Acad. Sci. Paris II* **304**, 553 (1987).
- [17] A. Sharma and E. Ruckenstein, *J. Colloid Interface Sci.* **133**, 358 (1989).
- [18] F. Brochard-Wyart and J. Dailant, *Can. J. Phys.* **68**, 1084 (1990).
- [19] C. Redon, F. Brochard-Wyart and F. Rondelez, *Phys. Rev. Lett.* **66**, 715 (1991).

- [20] F. Brochard-Wyart, C. Redon and C. Skykes, *C.R. Acad. Sci. Paris II* **314**, 19 (1992).
- [21] G. Reiter, *Phys. Rev. Lett.* **68**, 75 (1992).
- [22] C. Redon, J.B. Brzoska and F. Brochard-Wyart, *Macromolecules* **27**, 468 (1994).
- [23] L.D. Landau and E.M. Lifschitz, *Lehrbuch der theoretischen Physik, Band VI, Hydrodynamik* 5th ed. (Verlag Harri Deutsch: Frankfurt, 2007).
- [24] C.L.M.H. Navier, *Mem. Acad. Sci. Inst. Fr.* **6**, 389 and 432 (1823).
- [25] A. Oron, S.H. Davis and S.G. Bankoff, *Rev. Mod. Phys.* **69**, 931 (1997).
- [26] K. Kargupta, A. Sharma and R. Khanna, *Langmuir* **20**, 244 (2004).
- [27] A. Münch, B.A. Wagner and T.P. Witelski, *J. Eng. Math.* **53**, 359 (2005).
- [28] R. Fetzer, K. Jacobs, A. Münch, B. Wagner, and T.P. Witelski, *Phys. Rev. Lett.* **95**, 127801 (2005).
- [29] R. Fetzer, A. Münch, B. Wagner, M. Rauscher and K. Jacobs, *Langmuir* **23**, 10559 (2007).
- [30] R. Blossey, *Phys. Chem. Chem. Phys.* **10**, 5177 (2008).
- [31] P.G. de Gennes, *Rev. Mod. Phys.* **57**, 827 (1985).
- [32] F. Brochard-Wyart, P.G. de Gennes, H. Hervet, and C. Redon, *Langmuir* **10** 1566 (1994).
- [33] K. Jacobs, R. Seemann, G. Schatz, and S. Herminghaus, *Langmuir* **14**, 4961 (1998).
- [34] R. Fetzer and K. Jacobs, *Langmuir* **23**, 11617 (2007).
- [35] G. Binnig, C.F. Quate and C. Gerber, *Phys. Rev. Lett.* **56**, 930 (1986).
- [36] B. Bhushan (ed.), *Springer Handbook of Nanotechnology* (Springer: Berlin, Heidelberg, New York, 2004).
- [37] H.G. Tompkins, *A User's Guide to Ellipsometry* (Academic Press Inc.: San Diego, 1993).
- [38] R.M.A. Azzam and N.M. Bashara, *Ellipsometry and Polarized Light* (North Holland: Amsterdam, 1977).
- [39] R. Fetzer, *Einfluss von Grenzflächen auf die Fluidik dünner Polymerfilme*, Dissertation (Saarland University, 2006) and Logos Verlag Berlin, ISBN 3-8325-1354-X.
- [40] J. Sagiv, *J. Am. Chem. Soc.* **102**, 92 (1980).
- [41] K. Jacobs, *Stabilität und Dynamik flüssiger Polymerfilme*, Dissertation (University of Konstanz, 1997) and UFO Verlag Allensbach **311**, ISBN 3-930803-10-0 (1997).
- [42] R. Sherman, D. Hirt and R. Vane, *J. Vac. Sci. Technol. A* **12**, 1876 (1994).
- [43] R. J. Good and L. A. Girifalco, *J. Phys. Chem.* **64**, 561 (1960).
- [44] T. Young, *Philos. Trans. Soc. London* **95**, 65 (1805).
- [45] J. Brandrup, E.H. Immergut and E.A. Grulke, *Polymer Handbook* 4th ed. (John Wiley & Sons Inc.: New York, 1999).

- [46] T. Pompe and S. Herminghaus, *Phys. Rev. Lett.* **85**, 1930 (2000).
- [47] R. Seemann, K. Jacobs and R. Blossey, *J. Phys.: Condens. Matter* **13**, 4915 (2001).
- [48] M. Rubinstein and R. Colby, *Polymer Physics* (Oxford University Press Inc.: New York, 2003).
- [49] D. Podzimek, A. Saier, R. Seemann, K. Jacobs, and S. Herminghaus, *arXiv:cond-mat/0105065v1* (2001).
- [50] M.L. Williams, R.F. Landel and J.D. Ferry, *J. Am. Chem. Soc.* **77**, 3701 (1955).
- [51] F. Brochard-Wyart and C. Redon, *Langmuir* **8**, 2324 (1992).
- [52] P.G. de Gennes, *C. R. Acad. Sci. B* **288**, 219 (1979).
- [53] F. Brochard-Wyart, G. Debregeas, R. Fondcave, and P. Martin, *Macromolecules* **30**, 1211 (1997).
- [54] R. Seemann, S. Herminghaus and K. Jacobs, *Phys. Rev. Lett.* **87**, 196101 (2001).
- [55] D. Podzimek, *Nanorheologie komplexer Flüssigkeiten*, Dissertation (Saarland University, 2005).
- [56] G. Reiter, M. Hamieh, P. Damman, S. Slavovs, S. Gabriele, T. Vilmin, and E. Raphaël, *Nature Materials* **4**, 754 (2005).
- [57] P. Damman, S. Gabriele, S. Coppée, S. Desprez, D. Villers, T. Vilmin, E. Raphaël, M. Hamieh, S. Al Akhrass, and G. Reiter, *Phys. Rev. Lett.* **99**, 036101 (2007).
- [58] R. Fetzer, M. Rauscher, A. Münch, B.A. Wagner, and K. Jacobs, *Europhys. Lett.* **75**, 638 (2005).
- [59] S. Herminghaus, K. Jacobs and R. Seemann, *Eur. Phys. J. E* **5**, 531 (2001).
- [60] S. Herminghaus, K. Jacobs and R. Seemann, *Eur. Phys. J. E* **12**, 101 (2003).
- [61] M. Müller, Personal Communication, 2009.
- [62] P.G. de Gennes, *J. Chem. Phys.* **55**, 573 (1971).
- [63] P.G. de Gennes, *Scaling Concepts in Polymer Physics* (Cornell University Press: Ithaca, New York, 1979).
- [64] J.-L. Barrat and L. Bocquet, *Phys. Rev. Lett.* **82**, 4671 (1999).
- [65] H.R. Brown and T.P. Russell, *Macromolecules* **29**, 798 (1996).
- [66] J. Kraus, P. Müller-Buschbaum, T. Kuhlmann, D.W. Schubert, and M. Stamm, *Europhys. Lett.* **49**, 210 (2000).
- [67] L. Si, M.V. Massa, K. Dalnoki-Veress, H.R. Brown, and R.A.L. Jones, *Phys. Rev. Lett.* **94**, 127801 (2005).
- [68] H.D. Rowland, W.P. King, J.B. Pethica, and G.L.W. Cross, *Science* **322**, 720 (2008).

- [69] D.R. Barbero and U. Steiner, *Phys. Rev. Lett.* **102**, 248303 (2009).
- [70] M. Vladkov and J.-L. Barrat, *Macromolecules* **40**, 3797 (2007).
- [71] H. Meyer, T. Kreer, A. Cavallo, J.P. Wittmer, and J. Baschnagel, *Eur. Phys. J. Special Topics* **141**, 167 (2007).
- [72] S. Al Akhrass, G. Reiter, S.Y. Hou, M.H. Yang, Y.L. Chang, F.C. Chang, C.F. Wang, and A.C.-M. Yang, *Phys. Rev. Lett.* **100**, 178301 (2008).
- [73] K. Kostourou, Personal Communication, 2009.
- [74] F. Brochard and P.G. de Gennes, *Langmuir* **8**, 3033 (1992).
- [75] C. Yu, G. Evmenenko, J. Kmetko, and P. Dutta, *Langmuir* **19**, 9558 (2003).
- [76] S. Lichter, A. Martini, R.Q. Snurr, and Q. Wang, *Phys. Rev. Lett.* **98**, 226001 (2007).
- [77] P. Gutfreund, Personal Communication, 2009.
- [78] V. Schön, Personal Communication, 2009.
- [79] M. Buck (School of Chemistry, University of St. Andrews, UK), Personal Communication, 2009.
- [80] R.A.L. Jones, L.J. Norton, E.J. Kramer, R.J. Composto, R.S. Stein, T.P. Russell, A. Mansour, A. Karim, G.P. Felcher, M.H. Rafailovich, J. Sokolov, X. Zhao, and S.A. Schwarz, *Europhys. Lett.* **12**, 41 (1990).
- [81] L. Bocquet and J.-L. Barrat, *Soft Matter* **3**, 685 (2007).
- [82] M. Lessel, *Entnetzungs-dynamik auf strukturierten Oberflächen - Dünne Polymerfilme auf porösen Substraten*, Diploma Thesis (Saarland University, 2008).
- [83] D.M. Huang, C. Sendner, D. Horinek, R.R. Netz, and L. Bocquet, *Phys. Rev. Lett.* **101**, 226101 (2008).
- [84] J.-H.J. Cho, B.M. Law and F. Rieutord, *Phys. Rev. Lett.* **92**, 166102 (2004).
- [85] J.A. Forrest, K. Dalnoki-Veress and J.R. Dutcher, *Phys. Rev. E* **56**, 5705 (1997).
- [86] Z. Fakhraai and J.A. Forrest, *Science* **319**, 600 (2008).
- [87] M. Rauscher, A. Münch, B. Wagner, and R. Blossey, *Eur. Phys. J. E* **17**, 373 (2005).
- [88] R. Blossey, A. Münch, M. Rauscher, and B. Wagner, *Eur. Phys. J. E* **20**, 267 (2006).
- [89] M. Lessel, Personal Communication, 2009.
- [90] J. Servantie and M. Müller, *Phys. Rev. Lett.* **101**, 026101 (2008).
- [91] M. Müller, C. Pastorino and J. Servantie, *J. Phys.: Condens. Matter* **20**, 494225 (2008).
- [92] S. Merabia and J.B. Avalos, *Phys. Rev. Lett.* **101**, 208304 (2008).
- [93] A. Münch and B. Wagner, *Physica D* **209**, 178 (2005).

Bibliography

- [94] J. Mainka, *Instabilitäten in flüssigen Filmen - Strukturbildung beim Entnetzen*, Diploma Thesis (Saarland University, 2007).
- [95] J.R. King, A. Münch and B. Wagner, *J. Eng. Math.* **63**, 177 (2009).
- [96] L. Marquant, O. Bäumchen, J. Mainka, A. Münch, B. Wagner, F. Müller, and K. Jacobs, *to be published* (2010).
- [97] M. Rauscher, R. Blossey, A. Münch, and B. Wagner, *Langmuir* **24**, 12290 (2008).

Bibliography

Publications and Conference Contributions

Publications

- K. JACOBS, R. KONRAD, H. MANTZ, D. PODZIMEK, A. QUINN, M. MEIER, A. NAGEL, AND O. BÄUMCHEN, “Von Tropfen und Flüssigkeiten: Strukturbildung und Dynamik in makromolekularen Filmen“, *Magazin Forschung, Universität des Saarlandes*, **2** (2004).
- O. BÄUMCHEN, R. FETZER, AND K. JACOBS, “Probing Slippage and Flow Dynamics of Thin Dewetting Polymer Films“, *Proceedings of the 1st European Conference on Microfluidics - Microfluidics 2008, Bologna, December 10-12, 2008*, μ Flu08-194, ISBN 2-906831-76-X (2008).
- O. BÄUMCHEN, R. FETZER, A. MÜNCH, B. WAGNER, AND K. JACOBS, “Comprehensive Analysis of Dewetting Profiles to Quantify Hydrodynamic Slip“, *IUTAM Symposium on Advances in Micro- and Nanofluidics, IUTAM Bookseries, Vol. 15, pages 51-65*, Ed. by M. Ellero, X. Hu, J. Fröhlich, N. Adams, Springer, ISBN 978-90-481-2625-5 (2009).
- O. BÄUMCHEN, R. FETZER, AND K. JACOBS, “Reduced Interfacial Entanglement Density Affects the Boundary Conditions of Polymer Flow“, *Phys. Rev. Lett.* **103**, 247801 (2009).
- O. BÄUMCHEN, AND K. JACOBS, “Slip Effects in Thin Polymer Films“, *J. Phys.: Condens. Matter* **22**, 033102(21pp) (2010).
- O. BÄUMCHEN, M. LESSEL, R. FETZER, R. SEEMANN AND K. JACOBS, “Sliding Fluids: Dewetting Experiments Reveal the Solid/Liquid Boundary Condition“, *J. Phys.: Conf. Ser. (accepted)* (2010).
- O. BÄUMCHEN, AND K. JACOBS, “Can Liquids Slide? Stability and Dynamics of Liquids on Surfaces“, *Soft Matter (submitted)* (2010).

Awards

- Best Poster Award - O. BÄUMCHEN, R. FETZER, AND K. JACOBS, “Liquid Front Profiles Affected by Entanglement-Induced Slippage“, *Polymer Interfaces: Science and Technology*, Darmstadt (GER) (09/2009).
- 2nd Poster Prize - O. BÄUMCHEN, R. FETZER, AND K. JACOBS, “Reduced Interfacial Entanglement Density Affects the Boundary Conditions of Polymer Flow“, *Concluding Conference of the Priority Program - "Micro- and Nanofluidics"*, Norderney (GER) (02/2010).

Scientific Talks

- “Wetting Properties of Nanostructured Composite Surfaces and Patterning of Monolayer and Polymer Surfaces“,
Group Seminar, Oberstdorf (GER) (03/2006).
- “Wetting Properties of Nanostructured Surfaces“,
Seminar of the Graduate College 1276, Saarbrücken (GER) (07/2006).
- “Impact of the Solid/Liquid Interface on Flow Dynamics of Thin Polymer Films“,
Feldberg Winter School, Feldberg (GER) (12/2006).
- “Impact of the Solid/Liquid Interface on Flow Dynamics of Thin Polymer Films“,
PhD Students’ Day, Saarbrücken (GER) (03/2007).
- “Impact of the Solid/Liquid Interface on Flow Dynamics of Thin Polymer Films“,
DPG Spring-Meeting, Regensburg (GER) (03/2007).
- “Impact of the Solid/Liquid Interface on Flow Dynamics of Thin Polymer Films“,
Workshop of the Priority Program - ”Micro- and Nanofluidics”, Bad Honnef (GER) (08/2007).
- “Impact of the Solid/Liquid Interface on Flow Dynamics of Thin Polymer Films“,
IUTAM Symposium on Advances in Micro- and Nanofluidics, Dresden (GER) (09/2007).
- “Quantifying Hydrodynamic Slip: Analysis of Dewetting Profiles of Thin Polymer Films on Smooth Hydrophobic Substrates“,
Feldberg Winter School, Feldberg (GER) (12/2007).
- “Flow Dynamics of Thin Polymer Films on Smooth Hydrophobic Surfaces“,
PhD Students’ Day, Saarbrücken (GER) (04/2008).
- “Slippage vs. Viscoelasticity in Thin Dewetting Polymer Films“,
Feldberg Winter School, Feldberg (GER) (12/2008).
- “Slippage at the Solid/Liquid Interface - Probing the Hydrodynamic Boundary Condition by Dewetting Experiments“,
Seminar Talk at the McMaster University, Hamilton / Ontario (CAN) (07/2009).
- “Slippage at the Solid/Liquid Interface - Probing the Hydrodynamic Boundary Condition by Dewetting Experiments“,
Seminar Talk at the Boston University, Boston / Massachusetts (USA) (08/2009).
- “Nanofluidics and Interfaces“,
German-Chinese Summer School for Microsystems, Saarbrücken (GER) (09/2009).
- “Reduced Interfacial Entanglement Density Affects the Boundary Conditions of Polymer Flow“,
Feldberg Winter School, Feldberg (GER) (12/2009).

Poster Presentations

- “Wetting Properties of Nanostructured Surfaces“, *DPG Spring-Meeting*, Dresden (GER) (03/2006).
- “Slippage at the Solid/Liquid Interface - Growth of Holes in Metastable Polymer Films, *ESF Conference Solid/Fluid Interfaces - Complex Fluid Interfaces and Nanofluidics*, Obergurgl (AUT) (09/2006).
- “Slippage at the Solid/Liquid Interface - Growth of Holes in Metastable Polymer Films, *Workshop of the Priority Program - "Micro- and Nanofluidics"*, Bad Honnef (GER) (10/2006).
- “Impact of the Solid/Liquid Interface on Flow Dynamics of Thin Polymer Films“, *Workshop of the Graduate College 1276*, Saarbrücken (GER) (09/2007).
- “Impact of the Solid/Liquid Interface on Flow Dynamics of Thin Polymer Films“, *International Soft Matter Conference*, Aachen (GER) (10/2007).
- “Probing Slippage of Thin Polymer Films on Smooth Hydrophobic Surfaces“, *DPG Spring-Meeting*, Berlin (GER) (02/2008).
- “Impact of Slippage on Thin Polymer Film Dewetting on Smooth Hydrophobic Substrates“, *Liquid Matter Conference*, Lund (SWE) (06/2008).
- “Impact of Slippage on Thin Polymer Film Dewetting on Smooth Hydrophobic Substrates“, *Workshop of the Priority Program - "Micro- and Nanofluidics"*, Bad Honnef (GER) (07/2008).
- “Analysis of Dewetting Dynamics and Profiles to Quantify Hydrodynamic Slippage“, *Chemical Nanotechnology Talks IX*, Frankfurt (GER) (11/2008).
- “Probing Slippage and Flow Dynamics of Thin Dewetting Polymer Films“, *First European Conference on Microfluidics* (Poster and Short Oral Presentation), Bologna (ITA) (12/2008).
- “Slippage at the Solid/Liquid Interface - Probing the Hydrodynamic Boundary Condition by Dewetting Experiments“, *Gordon Research Conference on Physics and Chemistry of Liquids*, Holderness / New Hampshire (USA) (08/2009).
- “Reduced Interfacial Entanglement Density Affects the Boundary Conditions of Polymer Flow“, *Concluding Conference of the Priority Program - "Micro- and Nanofluidics"*, Norderney (GER) (02/2010).

Selection of further Conference (Poster) Contributions

- “Fingering Instabilities in Thin Polymer Films“,
DPG Spring-Meeting, Regensburg (GER) (03/2007).
- “Fingering Instabilities in Thin Polymer Films“,
Workshop of the Priority Program - "Micro- and Nanofluidics", Bad Honnef (GER) (08/2007).
- “Flow of Thin Polymer Films on Mesoporous Silicon Surfaces“,
Liquid Matter Conference, Lund (SWE) (06/2008).
- “Flow of Thin Polymer Films on Mesoporous Silicon Surfaces“,
Workshop of the Priority Program - "Micro- and Nanofluidics", Bad Honnef (GER) (07/2008).
- “Thin Dewetting Polymer Film: Fingering and the Effect of Interfaces“,
Workshop of the Priority Program - "Micro- and Nanofluidics", Bad Honnef (GER) (07/2008).
- “Roughness Affects Slippage and Slippage Affects Hydrodynamic Instabilities“,
DPG Spring-Meeting, Dresden (GER) (03/2009).
- “The Influence of Thermal Noise and Slippage on the Dynamics of Spinodally Dewetting Polymer Films“,
Workshop of the Priority Program - "Micro- and Nanofluidics", Bad Honnef (GER) (07/2009).

Acknowledgement

I would like to thank all people that contributed, in different ways, to the success of this thesis!

First of all, I would like to thank **Prof. Dr. Karin Jacobs** for giving me the opportunity to join her group, for supervising my diploma thesis and, finally, also for supervising this PhD thesis. I appreciate your ideas, support, enthusiasm and also the freedom making own decisions and following own pathways. I would like to thank you also for introducing me to the soft matter community by giving me the opportunity to visit other researchers and their groups and by participating in so many national and international conferences. I benefited from vivid discussions with e.g. Prof. Dr. Terry Blake (during his visit in Saarbrücken), Prof. Dr. Lyderic Bocquet, Prof. Dr. Elisabeth Charlaix and Prof. Dr. Jean-Louis Barrat (during my visit in Lyon/France), Prof. Dr. Kari Dalnoki-Veress (during my visit in Hamilton/Canada), Prof. Dr. Ophelia Tsui (during my visit in Boston/USA) and many other people especially the members of the priority program on *Micro-and Nanofluidics* of the German Science Foundation.

Moreover, I would like to thank all collaborators from theory, mathematics and also from experimental physics: At first, I thank **Dr. Renate Fetzner**, who completed with her PhD thesis the previous link in a series of experiments and theoretical models that started many years ago. I am happy and proud to be part of this and, moreover, I am still surprised how much information about fundamental physical aspects can be drawn from this system. It was also a great pleasure to work with you on publications; especially receiving your valuable comments in the morning (evening at Australian time) and ending my work with the feeling that the development of the manuscript is still in progress. Thanks for your help in the lab at the beginning of my thesis and for the numerous discussions (and very fruitful comments) via email between Adelaide and Saarbrücken.

Dr. Andreas Münch and **Dr. Barbara Wagner** developed the thin film models and the theoretical background of the rim profile analysis. It was always a great pleasure to be part of the enthusiastic discussions, either at meetings of the priority program or also via diverse electronic channels and devices between Oxford, Berlin and Saarbrücken. I would like to thank **Prof. Dr. Marcus Müller** for sharing his ideas concerning the link between polymer viscosity including chain entanglements, friction at the solid/liquid interface and the slip length. **Dr. Markus Rauscher** was also involved in the project and I learned a lot from the discussions with him, especially at the beginning of my work. Furthermore, I would like to express my gratitude to **Prof. Dr. Ralf Seemann**, whose relocation from Göttingen to Saarbrücken is a great benefit for the soft matter community in Saarbrücken.

Besides support from theoretical physics and mathematics, this work was also supported by other experimental groups: I would like to thank **Prof. Dr. Hartmut Zabel**, **Prof. Dr. Andreas Magerl** and their groups for performing scattering experiments and for sharing the

enthusiasm to explore the solid/polymer interface by scattering techniques: **Dr. Max Wolff**, **Marco Walz**, **Nicole Voss**, **Stefan Gerth** and **Philipp Gutfreund**. At Saarland University, I thank **Volker Schön** and **Dr. Patrick Huber** for providing great X-ray scattering results of our self-assembled monolayer preparation.

Many thanks also to all the members of the **Soft Matter Group**! Thank you for the amazing support and the team spirit. This includes also the former members, especially **Dr. Hubert Mantz** who supported the work of the whole group with his kind and cooperative character, his ideas and his great commitment (also for small but nevertheless very important problems). I would like to thank **Julia Mainka** and **Matthias Lessel**, whose diploma theses (about the liquid rim instabilities and the influence of topographically structured substrates on dewetting) I supervised. Concerning the "instability project", I also appreciate the collaboration and valuable discussions with **Ludovic Marquant**, who completes the "polymer division" of the group.

Thanks to **Hendrik Hähl** not only for sharing a great time in the office and in the labs, but also for sharing the enthusiasm about physics (and skiing, rock climbing, music and so on) and the ups and downs during our PhD. Thank you also for the innumerable discussions about questions of physics and science in general.

I would like to thank my **fellow students** that made the time as a (PhD) student very pleasant. Moreover, I appreciate the support by my **family** and my **friends** (especially **Elina-Cara** and **Jaron**), that accorded me so much relief and directed my view also on other facets of life.

Maybe the most important part comes to my parents **Christine and Alois Bäumchen** who opened up all these possibilities to me, supported all my decisions and shared the ups and downs of my time as a student. This work would not have been possible without your support! Thank you!

Oliver

Curriculum Vitae

- **Personal Information**

Dipl.-Phys. Oliver Bäumchen

born at August 24th 1979 in Illingen / Germany, unmarried, German nationality

Private Address: Am Börrchen 30, D-66557 Illingen, Germany.

Work Address: Saarland University, Department of Experimental Physics, Campus, Building C6.3, Room 1.09, D-66123 Saarbrücken, Germany

Phone: +49(0)681/302-70489

Email: o.baeumchen@physik.uni-saarland.de

- **Work**

since 02/2006 - Co-worker and PhD Student in the Group of Prof. Dr. Karin Jacobs (Experimental Soft Matter Physics)

since 04/2006 - PhD Student within the Priority Program 1164 of the German Science Foundation on *Micro- and Nanofluidics*

04/2006 - 10/2007 - Scholarship of the Graduate College *Structure Formation and Transport in Complex Systems* 1276 of the German Science Foundation

10/2007 - 08/2008 - Lecturer for Experimental Physics at the University for Applied Sciences (HTW), Saarbrücken, Germany

- **Studies**

10/2000 - 01/2006 - Physics and Mathematics Studies at Saarland University, Saarbrücken, Germany

09/2002 - Intermediate Diploma in Mathematics

10/2002 - Intermediate Diploma in Physics

01/2006 - Diploma in Physics (Thesis in Experimental Physics with Prof. Dr. Karin Jacobs, *Wetting Properties of Nano-structured Materials: Scanning Probe Microscopy Studies of Nano-Composite and Wettability-Structured Surfaces*)

- **School and Alternative Civilian Service**

07/1990 - 06/1999 - German Abitur (General Qualification for University Entrance) at Illtal-Gymnasium, Illingen, Germany

07/1999 - 07/2000 - Alternative Civilian Service at St. Hedwigs Hospital, Illingen, Germany

Eidesstattliche Erklärung

Hiermit versichere ich an Eides statt, dass ich die vorliegende Arbeit selbständig und ohne Benutzung anderer als der angegebenen Hilfsmittel angefertigt habe. Die aus anderen Quellen oder indirekt übernommenen Daten und Konzepte sind unter Angabe der Quelle gekennzeichnet.

Die Arbeit wurde bisher weder im In- noch im Ausland in gleicher oder ähnlicher Form in einem Verfahren zur Erlangung eines akademischen Grades vorgelegt.

Saarbrücken, den 05. März 2010

(Oliver Bäumchen)